NASA/TP-2005-213766

High Reynolds Number Investigation of a Flush-Mounted, S-Duct Inlet With Large Amounts of Boundary Layer Ingestion

Bobby L. Berrier, Melissa B. Carter, and Brian G. Allan
Langley Research Center, Hampton, Virginia

September 2005

The NASA STI Program Office . . . in Profile

Since its founding, NASA has been dedicated to the advancement of aeronautics and space science. The NASA Scientific and Technical Information (STI) Program Office plays a key part in helping NASA maintain this important role.

The NASA STI Program Office is operated by Langley Research Center, the lead center for NASA's scientific and technical information. The NASA STI Program Office provides access to the NASA STI Database, the largest collection of aeronautical and space science STI in the world. The Program Office is also NASA's institutional mechanism for disseminating the results of its research and development activities. These results are published by NASA in the NASA STI Report Series, which includes the following report types:

- TECHNICAL PUBLICATION. Reports of completed research or a major significant phase of research that present the results of NASA programs and include extensive data or theoretical analysis. Includes compilations of significant scientific and technical data and information deemed to be of continuing reference value. NASA counterpart of peer-reviewed formal professional papers, but having less stringent limitations on manuscript length and extent of graphic presentations.

- TECHNICAL MEMORANDUM. Scientific and technical findings that are preliminary or of specialized interest, e.g., quick release reports, working papers, and bibliographies that contain minimal annotation. Does not contain extensive analysis.

- CONTRACTOR REPORT. Scientific and technical findings by NASA-sponsored contractors and grantees.

- CONFERENCE PUBLICATION. Collected papers from scientific and technical conferences, symposia, seminars, or other meetings sponsored or co-sponsored by NASA.

- SPECIAL PUBLICATION. Scientific, technical, or historical information from NASA programs, projects, and missions, often concerned with subjects having substantial public interest.

- TECHNICAL TRANSLATION. English-language translations of foreign scientific and technical material pertinent to NASA's mission.

Specialized services that complement the STI Program Office's diverse offerings include creating custom thesauri, building customized databases, organizing and publishing research results ... even providing videos.

For more information about the NASA STI Program Office, see the following:

- Access the NASA STI Program Home Page at ***http://www.sti.nasa.gov***

- E-mail your question via the Internet to help@sti.nasa.gov

- Fax your question to the NASA STI Help Desk at (301) 621-0134

- Phone the NASA STI Help Desk at (301) 621-0390

- Write to:
  NASA STI Help Desk
  NASA Center for AeroSpace Information
  7121 Standard Drive
  Hanover, MD 21076-1320

NASA/TP-2005-213766

High Reynolds Number Investigation of a Flush-Mounted, S-Duct Inlet With Large Amounts of Boundary Layer Ingestion

Bobby L. Berrier, Melissa B. Carter, and Brian G. Allan
Langley Research Center, Hampton, Virginia

National Aeronautics and
Space Administration

Langley Research Center
Hampton, Virginia 23681-2199

September 2005

Available from:

NASA Center for AeroSpace Information (CASI)
7121 Standard Drive
Hanover, MD 21076-1320
(301) 621-0390

National Technical Information Service (NTIS)
5285 Port Royal Road
Springfield, VA 22161-2171
(703) 605-6000

Abstract

An experimental investigation of a flush-mounted, S-duct inlet with large amounts of boundary layer ingestion has been conducted at Reynolds numbers up to full-scale. The study was conducted in the NASA Langley Research Center 0.3-Meter Transonic Cryogenic Tunnel. In addition, a supplemental computational study on one of the inlet configurations was conducted using the Navier-Stokes flow solver, OVERFLOW. The objectives of this investigation were to (1) develop and check out a new high Reynolds number test capability for flush-mounted inlets, (2) evaluate the performance of S-duct inlets with large amounts of boundary layer ingestion at Reynolds numbers up to full-scale, (3) provide a database for CFD tool validation on this class of inlet, and (4) provide a baseline inlet for future inlet flow-control studies. Tests were conducted at Mach numbers from 0.25 to 0.83, Reynolds numbers (based on aerodynamic interface plane diameter) from 5.1 million to 13.9 million (full-scale value) and inlet mass-flow ratios from 0.29 to 1.22, depending on Mach number. Results of the study indicated that increasing Mach number, increasing boundary layer thickness (relative to inlet height) or ingesting a boundary layer with a distorted profile decreased inlet performance. At Mach numbers above 0.4, increasing inlet airflow increased inlet pressure recovery but also increased distortion. Finally, inlet distortion was relatively insensitive to Reynolds number, but pressure recovery increased slightly with increasing Reynolds number.

Introduction

Highly integrated boundary layer ingesting (BLI), offset or S-duct inlets have the potential benefits of reduced drag, size and weight by eliminating the boundary layer diverter and shortening the inlet duct; reduced ram drag by reducing the momentum of the inlet flow (refs. 1 and 2); and lowered observability. However, to obtain these benefits from a system level requires that acceptable pressure recovery and distortion levels be maintained for engine operation.

The use of S-duct inlets is not new, even for commercial vehicles. The Boeing 727 (ref. 3) and Lockheed L-1011 (ref. 4) successfully used offset or S-duct inlet designs. In addition, because many new military aircraft have diverterless S-duct inlet systems, design issues have obviously been solved when the inlet is integrated on the forward portion of the vehicle with small amounts of boundary layer to ingest. Design guidelines for S-duct diffusers without significant amounts of BLI seem to be well defined (refs. 5–7).

However, design issues become more intractable when the inlet is integrated on the aft portion of the vehicle. The early Blended-Wing-Body (BWB) transport configuration (refs. 8 and 9) with either mail-slot or individual flush mounted inlets is an example of this type of inlet integration. The BWB has approximately a 25-in. thick boundary layer near the wing-body trailing edge, which is about 25- to 30-percent of the inlet height for a flush-mounted inlet on this configuration. Although this amount of BLI may be a formidable challenge, several published (ref. 2) and unpublished system studies have indicated large benefits for this amount of BLI (up to 10-percent reduction in fuel burn, for example) if the problems associated with BLI can be solved.

The two major technical challenges that must be addressed for BLI, S-duct inlets integrated on the aft portion of the vehicle are the complex external inlet aerodynamics and the nonuniform engine-face flow distribution. The complex external inlet aerodynamics is driven by thick, degraded boundary layers approaching the inlet, wing/body shocks at transonic speeds, and adverse pressure gradients caused by wing/body closure and inlet blockage. Nonuniform engine face distributions are driven by S-duct diffuser effects (secondary- or cross flows for example), ingested low-momentum boundary layer flow, and internal separation. Failure to adequately resolve these issues results in low inlet pressure recovery and high inlet pressure distortion, thus reducing available thrust and engine operability and possibly negating the benefits realized from the configuration design.

A search of open literature revealed no experimental information on BLI S-duct inlet performance for inlets with large amounts of BLI operating at realistic conditions. Most BLI investigations reported in the literature either considered only small amounts of BLI (maximum boundary layer thickness of 10 percent inlet diameter) or were conducted at extremely low Mach and Reynolds numbers (refs. 10 to 14). The objectives of this study were to develop a new high Reynolds number inlet test capability for BLI inlets, evaluate the performance of S-duct inlets with large amounts of BLI (boundary layer thickness of about 30-percent of inlet height) at realistic operating conditions (high subsonic Mach numbers and full-scale Reynolds numbers), provide a unique data set for CFD tool validation, and provide a baseline inlet for future inlet flow-control studies.

Symbols

Figure 1 presents sketches showing the definition of several of the most important inlet geometric parameters.

a	distance between the inlet lip highlight station (x = 0) and the inlet throat station (see fig. 1), in.
A	area, in^2
A_C	inlet capture (highlight) area; area enclosed by inlet highlight (see fig. 1 for highlight definition), and tunnel wall, in^2
A_i	inlet throat area, in^2
A_0	inlet mass-flow streamtube at freestream conditions, in^2
A_2	area at AIP station (diffuser exit), in^2
A_0/A_C	inlet mass-flow ratio, ratio of actual airflow to the ideal capture airflow
AR	aspect ratio, $W_i/2H_i$
b	distance between inlet highlight height and inlet throat height (see fig. 1), in.
C_p	static pressure coefficient, $(p-p_\infty)/q_\infty$
D_2	duct diameter at AIP (see fig. 1), in.
$DPCP_{avg}$	average SAE circumferential distortion descriptor
$DPRP_i$	SAE radial distortion descriptor for ring i on AIP total-pressure rake
e	super ellipse shape parameter
H	boundary layer shape factor, δ^*/θ
H_i	height of inlet throat (see fig. 1), in.
H_{max}	maximum height of inlet cowl (see fig. 1), in.
ΔH	distance between inlet throat centroid and inlet duct centroid, or total distance between inlet throat centroid and duct exit centroid, in.
i	ring number on AIP total-pressure rake (Value increases from hub region to tip region.)
L	length of inlet duct from throat to AIP (see fig. 1), in.

M free-stream Mach number

M_{AIP} local Mach number at AIP station based on wall $p/p_{t,\infty}$ ratio (See fig. 1 and table 1 for AIP location.)

M_{match} Mach number required by CFD to match boundary layer velocity profile of experiment

M_t local throat Mach number based on wall $p/p_{t,\infty}$ ratio (See fig. 1 and table 1 for throat location.)

p local static pressure, psi

$p_{avg,i}$ average total pressure for ring i on AIP total-pressure rake

$p_{l,avg,i}$ average total pressure in low-pressure region (defined by extent) for ring i on AIP total-pressure rake

p_{sls} sea level standard pressure, 14.696 psi

p_t total pressure, psi

$p_{t,BL}$ total pressure measured by boundary layer rake, psi

$p_{tPlug,avg}$ average total pressure at mass-flow plug, psi

$p_{t,2}$ total pressure measured at AIP station, psi

$p_{t,2,avg}$ area weighted average total pressure at AIP

$p_{t,\infty}$ free-stream total pressure, psi

p_∞ free-stream static pressure, psi

$p_{t,2}/p_{t,\infty}$ inlet pressure recovery, $p_{t,2,avg}/p_{t,\infty}$

q_∞ free-stream dynamic pressure, psi

r curve fit correlation factor

R radius, in.

Re/FT Reynolds number per foot, 1/ft

Re_{D2} Reynolds number based on duct AIP diameter

T_{sls} sea level standard temperature, 518.7°R

$T_{tPlug,avg}$ average total temperature at mass-flow plug, °R

$T_{t,\infty}$ free-stream total temperature, °R

W_{act} airflow rate measured by venturi, lb/sec

W_i inlet throat maximum width (see fig. 1), in.

W_{PlugC} corrected airflow rate at mass-flow plug, lb/sec

W_{2C} corrected airflow rate at AIP, lb/sec

x axial distance downstream of inlet lip highlight (see fig. 1), in.

x_1 axial distance downstream of inlet throat (see fig. 1), in.

y lateral distance from inlet centerline, positive to right looking upstream, in.

z vertical distance measured from tunnel wall, positive away from wall (see fig. 1), in.

z_1 vertical distance measured from estimated boundary layer displacement thickness (δ_{est}^*) at start of lower duct wall (see fig. 1), in.

δ measured boundary layer thickness, in.

δ_{est} estimated tunnel wall boundary layer thickness at M = 0.85, 0.501 in.

δ^* measured boundary layer displacement thickness, in.

δ^*_{est} estimated boundary layer displacement thickness, $\delta_{est}/8$, 0.063 in.

θ measured boundary layer momentum thickness, in.

Abbreviations:

AIP	aerodynamic interface plane
BLI	boundary layer ingesting
BWB	blended wing body
CD	compact disk
CFD	computational fluid dynamics
IGES	Initial Graphics Exchange Specification
MPI	message-passing interface
SAE	Society of Automotive Engineers
SST	Shear-Stress Transport

Apparatus and Methods

Test Facility

The experimental study was conducted in the NASA Langley Research Center 0.3-Meter Transonic Cryogenic Tunnel (refs. 15 and 16). The closed-loop, fan-driven tunnel has a 13- by 13-in. test cross-section with adaptive upper and lower walls. The facility can run in air or gaseous nitrogen. For high Reynolds number testing, the test medium is gaseous nitrogen, which is injected as a cryogenic liquid that permits testing at temperatures as low as 140°R. The wind tunnel can operate with total pressure ranging from 14.7 to 88 psi, Mach numbers ranging from 0.1 to 0.9, and Reynolds numbers up to 100 million per ft. Varying free-stream total pressure and total temperature can independently control Reynolds number and free-stream dynamic pressure.

Model

The Boeing Company, under contract with NASA, designed four BLI S-duct inlets (denoted inlets A, B, C, and D herein) to fit in the design space of a large BWB transport configuration as well as smaller military fighter type applications with flush-mounted inlets. Geometry of the four inlet designs is included on the enclosed compact disk (CD) in Initial Graphics Exchange Specification (IGES) and Unigraphics formats. A new tunnel sidewall was designed and fabricated so that the inlet models could be mounted flush with the wall. Photographs of one of the inlets mounted on the new sidewall are shown in figure 2. The diffuser section of the inlet extended through the wall into the wind-tunnel plenum. Figure 3 presents a photograph of the plenum side of the inlet installation with the outer wind-tunnel wall removed. At the exit of the diffuser, the flow entered an instrumentation section for measuring inlet distortion and pressure recovery at the Aerodynamic Interface Plane (AIP). After being ducted through a 180-degree turn (see fig. 3), the flow proceeded through a mass-flow plug assembly that included pressure and temperature instrumentation and a calibrated bellmouth/plug combination for measuring inlet mass-flow rate. An insulated and heated motor box contained the motor and gear drive system that permitted the mass-flow plug to operate at cryogenic temperatures. Finally, the flow was ducted outside the wind tunnel and vented into atmospheric conditions.

The inlet flow was driven by the pressure differential between the tunnel total pressure and the atmospheric pressure, that is, the tunnel total pressure had to be set higher than atmospheric pressure for the inlet to operate. A ratio of free-stream total pressure to atmospheric pressure greater than two was maintained for the entire test. Thus, unlike most inlet models, the current test apparatus contained no ejector system to pump the inlet flow.

Figure 4 presents details of the model geometry, and values of important inlet geometric parameters are tabulated for each inlet in table 1. Two inlets (A and B) had nearly semicircular throat aperture shapes with an aspect ratio, $W_i/2H_i$, of 0.95, while the other two inlets, C and D, had semi-elliptic throat aperture shapes with an aspect ratio of 1.42 (see table 1). By moving the upper duct wall closer to the lower duct wall, it was hypothesized that the semi-elliptical aperture shape might impart a favorable pressure field from the upper diffuser wall upon the lower diffuser wall.

Inlet lip geometries associated with each inlet are shown in figure 4(e). Inlets A and C had an a/b ratio (a measure of lip thickness) equal to 2.0 (denoted “thick lip” herein); inlets B and D had an a/b ratio equal to 3.0 (denoted “thin lip” herein). It was hypothesized that the thin lip design (a/b = 3.0) would improve performance at Mach numbers near cruise (M = 0.85) when compared to the performance of the thick lip design (a/b = 2.0), which generally would be expected to provide better inlet performance at low speeds (ref. 14).

The diffuser “centerline” distribution was the same on all four inlets; however, because of the two different aperture shapes, there were two different diffuser designs with inlets A and B having one design, and inlets C and D sharing the other. Diffuser geometry design parameters are shown in figure 4(f) for inlets A and B, and in figure 4(g) for inlets C and D. The diffuser “centerline” distribution, which starts at δ_{est}* at the inlet throat (z_1 = 0, see fig. 1(a)) and ends at the center of the round duct at the AIP station, and the duct cross-sectional area distribution are presented in the top half of figures 4(f) and 4(g). Duct aspect ratio (AR) distribution and duct superellipse shape parameter (e) distribution are presented in the bottom half of figures 4(f) and 4(g) as a function of duct quadrant. The diffuser is divided into four quadrants about the duct centerline distribution with the quadrants being symmetrical about the vertical plane of symmetry. The quadrant shapes are defined by the superellipse shape parameter e and equation 1.

$$|x_1|^e + |z_1|^e = 1.0 \qquad (1)$$

Finally, Gerlach shaping was used in the design of the diffuser cross sections to help control secondary flows. Gerlach shaping controls secondary flows by altering the localized cross-sectional areas. In regions of low-speed flow, the area is decreased to accelerate the flow, and the area is increased to decelerate the flow in regions of high-speed flow.

As shown in the figure 2 photographs, the inlets were mounted flush on the tunnel wall to simulate a boundary layer ingesting inlet. Thus, the inlet model scale was dictated by the wind tunnel wall boundary layer height, combined with the objective of obtaining about 30 percent boundary layer ingestion based on inlet height (approximately what would occur on a BWB aircraft). An estimated wind tunnel wall boundary layer height δ_{est} of 0.501 in. was obtained from reference 17, and the inlets were scaled to 2.5 percent of a full-scale BWB aircraft to obtain δ/H_i values of about 0.29 and 0.36 for the semicircular and semi-elliptical inlets, respectively.

Model inlet throat area was determined by the full-scale BWB maximum corrected airflow at top of climb flight conditions (2080 lb/sec), δ_{est}, and model scale. The corresponding maximum corrected airflow desired for the model was 1.30 lb/sec (2080 lb/sec × 0.025^2). However, geometric area at the inlet throat had to be larger than the computed throat flow area (based on the maximum corrected airflow) to accommodate the ingested boundary layer. Thus, the geometric area at the inlet throats was increased over the computed throat flow area by an amount equal to the estimated boundary layer displacement thickness ($\delta_{est}* = \delta_{est}/8$) times the inlet throat width W_i.

As mentioned previously, the wind tunnel wall boundary layer was used to simulate the aircraft boundary layer buildup in front of a flush mounted inlet. The boundary layer growth on a flat plate is probably not a true simulation of the boundary layer growth on the aft part of a fuselage or wing. Such boundary layers are likely to have high values of shape factor caused by adverse pressure gradients, shock boundary layer interactions (at cruise) and possibly even boundary layer separation. In an attempt to determine the impact of a distorted (but not necessarily realistic) boundary layer profile on inlet performance, tests were conducted with two “fences” installed in front of inlet configuration A, as shown in figures 2(b) and 4(h).

Instrumentation

Figure 5 contains sketches and tables that show model instrumentation locations. Instrumentation sketches and locations (including tunnel wall instrumentation that is not included in this report) are also provided on the enclosed CD. The instrumentation in the inlet diffusers consisted of 72 or 73 static pressure orifices; inlets C and D have one additional static pressure orifice on the diffuser top wall centerline (total of 30) than do inlets A and B (total of 29). There are 29 orifices on each of the inlet lower wall centerlines and 7 orifices on each sidewall centerline of each inlet. Locations of the diffuser static pressure orifices are listed in figures 5(b) and 5(c). In addition to diffuser internal static pressures, static pressures were also measured at 10 locations on the tunnel wall centerline upstream of the inlet installation; these locations are provided in figure 5(d).

An equal area-weighted 40-probe total pressure rake (see fig. 5(a)) that consisted of 8 arms located 45° apart, with 5 probes on each arm, was installed at the AIP (duct exit) to measure total pressure distributions at the AIP. A portion of the AIP total pressure rake can be seen in the figure 2(a) photograph.

The instrumentation in the mass-flow plug assembly downstream of the AIP station (see fig. 3) included 3 rakes located 120° apart, 3 rings, each containing 3 static pressures, located in the bellmouth wall; and a potentiometer that measured plug position ($r^2 = 0.999978$). Each of the 3 rakes contained 5 total pressures, 1 static pressure, and 1 total temperature port.

The boundary layer on the wind-tunnel wall was measured by using an 8-probe boundary layer rake and static pressure orifice mounted outside the inlet at the nominal inlet highlight plane (see fig. 2(b)). Figure 5(e) presents location information of the rake probe faces relative to each inlet highlight.

Data Reduction

Facility flow parameters, wall static pressures, and model pressures were computed from measurements that use standard facility instrumentation that resulted in the following uncertainty values:

Parameter	Uncertainty
M	0.002
$p_{t,\infty}$	0.3 psia
$T_{t,\infty}$	0.1 °K
p	0.015 psia
$p_{t,2}$	0.030 psia

The mass-flow plug assembly (see fig. 3) was calibrated against a secondary mass-flow standard (multiple critical venturis) at the NASA Langley Research Center's Jet Exit Facility to provide corrected airflow rate at the mass-flow plug station W_{plugC} as a function of plug position and total pressure. The secondary mass-flow standard had a quoted accuracy of 0.1 percent over a mass-flow range of 0.1 to 20.0 lb/sec. The calibration of the mass-flow plug assembly consisted of runs during which the mass-flow plug position was held constant (relative to the bellmouth) while the total pressure was increased. Eleven different plug locations were tested with multiple runs to assess repeatability. Actual mass-flow rate W_{act} through the mass-flow plug assembly was measured by a critical venturi. The corrected airflow rate at the AIP W_{2C} is then defined by equations (2a) and (2b).

$$W_{PlugC} = \frac{W_{act}\left(\sqrt{T_{tPlug,avg}/T_{sls}}\right)}{p_{tPlug,avg}/p_{sls}} \tag{2a}$$

$$W_{2C} = W_{PlugC}\left(p_{tPlug,avg}/p_{t2}\right) \tag{2b}$$

The ring intensity (magnitude of the circumferential pressure defect for each AIP rake ring); ring extent (angular region or extent, in degrees, in which ring pressures are below the average pressure of the rake ring); DPRP (radial distortion descriptor), $DPCP_{avg}$ (average circumferential distortion descriptor); and $p_{t,2}/p_{t,\infty}$ (inlet pressure recovery) were computed by using the SAE recommended practices reported in reference 18. All empirical sensitivity constants in the SAE distortion descriptors defined in reference 18 were set to 1.0 and the offset terms were set to 0.0. As a result, the average circumferential distortion descriptor $DPCP_{avg}$ is equal to the average of the ring intensities and is defined by equations (3a) and (3b); inlet pressure recovery is defined by equation (4); and the SAE radial distortion descriptor is defined by equation (5).

$$DPCP_{avg} = \sum_{i=1}^{i=5} \frac{\text{Intensity}_i}{5}, \qquad (3a)$$

where $$\text{Intensity}_i = \frac{p_{avg,i} - p_{l,avg,i}}{p_{avg,i}} \qquad (3b)$$

and i = ring number

$$p_{t,2}/p_{t,\infty} = p_{t,2,avg}/p_{t,\infty} \qquad (4)$$

$$DPRP_i = \frac{p_{t,2,avg} - p_{avg,i}}{p_{t,2,avg}} \qquad (5)$$

Test Conditions

One of the test objectives was to evaluate the performance of S-duct inlets with large amounts of BLI at realistic operating conditions (high subsonic Mach numbers and full-scale Reynolds numbers). To obtain full-scale Reynolds numbers, the current test was conducted with gaseous nitrogen, injected as a cryogenic liquid, as the test medium. A nominal full-scale Reynolds number (based on engine diameter) for a notional BWB transport aircraft is 13.9×10^6 at Mach 0.85 and 39 000 feet altitude. The nominal test conditions for this study are listed in table 2. Actual test conditions for each inlet configuration tested (including inlet A with boundary fences installed) are shown in tables 3 through 7.

Because the model was attached to the tunnel sidewall, angle of attack and angle of sideslip were fixed at zero degrees. Although the goal of the study was to test at the cruise Mach number of 0.85, the facility adaptive wall capability was inoperable during the study, and the walls were locked in a fixed position. As a result, the maximum Mach number that could be tested was M = 0.83, and the inlet was tested over a Mach range of 0.25 to 0.83 at the full-scale cruise Reynolds number (or maximum possible at M = 0.25 and 0.40) of 13.9×10^6. As indicated in table 2, a Reynolds number sweep was conducted at M = 0.83. In addition, the Reynolds number case of 8.6×10^6 was tested at two different combinations of tunnel total temperature and total pressure.

As mentioned previously, model design, including inlet throat area, was driven by an estimated wind tunnel wall boundary layer height δ_{est} of 0.501 in. and a desire to obtain δ/H_i values of about 0.29 and 0.36 for the semi-circular and semi-elliptical inlets, respectively. Unfortunately, the actual boundary layer height measured during the test was approximately 30 percent larger than the estimated height; the larger measured δ and δ/h_i values are listed in tables 3 through 7.

The inlet mass-flow was adjusted by changing the plug position relative to the bellmouth. The maximum design value (at top of climb) of the mass-flow rate per inlet throat area (W_{2C}/A_i) was nominally about 42 $lbm/s{\cdot}ft^2$ (1.3 lbm/sec ÷ A_i, ft^2). As discussed previously, to pass this amount of airflow, the inlet throat was increased by an amount equal to an estimated displacement thickness δ_{est}* to account for the ingested boundary layer. Due to the larger than estimated boundary layer thickness on the tunnel wall, the inlet throat was undersized (too small a displacement thickness accounted for) and the actual maximum airflow value obtained was less than the desired 42.8 $lbm/s{\cdot}ft^2$ as shown in table 2. A correlation of corrected airflow per unit of inlet area W_{2C}/A_i with inlet mass-flow ratio A_0/A_C is provided in figure 6 for each inlet investigated to allow the reader to convert airflow into either parameter.

Numerical Approach

The steady-state flow field for the BLI inlet A was computed by using the flow solver code, OVERFLOW (refs. 19 and 20), developed at NASA. This code solves the compressible Reynolds averaged Navier-Stokes (RANS) equations using the diagonal scheme of reference 21. The RANS equations are solved on structured grids by using the overset grid framework reported in reference 22. This overset grid framework allows for the use of structured grids for problems that have complex geometries. To improve the convergence of the steady-state solution, the OVERFLOW code also includes a low-Mach number preconditioning option and a multi-grid acceleration routine. All simulations in this study used the two-equation (k-ω) Shear-Stress Transport (SST) turbulence model (ref. 23).

The numerical simulations were performed using the parallel version of the OVERFLOW code (ref. 24). This code uses the Message-Passing Interface (MPI) and can run on a tightly coupled parallel machine or a network of workstations. The code distributes zones to individual processors and can split larger individual zones across multiple processors by using a domain decomposition approach.

The structured overset grid system was generated using the Chimera Grid Tools package reported in reference 25. Two views of the computational grid are shown in figure 7. The upper portion of figure 7 shows a close-up view of the overset grids on the inlet surface. The numerical simulations had seven overset grids with approximately five million grids points. Table 8 shows a summary of the grids and their dimensions. The internal inlet flow was discretized by using two grids, a hyperbolic grid for the near wall flow and a grid for the inlet core flow. This two-grid approach was used to obtain good orthogonal grid spacing at the inlet wall in the semicircular region at the entrance of the inlet. Other grids included a grid around the inlet lip and cowling. A background flat-plate grid was used to generate the boundary layer ingested by the inlet. Two block grids were used to create a transition from the coarse background grid to the finer inlet grids.

The numerical simulations modeled the BLI inlet and flat plate, neglecting the effects of the tunnel walls present during the experimental study. To match the experimental flow conditions, the flat plate length ahead of the inlet and the free-stream Mach number were adjusted to closely match the boundary layer velocity measured near the inlet face. In the first numerical simulation, the flat-plate length was adjusted to match the experimental boundary layer height. This simulation used the experimental free-stream Mach number that was measured upstream of the test section. Figure 8 shows the boundary layer rake data for the high and low Mach number cases at a given inlet mass-flow rate. Figure 8 indicates that the Mach number at the boundary layer edge for the numerical simulations was slightly higher than the experiment. The free-stream Mach number for the simulations was then adjusted to match the velocity measured at the boundary layer rake. The free-stream Mach number for the $M = 0.25$ case was adjusted to $M_{match} = 0.234$ in the numerical simulation, producing a better match to the boundary layer velocity, as shown in figure 8. For the $M = 0.833$ case, the free-stream Mach number was reduced to $M_{match} = 0.784$, which resulted in a better match to the boundary layer velocity.

The boundary layer comparison in figure 8 shows that the boundary layer profile is slightly different in the experiment for the high Mach number case as compared to the numerical simulations. The boundary layer in the experiment has less energy near the wall than the numerical simulation does. The boundary layer for the experiment was generated from the tunnel wall and not from a splitter plate, which may account for the difference in the boundary layer profiles.

The distortion for the numerical simulations was computed by interpolating the total pressure from the fine grid numerical solutions onto locations of the 40-probe rake. These interpolated total pressure values were then used to compute distortion by using the same analysis as performed on the experimental data to eliminate the resolution sensitivity of the distortion calculation.

Results

Results of this investigation are presented in plotted, tabular, and electronic (see enclosed CD that also includes tunnel wall data not presented herein) forms. When data at similar test conditions are presented on the same plot from multiple data points, nominal or average test condition values are listed in keys and titles. Plotted experimental and computational results are presented as follows:

Discussion of Results

Typical Inlet Performance

Inlets for podded transport nacelles at subsonic cruise typically have pressure recovery values of 0.98 or better and negligible distortion. Any pressure recovery losses incurred for this inlet type are dominated by friction drag and lip separation (only at off-design conditions). It is not unusual to assume perfect pressure recovery ($p_{t,2}/p_{t,\infty} = 1.0$) during aircraft conceptual design for these type inlets (ref. 26).

For BLI S-duct inlets, duct curvature and boundary layer ingestion introduces additional losses to inlet pressure recovery and increases flow distortion at the AIP. The first bend in an S-duct inlet diffuser causes a top-to-bottom pressure differential that creates secondary flows along the diffuser wall (refs. 11 and 27); this secondary flow tends to migrate the wall boundary layer toward the low pressure side of the bend (lower wall for the current investigation). If sufficient boundary layer is accumulated, it produces a lift-off effect or separation of the inlet core flow. Although it might be expected that the second bend in an S-duct would reverse or mitigate this effect, studies have indicated that such is not the case. Typical pressure recovery losses for an S-duct relative to a straight duct are about 2 percent (refs. 11 and 26). An additional pressure recovery penalty is incurred because of boundary layer ingestion. Studies have indicated that increasing ingested boundary layer thickness to nominal δ/H_i values of about 0.1 to 0.2 (significantly less than the δ/H_i of the current investigation; see tables 3 through 7) causes about a 2 percent penalty (refs. 7 and 13).

Effect of Mach Number and Inlet Airflow

Figures 9 through 12 present the effects of Mach number and airflow on the static pressure distributions on the tunnel wall that leads into the inlet and inside the inlet diffuser. One of the electronic scanning pressure measurement devices was initially undersized, and some of the pressures on Inlet A were off-scale at some test conditions. These data are replaced by a dashed line fairing (see figures 9(c) through 9(e)). This problem was corrected for tests conducted on the other inlets.

Based on the static pressure ratios shown in figures 9 through 12, throat Mach number M_t ranges from about 0.25 to about 0.60 for the test conditions of the current test and increases with free-stream Mach number and inlet airflow. At M = 0.25, the external flow on the tunnel wall accelerates or expands (as indicated by a decreasing pressure ratio trend) as it approaches the inlet, particularly at high inlet airflows ($A_0/A_C > 1.0$). Except for the highest value of W_{2C}/A_i at M = 0.40, when $A_0/A_C < 1.0$, the external flow decelerates or compresses as it approaches the inlet at all other test conditions.

The previously discussed flow features on the wall ahead of the inlet face can also be seen in the CFD results shown in figures 13 and 14. At inlet mass-flow ratios greater than 1.0 (see figs. 13(a) and 14(a)), Mach number increases (flow accelerates), and static pressure on the wall decreases as the inlet streamtube converges as it approaches the inlet face. At inlet mass-flow ratios less than 1.0 (see figs. 13(b) and 14(b)), the Mach number decreases (flow decelerates) and static pressure on the wall increases as the inlet streamtube diverges as it approaches the inlet face.

For semicircular inlets A and B, the flow inside the diffuser generally decelerates on the bottom wall, accelerates on the upper wall, and remains at a relatively constant velocity on the sidewalls (see figs. 9 and 10). A small region of flow separation and reattachment, indicated by a pressure plateau that is more easily observed in figure 15, possibly occurs at some conditions on the top diffuser wall at approximately $2.5 < x/D_2 < 3.0$. For semi-elliptical inlets C and D at high values of inlet airflow, the diffuser flow initially accelerates on the bottom wall and decelerates on the upper wall up to about $x/D_2 = 0.06$ (see figs. 11 and 12). At $x/D_2 = 0.06$, it appears that the flow on the lower wall separates and a pressure plateau is reached between $0.06 < x/D_2 < 1.8$. This separation region creates a virtual diffuser wall that causes a reduction in the diffuser cross-sectional area and flow acceleration on the top wall in this same region of the diffuser. At about $x/D_2 = 1.8$, the flow on the bottom wall reattaches and decelerates in the compression turn ahead of the AIP. The flow on the top wall downstream of $x/D_2 = 1.8$, where the flow again fills the diffuser duct, finishes a deceleration caused by the first (compression) turn on the top wall and then accelerates around the upper wall second (expansion) turn ahead of the AIP.

The effect of inlet airflow on the measured tunnel wall, boundary layer profiles is shown in figure 16, and the effect of Mach number on the measured tunnel wall boundary layer profiles is shown in figure 17. The location of the boundary layer rake, relative to the inlet, is shown in figures 2(b), 4(h), and 5(e). The boundary layer characteristics (height, momentum thickness, and displacement thickness) derived from the boundary layer profiles (see ref. 28) are provided in tables 3 through 7. It should be noted that the tunnel wall boundary layer thickness was underestimated and the boundary layer rake was fabricated too short (top probe at z = 0.58 compared to maximum boundary layer thickness of over 0.62). The boundary layer profile data were extrapolated to obtain boundary layer thickness δ values; this procedure introduces additional error into the boundary layer characteristics computed from the boundary layer profiles.

As indicated in figure 16, inlet airflow had relatively little effect on boundary layer profile; this result indicates that the sensitivity of the tunnel wall boundary layer measurements—with varying inlet flow streamtube upstream of the inlet face (small for low values of A_0/A_C and large for high values of A_0/A_C)—was low. Varying Mach number had a large impact on boundary layer profiles, as shown in figure 17. Boundary layer total pressure decreased significantly with increasing Mach number (often termed degraded boundary layer "health"). An examination of the data in tables 3 through 7 indicates that, except for M = 0.25, which had a large amount of data scatter, boundary layer height generally ranged between 0.53 in. and 0.67 in. and had no discernable trend with inlet airflow or free-stream Mach number. Such was not the case for boundary layer shape factor. Figure 18 presents the effect of inlet airflow and free-stream Mach number on the boundary layer shape factor. The lines shown in this figure represent a linear curve fit of all the shape factor data obtained at each Mach number tested. Increasing Mach number causes significant increases in boundary layer shape factor (deterioration of boundary layer health); boundary layer separation occurs at H ≈ 1.8 to 2.4 (ref. 29). A slight increasing trend of H with increasing inlet mass-flow ratio is also indicated. Thus, the boundary layer measurements were not totally independent of inlet airflow.

Figures 19 through 23 present total-pressure-ratio contour maps, distortion descriptor details (computed by using the SAE recommended practices given in reference 18), and pressure recovery values for all inlet configurations and test conditions. Data from these figures are plotted in figure 24 to show the effects of Mach number and inlet airflow on pressure recovery and SAE circumferential distortion. Several total pressure contour maps at the AIP are also transferred to this figure. Descriptions of the distortion parameters are provided in the "Data Reduction" section of this report. Corresponding internal duct static pressure distributions are shown in figures 9 through 12 and boundary layer profiles are shown in figures 16 and 17.

The effects of Mach number and inlet airflow on pressure recovery $p_{t,2}/p_{t,\infty}$ are shown on the upper portion of figure 24. Increasing Mach number resulted in very large reductions in inlet pressure recovery. This trend with Mach number is typical of most inlets, but the losses are exaggerated by the S-duct diffuser shape and the large amount of boundary layer ingestion. As discussed previously, total pressure in the boundary layer (over 30 percent of the total inlet flow) decreased significantly with increasing free-stream Mach number (see fig. 17). The losses indicated in figure 24 are larger than those reported from previous investigations of BLI. At M = 0.25, where measured losses were less than 1 percent, the pressure recovery loss is primarily caused by skin friction and some small BLI effects (note the total-pressure-ratio contour maps at M = 0.25 in fig. 24). As indicated by the total-pressure-ratio contour plots at M = 0.83 that show a large low-pressure region near the diffuser bottom wall (particularly at high airflow rates near cruise), pressure recovery losses at high Mach numbers are dominated by duct curvature and BLI effects, and pressure recovery losses of up to 6.7-percent were measured depending on inlet airflow and configuration. Pressure recovery losses were largest for inlets C and D that had larger amounts of BLI. Pressure recovery losses this high could be devastating to engine performance and commercial viability of a BLI transport concept unless the losses can be mitigated by advanced technology or the benefits of BLI (reduced weight, drag, and so on) that were discussed in the "Introduction" more than offset the pressure recovery (thrust) losses in a total system analysis.

As indicated in figure 24, inlet pressure recovery is also a function of inlet airflow. At M = 0.25, where duct curvature and BLI effects are very small, pressure recovery decreases slightly with increasing airflow, while at M > 0.4, pressure recovery increases with increasing airflow.

At low Mach numbers and low airflow or throttle settings, the inlet is able to meet airflow requirements with very small losses (basically friction) and thus pressure recovery is high. However, at high throttle settings, the inlet throat is too small and the inlet must pull more air into the duct from the surrounding flow field (streamtube larger than inlet capture area; $A_0/A_C > 1.0$) as indicated by the converging CFD wall surface streamlines presented in figure 14(a). This converging inlet airflow streamtube may not only cause larger lip losses (internal lip separation can occur in the extreme case, especially for thin lips) but also pull additional boundary layer into the inlet from the inlet sides and thus lower pressure recovery. Figure 6 can be used to convert the inlet airflow values given in figure 24 to inlet mass-flow ratio A_0/A_C values. For example, inlet mass-flow ratios vary from 0.76 to 1.17 at M = 0.25 for inlet A.

At high subsonic Mach numbers, the inlet is operating near design, and consequentially pressure recovery losses will be dominated by duct curvature and BLI effects because all other losses will be small. Since the percentage of BLI relative to total airflow decreases with increasing airflow (the amount of BLI remains nearly constant), pressure recovery increases with increasing airflow at M > 0.4.

The effect of Mach number and inlet airflow on the SAE circumferential distortion descriptor (ref. 18) is shown on the bottom portions of figure 24. Acceptable static distortion levels are generally considered to be below about 0.04 to 0.05 for commercial applications. Based on this criterion, the distortion levels for the current inlets are unacceptable at Mach numbers and airflows near maximum cruise (M = 0.85 and W2C/Ai ≈ 42.0 lb/sec-ft^2).

Inlet distortion generally increased with increasing Mach number until a peak was reached and then decreased. The Mach number at which $DPCP_{avg}$ peaked increased with increasing inlet airflow and the peak value increased with increasing inlet airflow. The peak distortion value was not reached for the highest values of airflow tested. The worst distortion cases can easily be selected from the total-pressure ratio contour maps shown in figure 24. It should be noted that although increased airflow was beneficial to pressure recovery at M > 0.40, the opposite was generally true for distortion over the same range.

The distortion results discussed previously indicate that some form of flow control could be beneficial for the inlets of this study (refs. 11, 13, and 30 through 34). Experimental and CFD flow control results on the inlet A geometry are given in references 33 and 34.

Computational results on inlet A are compared to experimental results in figures 25 and 26. Additional CFD results on inlet A are reported in reference 33. Qualitatively, the experimental and computational studies give similar results as shown in figure 25. Both show little distortion at M = 0.25 and a large area of low total pressure near the duct bottom wall at M = 0.83. As discussed previously, these low pressure regions are caused by the ingestion of large amounts of low energy boundary layer flow and secondary flow effects induced by the S-duct diffuser geometry and would result in reduced inlet pressure recovery and increased inlet distortion. Both studies also indicate that the low-pressure regions grow in size and intensity at M = 0.83 with increasing inlet airflow. Some flow asymmetry can be noted in the experimental contour map at M = 0.83 and A_0/A_C = 0.556; such flow asymmetries are not captured by the CFD because the geometry and flow conditions are assumed to be left/right symmetrical.

Quantitative CFD results are shown in figure 26 by solid symbols. The four CFD data points correspond to the four total-pressure contour maps shown in figure 25. Although the CFD results predict pessimistic pressure recovery results (larger losses), the trends of pressure recovery with increasing Mach number and inlet airflow are well predicted. The reversal in trend with increasing inlet airflow at M = 0.25 and M = 0.83 is captured by the CFD predictions. CFD predictions for distortion are in excellent agreement with experimental data.

Effect of Inlet Geometry

Four inlet geometries, two aperture shapes (semi-circular and semi-elliptical) with two lip thicknesses each, were tested in the current investigation. The semi-circular shape (inlets A and B) is similar to the BWB BLI inlet design (refs. 8, 9, and 11). The semi-elliptical shape was selected as a variable to (1) take advantage of a potentially favorable pressure field of the upper diffuser wall upon the lower diffuser wall and thus weaken internal secondary flows, and (2) increase the amount of boundary layer ingested and thus take advantage of potential BLI benefits (refs. 1 and 2). Note that these benefits are not addressed in the current investigation. The thick lip (a/b = 2.0) was designed for cruise conditions between 0.77 < M < 0.83 and the thin lip (a/b = 3.0) was designed for cruise at M > 0.83. Figure 27 presents a comparison of the inlet performance for these configurations as a function of Mach number. Figure 15 presents comparisons of duct static pressure distributions for the four inlet configurations. The effects of inlet geometry were small at low speeds (M ≤ 0.40). At M > 0.40, the semi-circular aperture shape (inlets A and B) generally produced higher pressure recovery and lower distortion than the semi-elliptical aperture shape (inlets C and D). For a given inlet throat area, a flush-mounted semi-elliptical inlet will ingest more boundary layer than a semi-circular inlet because it is wider than and not as tall as a semi-circular inlet, which results in an increase in measured nominal δ/H_i from 0.358 for the semi-circular inlets to 0.434 for the semi-elliptical inlets. If the semi-elliptical shape produced any favorable effects on the internal, induced secondary flows, they were more than offset by the detrimental effects of BLI discussed previously for figure 24. In fact, the pressure distributions shown in figure 15 indicate that the static pressures on the duct bottom wall were relatively independent of inlet cowl geometry.

In general, inlet lip thickness only had a minor effect on inlet performance. As mentioned previously, the facility adaptive wall capability was inoperable at the time of this study, and Mach numbers above 0.83 could not be obtained. Thus, the potential benefits of a thinner lip at $M > 0.83$ could not be verified, but regardless, any potential benefit would appear to be small from simple extrapolation of the data.

Effect of Reynolds Number

The 0.3-Meter Transonic Cryogenic Tunnel has the capability to vary Reynolds number (by varying temperature and total pressure) for a constant value of free-stream Mach number. As indicated by the nominal test conditions shown in table 2, Re/FT values from 25×10^6 to 68×10^6 were tested for each inlet configuration at $M = 0.83$. The Re/Ft value of 68×10^6 provides the full-scale Reynolds number value of 13.9×10^6 (based on D_2) for a BWB transport aircraft. The boundary layer characteristics with varying Reynolds number are tabulated in the (b) part of tables 3 through 7. Distortion and pressure recovery data with varying Reynolds number are tabulated in tables 9 through 13.

Figure 28 presents the effect of Reynolds number on static pressure ratio distributions (facility wall and internal duct) for inlet B; these data are typical for the other inlets. Although the effect is small, $p/p_{t,\infty}$ tends to increase slightly with increasing Reynolds number.

The effect of Reynolds number on the boundary layer profiles is shown in figure 29 and is generally small. As would be expected from the boundary layer profile results, the effects of Reynolds number on the boundary layer characteristics shown in figure 30 are also small, especially for shape factor H. The boundary layer data exhibit more scatter than typically expected and is more than likely the result of a boundary layer rake that was too short, as discussed previously. Evaluating the boundary layer height δ data as a set indicates that boundary layer thickness tends to decrease slightly with increasing Reynolds number as would be expected.

The effect of Reynolds number on inlet performance is presented in figure 31 as a function of airflow at a nominal Mach number of 0.831. Increasing Reynolds number increased inlet pressure recovery, $p_{t,2}/p_{t,\infty}$, by up to one half percent. Although it is difficult to correlate this effect with the boundary layer thickness results shown in figure 30 because of data scatter, this performance improvement is most likely the result of thinner boundary layers (less BLI) at the higher Reynolds numbers as indicated previously. As shown on the bottom of figure 31, Reynolds number has a negligible effect on the SAE circumferential distortion descriptor. The insensitivity of distortion to Reynolds number indicates that free-stream Reynolds number had little effect on the diffuser internal flow field (secondary flows, separation, and so on) for the inlets tested.

Effect of Boundary Layer Profile

The measured shape factor of the natural boundary layer in the 0.3-Meter Transonic Cryogenic Tunnel at the inlet face plane was about 1.5. In flight, the boundary layer entrance profile can be quite different from that created on a wind tunnel facility wall because of other factors such as shock-boundary layer interaction and/or separation, for example. To obtain a measure of inlet performance sensitivity to boundary layer profile shape, two boundary layer fences were mounted in front of inlet A. A photograph of the installation is shown in figure 2(b), and a sketch of the fence installation is shown in figure 4(h). Upstream devices such as chains, fences, and backward steps to perturb boundary layer characteristics have been used in several previous investigations (see refs. 10, 11 and 13). It should be noted that at some unknown time during the fence-on testing, a portion of the fence upper wires (see fig. 4(h)) broke and were lost downstream. However, all data at each test condition were recorded simultaneously; inlet performance, duct static pressure distributions, and boundary layer characteristics were all measured with the same fence condition at any given test condition. Measured boundary layer characteristics for inlet A with fences installed are tabulated in table 4, and inlet performance data with the fences on are tabulated in table 10 and figure 20.

Figure 32 presents the effect of the boundary layer fences on the diffuser static pressure ratio distributions. In general, static pressure ratio was slightly decreased throughout the duct by adding the boundary layer fences. As might be expected, addition of the boundary layer fences had a significant effect on boundary layer profiles as shown in figure 33. At Mach numbers above 0.25, the fences cause a significant defect in the boundary layer profile below $z/D_2 = 0.1$. This result indicates that the upper fence wires were probably lost before the M = 0.4 test condition was reached because the upper wire was located at z/D_2 of about 0.18, and the lower wire was located at z/D_2 of about 0.09. It might be expected that the effect of fences on the boundary layer profile would cause a significant impact on boundary layer shape factor H. The effect of the boundary layer fences on the boundary layer shape factor, as well as the boundary layer height, is shown in figure 30(e). The boundary layer fences caused an increase in boundary layer shape factor (H increased from about 1.5 to about 1.6), which indicates a deterioration of boundary layer health from the fence off case. Boundary layer separation can occur for values of H above 1.8 (ref. 29).

Figure 34 presents the effect of a distorted boundary layer profile on the performance of inlet A. Distortion of the boundary layer profile was detrimental to inlet pressure recovery and distortion. The results shown in the upper parts of figure 34 for the effect of a distorted boundary layer profile are almost identical to those reported in reference 13. The investigation reported in reference 13 used a backward facing step to perturb the boundary layer and measured a 0.0071 reduction in pressure recovery at a throat Mach number of 0.7 as a result of distorting the entrance profile; the current investigation resulted in a 0.004 to 0.006 reduction in pressure recovery at a free-stream Mach number of 0.6 and a 0.007 to 0.008 reduction in pressure recovery at a free-stream Mach number of 0.8 as a result of distorting the entrance profile. However, an opposite trend on inlet distortion was measured in the current investigation from that reported in reference 13. In reference 13, although a thick boundary layer and a thick boundary layer with distorted entrance profile both caused higher distortion than a thin boundary layer, perturbing the thick boundary layer actually reduced inlet distortion from that produced by the unperturbed thick boundary layer. In the current investigation, perturbing the entrance profile of a thick boundary layer (significantly thicker than that reported in ref. 13) increased inlet distortion. Although the fences used in the current investigation may not produce a realistic inlet entrance boundary layer profile, the results make it clear that inlet performance is not only a function of the amount of BLI but also a function of upstream disturbances and resulting boundary layer health (shape factor).

Conclusions

A new high Reynolds number test capability has been developed for the NASA Langley Research Center 0.3-Meter Transonic Cryogenic Tunnel. By using this new capability, an experimental investigation of four S-duct inlet configurations with large amounts of boundary layer ingestion (nominal boundary layer thickness of about 40-percent of inlet height) was conducted at realistic operating conditions (high subsonic

Mach numbers and full-scale Reynolds numbers). A computational study of one of the inlets was also conducted. The results from this investigation have indicated the following conclusions.

1. Ingestion of a large amount of boundary layer into an S-duct inlet causes a significant decrease in inlet pressure recovery in addition to the losses associated with duct friction, inlet lip separation, or duct curvature.

2. Increasing free-stream Mach number was generally detrimental to boundary layer ingesting (BLI) S-duct inlet performance (pressure recovery and distortion). Duct curvature and BLI effects dominate the losses at high subsonic speeds.

3. Increasing engine airflow (engine throttle setting) increased inlet pressure recovery at Mach numbers above 0.4 but also increased inlet distortion. The increase in pressure recovery is attributable to a reduction in the relative amount of BLI (absolute amount remains relatively constant) as inlet mass-flow is increased.

4. At a Mach number of 0.25, increasing the inlet throttle setting decreased inlet pressure recovery. At this speed, the inlet mass-flow ratio is generally greater than 1.0 (inlet flow stream tube area is larger than inlet throat area) and the amount of boundary layer pulled into the inlet from the adjacent surfaces beside the inlet increases with increasing engine throttle setting.

5. Because of increased boundary layer ingestion, inlets with semi-elliptical apertures have lower inlet performance (lower pressure recovery and higher distortion) than inlets with semi-circular apertures. Inlet lip thickness had only negligible effects on inlet performance for the range of variables tested in the current study.

6. Increasing Reynolds number had a negligible effect on inlet distortion but increased inlet pressure recovery.

7. Distorting the inlet entrance boundary layer profile had a significant adverse effect on inlet performance.

8. Computational fluid dynamics (CFD) was able to capture the inlet pressure recovery and distortion trends with increasing Mach number and inlet airflow. In particular, CFD predicted the reversal in pressure recovery trend with increasing inlet mass-flow at low and high Mach numbers

References

1. Smith, Leroy H.: Wake Ingestion Propulsion Benefit. *J. of Aircraft and Power*, vol. 9, no. 1, Jan.-Feb., 1993.

2. Daggett, David L.; Kawai, Ron; and Friedman, Doug: *Blended Wing Body Systems Studies: Boundary Layer Ingestion Inlets With Active Flow Control*. NASA/CR-2003-212670, Dec., 2003.

3. Ting, C.T.; Kaldschmidt, G.; and Syltebo, B.E.: Design and Testing of New Center Inlet and S-Duct for B-727 Airplane With Refanned JT8D Engines. AIAA Paper 75-0059, Jan., 1975.

4. Ingells, Douglas J.: *L-1011 TriStar and the Lockheed Story*. Aero Publishers, 1973.

5. Tindell, R.H.: Highly Compact Inlet Diffuser Technology. AIAA-87-1747, July, 1987.

6. Mayer, David W.; Anderson, Bernhard H.; and Johnson, Timothy A.: 3D Subsonic Diffuser Design and Analysis. AIAA 98-3418, 1998.

7. Little, B.H., Jr.; and Trimboli, W.S.: An Experimental Investigation of S-Duct Diffusers for High-Speed Prop-Fans. AIAA-82-1123, June, 1982.

8. Liebeck, R.H.; Page, M.A.; and Rawdon, B.K.: Blended-Wing-Body Subsonic Commercial Transport. AIAA 98-0438, Jan. 1998.

9. Roman, D.; Allen, J.B.; and Liebeck, R.H.: Aerodynamic Design Challenges of the Blended-Wing-Body Subsonic Transport. AIAA-2000-4335, 2000.

10. Anabtawi, Amer J.; Blackwelder, Ron F.; Liebeck, Robert; and Lissaman, Peter: Experimental Investigation of Boundary Layer Ingesting Diffusers of a Semi-Circular Cross Section. AIAA-98-0945, 1998.

11. Anabtawi, Amer J.; Blackwelder, Ron F.; Lissaman, Peter B.S.; and Liebeck, Robert H.: An experimental Investigation of Boundary Layer Ingestion in a Diffusing S-Duct With and Without Passive Flow Control. AIAA 99-0739, 1999.

12. Anabtawi, Amer J.; Blackwelder, Ron F.; Liebeck, Robert H.; and Lissaman, Peter B.S.: An Experimental Study of the Effect of Offset on Thick Boundary Layers Flowing Inside Diffusing Ducts. AIAA 99-3590, 1999.

13. Ball, W.H.: Tests of Wall Blowing Concepts for Diffuser Boundary Layer Control. AIAA-84-1276, 1984.

14. Seddon, J.; and Goldsmith, E. L.: Intake Aerodynamics. AIAA Educational Series, 1985.

15. Mineck, Raymond E.; and Hill, Acquilla S.: *Calibration of the 13- by 13-Inch Adaptive Wall Test Section for the Langley 0.3-Meter Transonic Cryogenic Tunnel*. NASA Technical Paper 3049, Dec. 1990.

16. Rallo, Rosemary A.; Dress, David A.; and Siegle, Henry J. A.: *Operating Envelope Charts for the Langley 0.3-Meter Transonic Cryogenic Wind Tunnel*. NASA TM 89008, Aug. 1986.

17. Seifert, Avi; and Pack, LaTunia G.: Active Control of Separated Flows on Generic Configurations at High Reynolds Numbers. AIAA 99-3403, 1999.

18. Anon.: Gas Turbine Engine Inlet Flow Distortion. *Soc. of Automotive Engineers* Report ARP-1420, March 1978.

19. Buning, P.G.; Jespersen, D.C.; Pulliam, T.H.; Klopfer, W.M.; Chan, W.M.; Slotnick, J.P.; Krist, S.E.; and Renze, K.J.: OVERFLOW User's Manual Version 1.8m, Tech. Rep., NASA Langley Research Center, 1999.

20. Jespersen, D.C.; Pulliam, T.H.; and Buning, P.G.: Vortex Generator Modeling for Navier-Stokes Codes, AIAA 97-0644, 1997.

21. Pulliam, T.H.; and Chaussee, D.S.: A Diagonal Form of an Implicit Approximate-Factorization Algorithm, *J. of Computational Physics*, vol. 39, February 1981, pp. 347-363.

22. Steger, J.L.; Dougherty, F.C.; and Benek, J.A.: A Chimera Grid Scheme, Advances in Grid Generation, edited by K.N. Ghia and U. Ghia, vol. 5 of *FED*, ASME, New York, NY, 1983.

23. Menter, F.: *Improved Two-Equation Turbulence Models for Aerodynamic Flows*, Tech. Rep. TM 103975, NASA Langley Research Center, Hampton, VA 23681-2199, 1992.

24. Murphy, K.; Buning, P.; Pamadi, B.; Scallion, W.; and Jones, K.: Status of Stage Separation Tool Development for Next Generation Launch Technologies, AIAA paper 04-2595, June 2004.

25. Chan, W.M.; and Gomez, R.J.: Advances in Automatic Overset Grid Generation Around Surface Discontinuities, AIAA Paper 99-3303, July 1999.

26. Raymer, Daniel P.: Aircraft Design: A Conceptual Approach. Third Edition. AIAA Educational Series. AIAA, Inc., 1999.

27. Wellborn, S.R.; Reichert, B.A.; and Okiishi, T.H.: An Experimental Investigation of the Flow in a Diffusing S-Duct. AIAA-92-3622, 1992.

28. Coles, D.: The Law of the Wake in the Turbulent Boundary Layer. *J. of Fluid Mech.* 1:191-226, 1956.

29. Schlichting, Hermann: *Boundary Layer Theory*. McGraw-Hill Book Company, Inc. 1960.

30. Anderson, B.H.; and Gibb, J.: Vortex-Generator Installation Studies on Steady-State and Dynamic Distortion. *J. of Aircraft*, vol. 35, no. 4, pp. 513-520, 1998.

31. Anderson, B.H.; and Gibb, J.: Vortex Flow Control Applied to Aircraft Intake Ducts. *Proceedings of the Royal Aeronautical Society Conference on High Lift and Separation Control.* Paper No. 14, Bath, UK, March, 1995.

32. Anderson, Jason M.; Burdisso, Ricardo; and Ng, Wing: An Active Flow Distortion Control System for Serpentine Inlets. *Proceedings of International Mechanical Engineering Congress and Exposition*, New Orleans, LA. IMECE2002-NCA-33049, Nov. 2002.

33. Allan, Brian G.; Owens, Lewis R.; Berrier, Bobby L.: Numerical Modeling of Active Flow Control in a Boundary Layer Ingesting Offset Inlet. *2nd AIAA Flow Control Conference*, Portland, Oregon. AIAA-04-2318. June, 2004.

34. Gorton, Susan Althoff; Owens, Lewis R.; Jenkins, Luther N.; Allan, Brian G.; and Schuster, Ernest P.: Active Flow Control on a Boundary-Layer-Ingesting Inlet. AIAA-2004-1203.

Table 1. Values of Important Geometric Parameters

Variable	Inlet A	Inlet B	Inlet C	Inlet D
H_{max}, in.	2.185	2.143	1.757	1.691
L, in.	7.697	7.697	7.684	7.684
L + a, in.	8.174	8.355	8.033	8.109
a, in.	0.477	0.658	0.349	0.425
b, in.	0.239	0.219	0.174	0.142
a/D_2	0.195	0.269	0.143	0.174
H_i, in.	1.703	1.703	1.405	1.405
W_i, in.	3.249	3.249	3.980	3.980
A_i, in^2	4.400	4.400	4.455	4.455
A_C, in^2	5.760	5.634	5.876	5.634
ΔH, in.	2.543	2.543	2.417	2.417
D_2, in.	2.448	2.448	2.448	2.448
A_2, in^2	4.707	4.707	4.707	4.707
L/D_2	3.144	3.144	3.139	3.139
$\Delta H/L$	0.330	0.330	0.314	0.314
A_2/A_i	1.070	1.070	1.057	1.057
$W_i/2H_i$ or AR	0.95	0.95	1.42	1.42
a/b	2.0	3.0	2.0	3.0

Table 2. Nominal Test Conditions

M	$T_{t,\infty}$, °R	$p_{t,\infty}$, lbf/in^2	Re/FT x 10^{-6}	Re_{D2} x 10^{-6}	W_{2C}/A_i, lb/sec·ft^2	A_0/A_C	
0.25	180	65	34	6.9	20.0 - 34.4	0.73 - 1.22	
0.40	180	63	51	10.4	20.0 - 34.9	0.48 - 0.81	
0.60	180	62	68	13.9	20.0 - 35.7	0.35 - 0.61	Mach sweep
0.80	180	51	68	13.9	20.0 - 36.1	0.30 - 0.55	
0.83	180	50	68	13.9	20.0 - 36.8	0.29 - 0.57	
0.83	180	42	57	11.6	20.0 - 36.8	0.29 - 0.57	
0.83	180	31	42	8.6	20.0 - 36.8	0.29 - 0.57	
0.83	260	53	42	8.6	20.2 - 38.0	0.29 - 0.57	Re sweep
0.83	260	44	35	7.1	20.2 - 38.0	0.29 - 0.57	
0.83	260	38	30	6.1	20.2 - 38.0	0.29 - 0.57	
0.83	260	32	25	5.1	20.2 - 38.0	0.29 - 0.57	

Note: The Re/FT values at M = 0.25 and 0.40 were the maximum obtainable.

Table 3. Test Conditions and Boundary Layer Data for Inlet A, Fence Off

(a) Mass-flow sweeps

M	**Re/ft x 10^{-6}**	**W_{2C}, lbm/sec**	**A_0/A_C**	**δ, in**	**δ/H_i**	**δ^*, in**	**θ, in**	**H**
0.250	33.39	0.625	0.760	0.332	0.195	0.0326	0.0275	1.207
0.250	33.22	0.887	1.073	0.572	0.336	0.0663	0.0522	1.271
0.251	33.30	0.915	1.101	0.569	0.334	0.0704	0.0549	1.282
0.251	34.02	0.967	1.165	0.627	0.368	0.0796	0.0612	1.301
0.401	50.11	0.621	0.493	0.561	0.329	0.0616	0.0482	1.278
0.402	52.03	0.896	0.711	0.572	0.336	0.0655	0.0509	1.289
0.404	52.85	0.943	0.746	0.531	0.312	0.0595	0.0463	1.286
0.602	67.56	0.627	0.367	0.557	0.327	0.0613	0.0453	1.354
0.604	69.52	0.899	0.526	0.569	0.334	0.0647	0.0476	1.360
0.603	68.19	1.004	0.589	0.542	0.318	0.0615	0.0452	1.361
0.604	68.51	1.071	0.628	0.596	0.350	0.0696	0.0509	1.368
0.803	69.66	0.623	0.312	0.572	0.336	0.0664	0.0451	1.472
0.805	69.97	0.903	0.454	0.572	0.336	0.0682	0.0462	1.477
0.803	68.85	1.017	0.513	0.546	0.321	0.0638	0.0434	1.470
0.805	68.94	1.080	0.546	0.580	0.341	0.0699	0.0474	1.476
0.829	69.54	0.622	0.308	0.580	0.341	0.0699	0.0469	1.490
0.832	70.06	0.899	0.447	0.576	0.338	0.0708	0.0473	1.497
0.834	68.43	1.020	0.508	0.546	0.321	0.0664	0.0445	1.493
0.833	67.65	1.113	0.556	0.576	0.338	0.0711	0.0475	1.495

Table 3. Concluded

(b) Reynolds number sweeps

M	**Re/ft x 10^{-6}**	**W_{2C}, lbm/sec**	**A_0/A_C**	**δ, in**	**δ/H_i**	**δ^*, in**	**θ, in**	**H**
0.828	25.03*	0.627	0.309	0.627	0.368	0.0757	0.0506	1.495
0.829	30.10*	0.626	0.308	0.627	0.368	0.0748	0.0500	1.495
0.828	35.11*	0.628	0.310	0.627	0.368	0.0738	0.0494	1.494
0.830	42.06*	0.625	0.308	0.611	0.359	0.0734	0.0491	1.495
0.833	43.00	0.621	0.306	0.611	0.359	0.0741	0.0494	1.500
0.829	58.19	0.621	0.307	0.596	0.350	0.0709	0.0475	1.492
0.829	69.54	0.622	0.308	0.580	0.341	0.0699	0.0469	1.490
0.832	24.82*	1.133	0.564	0.611	0.359	0.0757	0.0502	1.510
0.832	29.81*	1.134	0.565	0.611	0.359	0.0739	0.0491	1.506
0.830	34.64*	1.135	0.567	0.596	0.350	0.0725	0.0483	1.502
0.829	41.15*	1.130	0.565	0.580	0.341	0.0714	0.0477	1.498
0.834	41.56	1.114	0.556	0.611	0.359	0.0740	0.0492	1.502
0.833	56.61	1.113	0.556	0.580	0.341	0.0718	0.0479	1.499
0.833	67.65	1.113	0.556	0.576	0.338	0.0711	0.0475	1.495

* Nominal $T_{t,\infty}$ = 260° R; nominal $T_{t,\infty}$ = 180° R for all other data.

Table 4. Test Conditions and Boundary Layer Data For Inlet A, Fence On

(a) Mass-flow sweeps

M	**Re/ft x 10^{-6}**	**W_{2C}, lbm/sec**	**A_0/A_C**	**δ, in**	**δ/H_i**	**δ^*, in**	**θ, in**	**H**
0.251	33.78	0.903	1.086	0.611	0.359	0.0894	0.0660	1.354
0.251	33.86	0.964	1.156	0.611	0.359	0.0984	0.0745	1.321
0.400	50.88	0.902	0.716	0.642	0.377	0.1131	0.0755	1.497
0.401	50.67	1.025	0.812	0.580	0.341	0.1010	0.0714	1.414
0.603	68.19	0.905	0.527	0.627	0.368	0.1017	0.0671	1.515
0.602	68.86	1.072	0.626	0.580	0.341	0.1030	0.0680	1.515
0.802	68.37	0.909	0.454	0.627	0.368	0.0922	0.0588	1.568
0.812	68.21	1.088	0.544	0.561	0.329	0.0925	0.0573	1.614
0.833	69.10	0.907	0.447	0.611	0.359	0.0901	0.0573	1.571
0.832	68.02	1.108	0.550	0.561	0.329	0.0902	0.0561	1.608

Table 4. Concluded

(b) Reynolds number sweep

M	Re/ft x 10^{-6}	W_{2C}, lbm/sec	A_0/A_C	δ, in	δ/H_i	δ^*, in	θ, in	H
0.834	25.11*	0.908	0.448	0.627	0.368	0.0883	0.0564	1.566
0.832	30.10*	0.909	0.449	0.611	0.359	0.0878	0.0560	1.567
0.831	34.97*	0.909	0.449	0.611	0.359	0.0875	0.0558	1.568
0.831	41.70*	0.909	0.449	0.611	0.359	0.0885	0.0563	1.571
0.830	41.78	0.908	0.449	0.611	0.359	0.0881	0.0564	1.562
0.832	57.17	0.908	0.448	0.611	0.359	0.0884	0.0565	1.566
0.833	69.10	0.907	0,447	0.611	0.359	0.0901	0.0573	1.571
0.830	24.98*	1.125	0.557	0.576	0.338	0.0911	0.0568	1.604
0.830	29.77*	1.127	0.558	0.572	0.336	0.0906	0.0563	1.609
0.830	35.38*	1.129	0.560	0.569	0.334	0.0904	0.0561	1.612
0.829	41.05*	1.129	0.560	0.565	0.332	0.0910	0.0562	1.617
0.832	41.64	1.115	0.551	0.569	0.334	0.0908	0.0565	1.607
0.839	57.26	1.115	0.551	0.565	0.332	0.0899	0.0560	1.605
0.832	68.02	1.108	0.550	0.561	0.329	0.0902	0.0561	1.608

* Nominal $T_{t,\infty}$ = 260° R; nominal $T_{t,\infty}$ = 180° R for all other data.

Table 5. Test Conditions and Boundary Layer Data for Inlet B

(a) Mass-flow sweeps

M	Re/ft x 10^{-6}	W_{2C}, lbm/sec	A_0/A_C	δ, in	δ/H_i	δ^*, in	θ, in	H
0.248	33.83	0.619	0.770	0.642	0.377	0.0788	0.0616	1.279
0.251	33.28	0.893	1.099	0.720	0.423	0.1077	0.0798	1.349
0.248	33.02	1.011	1.258	0.596	0.350	0.0753	0.0586	1.285
0.254	32.98	1.036	1.262	0.627	0.368	0.0762	0.0593	1.286
0.400	51.17	0.622	0.506	0.572	0.336	0.0656	0.0509	1.289
0.401	51.32	0.894	0.724	0.720	0.423	0.0994	0.0736	1.350
0.407	50.90	1.017	0.815	0.611	0.359	0.0737	0.0565	1.305
0.400	50.95	1.078	0.875	0.611	0.359	0.0682	0.0530	1.287
0.602	67.99	0.620	0.370	0.572	0.336	0.0649	0.0477	1.361
0.607	67.60	0.897	0.534	0.658	0.386	0.0812	0.0590	1.376
0.608	67.42	1.021	0.609	0.611	0.359	0.0712	0.0521	1.368
0.607	67.65	1.098	0.658	0.550	0.323	0.0654	0.0481	1.362
0.803	68.19	0.619	0.317	0.576	0.338	0.0672	0.0452	1.486
0.800	68.51	0.899	0.463	0.611	0.359	0.0673	0.0458	1.468
0.808	68.00	1.022	0.526	0.611	0.359	0.0703	0.0475	1.480
0.804	68.09	1.107	0.571	0.611	0.359	0.0734	0.0494	1.484
0.829	68.27	0.620	0.313	0.596	0.350	0.0706	0.0469	1.505
0.830	68.56	0.899	0.457	0.596	0.350	0.0676	0.0454	1.489
0.832	67.18	1.023	0.521	0.596	0.350	0.0688	0.0461	1.491
0.833	68.17	1.119	0.570	0.611	0.359	0.0733	0.0488	1.500

Table 5. Concluded

(b) Reynolds number sweeps

M	Re/ft x 10^{-6}	W_{2C}, lbm/sec	A_0/A_C	δ, in	δ/H_i	δ^*, in	θ, in	H
0.829	24.97*	0.624	0.314	0.627	0.368	0.0744	0.0492	1.513
0.829	29.94*	0.625	0.315	0.611	0.359	0.0727	0.0482	1.509
0.827	34.84*	0.626	0.316	0.611	0.359	0.0716	0.0475	1.506
0.829	41.87*	0.625	0.315	0.611	0.359	0.0704	0.0469	1.502
0.831	41.29	0.620	0.313	0.611	0.359	0.0736	0.0487	1.512
0.831	57.20	0.619	0.312	0.611	0.359	0.0713	0.0473	1.507
0.829	68.27	0.620	0.313	0.596	0.350	0.0706	0.0469	1.505
0.832	25.54*	1.130	0.575	0.580	0.341	0.0705	0.0469	1.505
0.827	30.57*	1.130	0.576	0.580	0.341	0.0699	0.0466	1.499
0.834	34.97*	1.133	0.576	0.576	0.338	0.0699	0.0465	1.503
0.834	41.69*	1.134	0.577	0.596	0.350	0.0699	0.0466	1.501
0.830	42.39	1.120	0.571	0.611	0.359	0.0739	0.0491	1.504
0.830	57.41	1.119	0.571	0.611	0.359	0.0730	0.0487	1.499
0.833	68.17	1.119	0.570	0.611	0.359	0.0733	0.0488	1.500

* Nominal $T_{t,\infty}$ = 260° R; nominal $T_{t,\infty}$ = 180° R for all other data.

Table 6. Test Conditions and Boundary Layer Data for Inlet C

(a) Mass-flow sweeps

M	Re/ft x 10^{-6}	W_{2C}, lbm/sec	A_0/A_C	δ, in	δ/H_i	δ^*, in	θ, in	H
0.247	34.05	0.613	0.734	0.891	0.634	0.1741	0.1203	1.447
0.249	33.08	0.891	1.059	0.829	0.590	0.1439	0.1024	1.405
0.248	33.03	1.001	1.195	0.813	0.579	0.1457	0.1022	1.425
0.252	33.17	1.036	1.217	0.642	0.457	0.0880	0.0670	1.314
0.400	50.95	0.616	0.479	0.689	0.490	0.0967	0.0724	1.335
0.400	50.62	0.892	0.694	0.673	0.479	0.0942	0.0702	1.342
0.396	49.82	1.014	0.795	0.658	0.468	0.0942	0.0700	1.347
0.403	50.60	1.049	0.811	0.611	0.435	0.0724	0.0555	1.306
0.597	68.58	0.615	0.351	0.673	0.479	0.0896	0.0643	1.394
0.601	67.60	0.897	0.514	0.611	0.435	0.0804	0.0578	1.390
0.601	67.66	1.017	0.583	0.627	0.446	0.0822	0.0589	1.395
0.604	67.76	1.071	0.613	0.576	0.410	0.0688	0.0503	1.368
0.803	68.43	0.615	0.297	0.627	0.446	0.0738	0.0500	1.476
0.801	68.41	0.897	0.438	0.627	0.446	0.0779	0.0523	1.489
0.802	67.74	1.021	0.500	0.611	0.435	0.0778	0.0522	1.490
0.801	68.02	1.087	0.534	0.572	0.407	0.0725	0.0488	1.487
0.833	68.50	0.615	0.292	0.611	0.435	0.0715	0.0479	1.492
0.835	68.00	0.896	0.431	0.611	0.435	0.0760	0.0505	1.504
0.831	68.40	1.033	0.499	0.611	0.435	0.0772	0.0511	1.511
0.830	67.99	1.100	0.533	0.569	0.405	0.0709	0.0473	1.500

Table 6. Concluded

(b) Reynolds number sweeps

M	**Re/ft x 10^{-6}**	**W_{2C}, lbm/sec**	**A_0/A_C**	**δ, in**	**δ/H_i**	**δ^*, in**	**θ, in**	**H**
0.829	25.07*	0.619	0.293	0.627	0.446	0.0711	0.0474	1.501
0.829	30.02*	0.621	0.295	0.611	0.435	0.0695	0.0464	1.498
0.829	35.00*	0.619	0.294	0.611	0.435	0.0683	0.0458	1.493
0.829	42.06*	0.620	0.295	0.596	0.424	0.0664	0.0446	1.491
0.835	42.06	0.616	0.292	0.611	0.435	0.0727	0.0485	1.500
0.832	57.16	0.615	0.292	0.611	0.435	0.0731	0.0489	1.496
0.833	68.50	0.615	0.292	0.611	0.435	0.0715	0.0479	1.492
0.827	25.10*	1.134	0.549	0.569	0.405	0.0674	0.0451	1.494
0.838	30.15*	1.135	0.547	0.557	0.397	0.0658	0.0439	1.498
0.829	34.85*	1.136	0.550	0.554	0.394	0.0646	0.0433	1.490
0.828	41.76*	1.137	0.552	0.546	0.389	0.0630	0.0424	1.486
0.830	42.22	1.108	0.536	0.596	0.424	0.0735	0.0488	1.505
0.831	57.18	1.104	0.535	0.572	0.407	0.0727	0.0483	1.506
0.830	67.99	1.100	0.533	0.569	0.405	0.0709	0.0473	1.500

* Nominal $T_{t,\infty}$ = 260° R; nominal $T_{t,\infty}$ = 180° R for all other data.

Table 7. Test Conditions and Boundary Layer Data for Inlet D

(a) Mass-flow sweeps

M	Re/ft x 10^{-6}	W_{2C}, lbm/sec	A_0/A_C	δ, in	δ/H_i	δ^*, in	θ, in	H
0.246	33.84	0.612	0.770	0.891	0.634	0.1659	0.1165	1.425
0.249	33.53	0.894	1.107	0.860	0.612	0.1601	0.1099	1.457
0.247	32.91	0.999	1.245	0.860	0.612	0.1614	0.1103	1.463
0.250	33.68	1.017	1.254	0.782	0.557	0.1415	0.1000	1.415
0.399	51.18	0.612	0.498	0.720	0.512	0.1025	0.0762	1.345
0.401	51.60	0.895	0.726	0.689	0.490	0.1013	0.0745	1.359
0.400	50.91	1.014	0.823	0.689	0.490	0.1001	0.0737	1.360
0.402	51.53	1.053	0.851	0.720	0.512	0.1020	0.0753	1.355
0.596	68.64	0.613	0.365	0.658	0.468	0.0877	0.0631	1.390
0.610	67.70	0.899	0.531	0.658	0.468	0.0904	0.0642	1.408
0.600	67.33	1.019	0.610	0.642	0.457	0.0894	0.0636	1.406
0.612	66.93	1.090	0.644	0.673	0.479	0.0904	0.0644	1.404
0.798	68.38	0.613	0.309	0.642	0.457	0.0756	0.0511	1.480
0.805	68.23	0.900	0.457	0.642	0.457	0.0843	0.0561	1.503
0.809	68.50	1.023	0.520	0.642	0.457	0.0874	0.0578	1.514
0.800	68.04	1.107	0.567	0.642	0.457	0.0875	0.0582	1.505
0.832	68.60	0.614	0.304	0.627	0.446	0.0723	0.0483	1.497
0.830	68.43	0.901	0.452	0.627	0.446	0.0805	0.0531	1.514
0.831	68.15	1.024	0.516	0.627	0.446	0.0848	0.0557	1.524
0.834	68.40	1.114	0.562	0.642	0.457	0.0850	0.0559	1.521

Table 7. Concluded

(b) Reynolds number sweeps

M	**Re/ft x 10^{-6}**	**W_{2C}, lbm/sec**	**A_0/A_C**	**δ, in**	**δ/H_i**	**δ^*, in**	**θ, in**	**H**
0.826	25.04*	0.617	0.304	0.627	0.446	0.0701	0.0467	1.501
0.828	30.07*	0.618	0.305	0.611	0.435	0.0682	0.0454	1.500
0.829	35.08*	0.618	0.305	0.611	0.435	0.0671	0.0448	1.498
0.828	42.03*	0.619	0.306	0.611	0.435	0.0657	0.0440	1.495
0.830	42.01	0.614	0.304	0.627	0.446	0.0715	0.0477	1.500
0.833	57.41	0.612	0.302	0.627	0.446	0.0720	0.0480	1.502
0.832	68.60	0.614	0.304	0.627	0.446	0.0723	0.0483	1.497
0.831	25.48*	1.126	0.566	0.642	0.457	0.0808	0.0533	1.515
0.828	29.99*	1.128	0.569	0.627	0.446	0.0784	0.0520	1.509
0.827	34.92*	1.129	0.570	0.611	0.435	0.0763	0.0507	1.505
0.838	42.37*	1.127	0.567	0.611	0.435	0.0749	0.0496	1.510
0.830	42.38	1.091	0.549	0.689	0.490	0.0993	0.0643	1.543
0.828	57.06	1.115	0.563	0.642	0.457	0.0863	0.0567	1.521
0.834	68.40	1.114	0.562	0.642	0.457	0.0850	0.0559	1.521

* Nominal $T_{t,\infty}$ = 260° R; nominal $T_{t,\infty}$ = 180° R for all other data.

Table 8. Grid Dimensions for BLI Inlet Numerical Simulations

Grid description	**Grid points**			**Total grid points**
	J direction	**K direction**	**L direction**	
Inlet boundary layer	101	301	57	1 732 857
Inlet core flow	101	51	51	262 701
Inlet lip	81	101	41	335 421
Inlet cowl	91	82	61	455 182
Block at inlet entrance	51	71	76	275 196
Flat plate block around inlet	111	96	126	1 342 656
Flat plate background	141	51	101	726291
			Total	**5 130 304**

Table 9. Pressure Recovery and Distortion Data for Reynolds Number Sweeps on Inlet A, Fence Off

M	$T_{t,\infty}$, °R	Re/ft x 10^{-6}	W_{2C}, lbm/sec	A_0/A_C	$p_{t,2}/p_{t,\infty}$	$DPCP_{avg}$
0.828	259.8	25.03	0.627	0.309	0.947	0.005
0.828	260.1	30.10	0.626	0.308	0.948	0.005
0.828	260.2	35.11	0.628	0.310	0.949	0.005
0.830	260.7	42.06	0.625	0.308	0.949	0.005
0.833	180.6	43.00	0.621	0.306	0.949	0.004
0.829	180.8	58.19	0.621	0.307	0.950	0.005
0.829	180.7	69.54	0.622	0.308	0.951	0.005
0.828	259.2	25.18	0.905	0.449	0.954	0.035
0.829	259.5	30.39	0.904	0.449	0.955	0.035
0.831	259.9	35.19	0.904	0.448	0.955	0.035
0.829	260.2	42.13	0.903	0.449	0.956	0.034
0.829	179.9	43.40	0.903	0.448	0.956	0.033
0.831	180.2	58.95	0.900	0.447	0.957	0.034
0.832	180.1	70.06	0.899	0.447	0.957	0.034
0.829	260.5	25.10	1.021	0.507	0.956	0.046
0.830	260.8	30.16	1.022	0.508	0.957	0.046
0.829	261.0	34.95	1.022	0.509	0.958	0.046
0.829	261.1	41.79	1.023	0.510	0.959	0.046
0.833	180.7	57.71	1.020	0.508	0.960	0.045
0.834	180.8	68.43	1.020	0.508	0.960	0.045
0.832	259.6	24.82	1.133	0.564	0.959	0.051
0.832	259.9	29.81	1.134	0.565	0.960	0.050
0.830	260.3	34.64	1.135	0.567	0.961	0.050
0.829	260.5	41.15	1.130	0.565	0.962	0.049
0.834	179.7	41.56	1.114	0.556	0.961	0.049
0.833	179.9	56.61	1.113	0.556	0.962	0.049
0.833	180.1	67.65	1.113	0.556	0.963	0.048

Table 10. Pressure Recovery and Distortion Data for Reynolds Number Sweeps on Inlet A, Fence On

M	$T_{t,\infty}$, °R	Re/ft x 10^{-6}	W_{2C}, lbm/sec	A_0/A_C	$p_{t,2}/p_{t,\infty}$	$DPCP_{avg}$
0.834	260.1	25.11	0.908	0.448	0.950	0.034
0.832	260.2	30.10	0.909	0.449	0.951	0.034
0.831	260.6	34.97	0.909	0.449	0.952	0.034
0.831	260.6	41.70	0.909	0.449	0.951	0.034
0.830	180.5	41.78	0.908	0.449	0.951	0.034
0.832	180.8	57.17	0.908	0.448	0.951	0.034
0.833	180.9	69.10	0.907	0.447	0.951	0.034
0.830	260.8	24.98	1.125	0.557	0.953	0.056
0.830	260.9	29.77	1.127	0.558	0.954	0.056
0.830	261.1	35.38	1.129	0.560	0.954	0.056
0.829	261.4	41.05	1.129	0.560	0.955	0.056
0.832	180.4	41.64	1.115	0.551	0.953	0.056
0.839	180.7	57.26	1.115	0.551	0.954	0.056
0.832	181.1	68.02	1.108	0.550	0.955	0.055

Table 11. Pressure Recovery and Distortion Data for Reynolds Number Sweeps on Inlet B

M	$T_{t,\infty}$, °R	Re/ft x 10^{-6}	W_{2C}, lbm/sec	A_0/A_C	$p_{t,2}/p_{t,\infty}$	$DPCP_{avg}$
0.829	260.9	24.97	0.624	0.314	0.947	0.004
0.829	261.1	29.94	0.625	0.315	0.948	0.004
0.827	261.4	34.84	0.626	0.316	0.949	0.004
0.829	261.3	41.87	0.625	0.315	0.950	0.004
0.831	180.9	41.29	0.620	0.313	0.949	0.004
0.831	181.2	57.20	0.619	0.312	0.950	0.004
0.829	181.1	68.27	0.620	0.313	0.951	0.004
0.828	260.6	25.12	0.899	0.456	0.955	0.033
0.828	261.0	29.95	0.900	0.457	0.956	0.034
0.828	261.2	34.96	0.900	0.457	0.956	0.034
0.829	260.9	41.92	0.901	0.458	0.957	0.034
0.831	180.5	41.95	0.898	0.456	0.956	0.033
0.831	180.7	57.33	0.898	0.457	0.957	0.033
0.830	180.7	68.56	0.899	0.457	0.958	0.033
0.829	260.6	24.99	1.022	0.520	0.957	0.046
0.836	261.0	30.22	1.023	0.519	0.957	0.046
0.836	261.0	34.89	1.023	0.520	0.958	0.046
0.830	260.6	40.63	1.023	0.521	0.959	0.045
0.830	180.3	56.47	1.023	0.521	0.959	0.045
0.832	180.5	67.18	1.023	0.521	0.960	0.045
0.832	260.4	25.54	1.130	0.575	0.958	0.053
0.827	260.3	30.57	1.130	0.576	0.959	0.053
0.834	260.3	34.97	1.133	0.576	0.959	0.053
0.834	259.7	41.69	1.134	0.577	0.959	0.053
0.830	180.1	42.39	1.120	0.571	0.959	0.052
0.830	179.8	57.41	1.119	0.571	0.960	0.051
0.833	179.9	68.17	1.119	0.570	0.960	0.051

Table 12. Pressure Recovery and Distortion Data for Reynolds Number Sweeps on Inlet C

M	**$T_{t,\infty}$, °R**	**Re/ft x 10^{-6}**	**W_{2C}, lbm/sec**	**A_0/A_C**	**$p_{t,2}/p_{t,\infty}$**	**$DPCP_{avg}$**
0.829	260.4	25.07	0.619	0.293	0.930	0.011
0.829	260.6	30.02	0.621	0.295	0.931	0.011
0.829	260.7	35.00	0.619	0.294	0.931	0.011
0.829	260.5	42.06	0.620	0.295	0.933	0.011
0.835	180.5	42.06	0.616	0.292	0.931	0.010
0.832	180.9	57.16	0.615	0.292	0.933	0.010
0.833	181.0	68.50	0.615	0.292	0.934	0.010
0.826	260.2	25.01	0.900	0.432	0.941	0.036
0.830	260.5	30.03	0.899	0.431	0.942	0.036
0.831	260.5	35.03	0.900	0.432	0.943	0.036
0.831	260.5	42.05	0.901	0.433	0.944	0.036
0.836	180.3	42.16	0.896	0.429	0.942	0.035
0.834	180.6	57.42	0.896	0.430	0.944	0.035
0.835	180.2	68.00	0.896	0.431	0.945	0.035
0.829	260.3	25.47	1.035	0.498	0.945	0.050
0.830	260.3	30.56	1.035	0.498	0.946	0.050
0.830	260.4	35.11	1.035	0.499	0.947	0.050
0.831	260.3	41.76	1.035	0.499	0.948	0.050
0.831	180.6	41.85	1.035	0.499	0.947	0.050
0.831	180.6	57.16	1.035	0.500	0.949	0.050
0.831	180.8	68.40	1.033	0.499	0.950	0.050
0.827	259.7	25.10	1.134	0.549	0.949	0.057
0.838	260.2	30.15	1.135	0.547	0.949	0.058
0.829	259.9	34.85	1.136	0.550	0.951	0.057
0.828	260.1	41.76	1.137	0.552	0.952	0.056
0.830	180.4	42.22	1.108	0.536	0.950	0.056
0.831	180.4	57.18	1.104	0.535	0.951	0.055
0.830	180.6	67.99	1.100	0.533	0.952	0.055

Table 13. Pressure Recovery and Distortion Data for Reynolds Number sweeps on Inlet D

M	$T_{t,\infty}$, °R	Re/ft x 10^{-6}	W_{2C}, lbm/sec	A_0/A_C	$p_{t,2}/p_{t,\infty}$	$DPCP_{avg}$
0.826	260.1	25.04	0.617	0.304	0.928	0.012
0.828	260.2	30.07	0.618	0.305	0.929	0.012
0.829	260.2	35.08	0.618	0.305	0.929	0.012
0.828	260.4	42.03	0.619	0.306	0.931	0.011
0.830	180.2	42.01	0.614	0.304	0.930	0.011
0.833	180.5	57.41	0.612	0.302	0.930	0.010
0.832	180.6	68.60	0.614	0.304	0.933	0.010
0.832	260.5	25.06	0.899	0.448	0.939	0.037
0.830	261.1	30.45	0.901	0.450	0.941	0.036
0.830	260.4	35.80	0.902	0.451	0.942	0.036
0.830	260.5	42.38	0.902	0.451	0.942	0.036
0.828	180.3	41.92	0.898	0.450	0.942	0.036
0.831	180.3	57.38	0.900	0.451	0.943	0.036
0.830	180.6	68.43	0.901	0.452	0.945	0.035
0.834	259.9	24.66	1.024	0.512	0.942	0.050
0.833	260.1	29.58	1.024	0.513	0.944	0.049
0.829	260.3	34.25	1.025	0.514	0.945	0.049
0.835	260.6	42.10	1.025	0.514	0.946	0.049
0.831	180.5	41.86	1.026	0.515	0.946	0.049
0.829	180.3	56.81	1.026	0.516	0.948	0.049
0.831	180.2	68.15	1.024	0.516	0.948	0.049
0.831	259.8	25.48	1.126	0.566	0.948	0.057
0.828	260.2	29.99	1.128	0.569	0.949	0.057
0.827	260.1	34.92	1.129	0.570	0.950	0.057
0.838	259.1	42.37	1.127	0.567	0.950	0.058
0.830	180.6	42.38	1.091	0.549	0.947	0.056
0.828	180.2	57.06	1.115	0.563	0.950	0.056
0.834	180.4	68.40	1.114	0.562	0.951	0.056

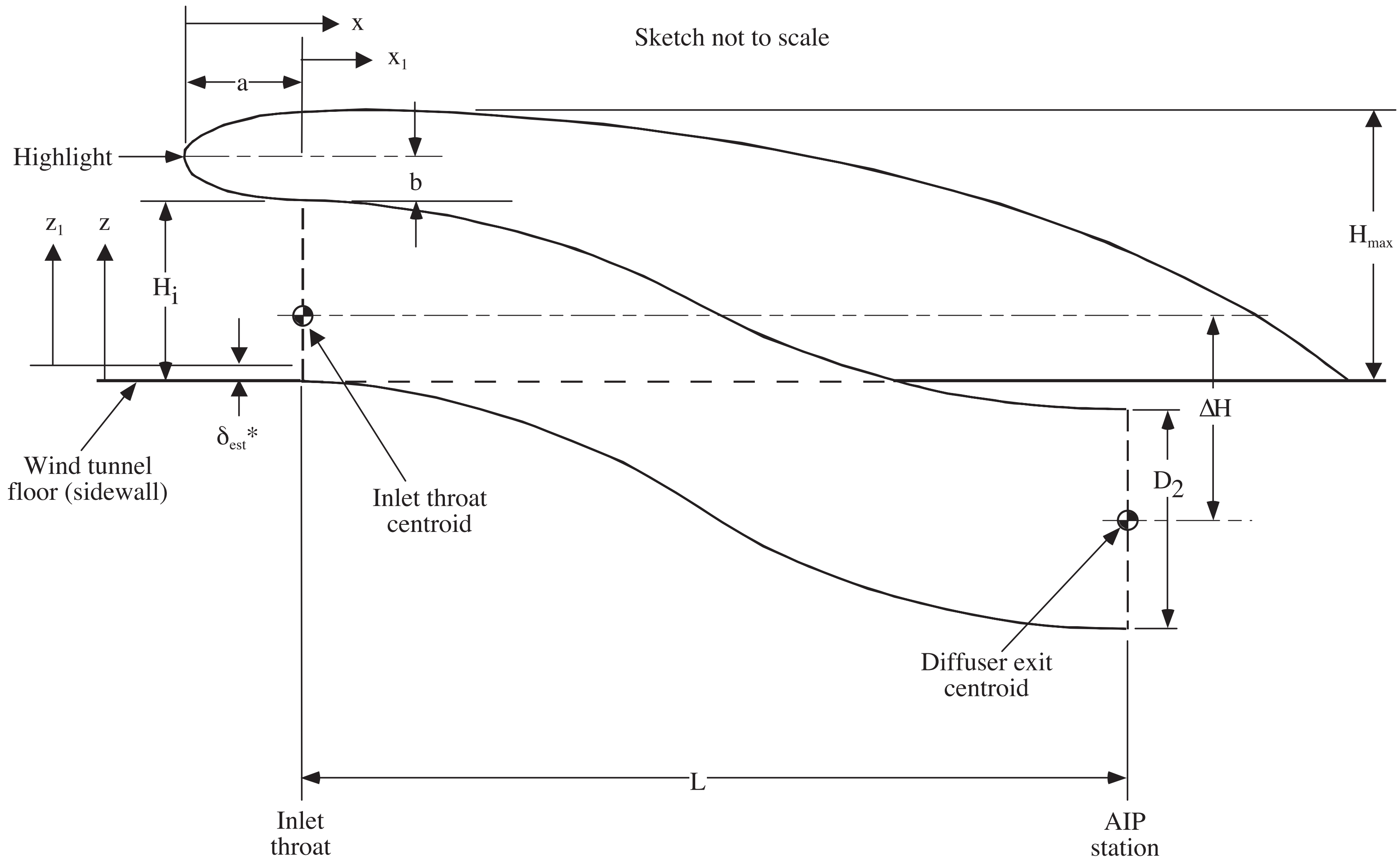

(a) Side view.

Figure 1. - Sketch showing definition of geometry parameters.

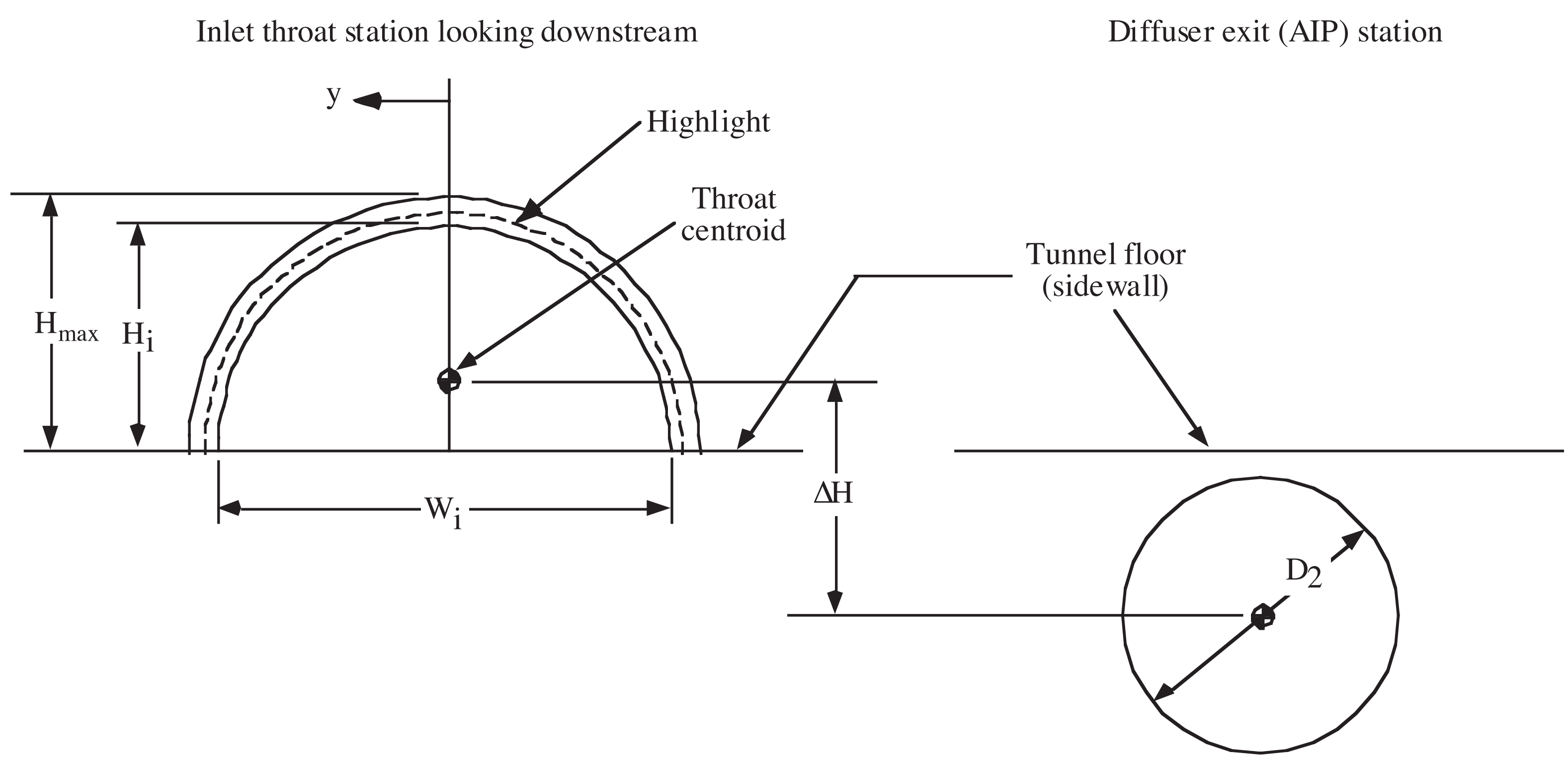

Inlet throat station and diffuser exit (AIP) station are offset for clarity

(b) Front view of flowpath at throat and diffuser exit stations.

Figure 1 - Concluded.

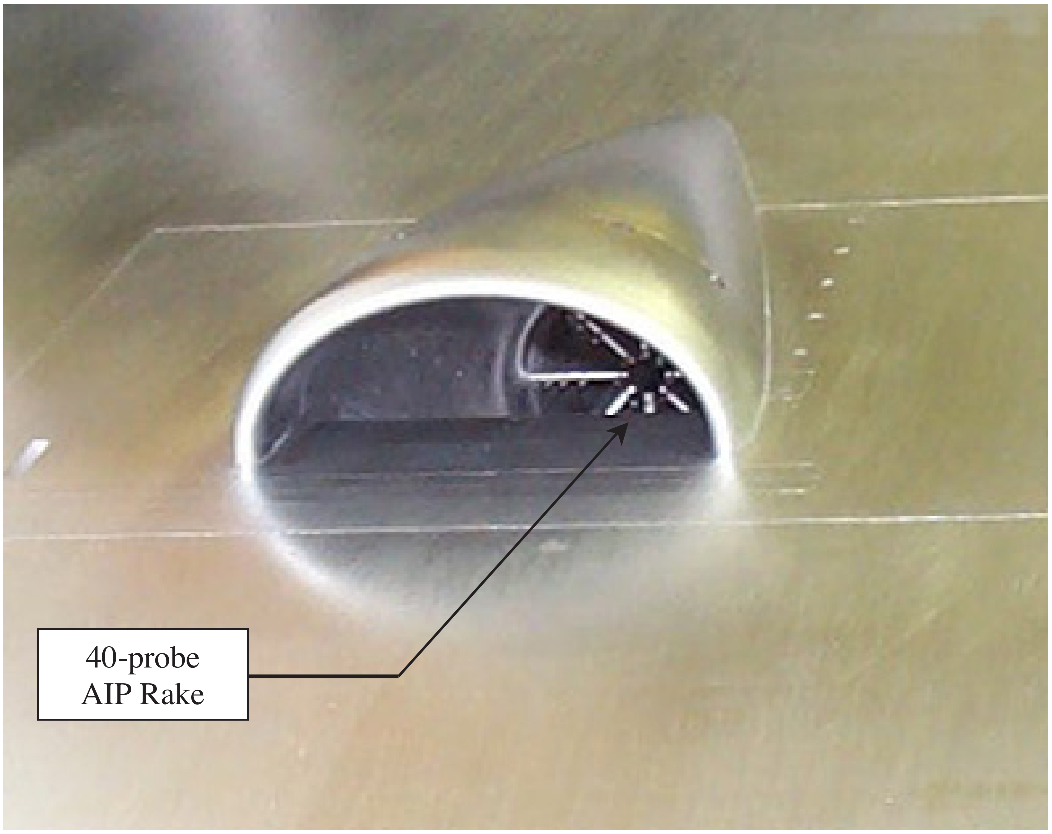

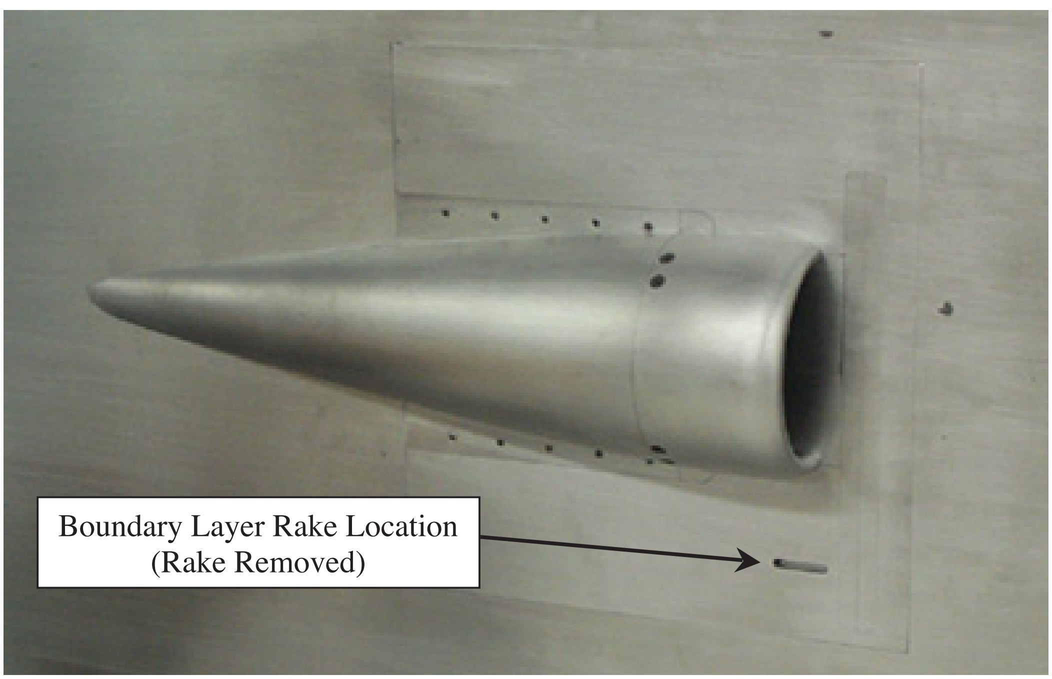

(a) Fence off.

Figure 2. - Photographs of model mounted on tunnel sidewall.

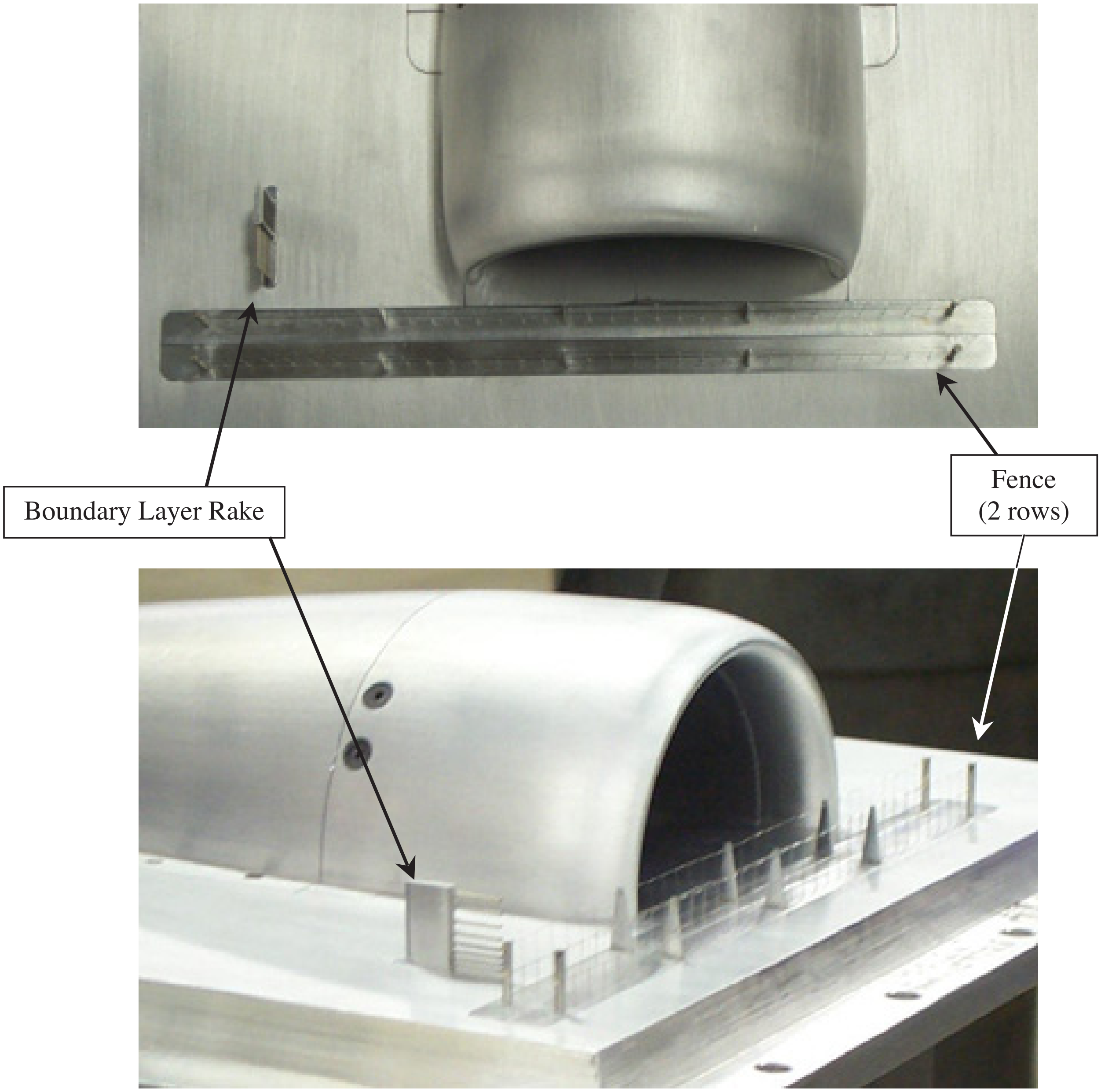

(b) Fence on.

Figure 2. - Concluded.

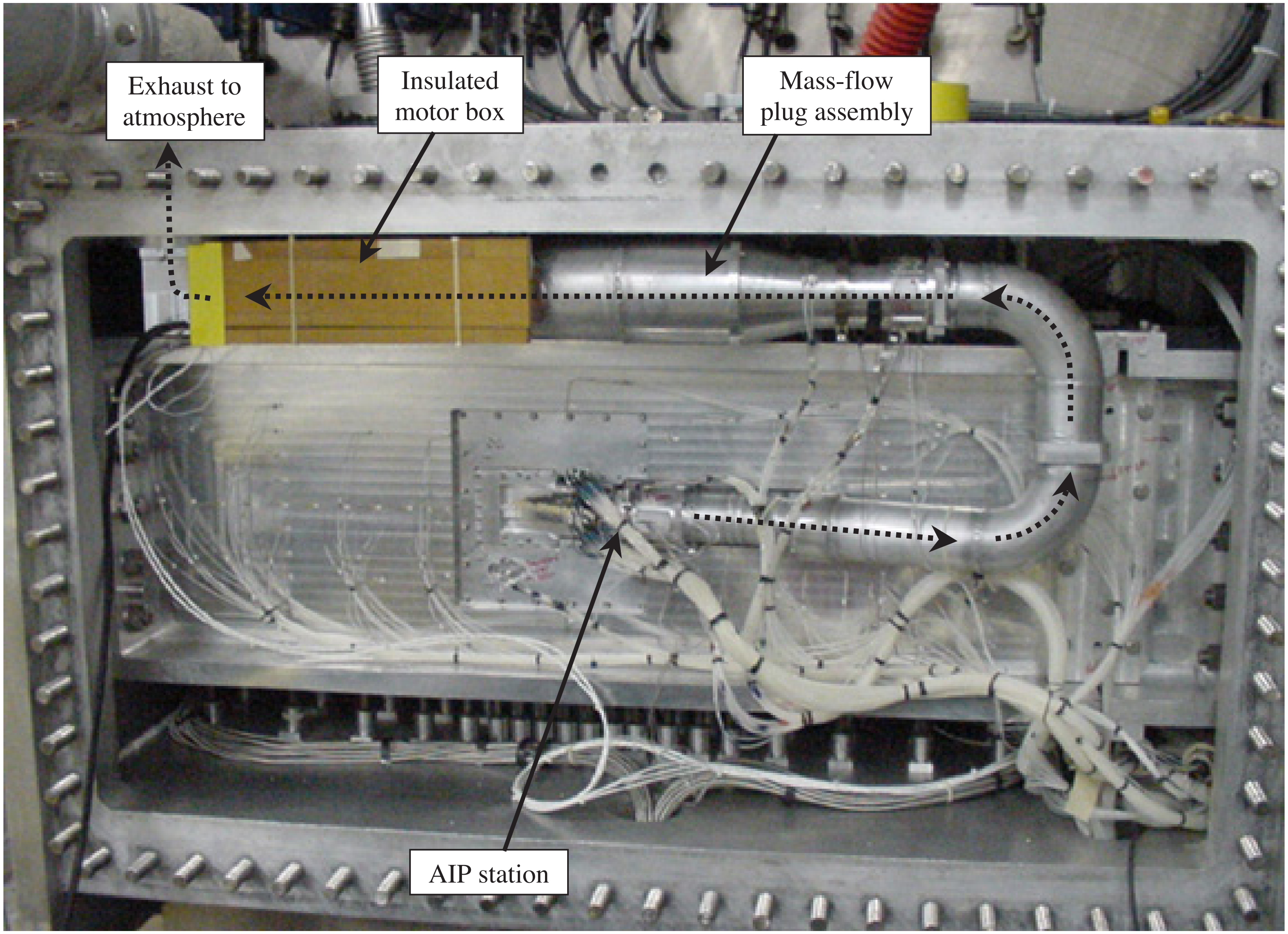

Figure 3. - Photograph showing inlet flow path from back side of tunnel wall. Tunnel pressure shell door removed.

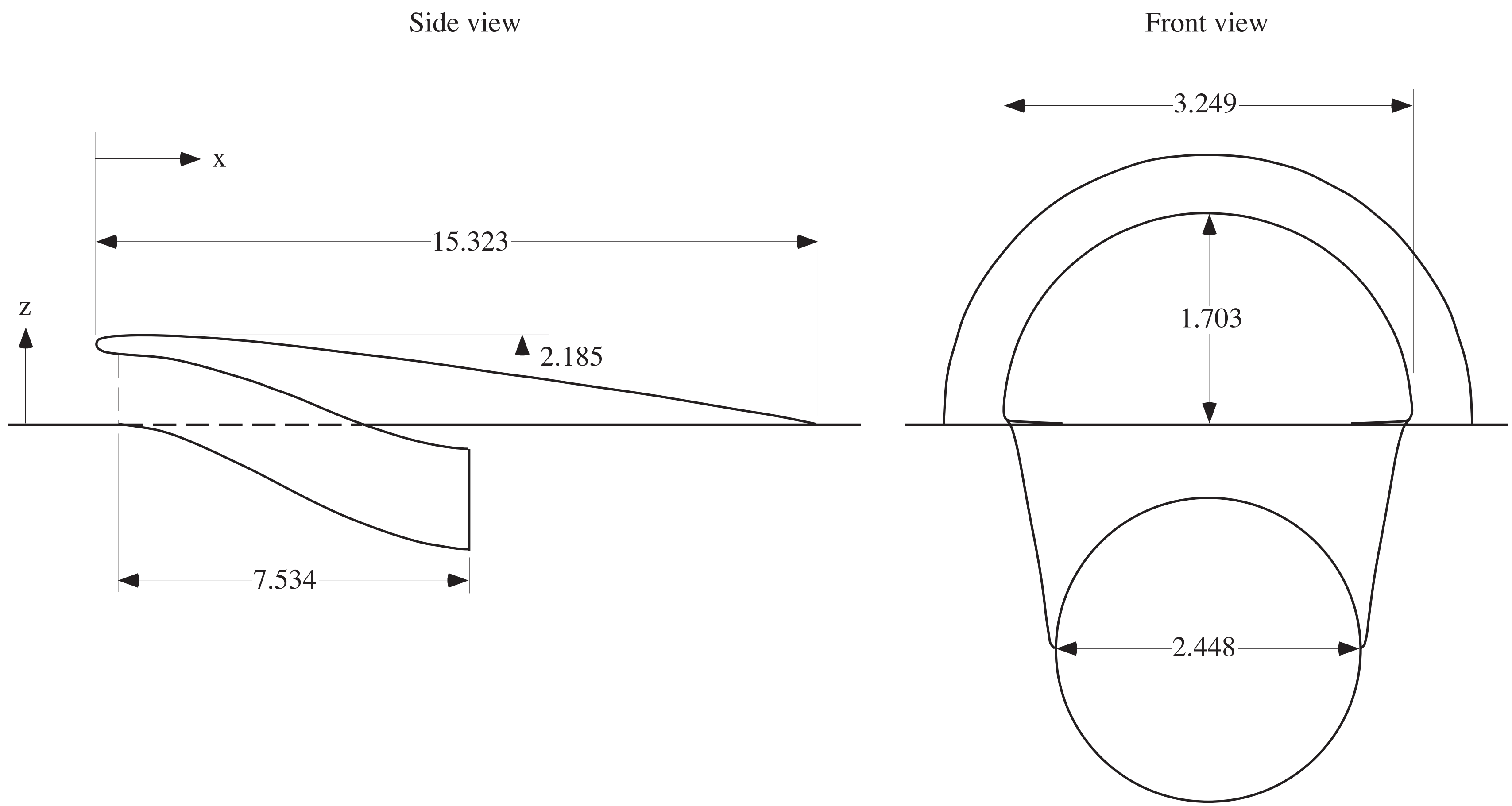

(a) Inlet A.

Figure 4 . - Details of inlet geometry. Side and front views not to same scale.
All dimensions are in inches.

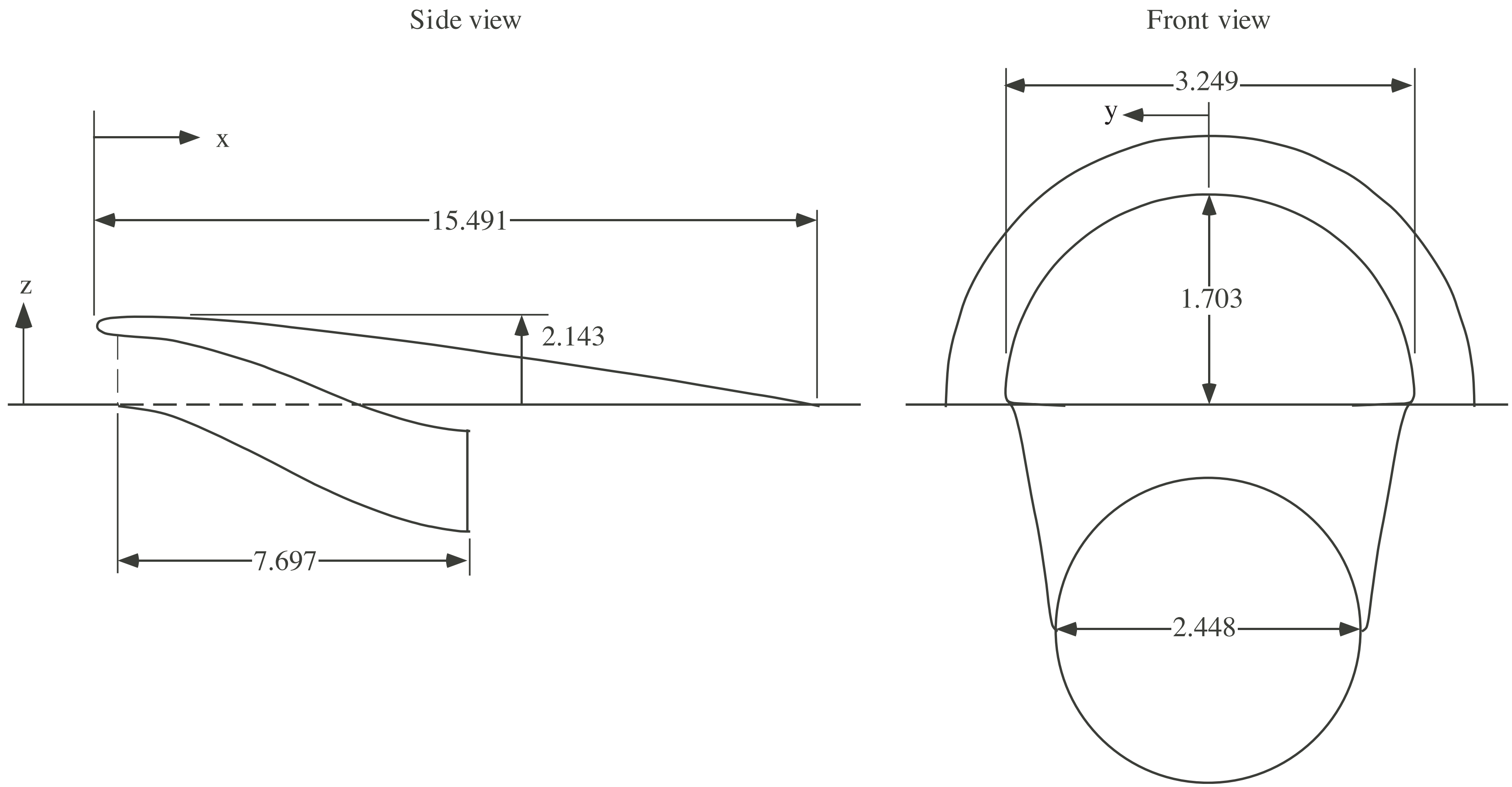

(b) Inlet B.

Figure 4.- Continued.

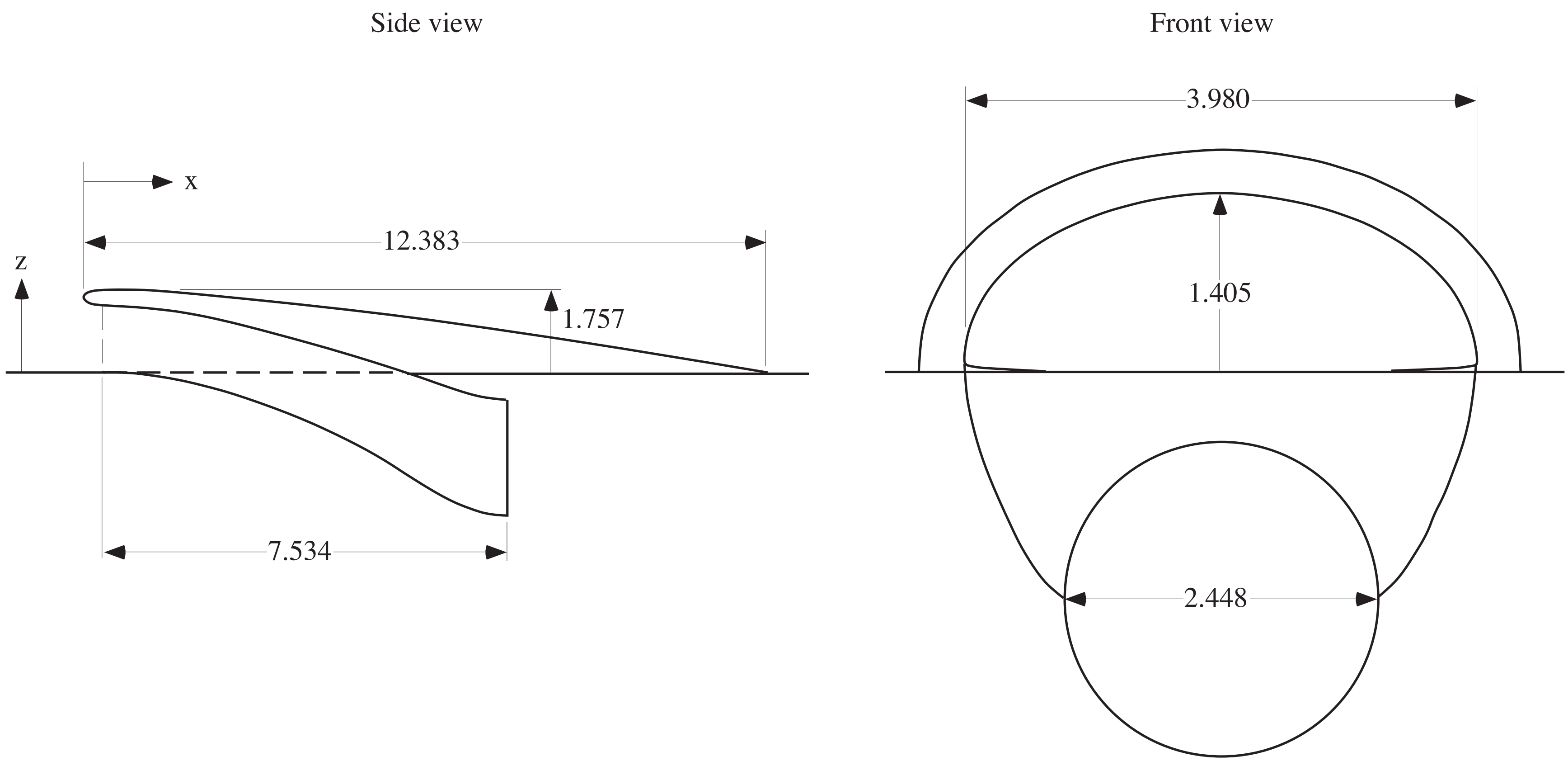

(c) Inlet C.

Figure 4 . - Continued.

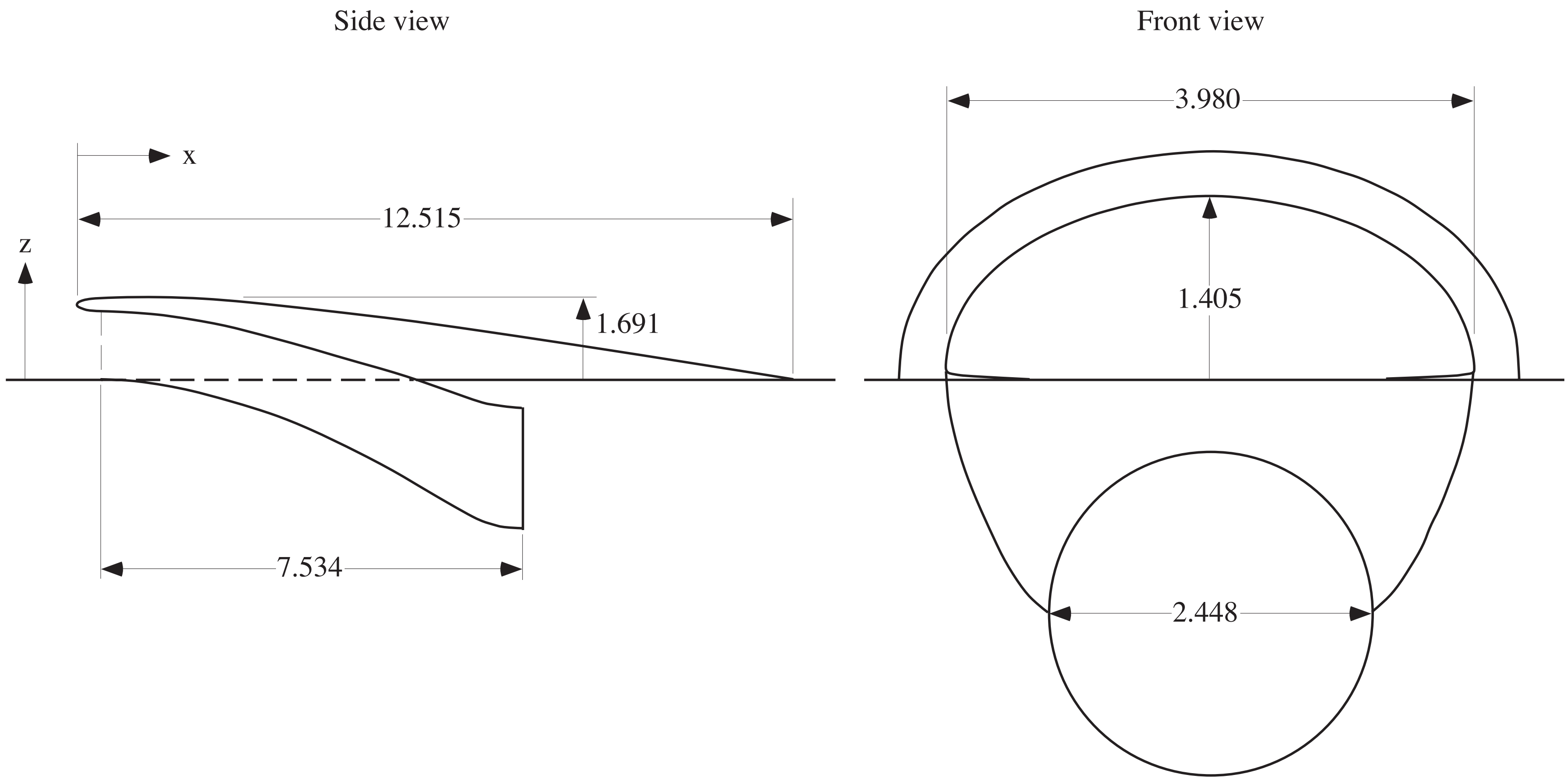

(d) Inlet D.

Figure 4 . - Continued.

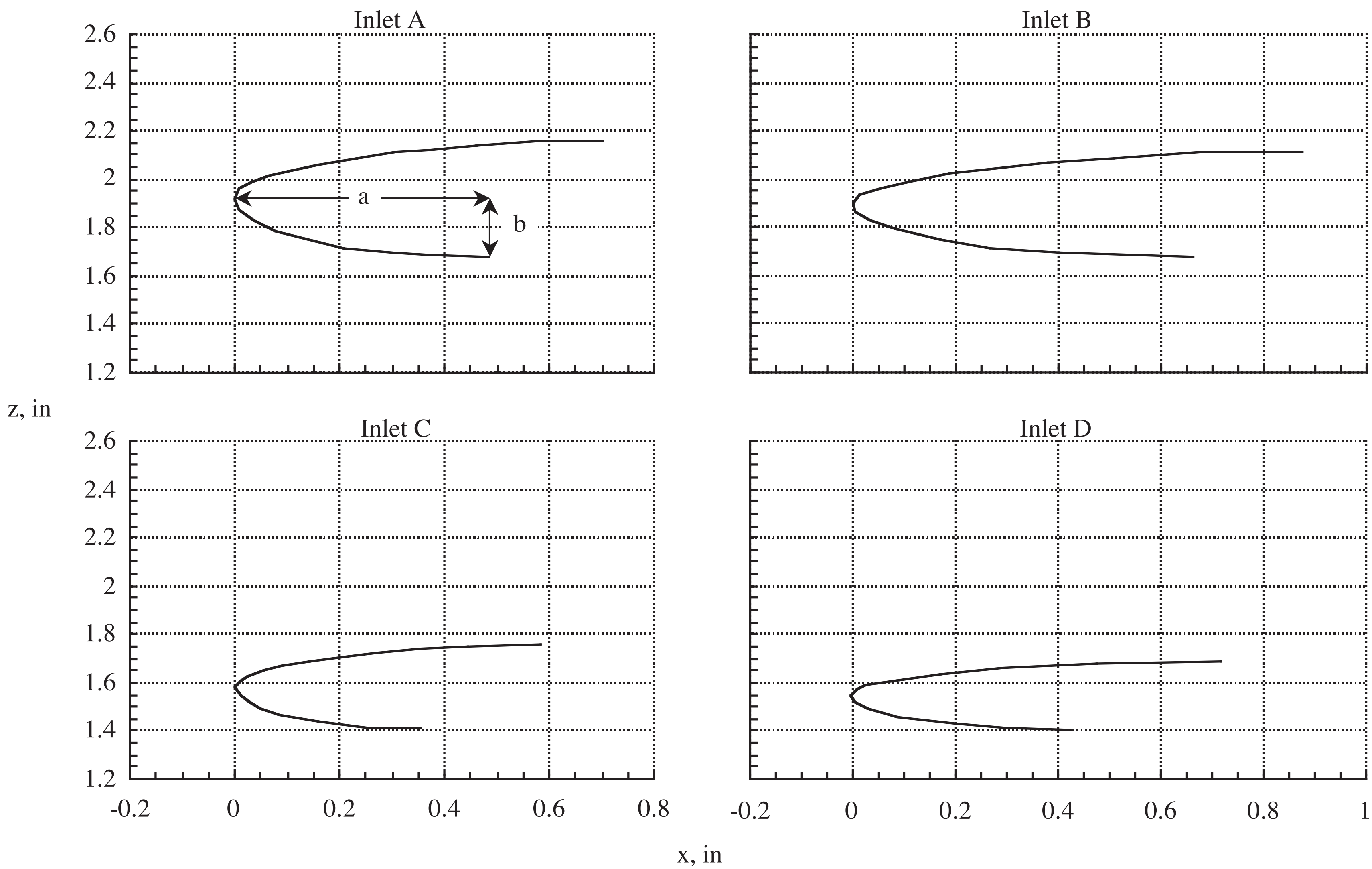

(e) Lip.

Figure 4. - Continued.

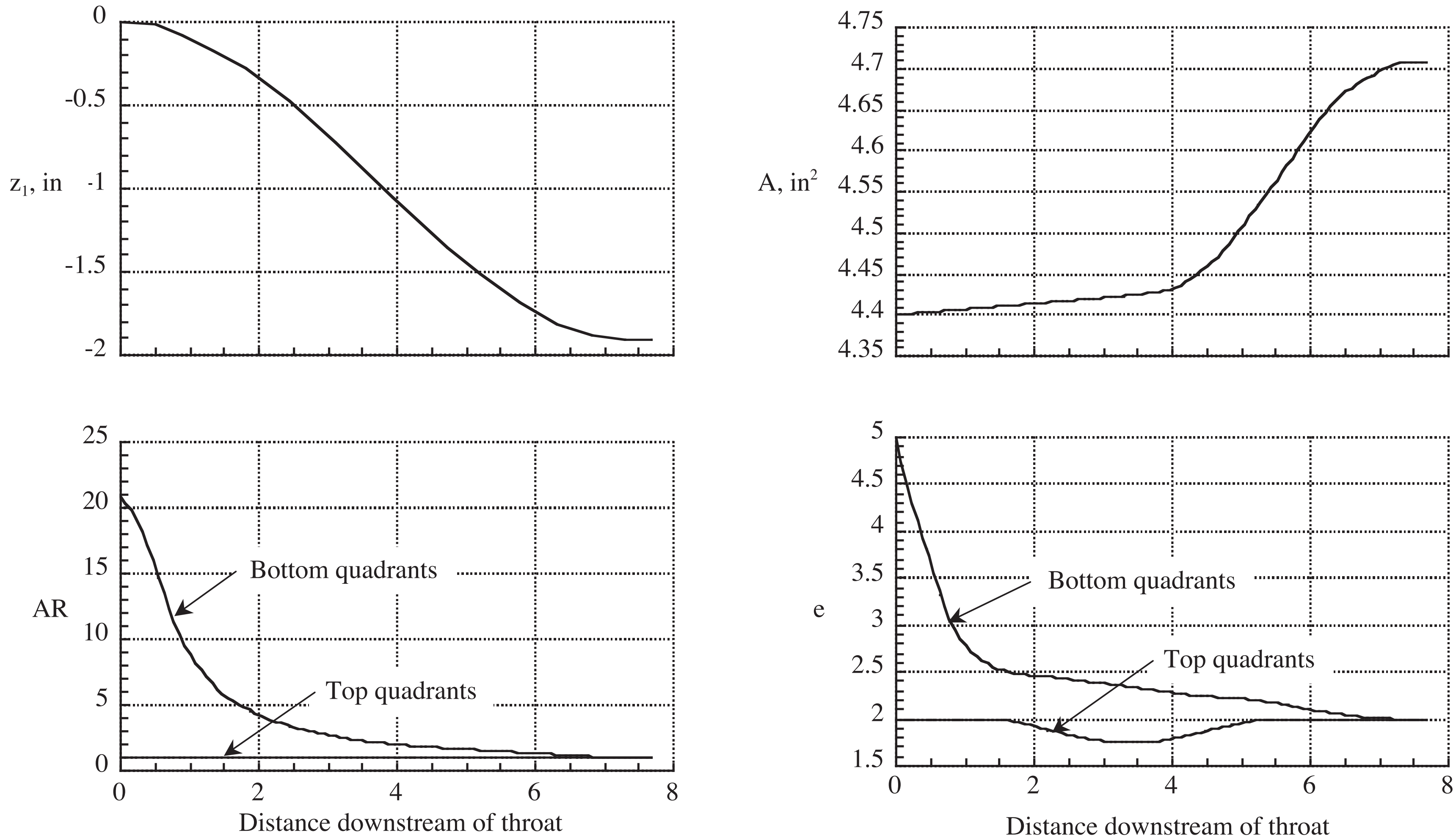

(f) Diffuser for inlets A and B.

Figure 4. - Continued.

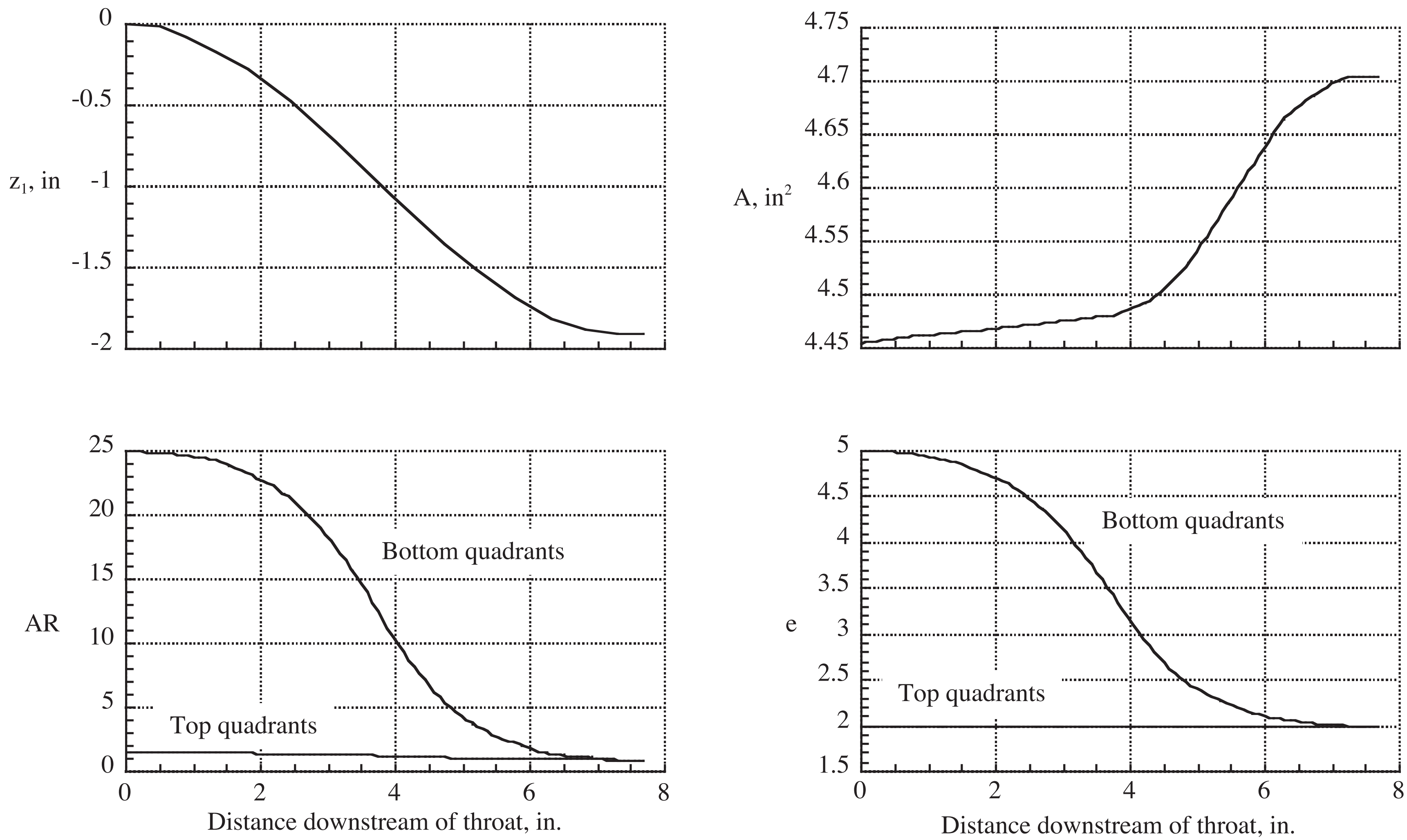

(g) Diffuser for inlets C and D.

Figure 4. - Continued.

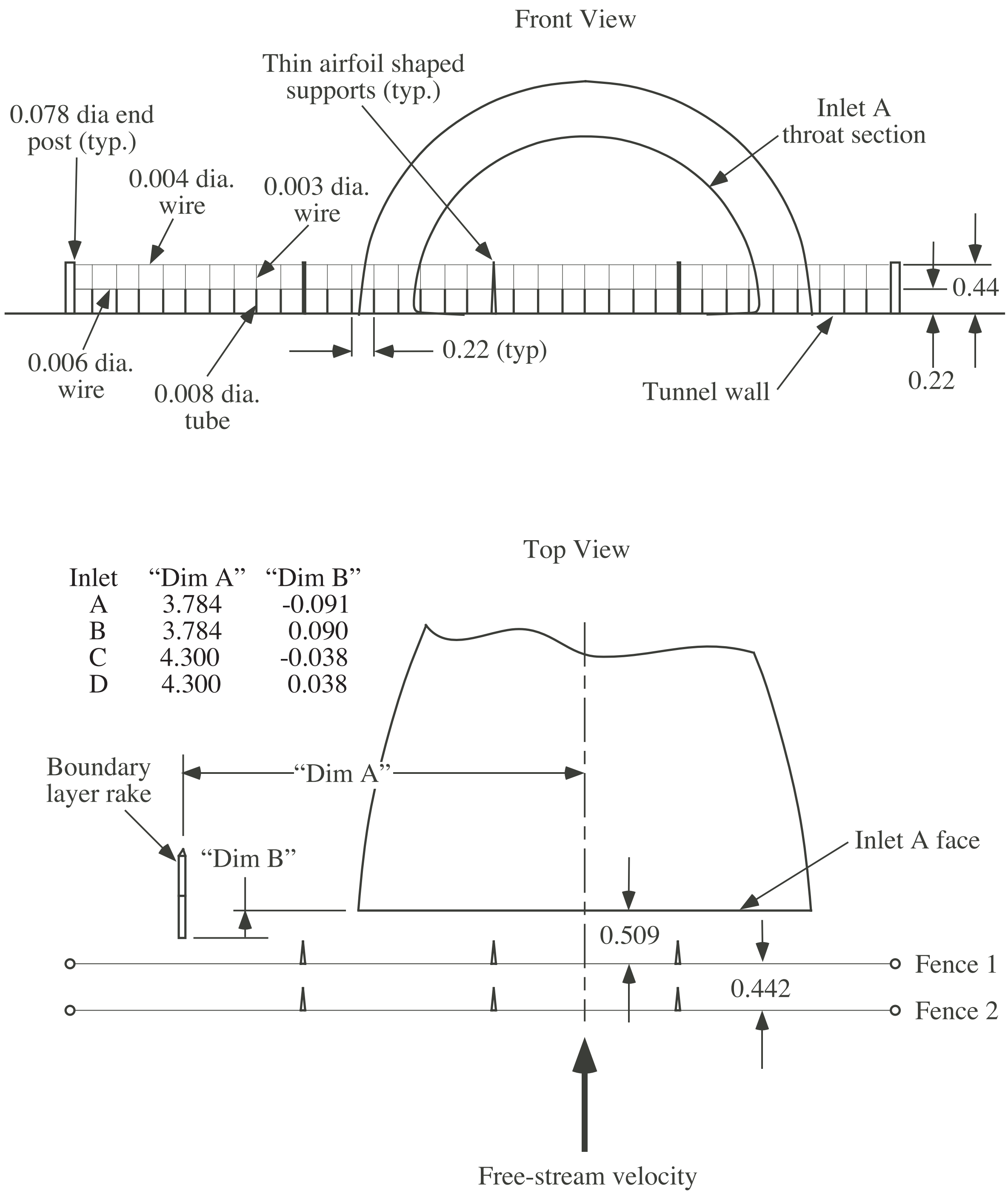

(h) Boundary layer fences.

Figure 4. - Concluded.

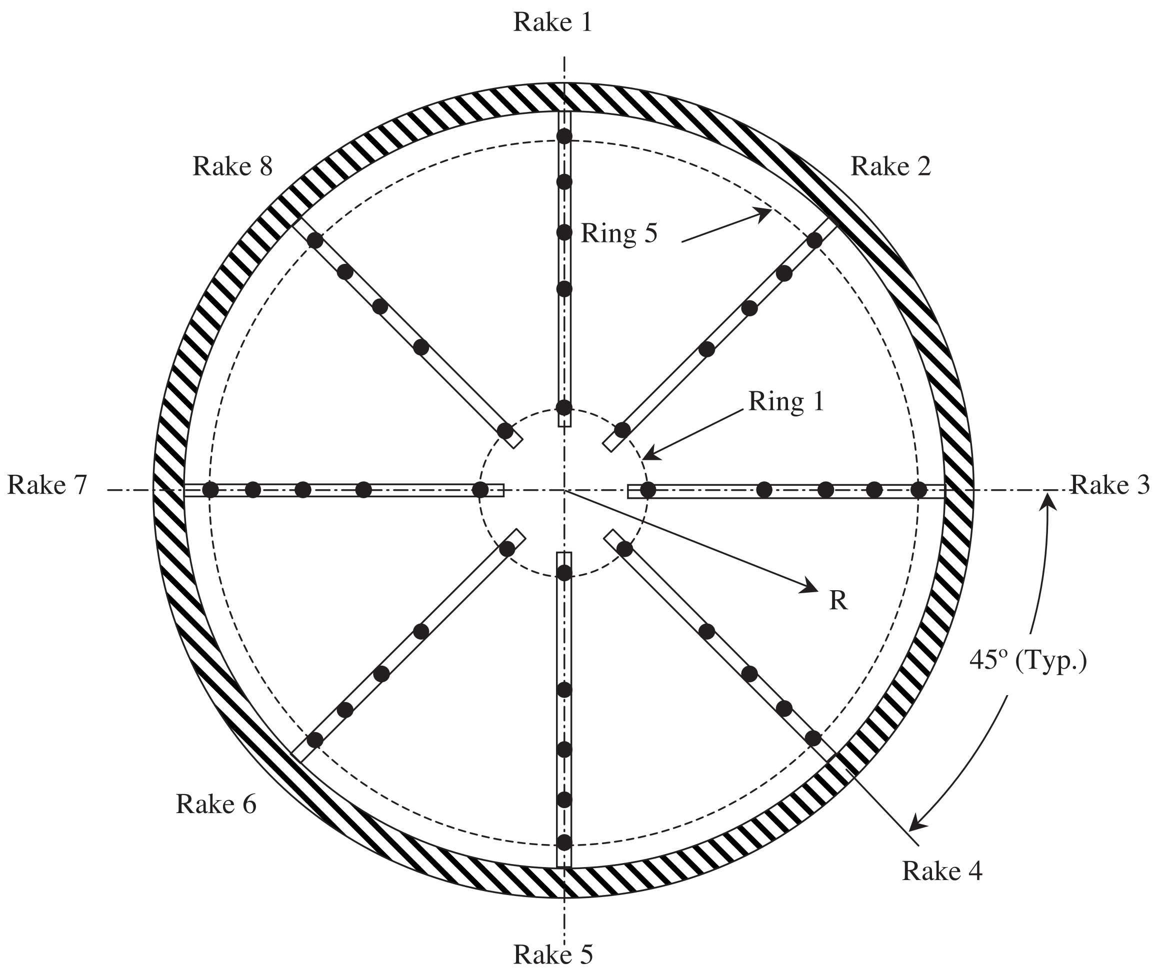

● Steady state pressure

Steady state pressure measurements located at R = 0.274, 0.660, 0.861, 1.021 and 1.159 on all rakes.

(a) AIP station.

Figure 5. - Sketches showing model instrumentation. All dimensions are in inches unless noted.

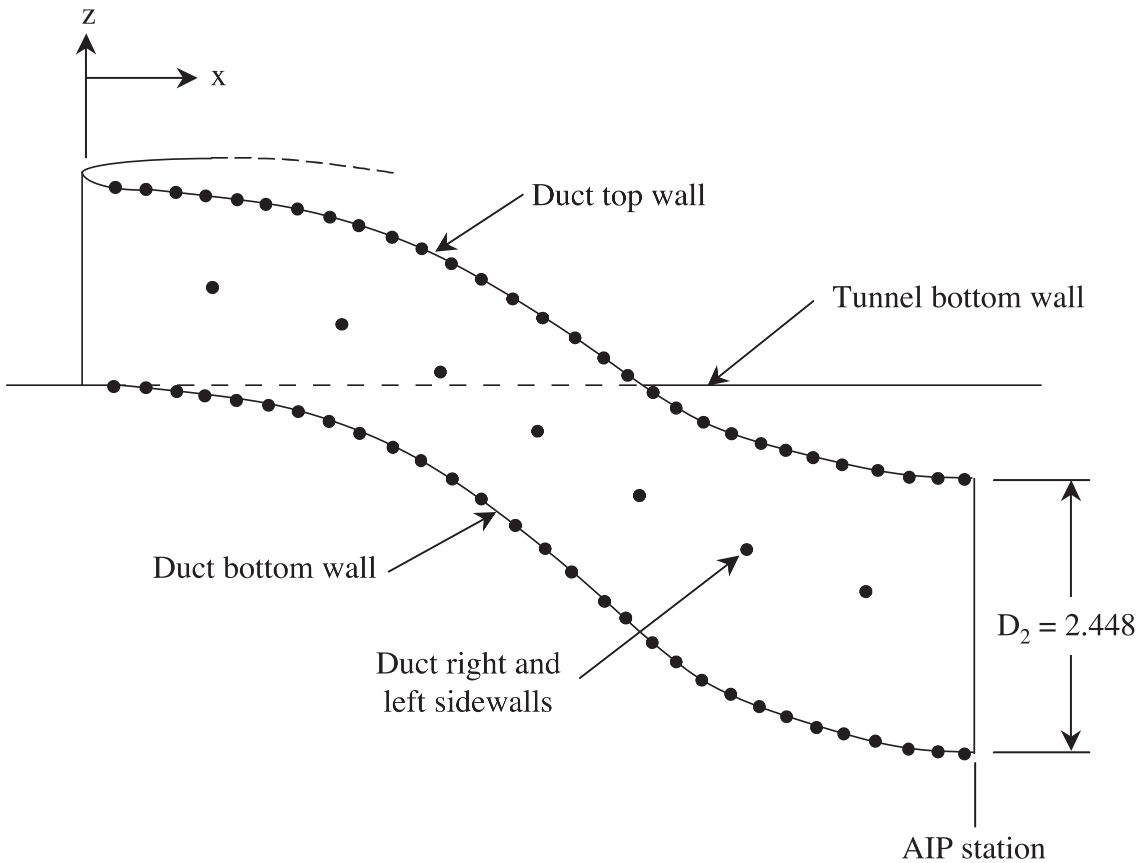

Values of x/D_2 for duct pressure orifices on left and right sidewalls							
Duct Left Sidewall				Duct Right Sidewall			
Inlet A	Inlet B	Inlet C	Inlet D	Inlet A	Inlet B	Inlet C	Inlet D
0.769	0.843	0.709	0.740	0.765	0.839	0.715	0.746
1.308	1.382	1.266	1.297	1.308	1.382	1.273	1.304
1.828	1.902	1.824	1.855	1.822	1.896	1.816	1.847
2.085	2.158	2.082	2.113	2.085	2.158	2.079	2.110
2.351	2.425	2.344	2.375	2.346	2.420	2.344	2.375
2.624	2.698	2.594	2.625	2.619	2.693	2.600	2.632
2.906	2.980	2.853	2.884	2.902	2.976	2.858	2.889

(b) Diffuser, duct left and right sidewalls.

Figure 5. - Continued.

Values of x/D_2 for duct pressure orifices on top and bottom walls							
Duct Top Wall				Duct Bottom Wall			
Inlet A	Inlet B	Inlet C	Inlet D	Inlet A	Inlet B	Inlet C	Inlet D
0.212	0.286	0.157	0.188	0.201	0.275	0.142	0.173
0.353	0.427	0.296	0.326	0.356	0.430	0.299	0.330
0.511	0.585	0.451	0.486	0.519	0.593	0.471	0.502
0.670	0.743	0.605	0.643	0.670	0.744	0.627	0.658
0.821	0.895	0.664	0.695	0.825	0.899	0.791	0.822
0.962	1.036	0.759	0.790	0.968	1.042	0.945	0.976
1.115	1.189	0.908	0.939	1.112	1.186	1.104	1.135
1.256	1.330	1.061	1.092	1.252	1.326	1.259	1.290
1.418	1.492	1.214	1.245	1.395	1.469	1.416	1.447
1.561	1.635	1.362	1.393	1.536	1.610	1.560	1.591
1.711	1.785	1.509	1.540	1.676	1.750	1.709	1.740
1.782	1.856	1.658	1.690	1.750	1.824	1.781	1.813
1.854	1.928	1.731	1.762	1.819	1.893	1.852	1.883
1.925	1.999	1.808	1.839	1.889	1.963	1.928	1.959
1.998	2.072	1.884	1.915	1.961	2.035	1.996	2.027
2.071	2.145	1.957	1.988	2.033	2.107	2.066	2.097
2.138	2.212	2.020	2.051	2.107	2.181	2.132	2.163
2.202	2.276	2.105	2.136	2.181	2.255	2.207	2.238
2.278	2.352	2.176	2.207	2.254	2.328	2.273	2.304
2.349	2.423	2.249	2.280	2.328	2.402	2.339	2.371
2.425	2.499	2.324	2.355	2.402	2.476	2.403	2.434
2.499	2.573	2.396	2.427	2.479	2.553	2.471	2.502
2.574	2.648	2.467	2.498	2.555	2.629	2.561	2.592
2.647	2.721	2.544	2.575	2.635	2.709	2.607	2.638
2.726	2.800	2.615	2.646	2.710	2.784	2.676	2.708
2.800	2.874	2.686	2.717	2.792	2.866	2.748	2.779
2.880	2.954	2.757	2.788	2.869	2.943	2.821	2.853
2.955	3.029	2.833	2.864	2.951	3.025	2.895	2.926
3.039	3.113	2.903	2.934	3.029	3.103	2.979	3.010
		2.981	3.012				

(c) Diffuser, duct top and bottom walls.

Figure 5. - Continued.

Values of x/D_2 for pressure orifices on tunnel wall centerline ahead of inlet face			
Inlet A	Inlet B	Inlet C	Inlet D
-8.883	-8.809	-8.936	-8.905
-8.070	-7.996	-8.123	-8.092
-7.249	-7.175	-7.302	-7.271
-6.433	-6.359	-6.486	-6.455
-5.616	-5.542	-5.669	-5.638
-4.797	-4.723	-4.850	-4.819
-3.165	-3.091	-3.218	-3.187
-2.352	-2.278	-2.405	-2.374
-1.531	-1.457	-1.584	-1.553
-0.770	-0.697	-0.824	-0.793

(d) Tunnel wall centerline ahead of inlet face.

Figure 5.- Continued.

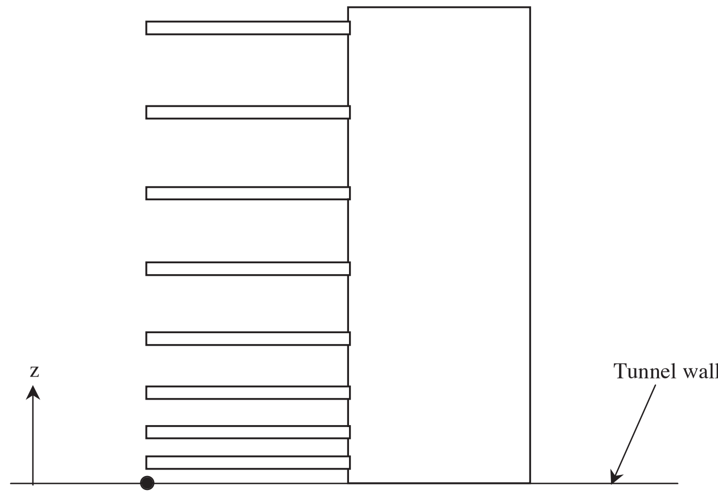

Inlet A			Inlet B			Inlet C			Inlet D		
x/D_2	y/D_2	z/D_2	x/D_2	y/D_2	z/D_2	x/D_2	y/D_2	z/D_2	x/D_2	y/D_2	z/D_2
-0.037	1.546	0.0	0.037	1.546	0.0	-0.016	1.757	0.0	0.016	1.757	0.0
-0.037	1.546	0.0139	0.037	1.546	0.0139	-0.016	1.757	0.0139	0.016	1.757	0.0139
-0.037	1.546	0.0327	0.037	1.546	0.0327	-0.016	1.757	0.0327	0.016	1.757	0.0327
-0.037	1.546	0.0560	0.037	1.546	0.0560	-0.016	1.757	0.0560	0.016	1.757	0.0560
-0.037	1.546	0.0837	0.037	1.546	0.0837	-0.016	1.757	0.0837	0.016	1.757	0.0837
-0.037	1.546	0.1160	0.037	1.546	0.1160	-0.016	1.757	0.1160	0.016	1.757	0.1160
-0.037	1.546	0.1536	0.037	1.546	0.1536	-0.016	1.757	0.1536	0.016	1.757	0.1536
-0.037	1.546	0.1953	0.037	1.546	0.1953	-0.016	1.757	0.1953	0.016	1.757	0.1953
-0.037	1.546	0.2369	0.037	1.546	0.2369	-0.016	1.757	0.2369	0.016	1.757	0.2369

(e) Boundary layer rake.

Figure 5. - Concluded.

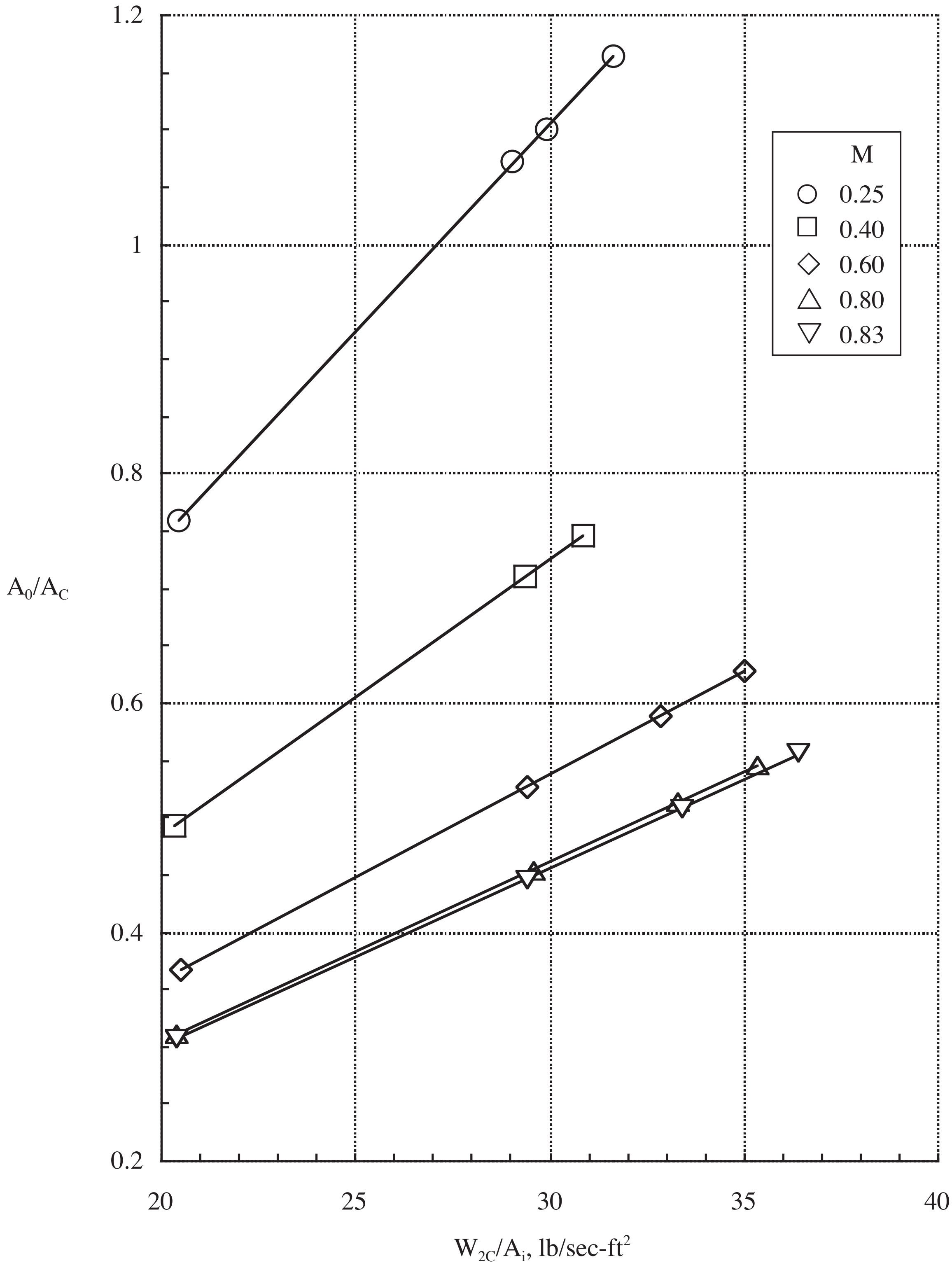

(a) Inlet A, fence off.

Figure 6. - Correlation of inlet mass-flow ratio with corrected inlet mass flow.

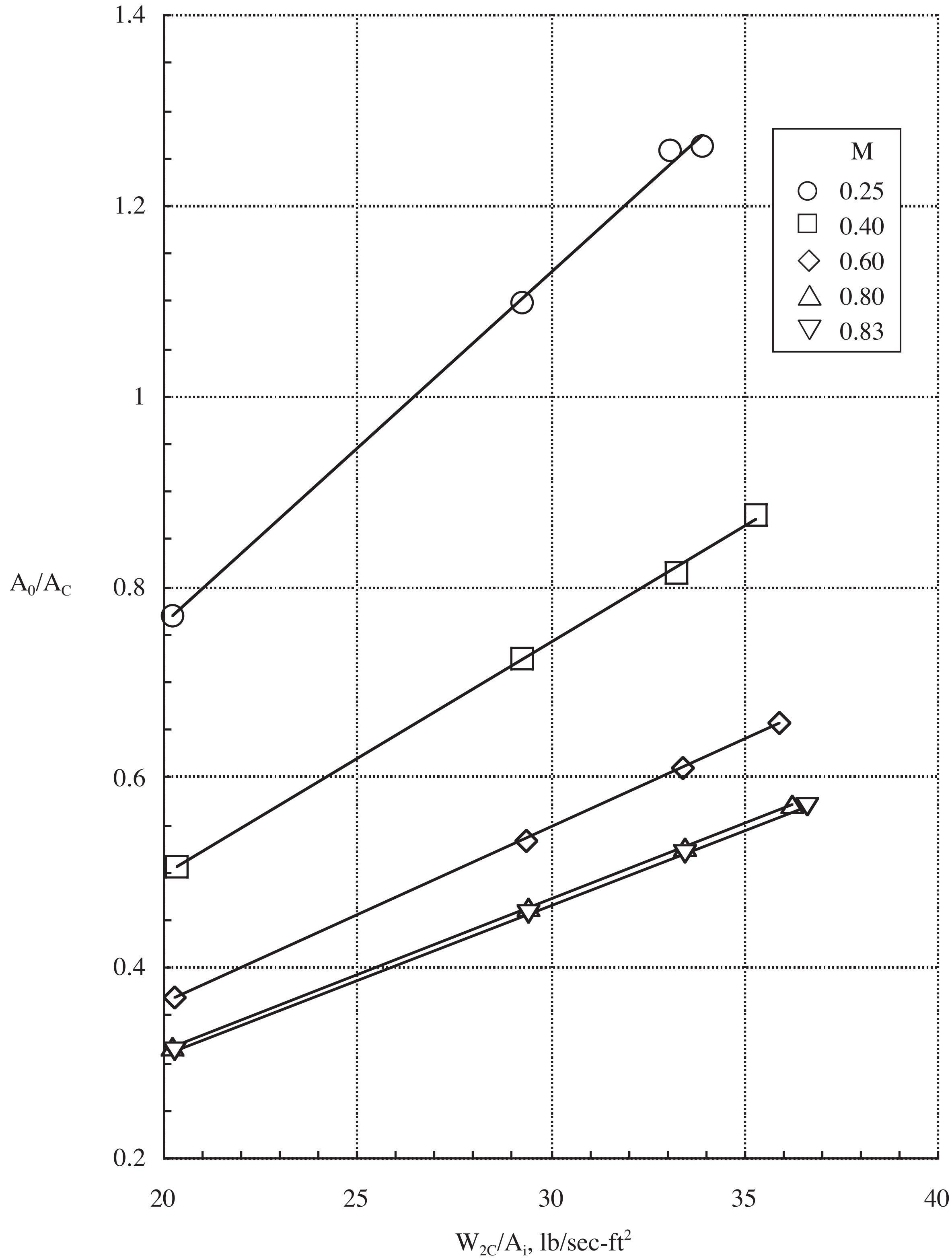

(b) Inlet B.

Figure 6. - Continued.

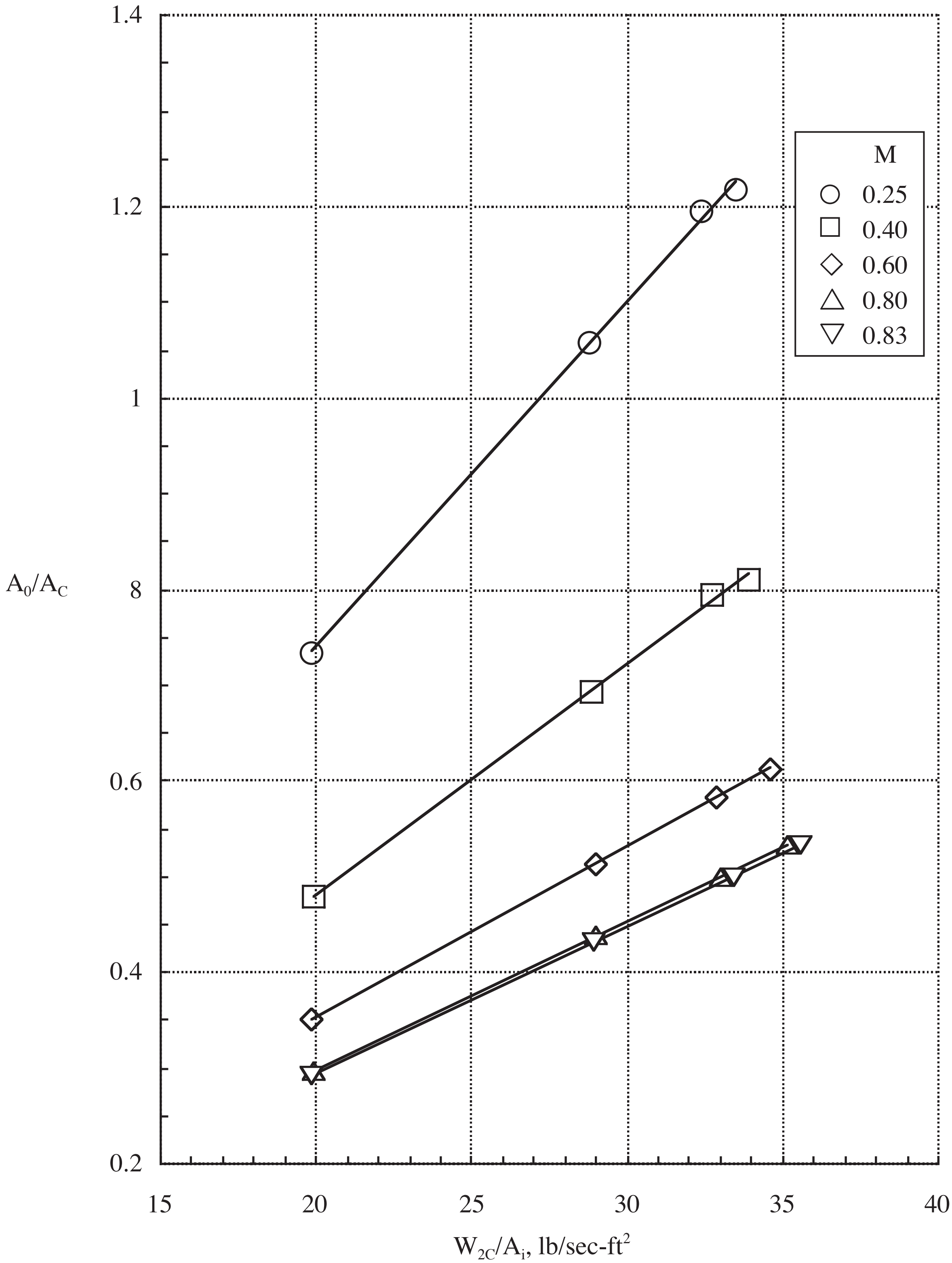

(c) Inlet C.

Figure 6. - Continued.

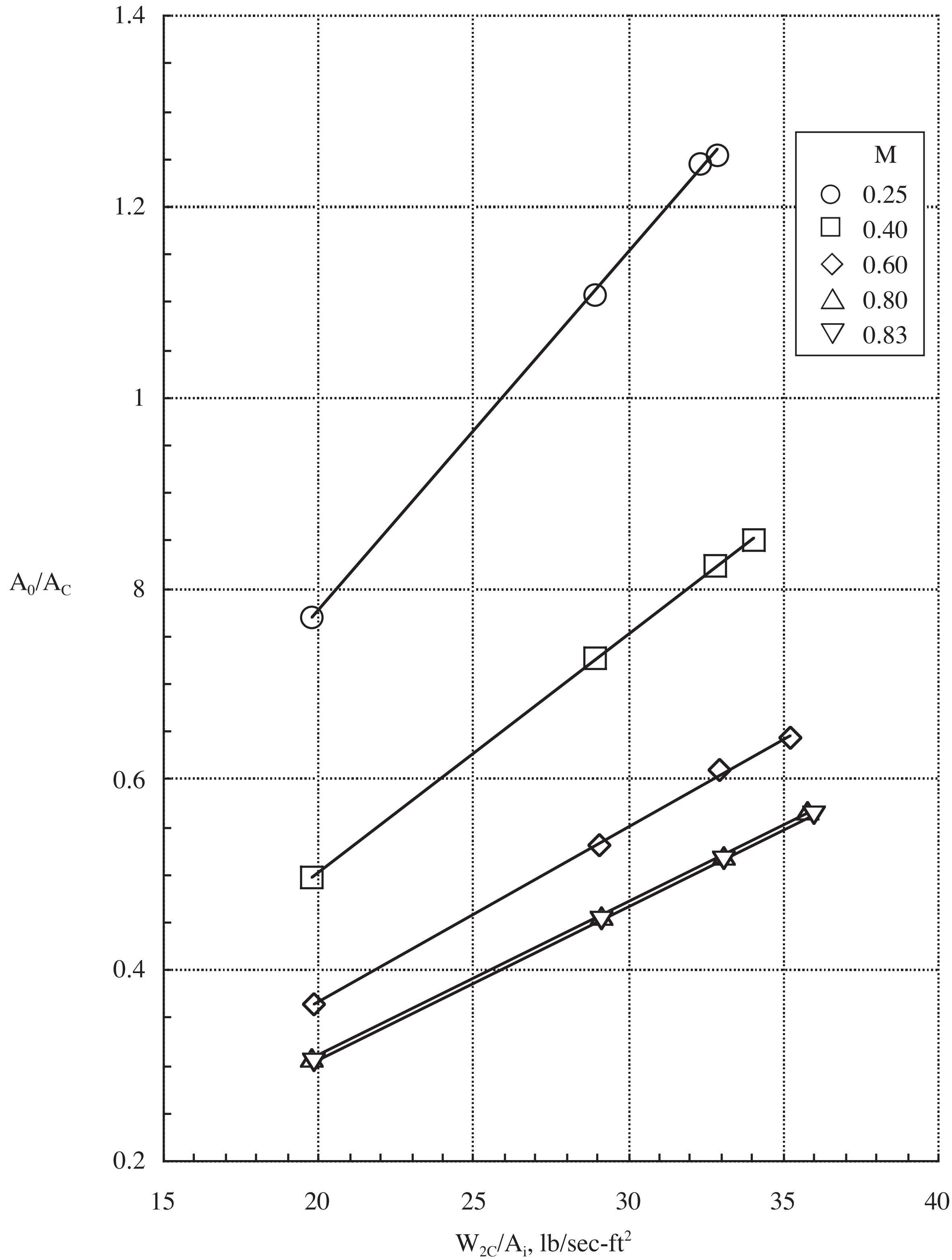

(d) Inlet D.

Figure 6. - Concluded.

Three quarter front view showing BLI inlet surface grids

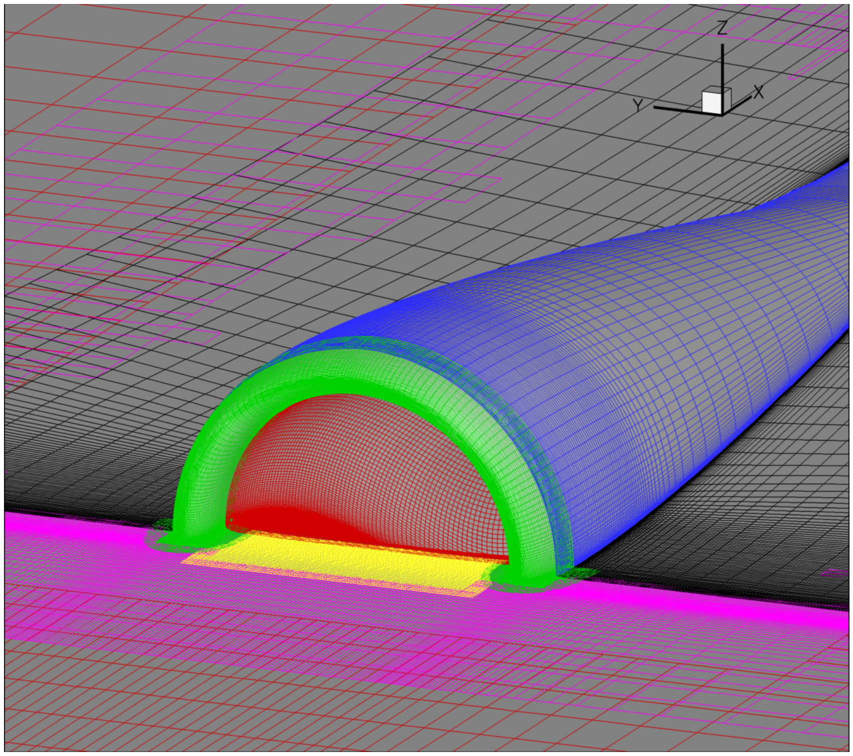

Side view section at centerline of the inlet

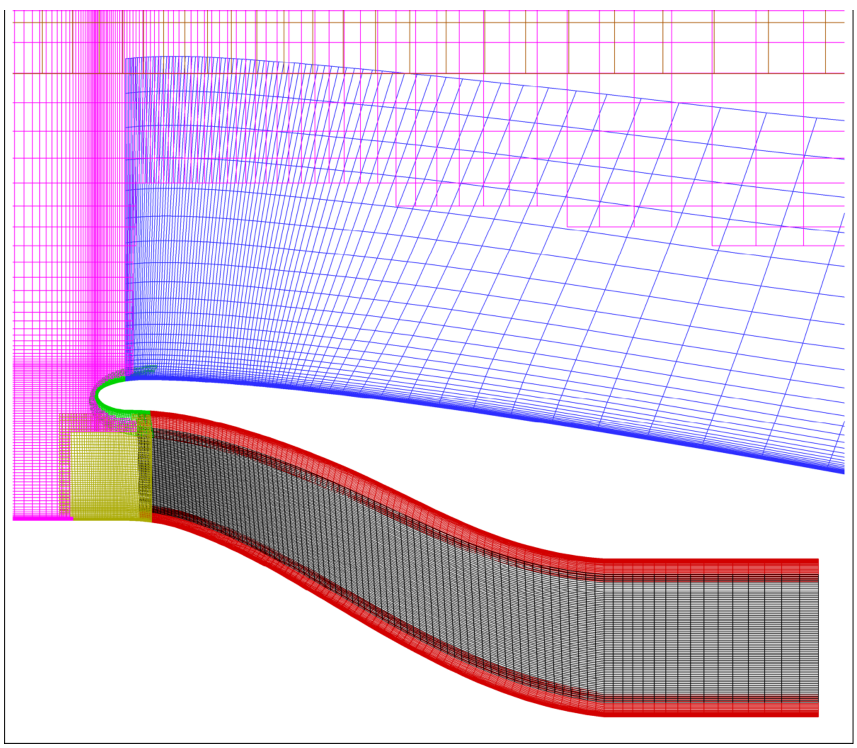

Figure 7. - Views of overset BLI inlet computational grids.

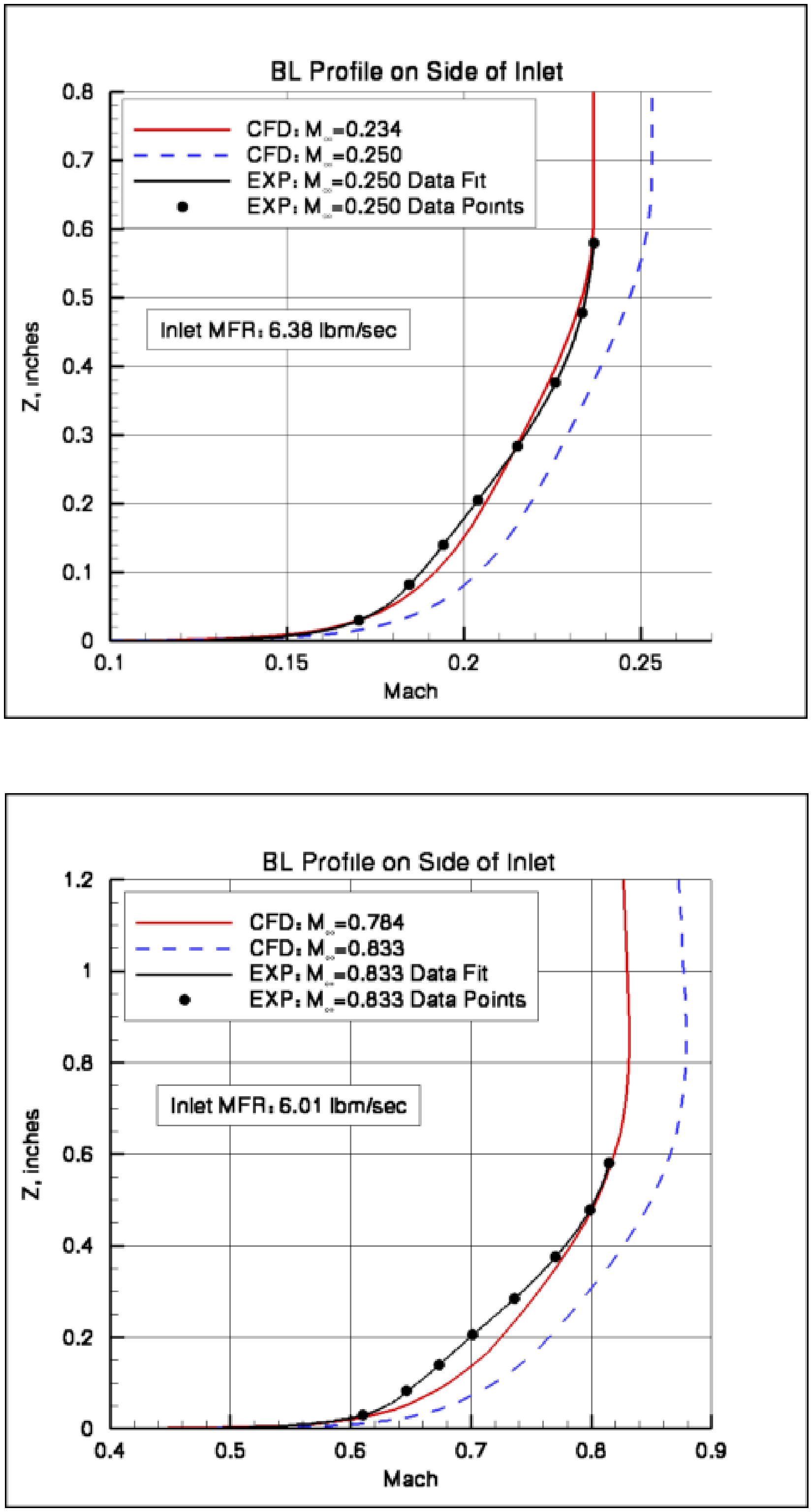

Figure 8. A comparison of boundary layer profiles on side of inlet for experiment and numerical simulations.

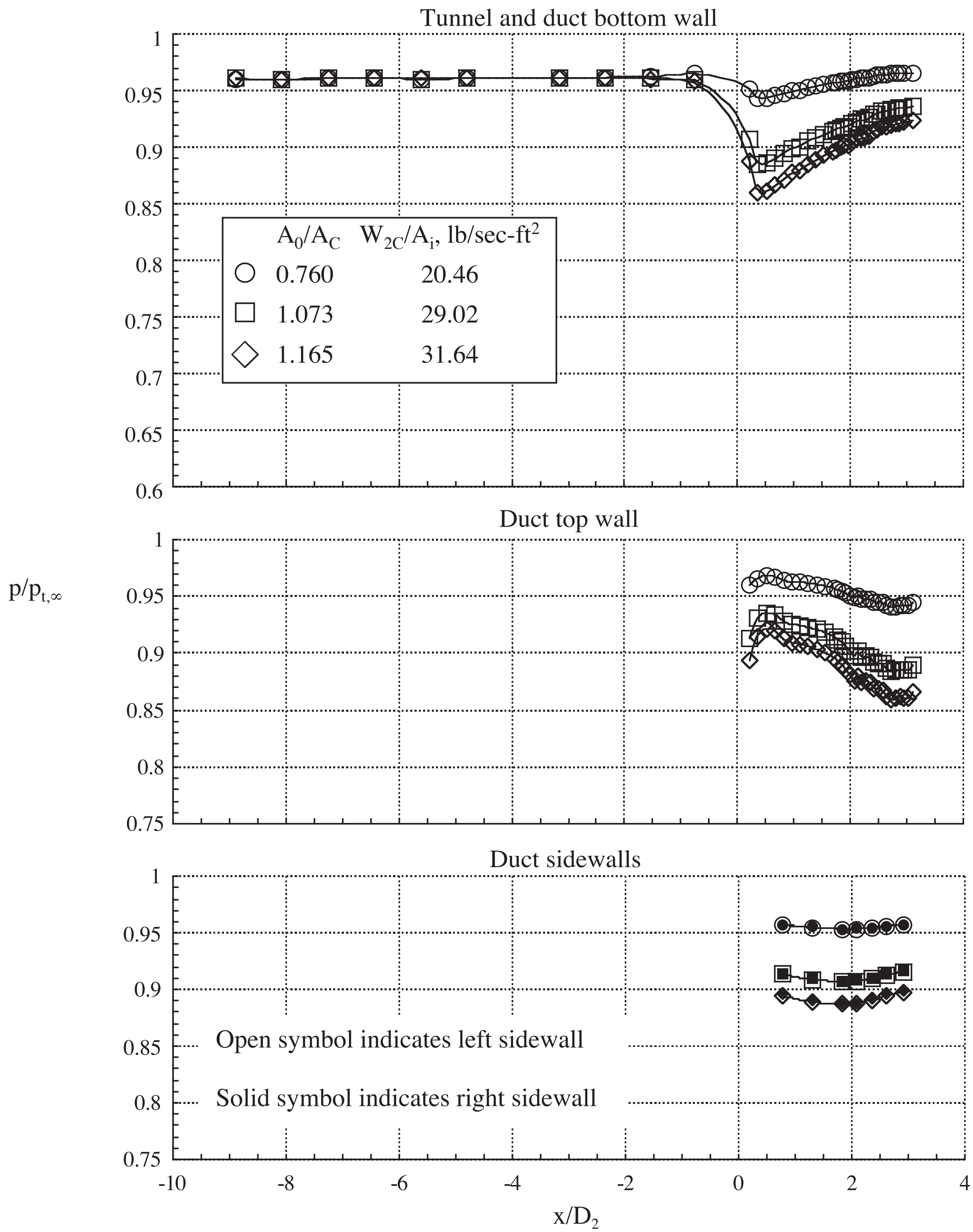

(a) M = 0.250, Re/FT = 33.48 x 10^6.

Figure 9.- Effect of inlet mass-flow ratio on inlet A duct pressure distributions.

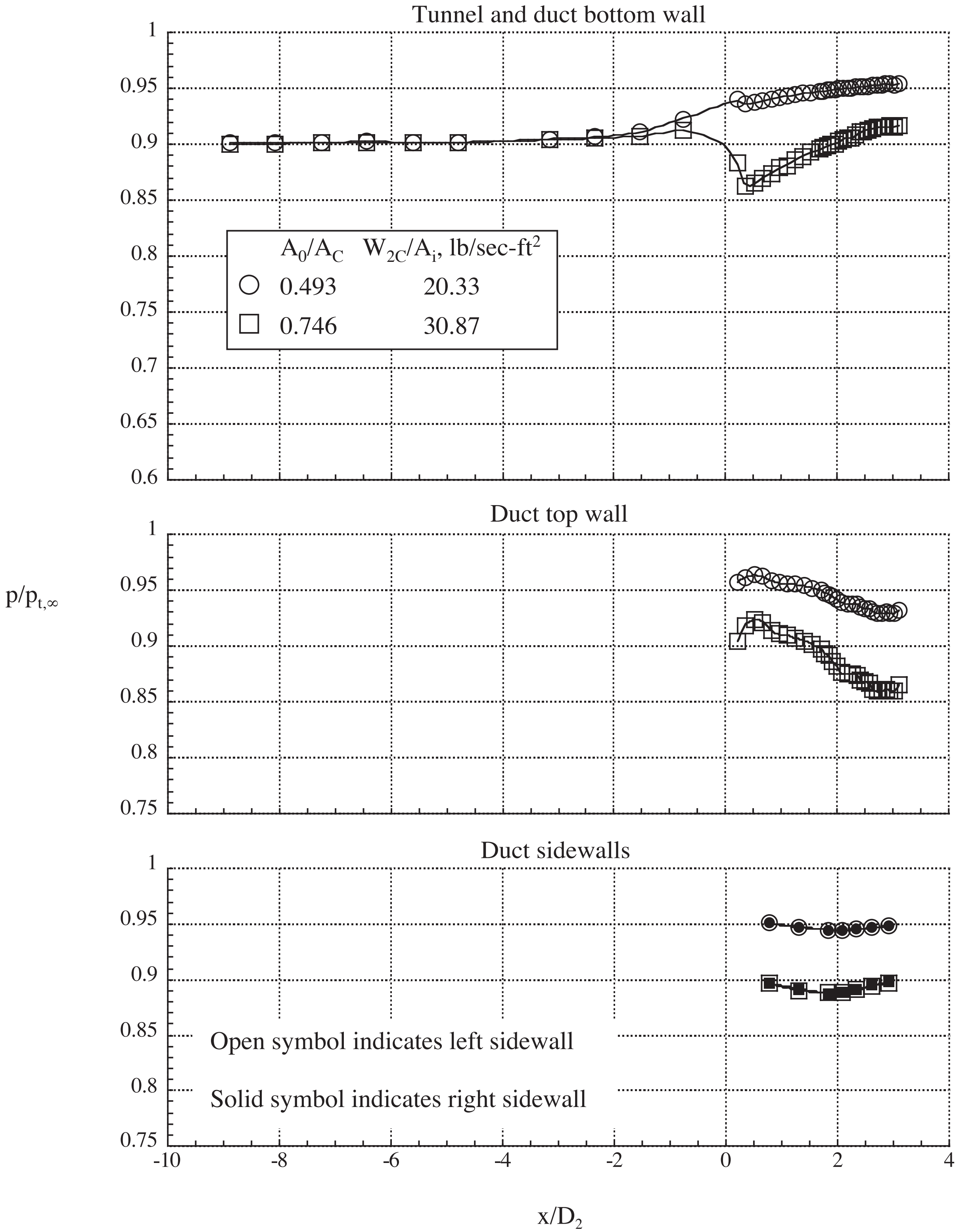

(b) M = 0.402, Re/FT = 51.66 x 10^6.

Figure 9.- Continued.

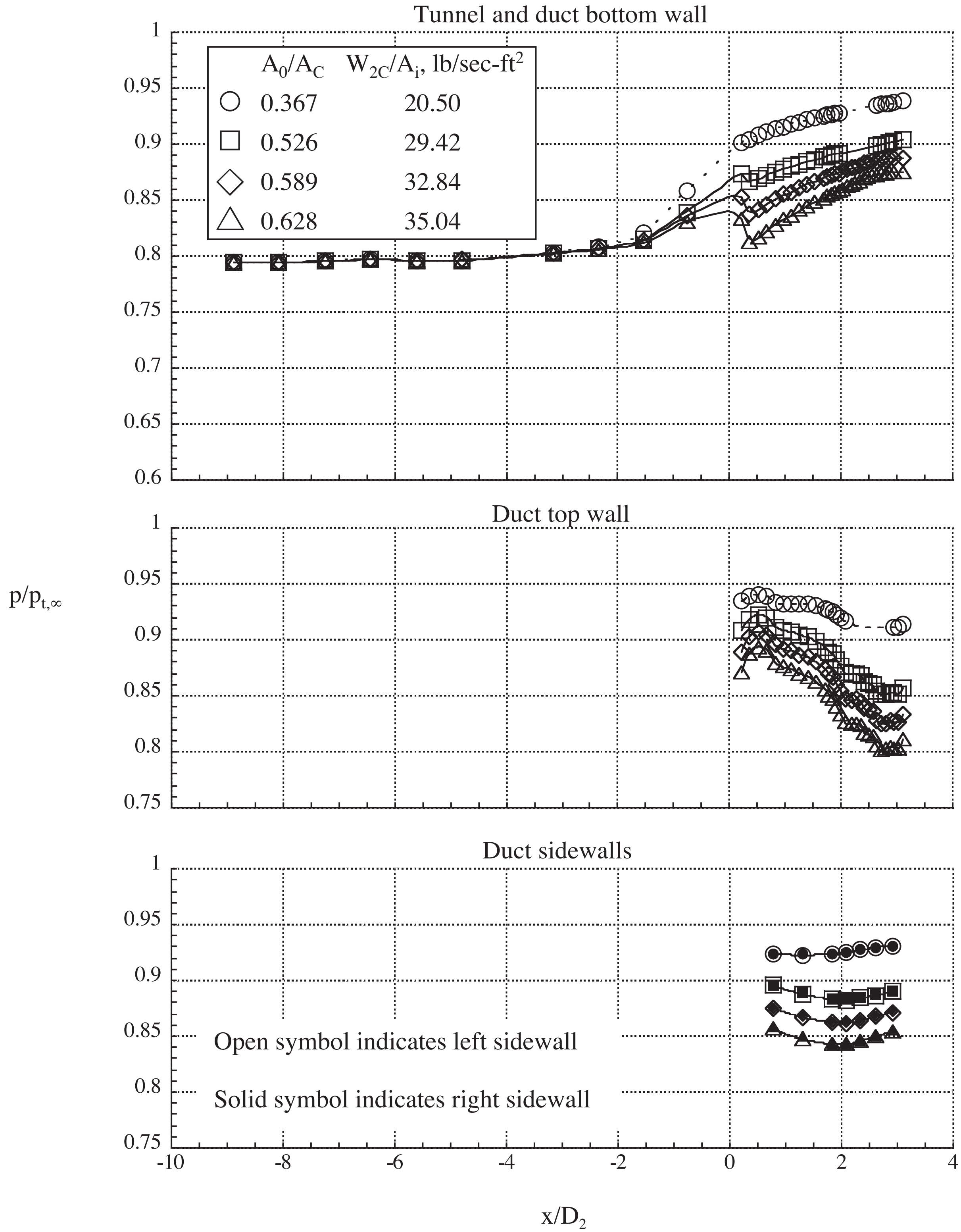

(c) M = 0.603, Re/FT = 68.44 x 10^6.

Figure 9.- Continued.

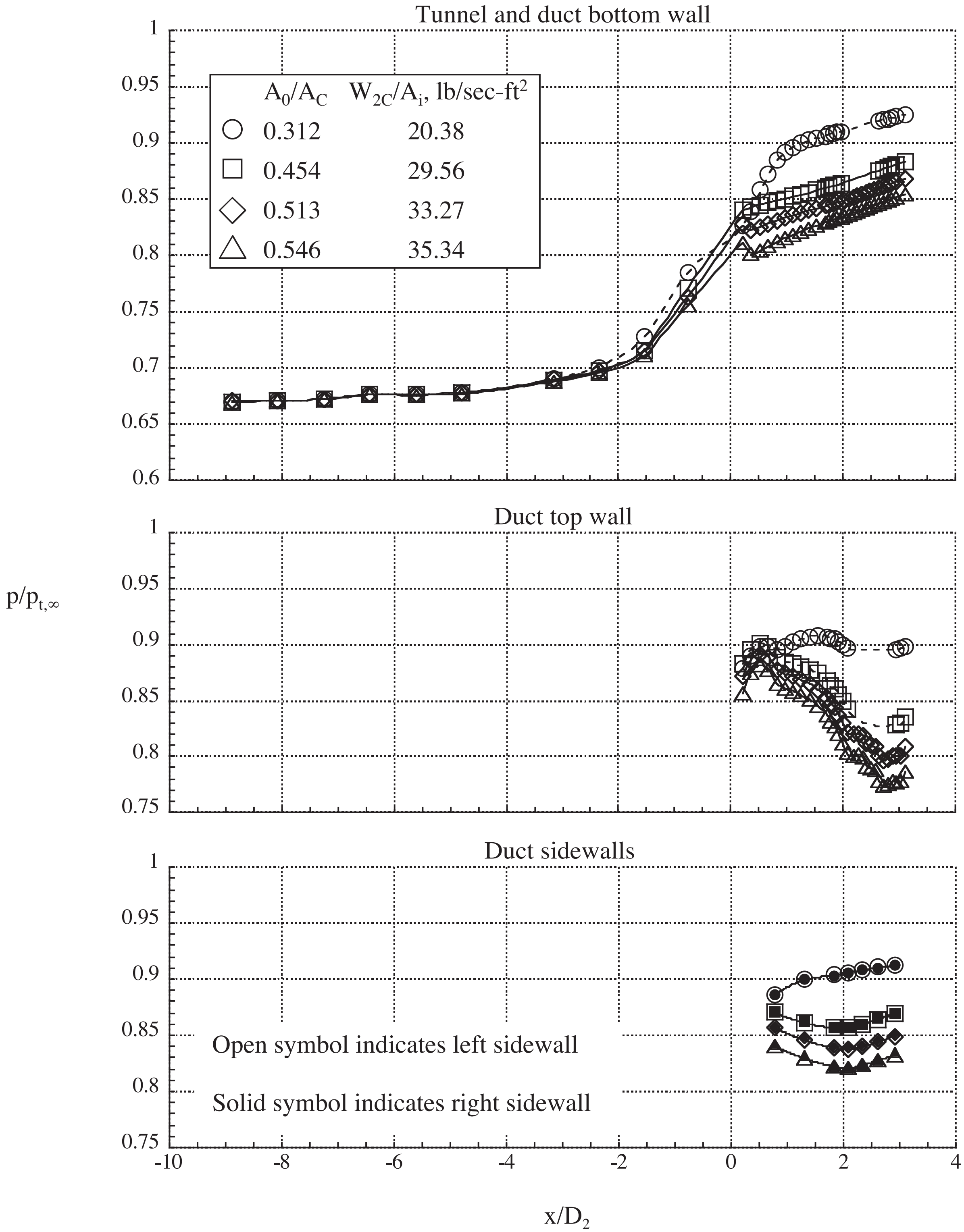

(d) M = 0.804, Re/FT = 69.36 x 10^6.

Figure 9. - Continued.

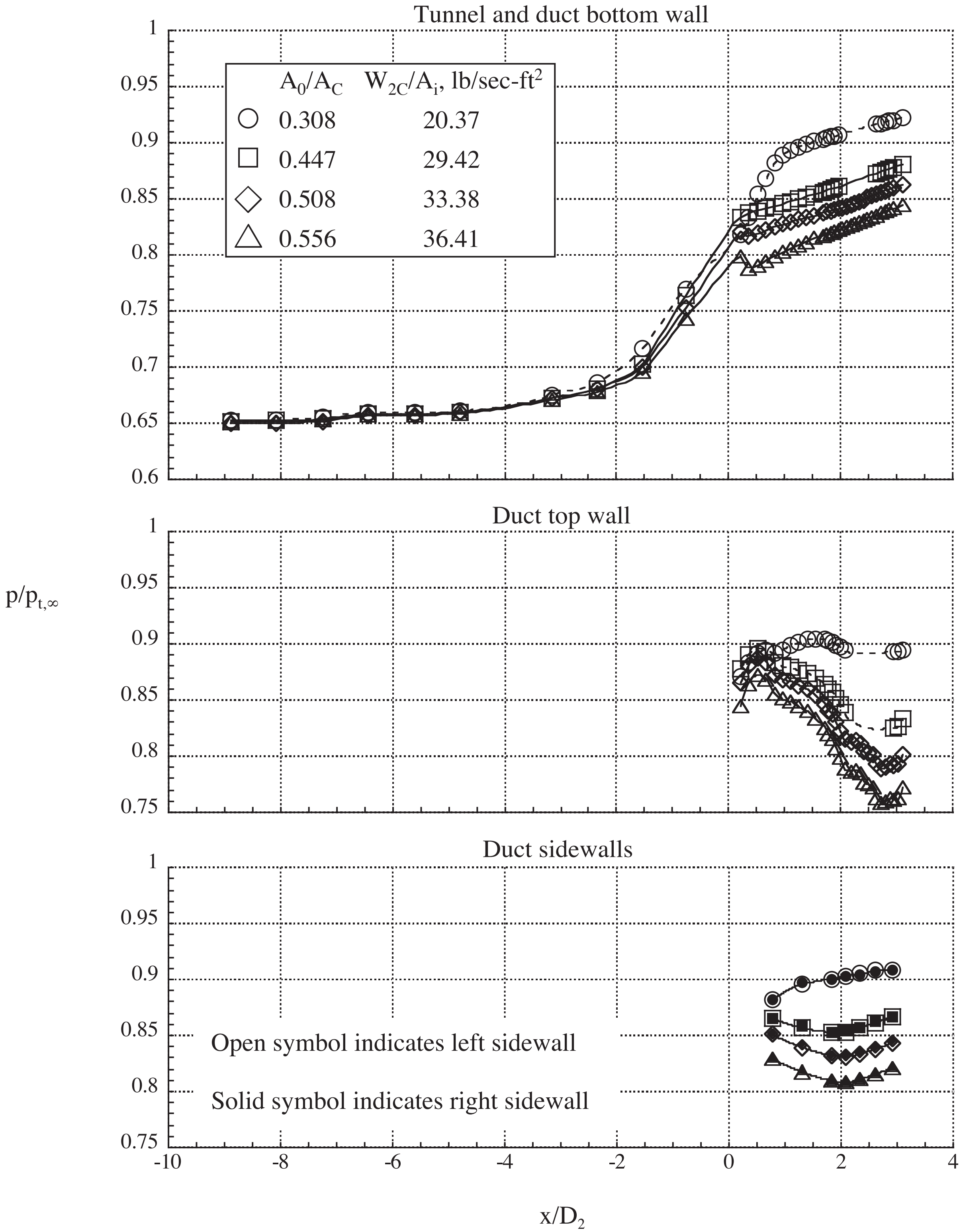

(e) M = 0.832, Re/FT = 68.92 x 10^6.

Figure 9.- Concluded.

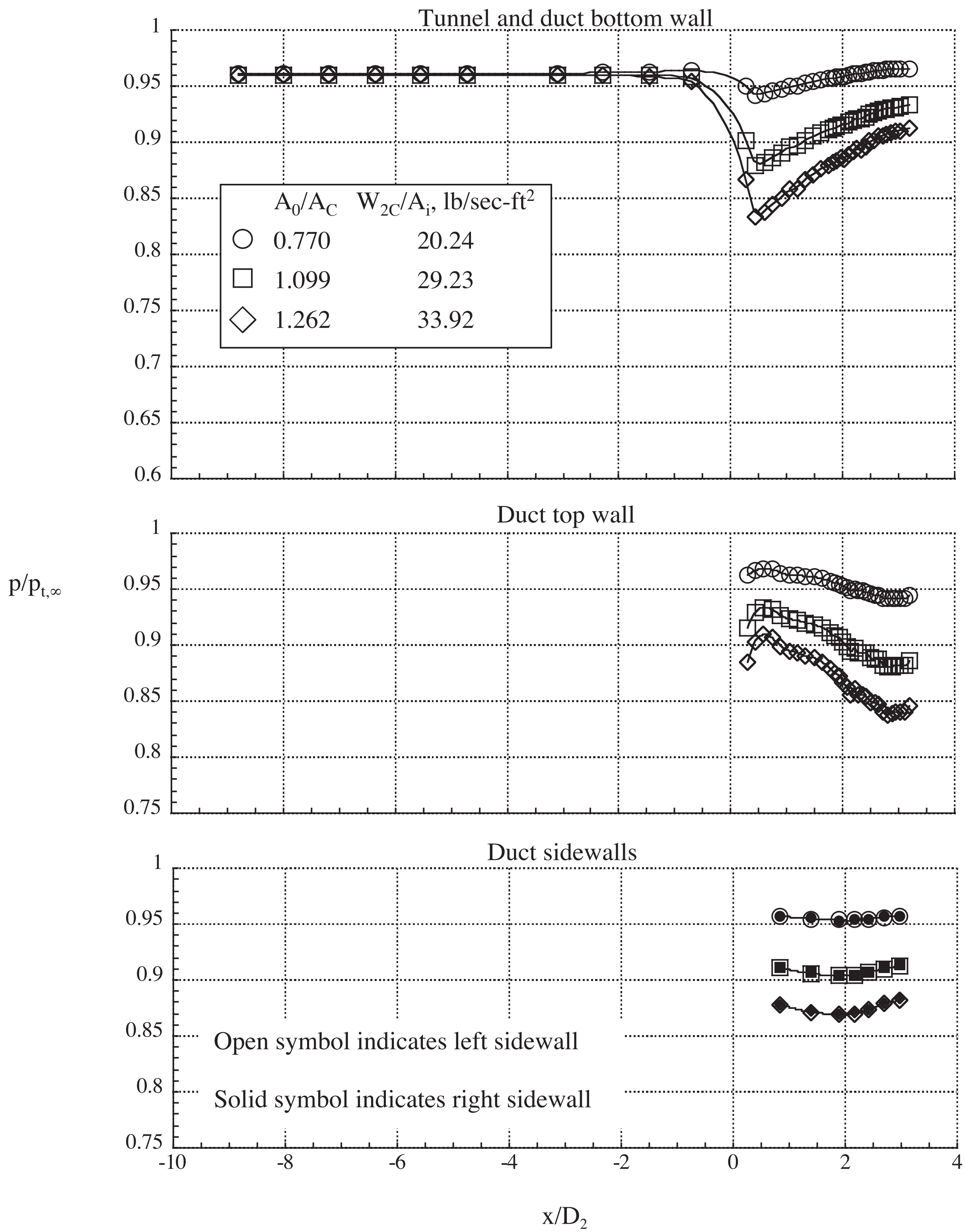

(a) $M = 0.250$, $Re/FT = 33.27 \times 10^6$.

Figure 10.- Effect of inlet mass-flow ratio on Inlet B duct pressure distributions.

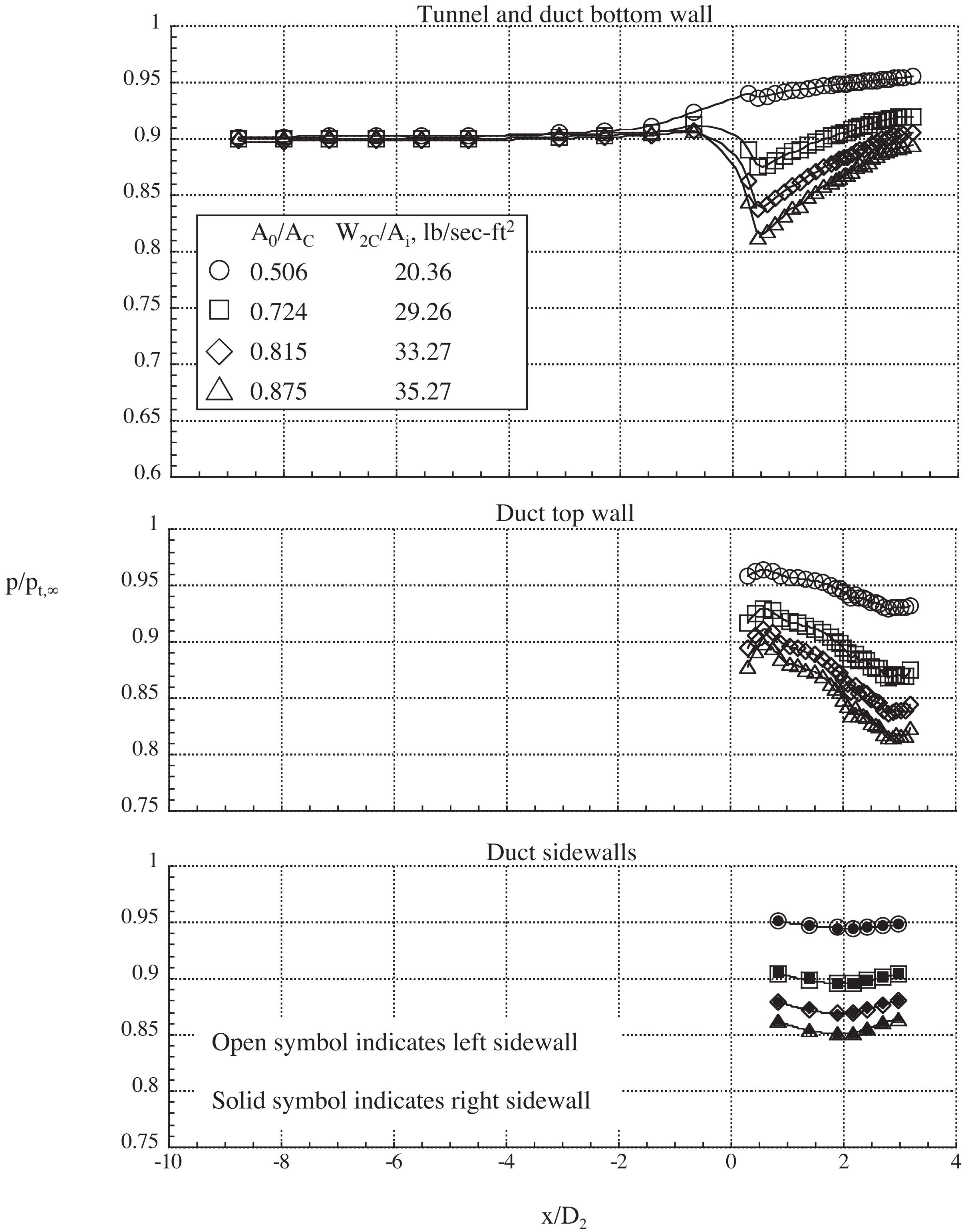

(b) M = 0.402, Re/FT = 51.09 x 10[6].

Figure 10.- Continued.

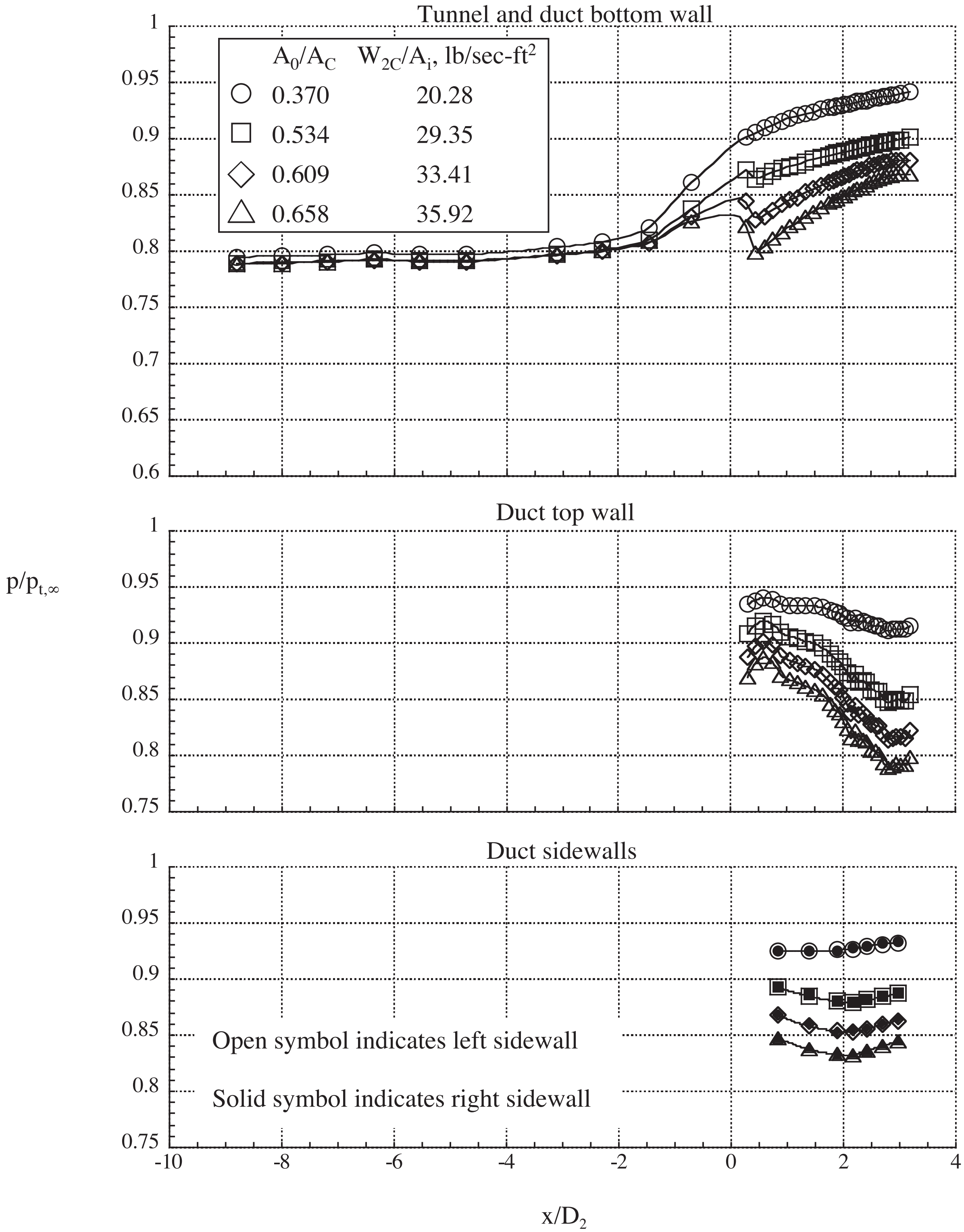

(c) M = 0.606, Re/FT = 67.67 x 10^6.

Figure 10.- Continued.

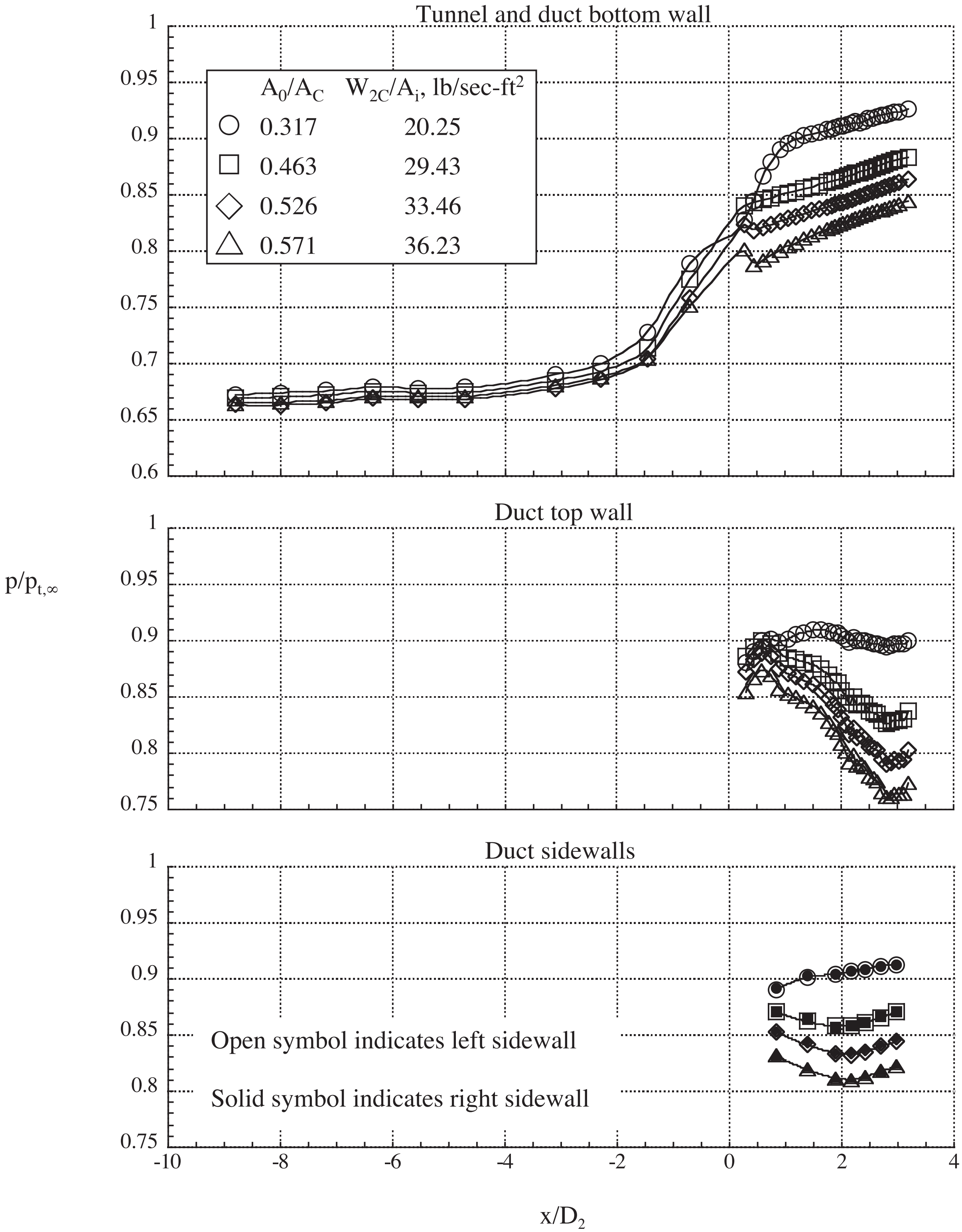

(d) M = 0.804, Re/FT = 68.20 x 10^6.

Figure 10.- Continued.

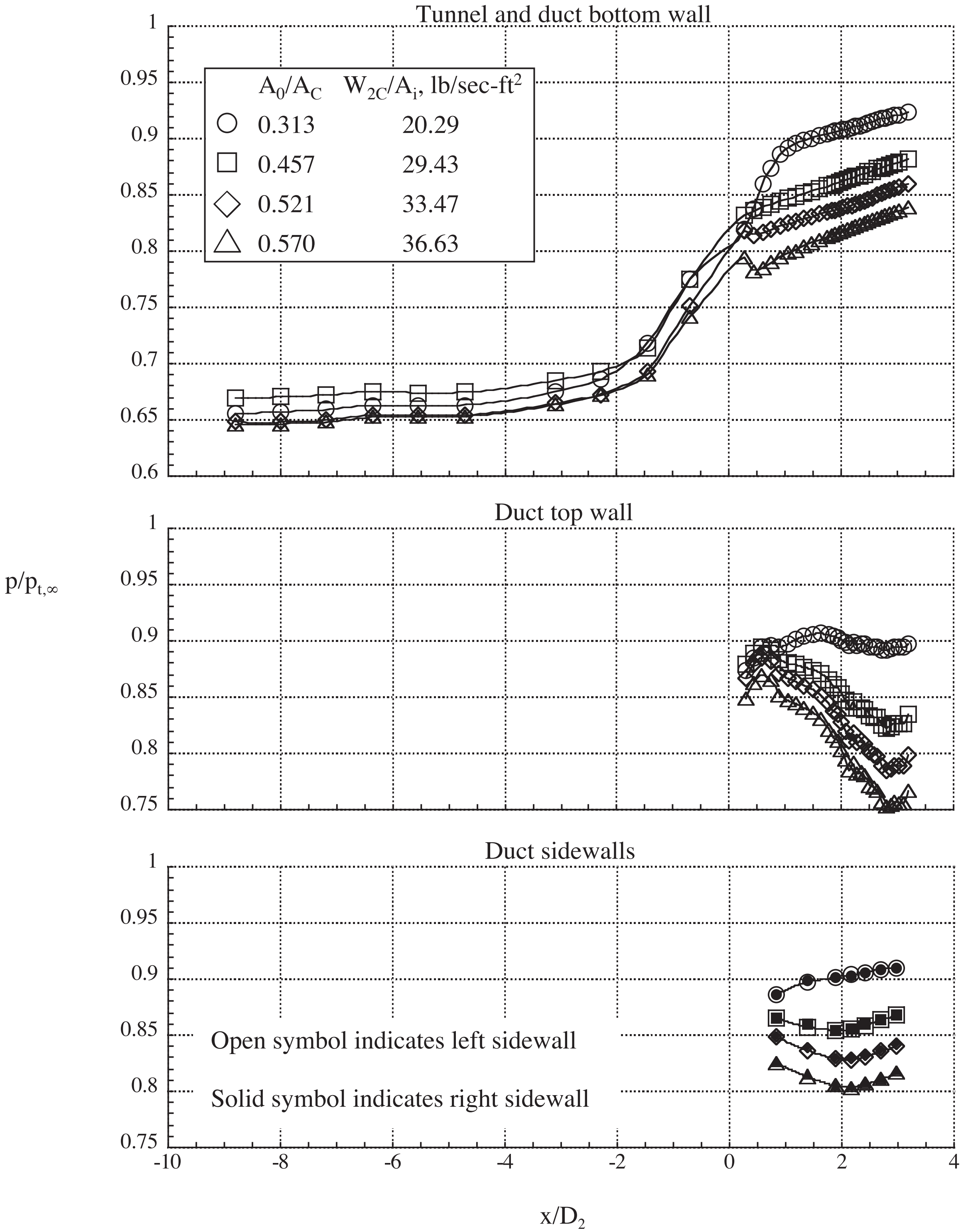

(e) $M = 0.831$, $Re/FT = 68.05 \times 10^6$.

Figure 10.- Concluded.

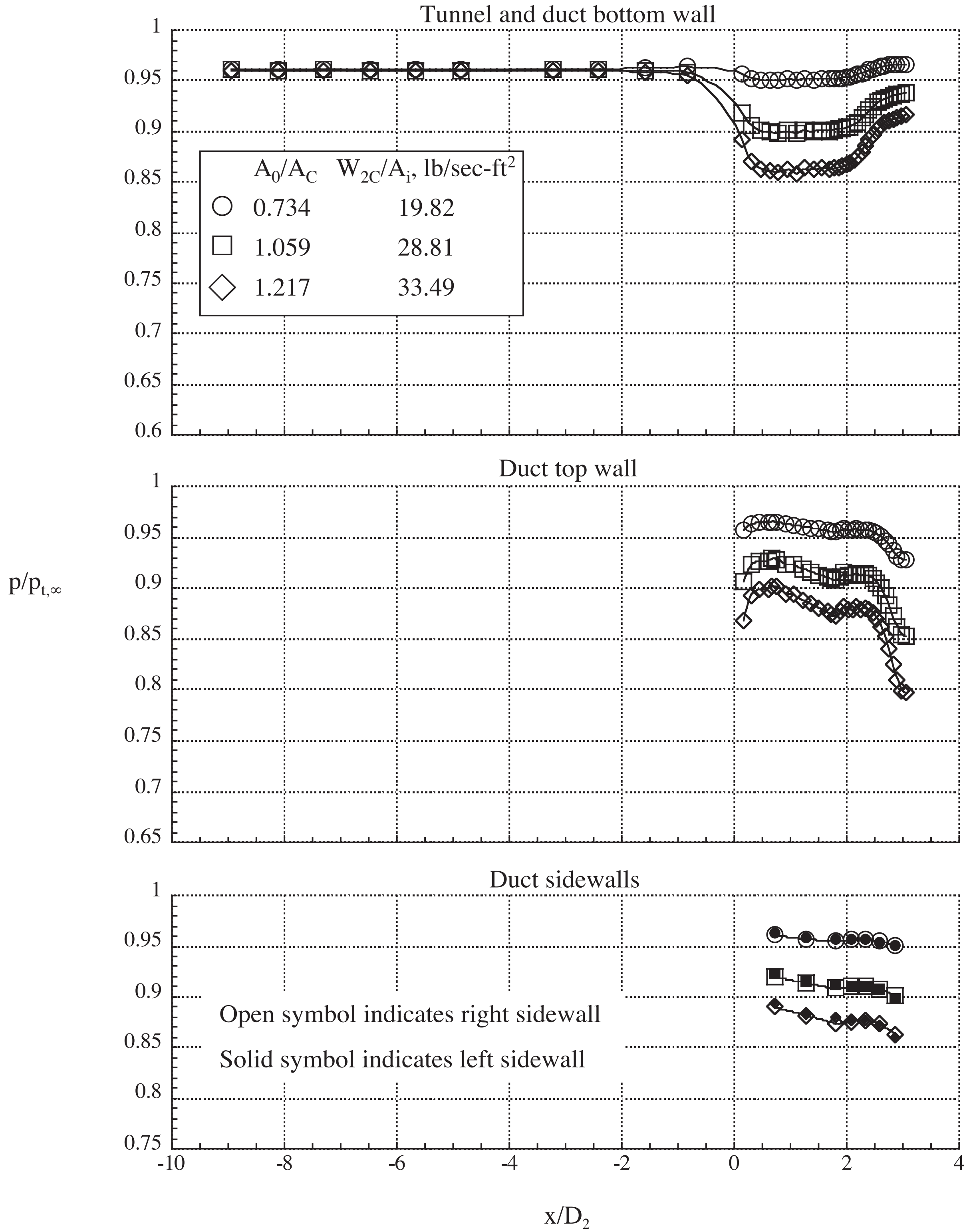

(a) M = 0.249, Re/FT = 33.33 x 10^6.

Figure 11.- Effect of inlet mass-flow ratio on Inlet C duct pressure distributions.

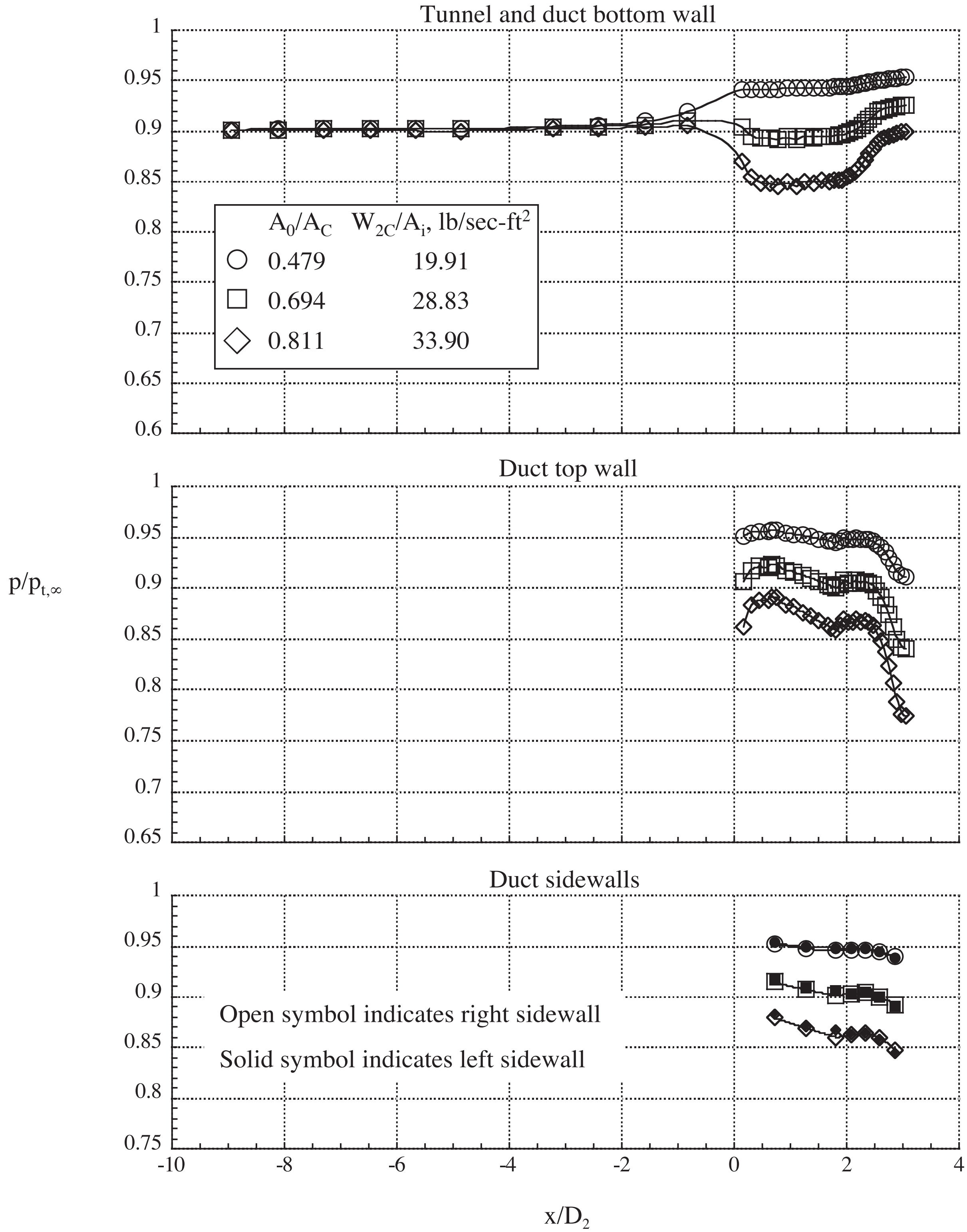

(b) M = 0.400, Re/FT = 50.50 x 10^6.

Figure 11.- Continued.

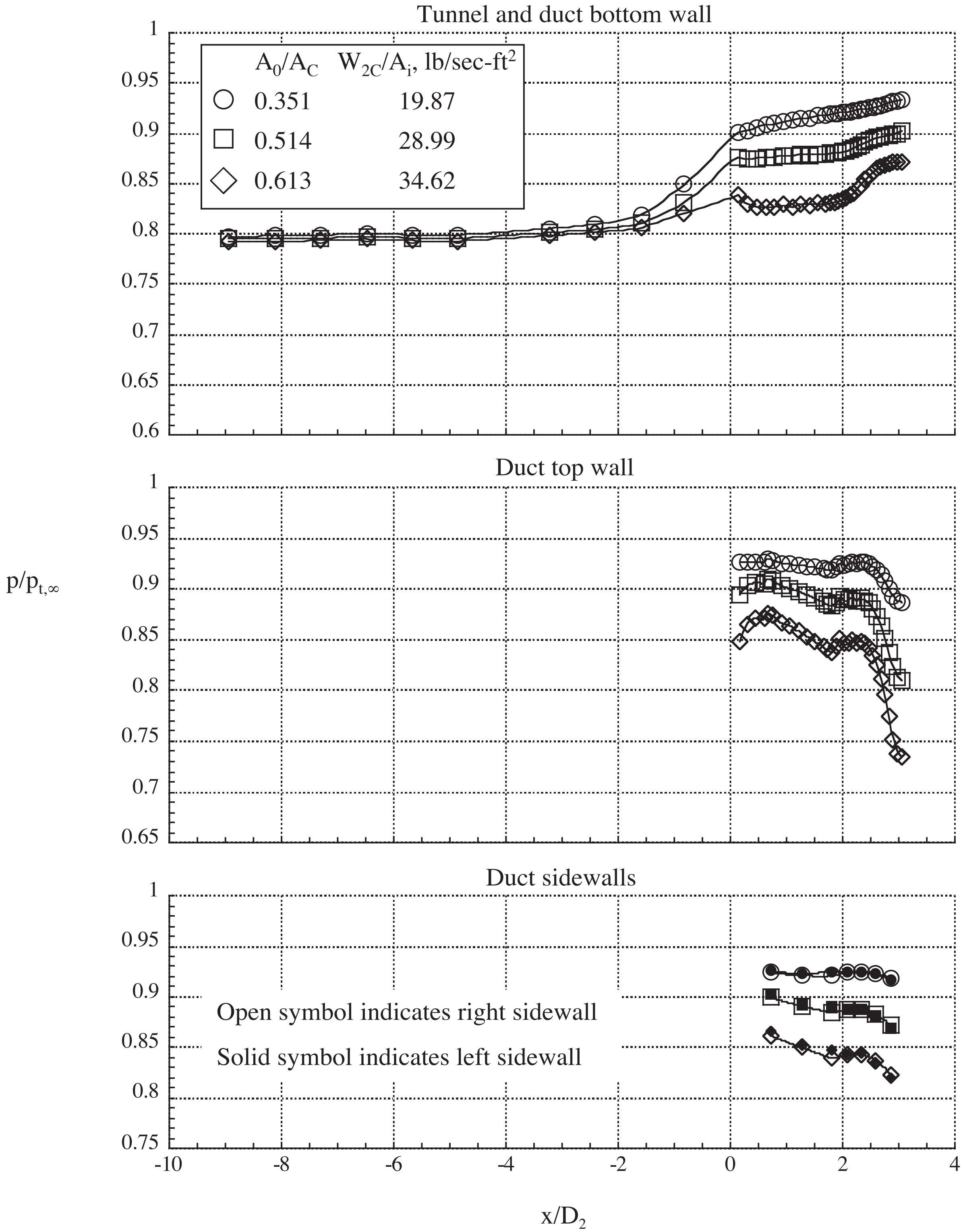

(c) M = 0.601, Re/FT = 67.90 x 10^6.

Figure 11.- Continued.

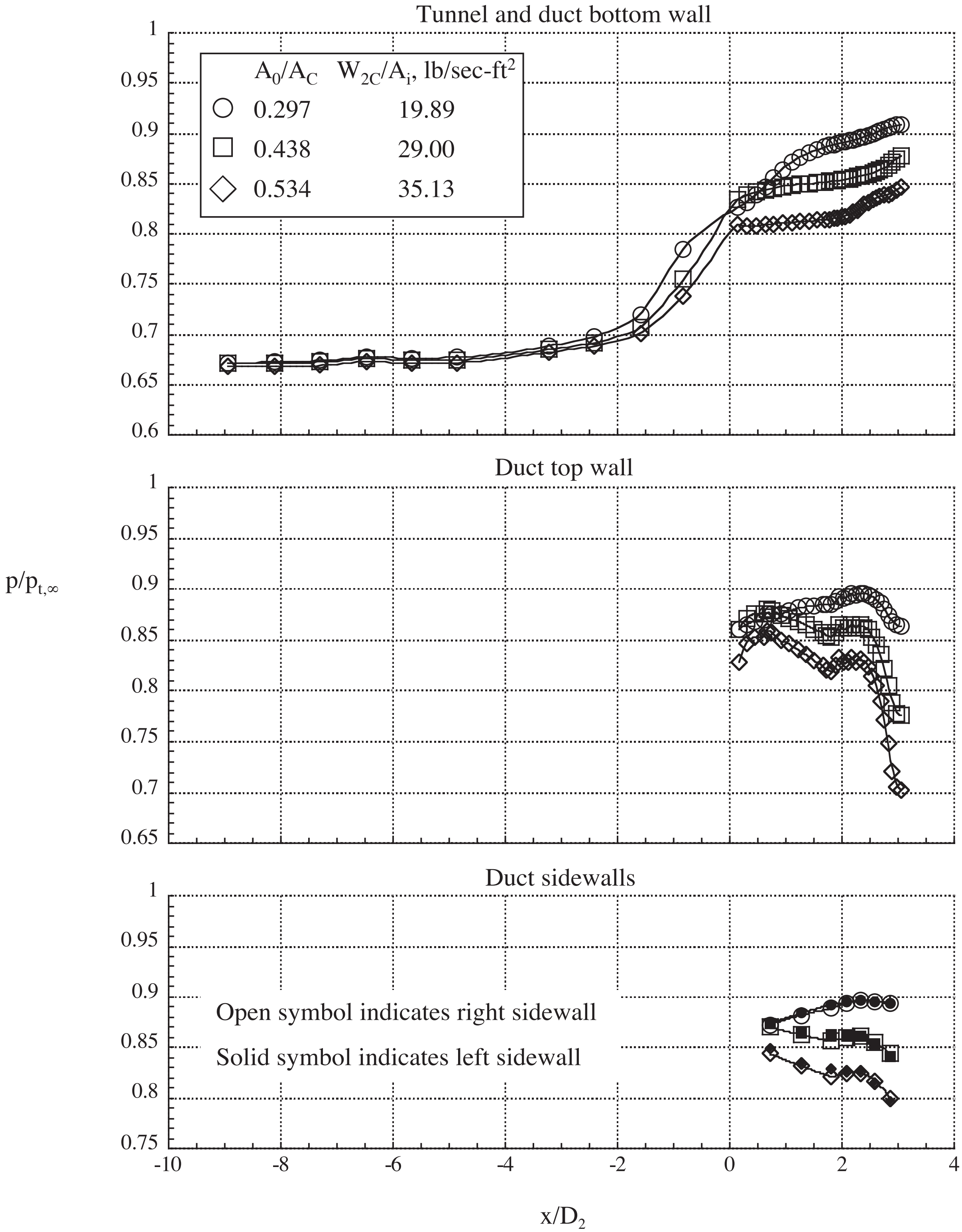

(d) $M = 0.802$, $Re/FT = 68.15 \times 10^6$.

Figure 11.- Continued.

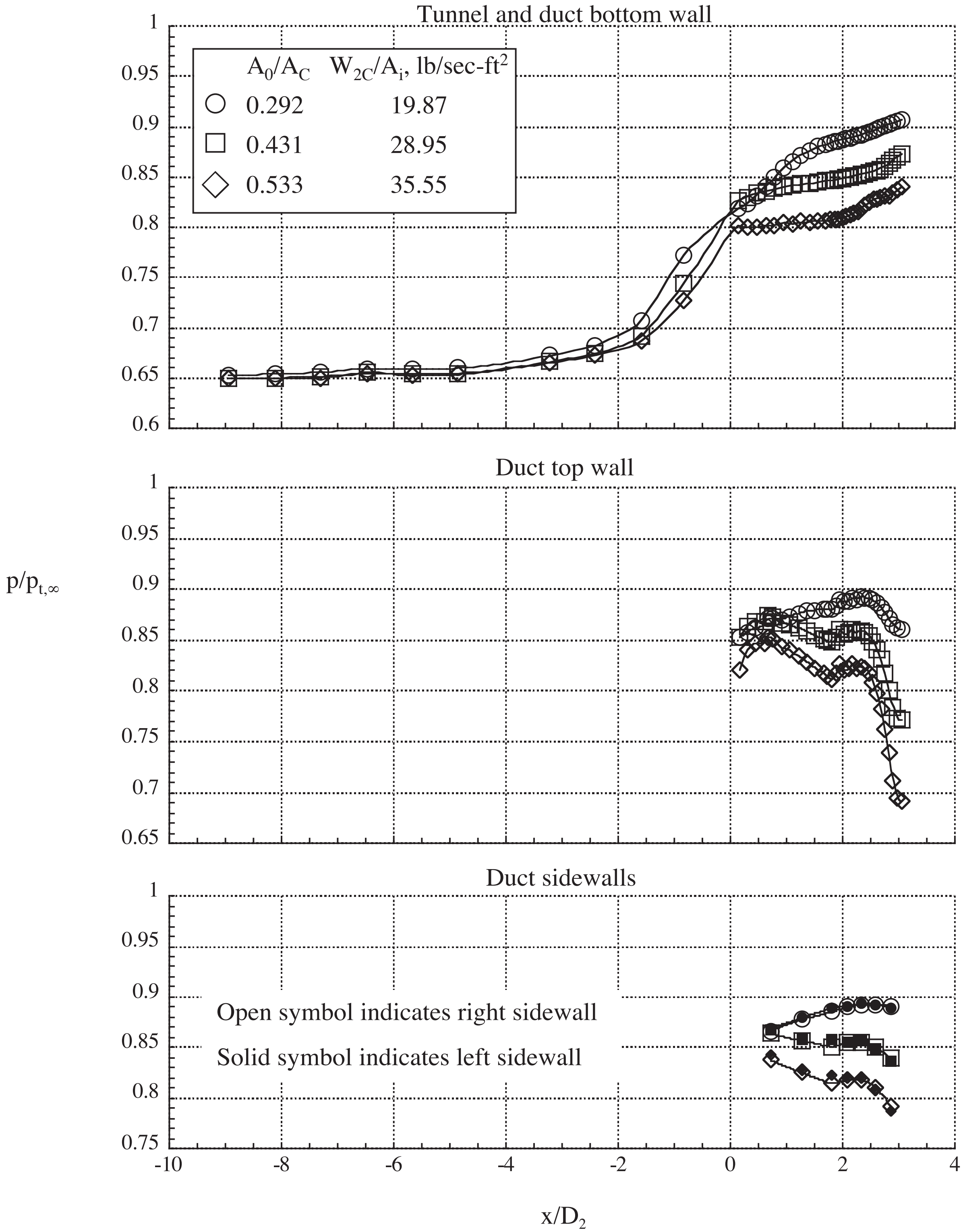

(e) M = 0.832, Re/FT = 68.22 x 10^6.

Figure 11.- Concluded.

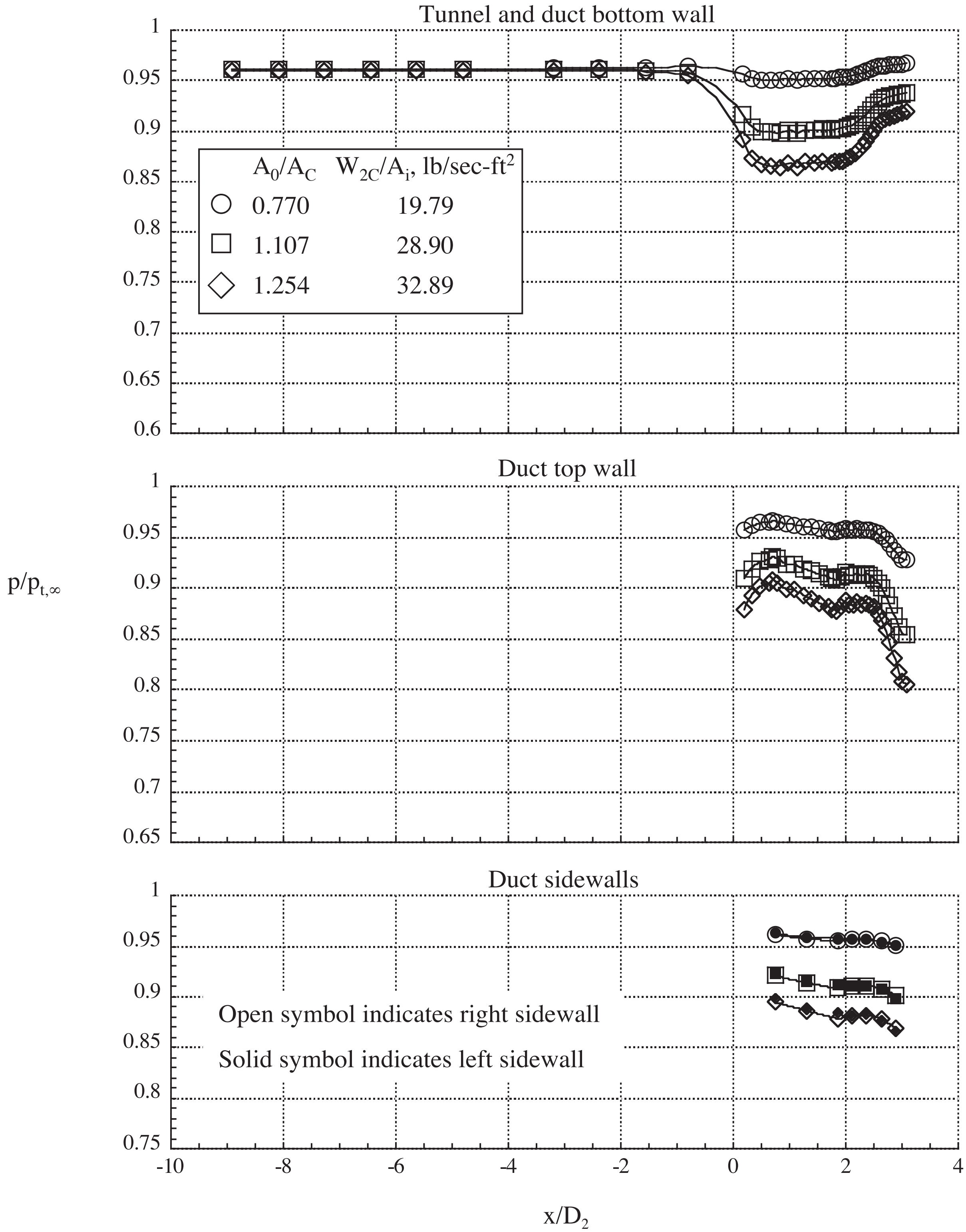

(a) M = 0.248, Re/FT = 33.47 x 10^6.

Figure 12.- Effect of inlet mass-flow ratio on Inlet D duct pressure distributions.

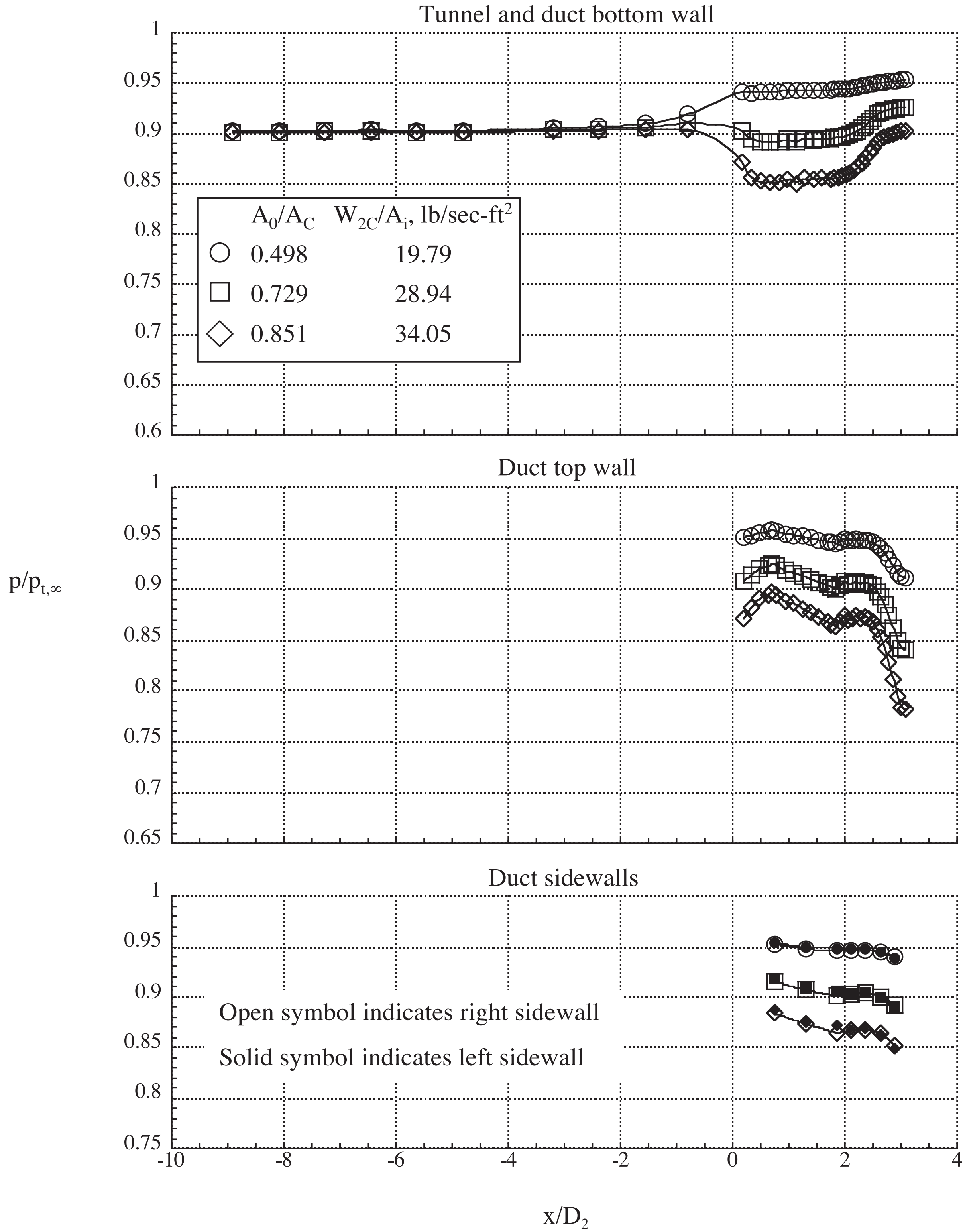

(b) M = 0.401, Re/FT = 51.20 x 10^6.

Figure 12.- Continued.

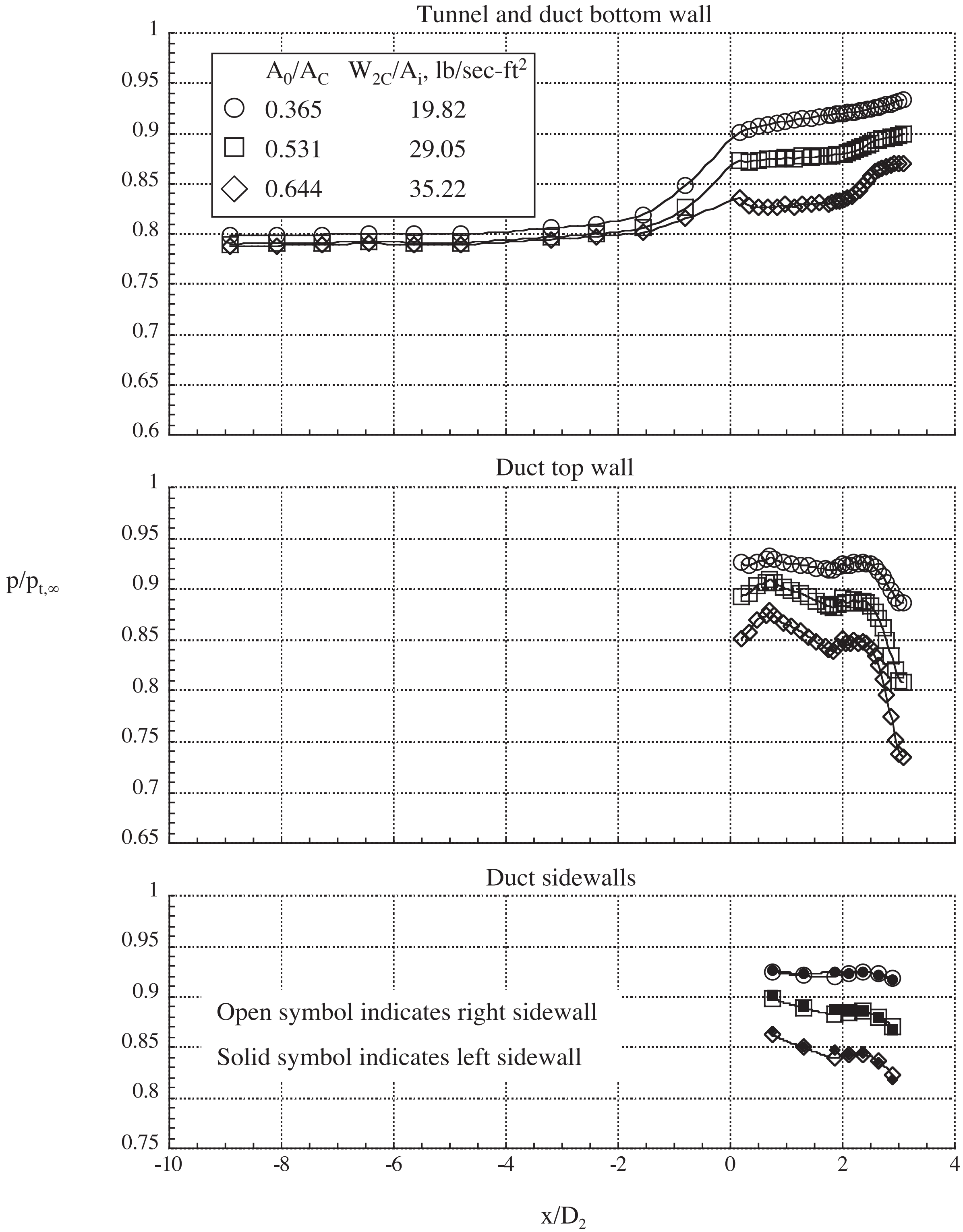

(c) M = 0.604, Re/FT = 67.80 x 10^6.

Figure 12.- Continued.

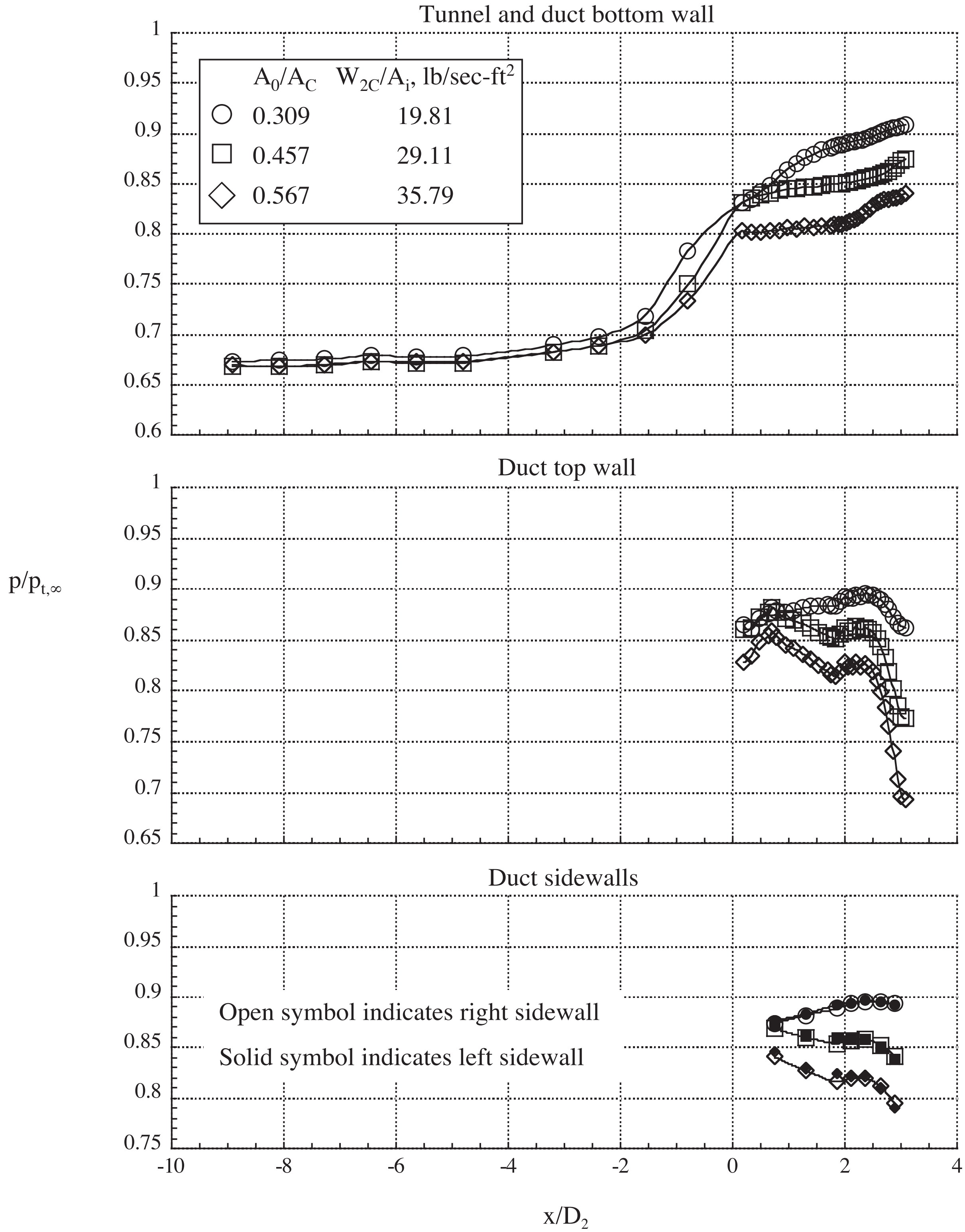

(d) M = 0.802, Re/FT = 68.21 x 10^6.

Figure 12.- Continued.

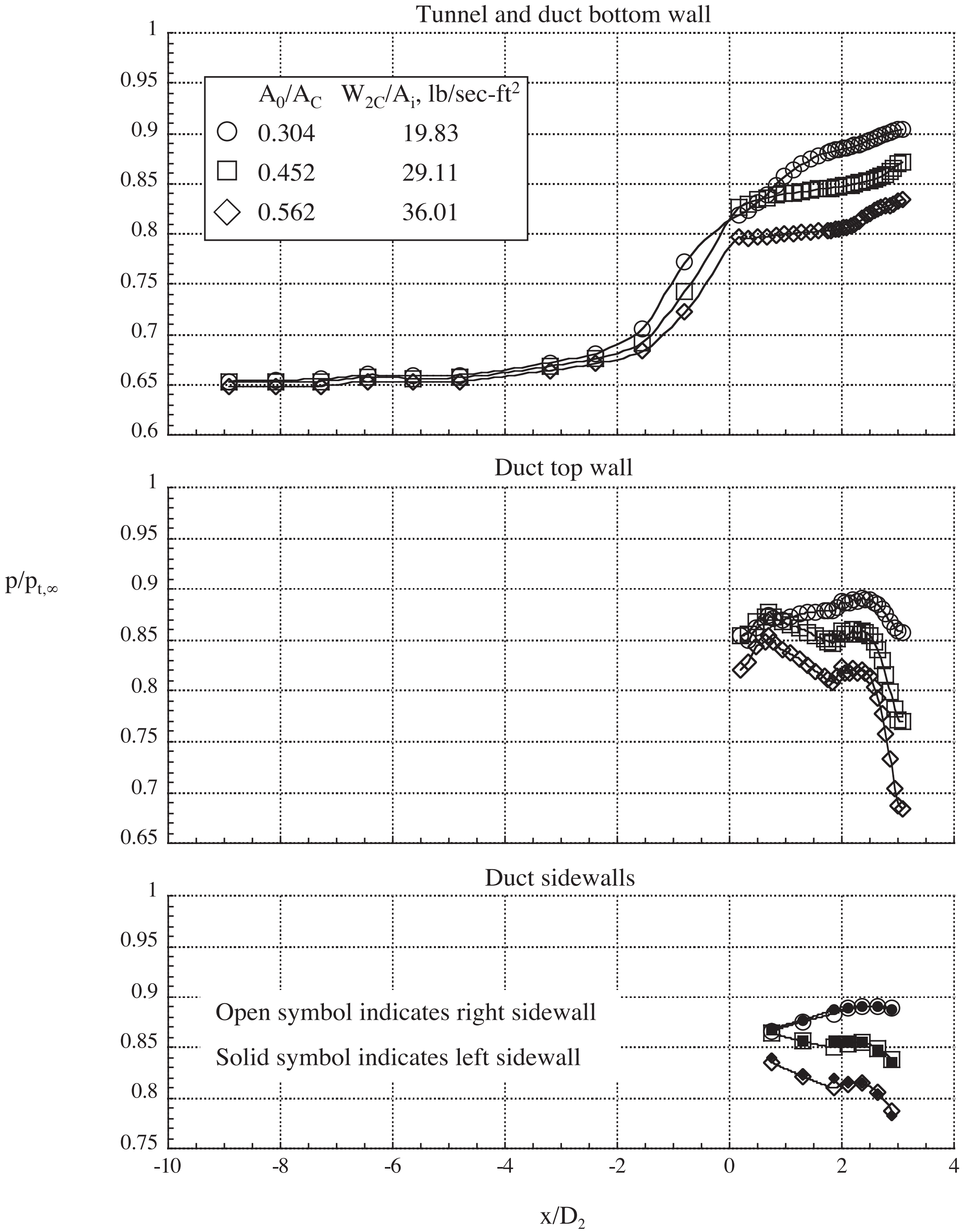

(e) M = 0.829, Re/FT = 68.28 x 10^6.

Figure 12.- Concluded.

M = 0.250, Re/FT = 34.0 x 10^6

W_{2C}/A_i = 29.02 lb/sec-ft^2, A_0/A_C = 1.073

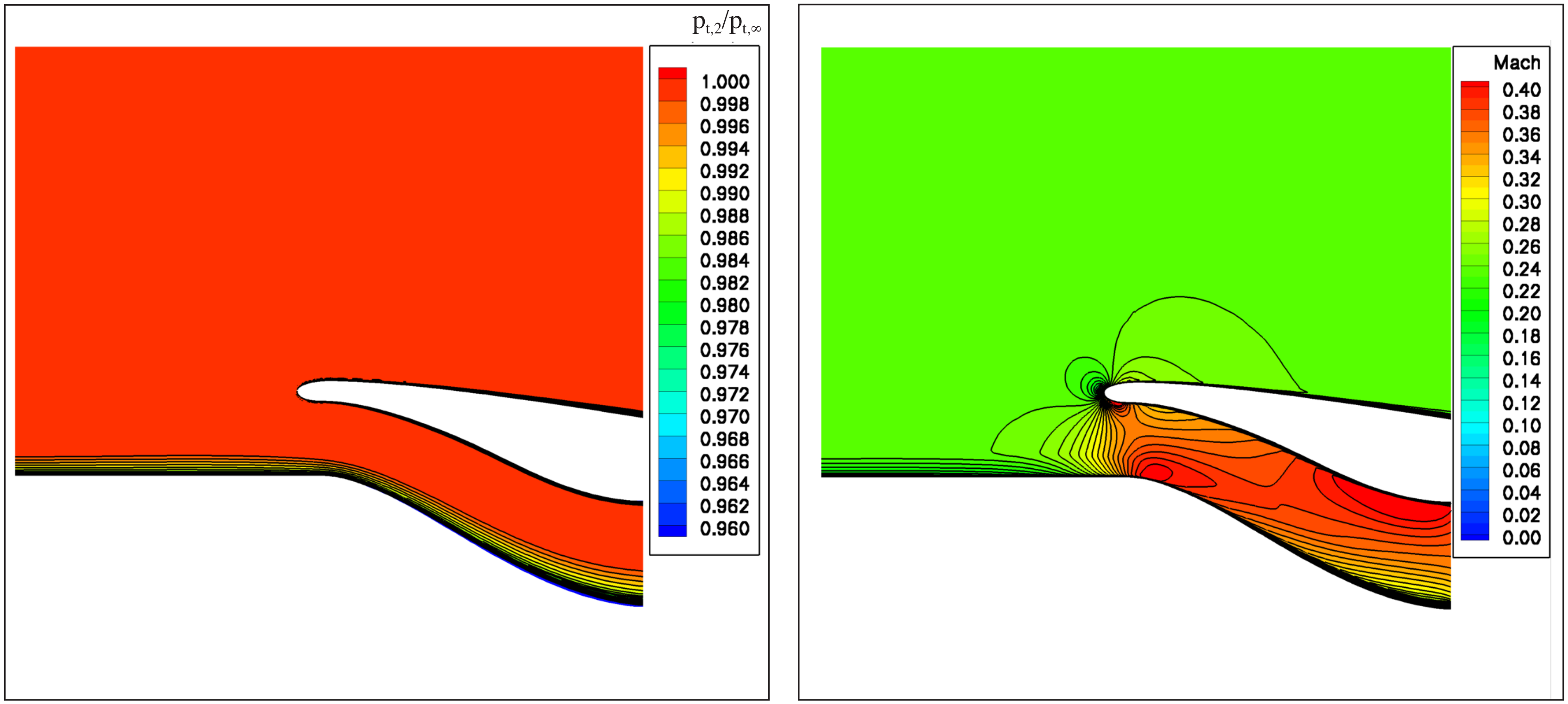

(a) M = 0.250, M_{match} = 0.234.

Figure 13. - CFD solution for total pressure and Mach contour maps on inlet A centerline.

$M = 0.833$, $Re/FT = 68.4 \times 10^6$

$W_{2C}/A_i = 36.41$ lb/sec-ft^2, $A_0/A_C = 0.556$

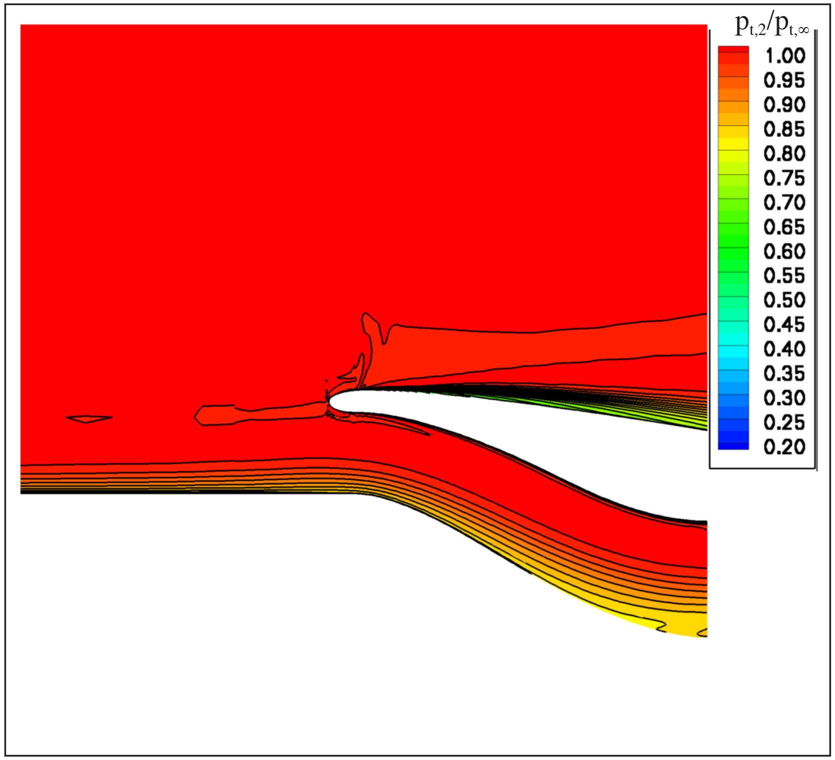

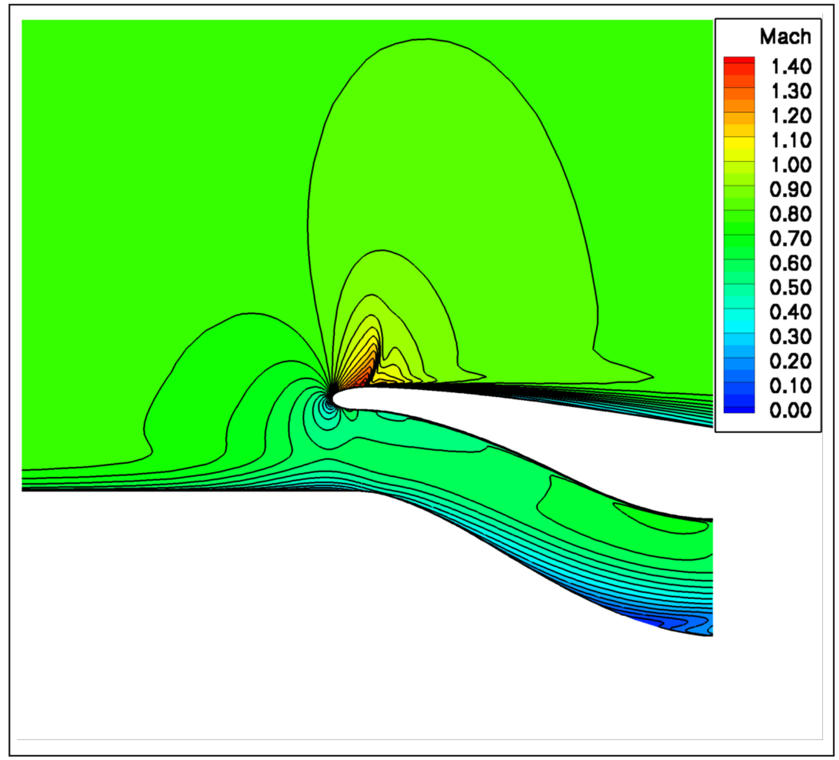

(b) $M = 0.833$, $M_{match} = 0.784$.

Figure 13. - Concluded.

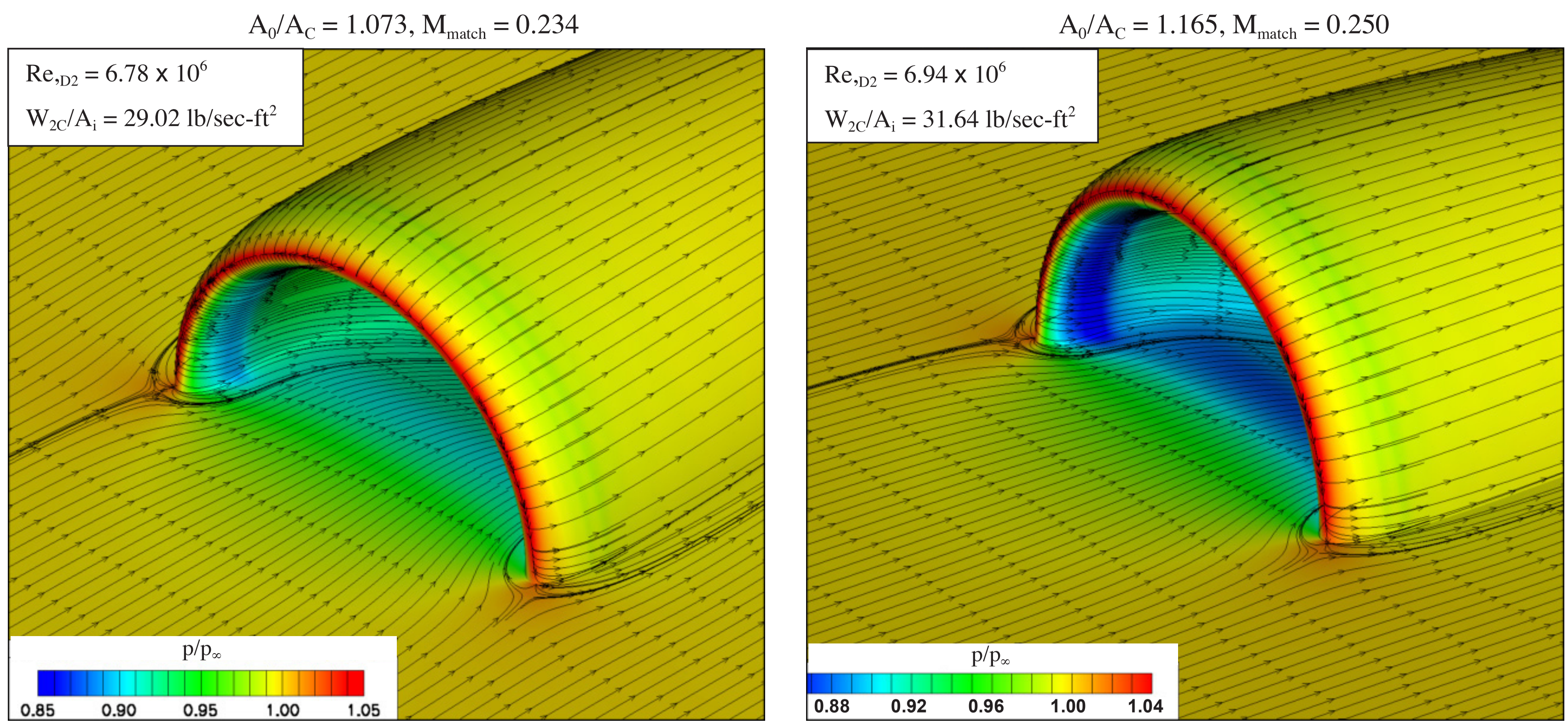

(a) $M = 0.250$, $M_{match} = 0.234$.

Figure 14. - Computational results on inlet A showing surface static pressure ratio and streamlines.

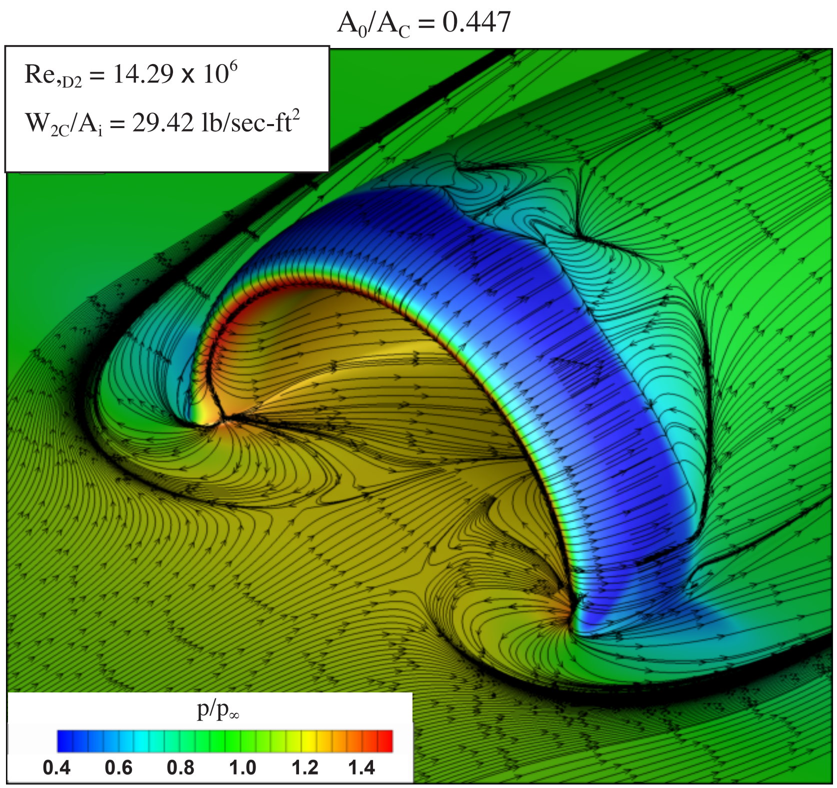

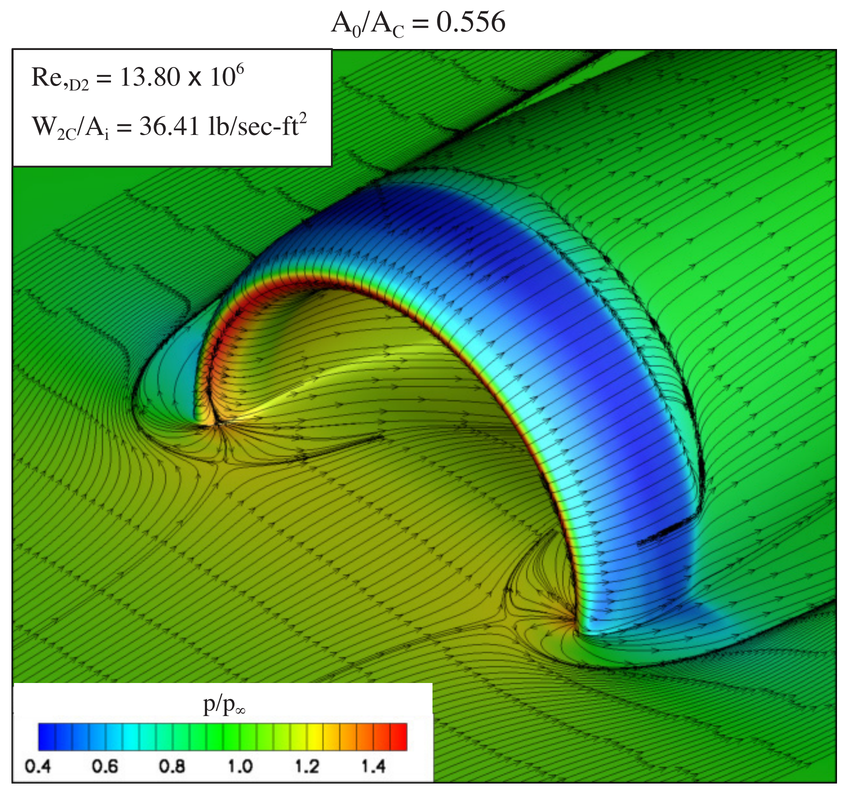

(b) $M = 0.833$, $M_{match} = 0.784$.

Figure 14. - Concluded.

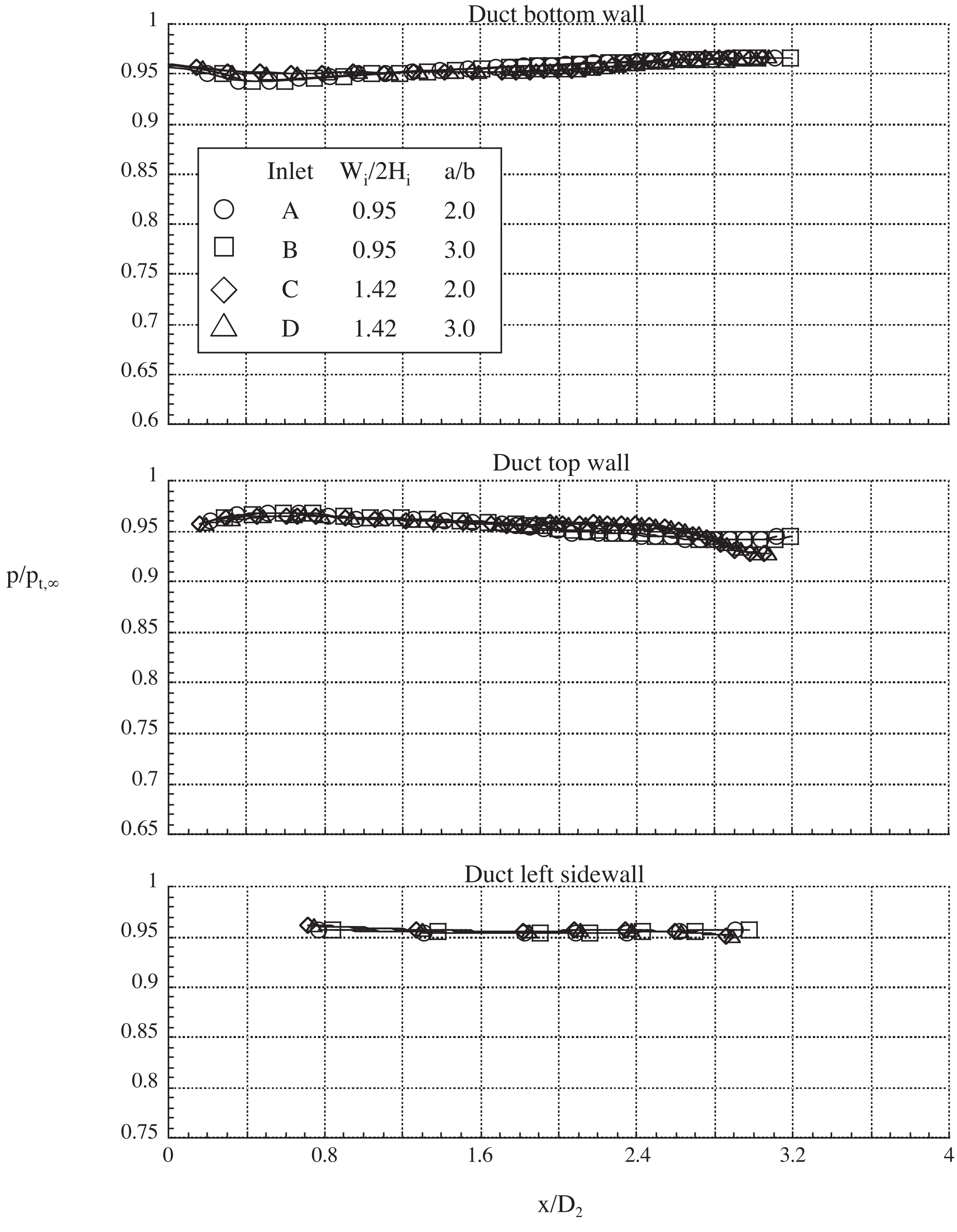

(a) $M = 0.248$, $Re/FT = 33.78 \times 10^6$, $A_0/A_C = 0.759$, $W_{2C}/A_i = 20.08$ lb/sec-ft^2.

Figure 15.- Effect of inlet geometry on duct pressure distributions.

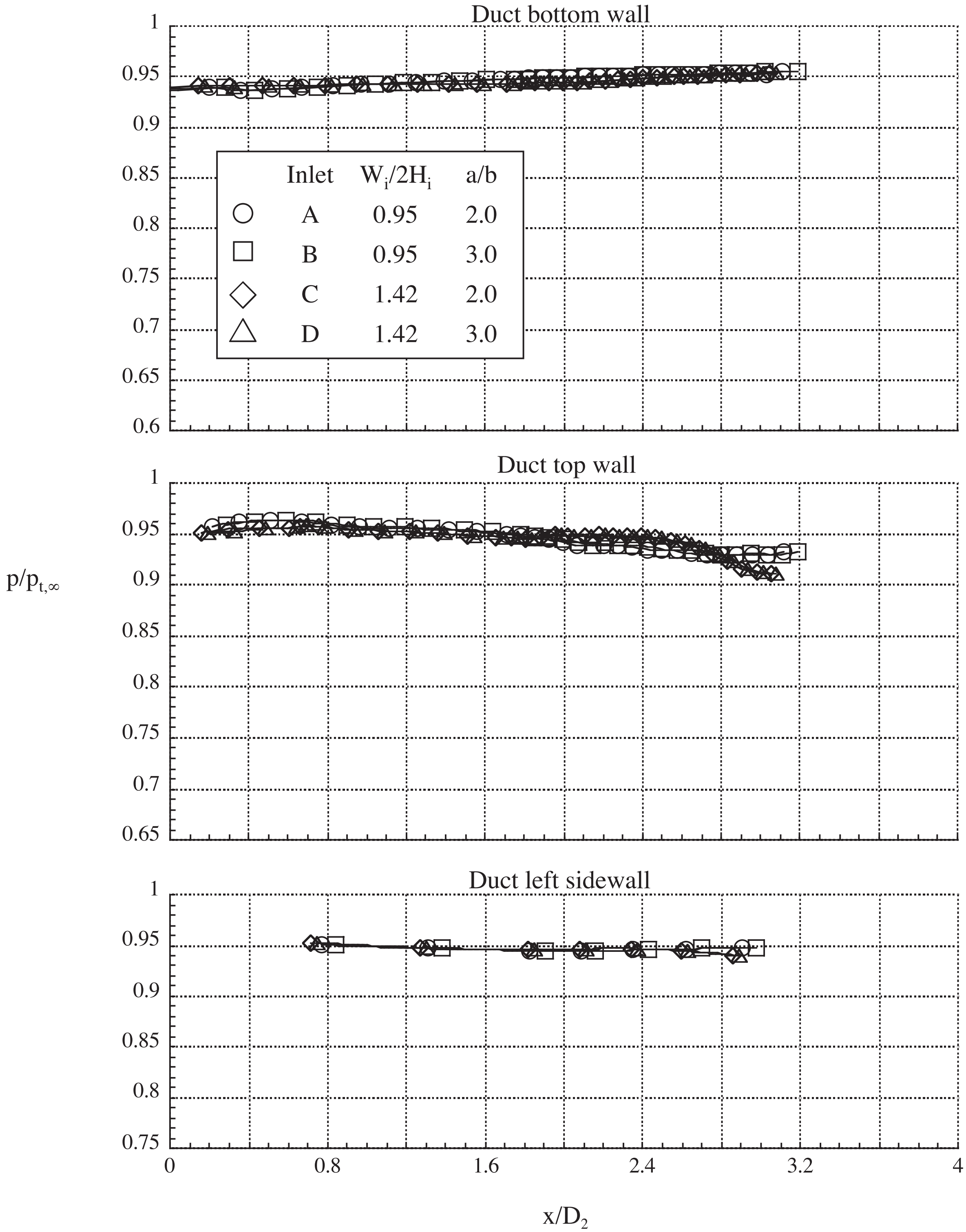

(b) M = 0.400, Re/FT = 50.77 x 10^6, A_0/A_C = 0.494, W_{2C}/A_i = 20.10 lb/sec-ft^2.

Figure 15.- Continued.

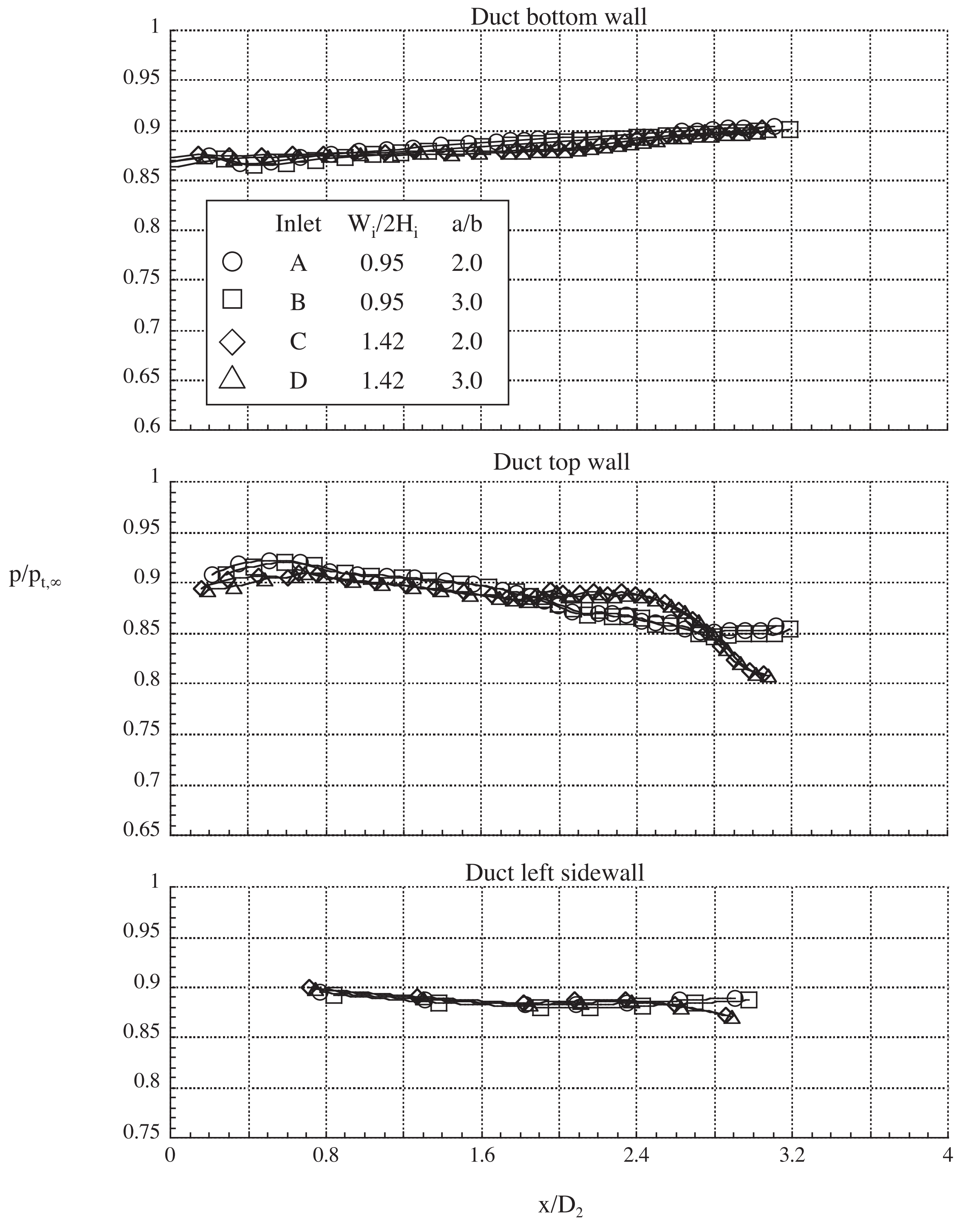

(c) $M = 0.606$, $Re/FT = 68.11 \times 10^6$, $A_0/A_C = 0.526$, $W_{2C}/A_i = 29.20$ lb/sec-ft^2.

Figure 15.- Continued.

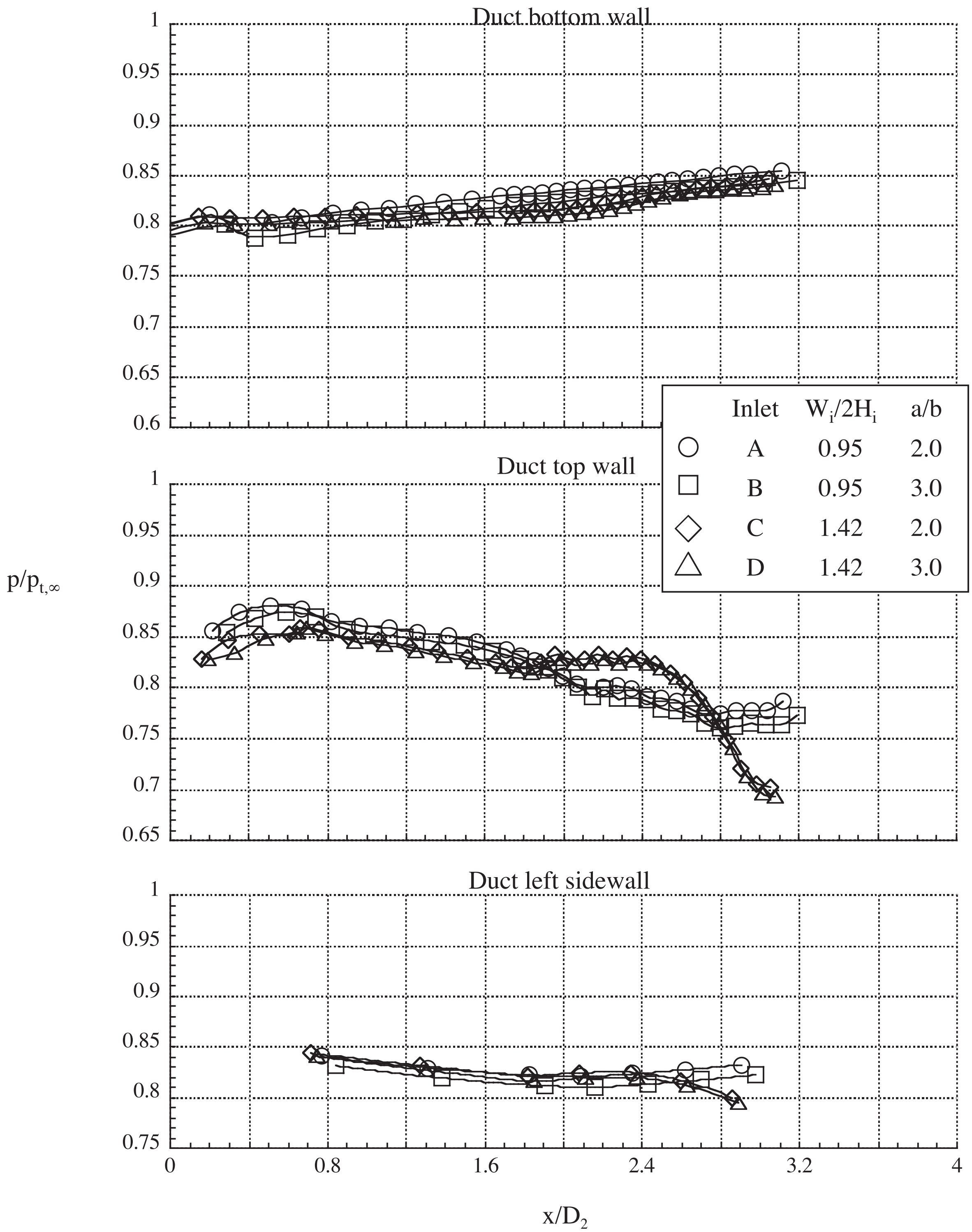

(d) $M = 0.803$, $Re/FT = 68.27 \times 10^6$, $A_0/A_C = 0.555$, $W_{2C}/A_i = 35.62$ lb/sec-ft^2.

Figure 15.- Continued.

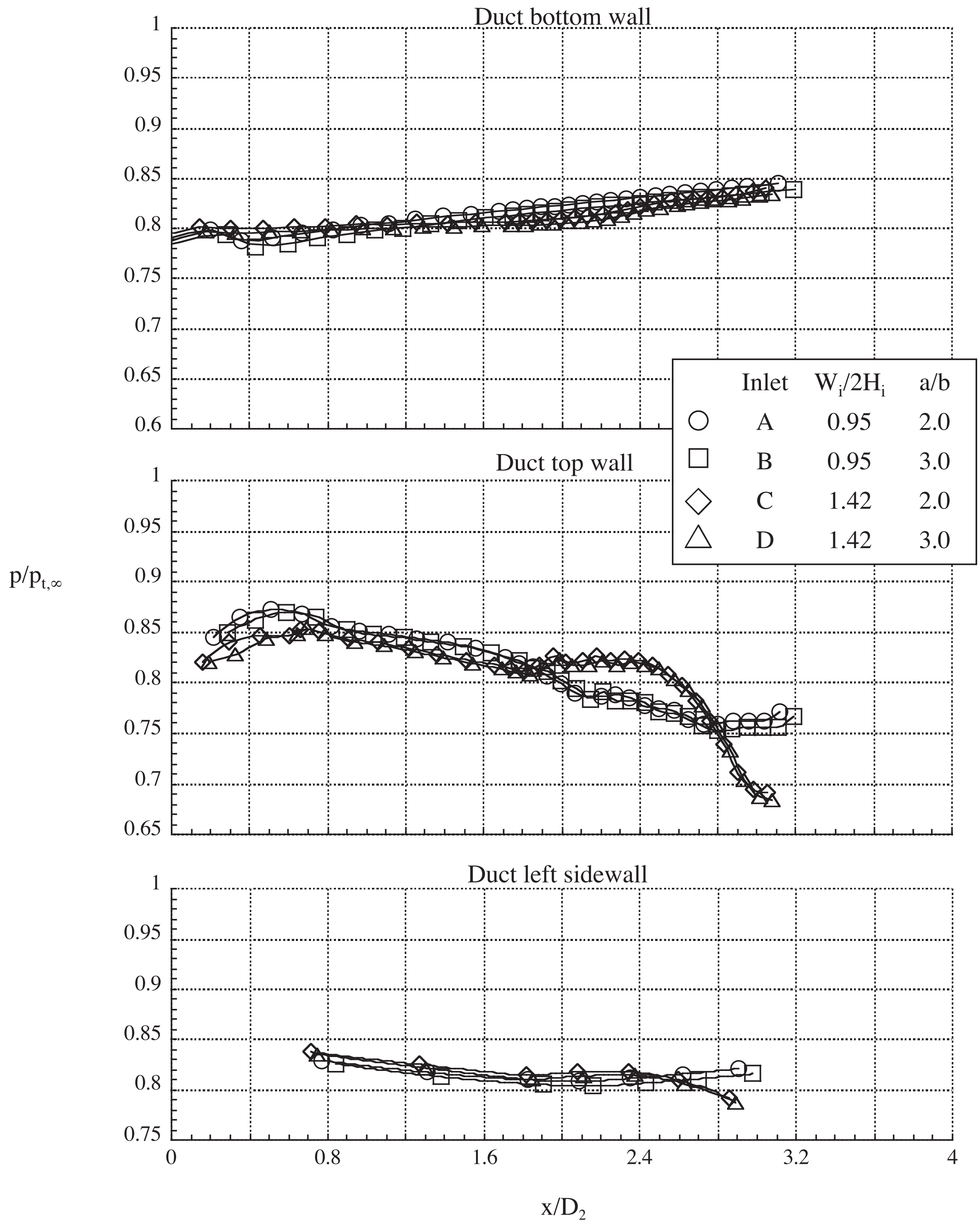

(e) $M = 0.833$, $Re/FT = 68.05 \times 10^6$, $A_0/A_C = 0.555$, $W_{2C}/A_i = 36.15$ lb/sec-ft^2.

Figure 15.- Concluded.

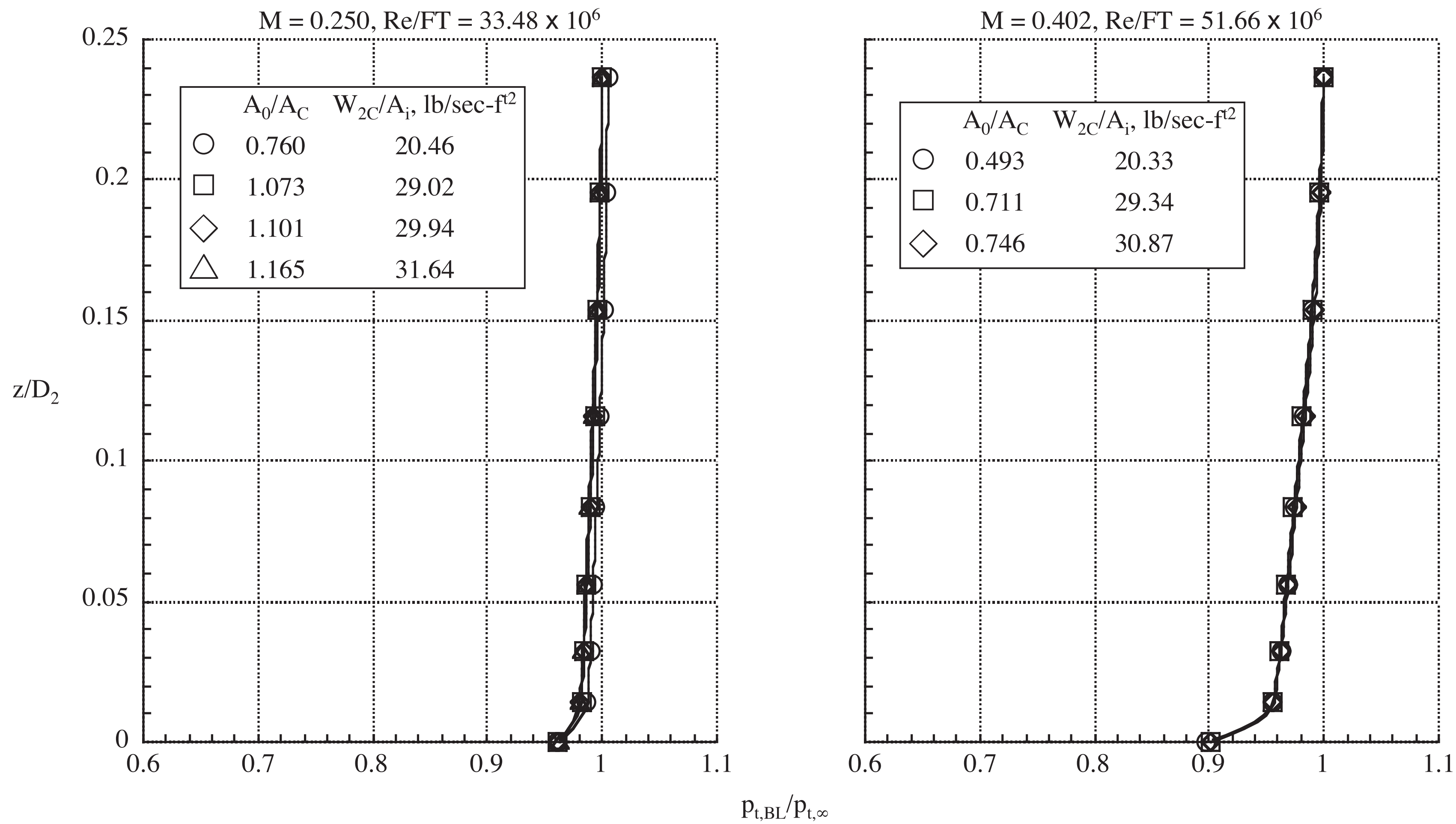

(a) M = 0.250 and M = 0.402.

Figure 16.- Effect of inlet mass-flow on tunnel wall boundary layer profiles. Inlet A.

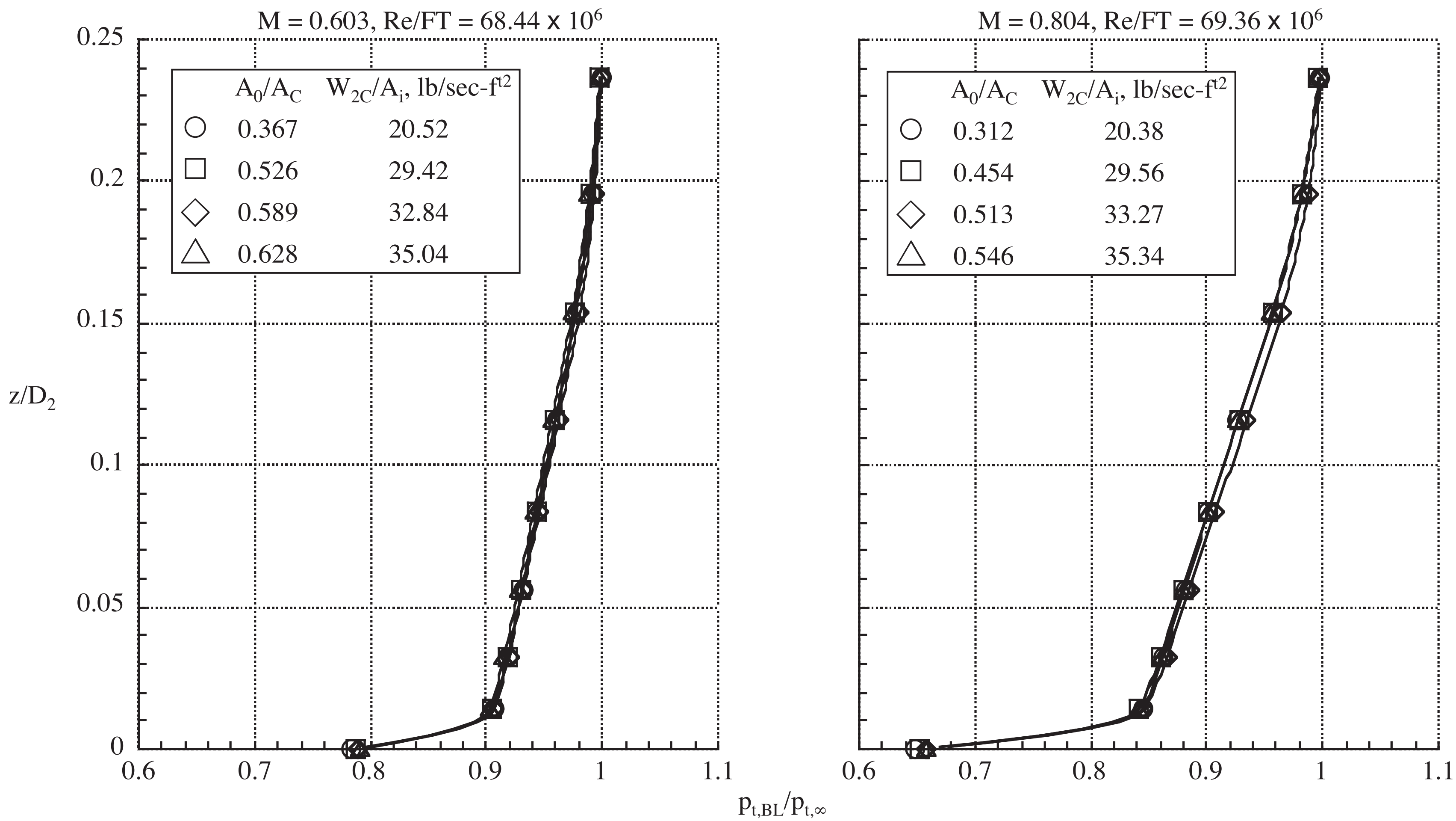

(b) M = 0.603 and M = 0.804.

Figure 16.- Concluded.

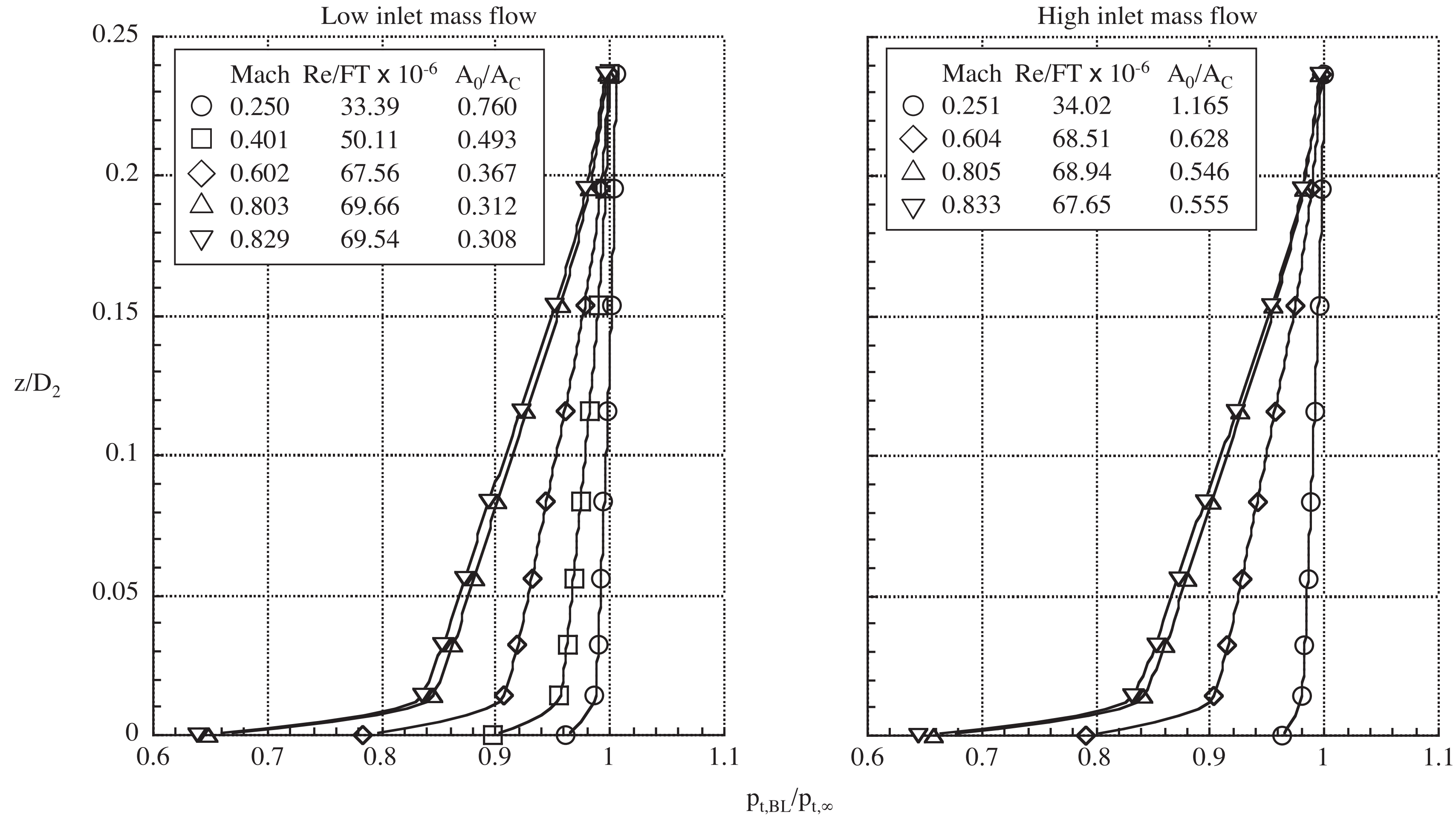

(a) Inlet A

Figure 17.- Effect of Mach number on tunnel wall boundary layer profiles.

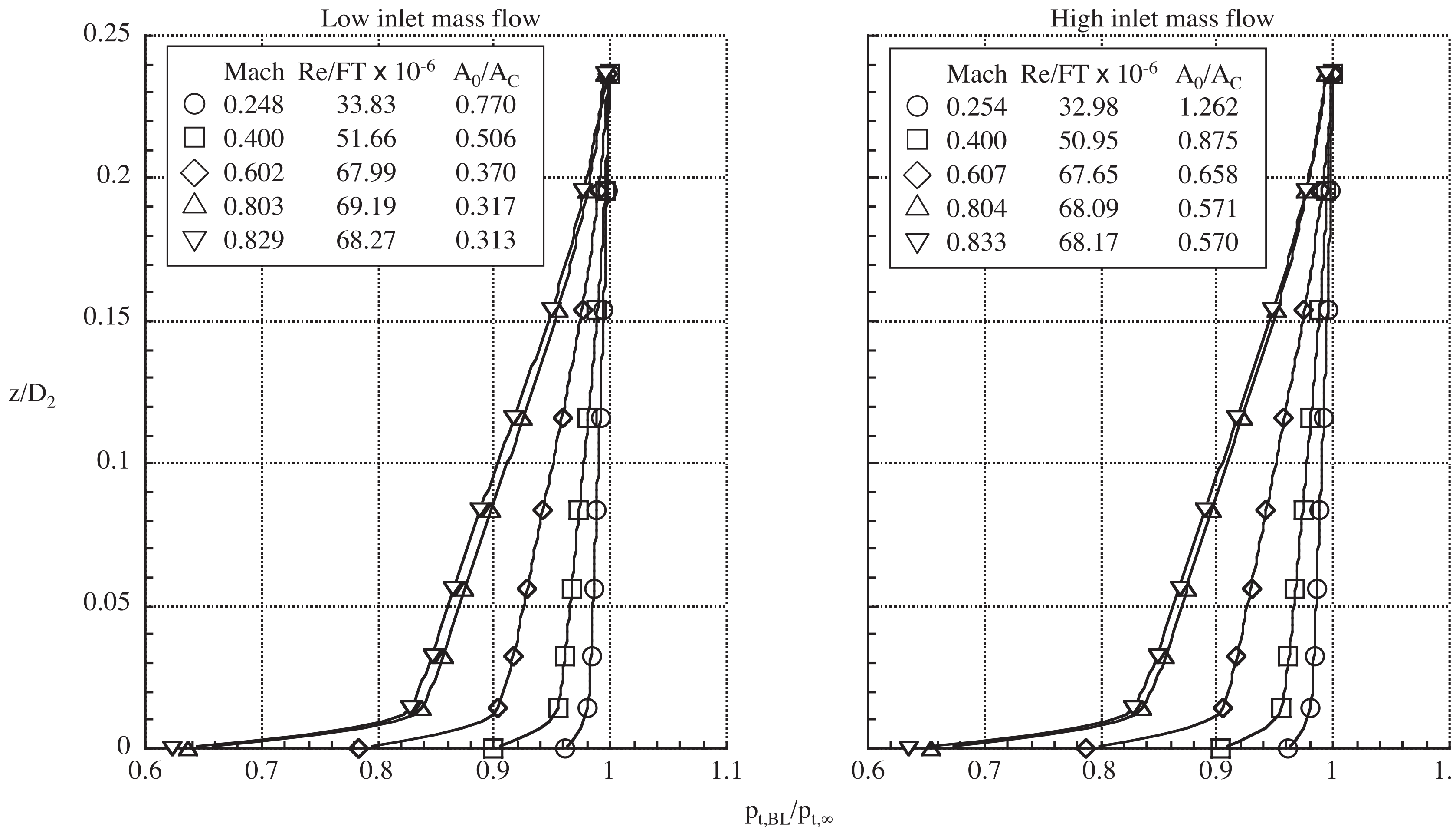

(b) Inlet B.

Figure 17.- Continued.

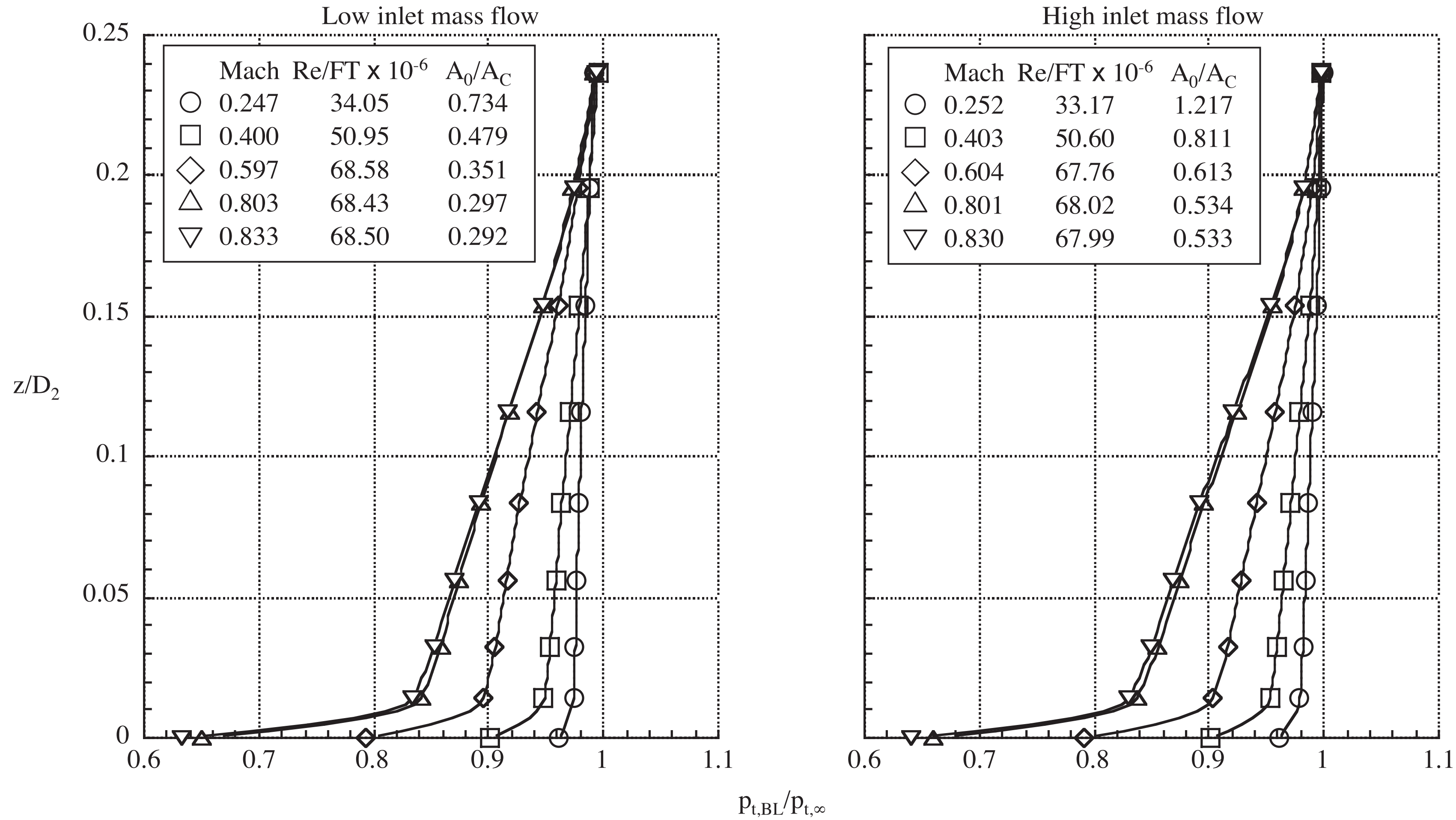

(c) Inlet C.

Figure 17.- Continued.

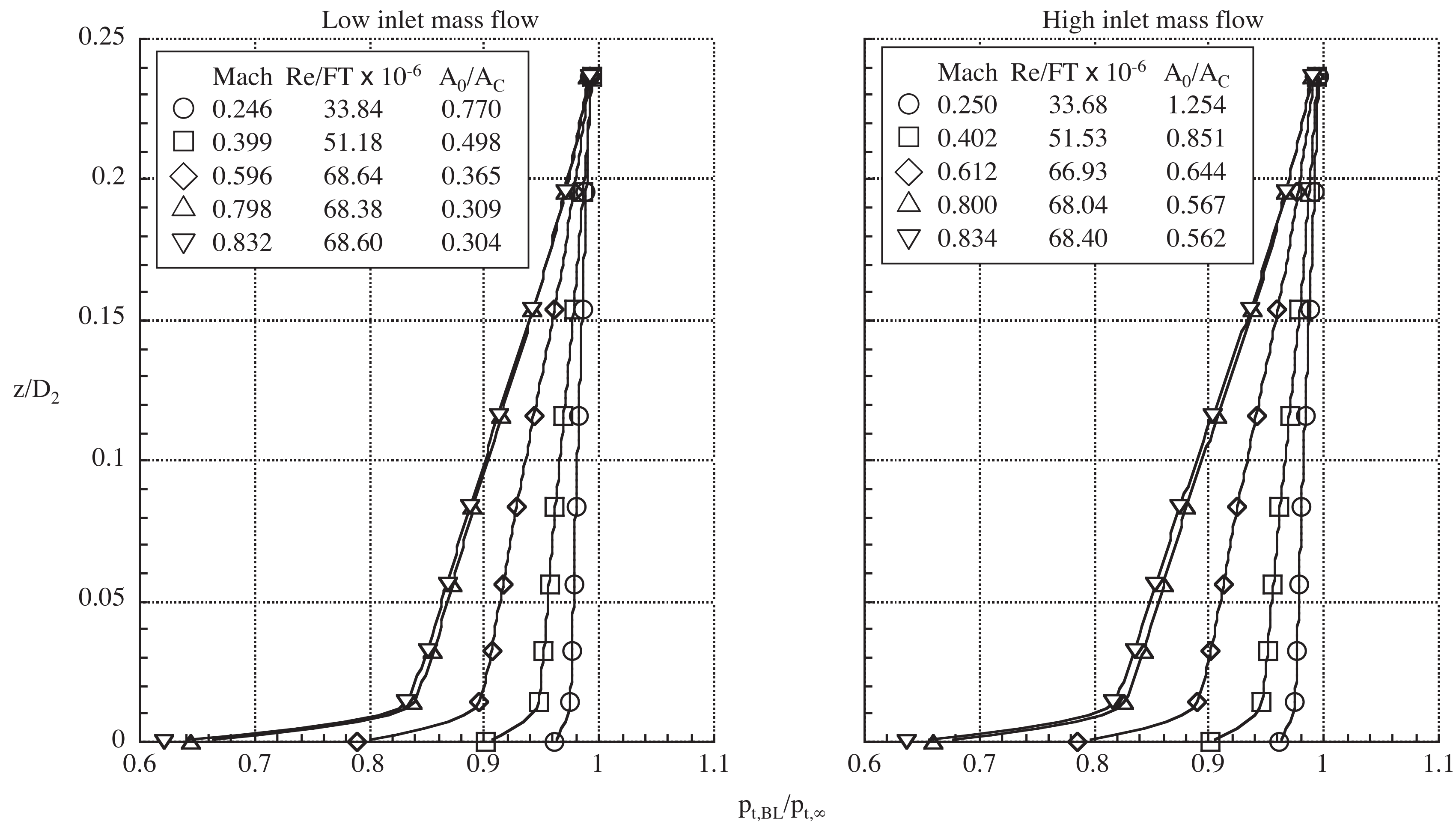

(d) Inlet D.

Figure 17.- Concluded.

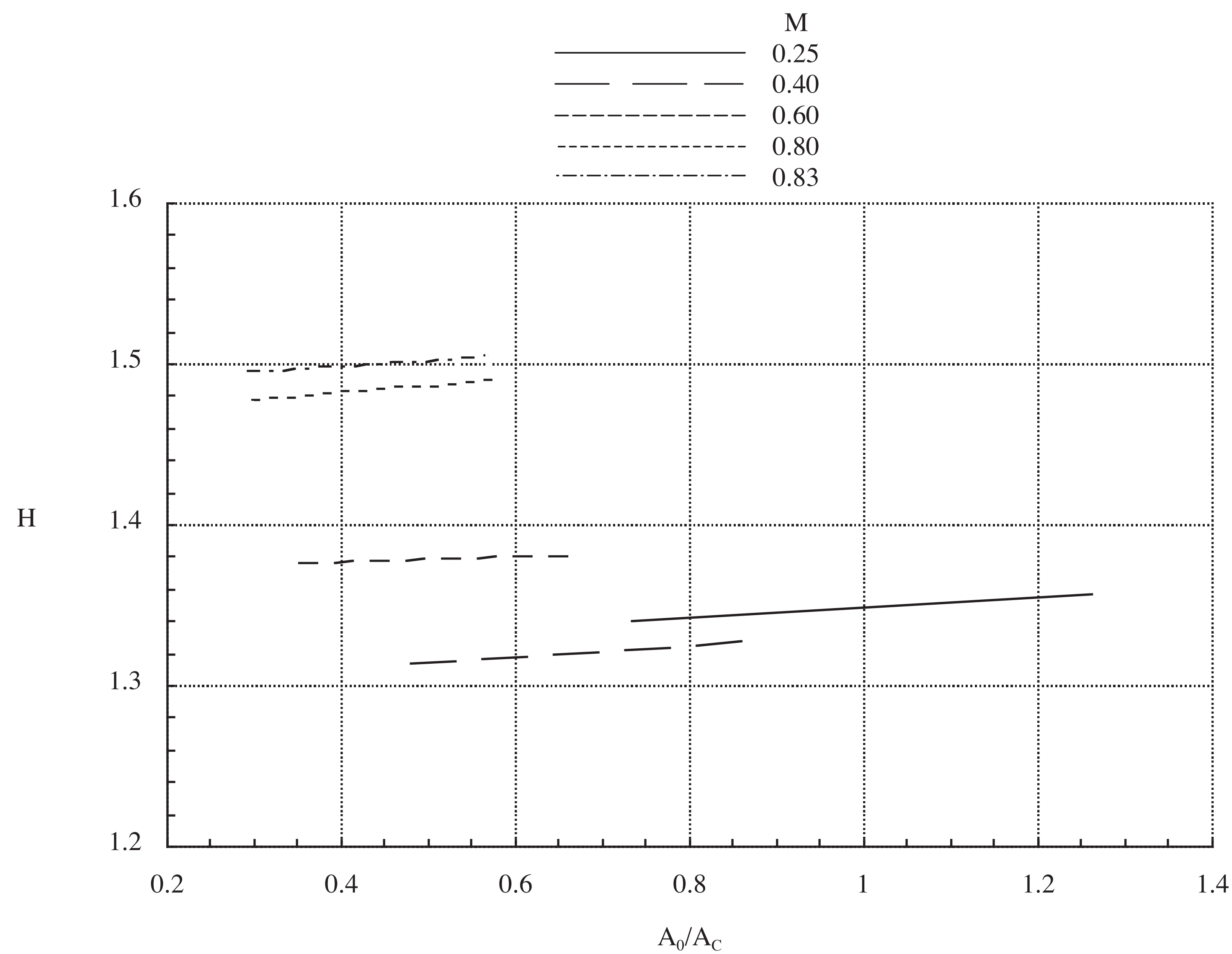

Figure 18. - Effect of inlet mass-flow ratio and Mach number on boundary layer shape factor.

W_{2C}/A_i = 20.46 lb/sec-ft^2, A_0/A_C = 0.760

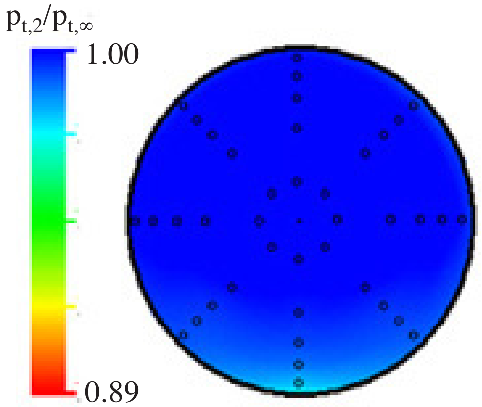

Ring	Intensity	Extent	DPRP
1(Hub)	0.000	67.5	-0.004
2	0.003	139.5	-0.002
3	0.006	144.0	0.000
4	0.007	141.6	0.001
5(Tip)	0.007	123.7	0.006

$DPCP_{avg}$ = 0.005 $p_{t,2}/p_{t,\infty}$ = 1.001

W_{2C}/A_i = 29.02 lb/sec-ft^2, A_0/A_C = 1.073

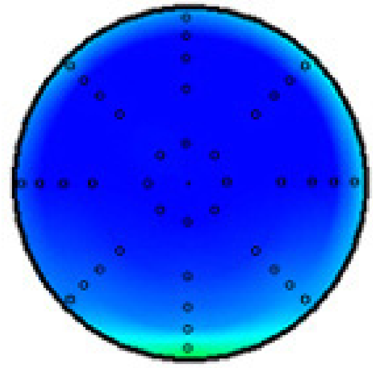

Ring	Intensity	Extent	DPRP
1(Hub)	0.000	78.8	-0.006
2	0.002	137.3	-0.004
3	0.005	143.3	-0.002
4	0.007	141.6	0.000
5(Tip)	0.011	81.7	0.012

$DPCP_{avg}$ = 0.005 $p_{t,2}/p_{t,\infty}$ = 0.994

W_{2C}/A_i = 29.94 lb/sec-ft^2, A_0/A_C = 1.101

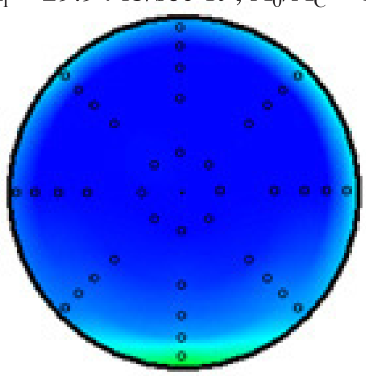

Ring	Intensity	Extent	DPRP
1(Hub)	0.000	78.8	-0.006
2	0.002	135.0	-0.004
3	0.005	143.3	-0.002
4	0.008	140.7	0.001
5(Tip)	0.012	77.9	0.013

$DPCP_{avg}$ = 0.005 $p_{t,2}/p_{t,\infty}$ = 0.994

W_{2C}/A_i = 31.64 lb/sec-ft^2, A_0/A_C = 1.165

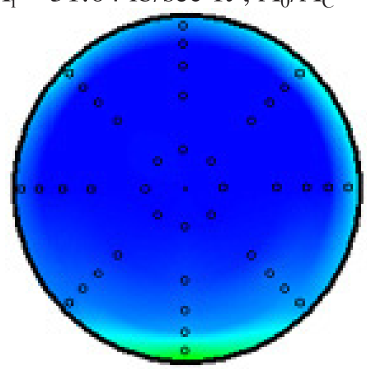

Ring	Intensity	Extent	DPRP
1(Hub)	0.000	67.5	-0.006
2	0.003	131.2	-0.005
3	0.005	142.4	-0.002
4	0.008	140.7	-0.001
5(Tip)	0.013	76.5	0.014

$DPCP_{avg}$ = 0.006 $p_{t,2}/p_{t,\infty}$ = 0.994

(a) M = 0.248, Re/FT = 33.47 x 10^6.

Figure 19. - Pressure recovery and distortion results for inlet A, fence off.

$W_{2C}/A_i = 20.33$ lb/sec-ft^2, $A_0/A_C = 0.711$

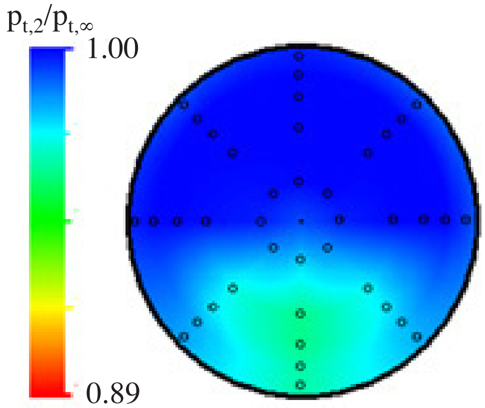

Ring	Intensity	Extent	DPRP
1(Hub)	0.008	147.2	-0.003
2	0.017	142.1	0.002
3	0.016	139.8	0.001
4	0.014	136.1	-0.001
5(Tip)	0.012	130.3	0.002

$DPCP_{avg} = 0.014$ $p_{t,2}/p_{t,\infty} = 0.990$

$W_{2C}/A_i = 29.34$ lb/sec-ft^2, $A_0/A_C = 0.493$

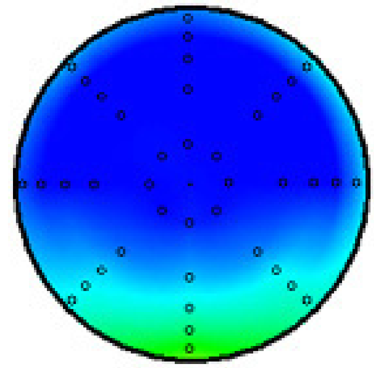

Ring	Intensity	Extent	DPRP
1(Hub)	0.001	97.5	-0.010
2	0.009	139.1	-0.005
3	0.014	142.9	0.000
4	0.018	140.6	0.002
5(Tip)	0.017	127.6	0.013

$DPCP_{avg} = 0.012$ $p_{t,2}/p_{t,\infty} = 0.989$

$W_{2C}/A_i = 30.87$ lb/sec-ft^2, $A_0/A_C = 0.746$

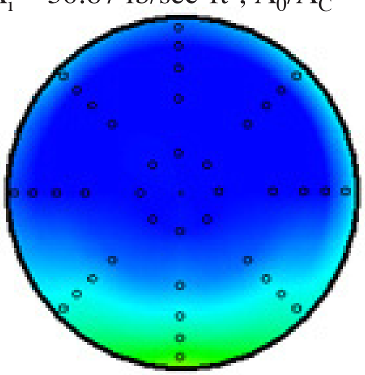

Ring	Intensity	Extent	DPRP
1(Hub)	0.001	73.1	-0.010
2	0.007	139.1	-0.005
3	0.013	143.1	-0.001
4	0.018	141.5	0.002
5(Tip)	0.017	127.7	0.014

$DPCP_{avg} = 0.011$ $p_{t,2}/p_{t,\infty} = 0.990$

(b) M = 0.402, Re/FT = 51.66 x 10^6.

Figure 19. - Continued.

W_{2C}/A_i = 20.52 lb/sec-ft^2, A_0/A_C = 0.367

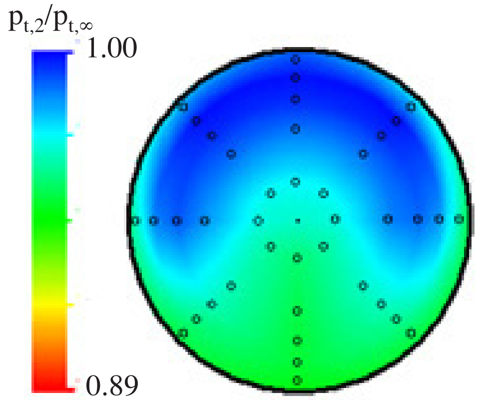

Ring	Intensity	Extent	DPRP
1(Hub)	0.005	152.1	0.008
2	0.014	144.5	-0.003
3	0.017	148.0	-0.007
4	0.018	162.5	-0.005
5(Tip)	0.012	196.2	0.007

$DPCP_{avg}$ = 0.013 $p_{t,2}/p_{t,\infty}$ = 0.975

W_{2C}/A_i = 29.42 lb/sec-ft^2, A_0/A_C = 0.526

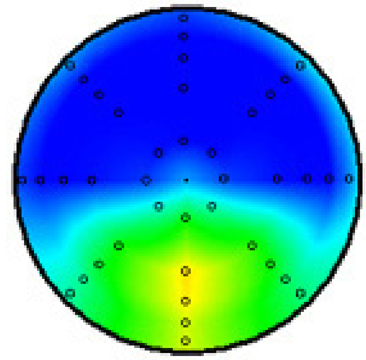

Ring	Intensity	Extent	DPRP
1(Hub)	0.020	146.1	0.008
2	0.037	141.1	-0.003
3	0.035	139.3	-0.007
4	0.030	136.5	-0.005
5(Tip)	0.025	131.3	0.007

$DPCP_{avg}$ = 0.029 $p_{t,2}/p_{t,\infty}$ = 0.977

W_{2C}/A_i = 32.84 lb/sec-ft^2, A_0/A_C = 0.589

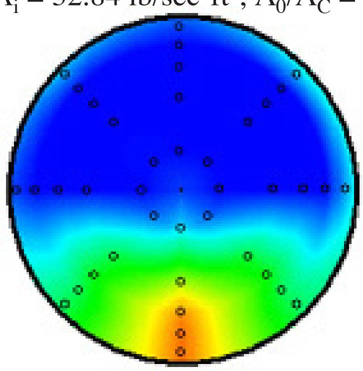

Ring	Intensity	Extent	DPRP
1(Hub)	0.009	133.0	-0.016
2	0.031	140.3	0.000
3	0.038	137.3	0.004
4	0.037	133.0	0.002
5(Tip)	0.031	126.2	0.011

$DPCP_{avg}$ = 0.029 $p_{t,2}/p_{t,\infty}$ = 0.978

W_{2C}/A_i = 35.04 lb/sec-ft^2, A_0/A_C = 0.628

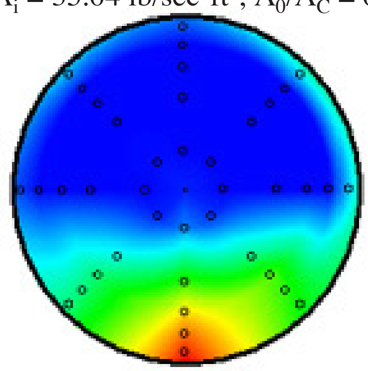

Ring	Intensity	Extent	DPRP
1(Hub)	0.005	1110	-0.018
2	0.025	137.7	-0.004
3	0.036	137.8	0.003
4	0.039	134.1	0.004
5(Tip)	0.033	125.2	0.015

$DPCP_{avg}$ = 0.028 $p_{t,2}/p_{t,\infty}$ = 0.979

(c) M = 0.603, Re/FT = 68.44 x 10^6.

Figure 19. - Continued.

W_{2C}/A_i = 20.38 lb/sec-ft^2, A_0/A_C = 0.312

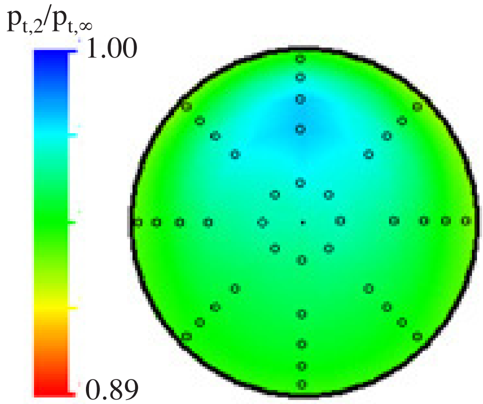

Ring	Intensity	Extent	DPRP
1(Hub)	0.003	179.1	-0.011
2	0.007	205.4	-0.008
3	0.007	219.4	-0.003
4	0.004	248.0	0.006
5(Tip)	0.004	93.2	0.016

$DPCP_{avg}$ = 0.005 $p_{t,2}/p_{t,\infty}$ = 0.954

W_{2C}/A_i = 29.56 lb/sec-ft^2, A_0/A_C = 0.454

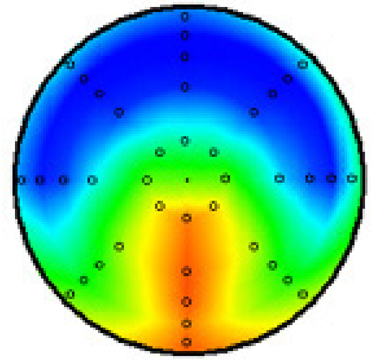

Ring	Intensity	Extent	DPRP
1(Hub)	0.020	180.0	0.026
2	0.037	154.1	-0.002
3	0.039	141.3	-0.011
4	0.038	138.9	-0.014
5(Tip)	0.033	144.4	0.001

$DPCP_{avg}$ = 0.033 $p_{t,2}/p_{t,\infty}$ = 0.960

W_{2C}/A_i = 33.27 lb/sec-ft^2, A_0/A_C = 0.513

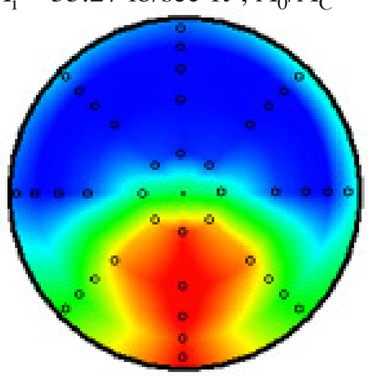

Ring	Intensity	Extent	DPRP
1(Hub)	0.038	167.5	0.012
2	0.053	146.2	0.003
3	0.048	139.9	-0.005
4	0.042	134.6	-0.011
5(Tip)	0.035	131.0	0.001

$DPCP_{avg}$ = 0.043 $p_{t,2}/p_{t,\infty}$ = 0.963

W_{2C}/A_i = 35.34 lb/sec-ft^2, A_0/A_C = 0.546

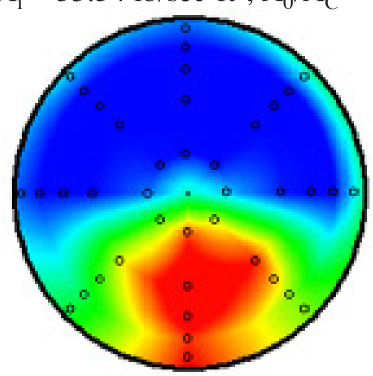

Ring	Intensity	Extent	DPRP
1(Hub)	0.040	149.6	-0.001
2	0.059	141.3	0.005
3	0.051	138.1	-0.001
4	0.043	135.3	-0.008
5(Tip)	0.036	131.1	0.005

$DPCP_{avg}$ = 0.046 $p_{t,2}/p_{t,\infty}$ = 0.965

(d) M = 0.804, Re/FT = 69.36 x 10^6.

Figure 19. - Continued.

W_{2C}/A_i = 20.37 lb/sec-ft^2, A_0/A_C = 0.308

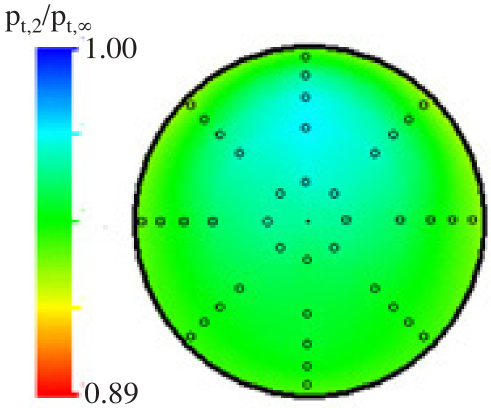

Ring	Intensity	Extent	DPRP
1(Hub)	0.004	176.3	-0.011
2	0.007	204.5	-0.008
3	0.006	224.8	-0.002
4	0.003	259.3	0.005
5(Tip)	0.004	92.3	0.015

$DPCP_{avg}$ = 0.005 $p_{t,2}/p_{t,\infty}$ = 0.951

W_{2C}/A_i = 29.42 lb/sec-ft^2, A_0/A_C = 0.447

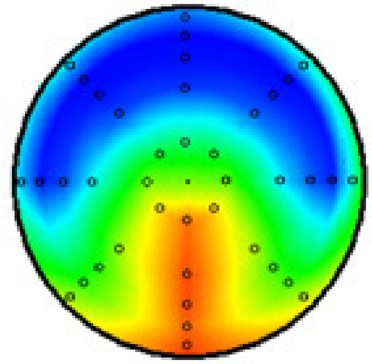

Ring	Intensity	Extent	DPRP
1(Hub)	0.018	175.2	0.027
2	0.036	153.0	-0.002
3	0.039	141.7	-0.013
4	0.041	140.3	-0.015
5(Tip)	0.033	148.6	0.003

$DPCP_{avg}$ = 0.034 $p_{t,2}/p_{t,\infty}$ = 0.957

W_{2C}/A_i = 33.38 lb/sec-ft^2, A_0/A_C = 0.508

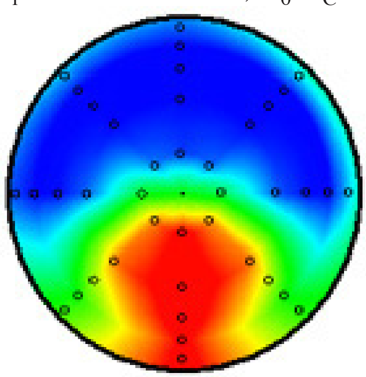

Ring	Intensity	Extent	DPRP
1(Hub)	0.039	171.3	0.015
2	0.055	147.0	0.003
3	0.050	139.5	-0.006
4	0.044	134.8	-0.012
5(Tip)	0.037	131.3	0.000

$DPCP_{avg}$ = 0.045 $p_{t,2}/p_{t,\infty}$ = 0.960

W_{2C}/A_i = 36.41 lb/sec-ft^2, A_0/A_C = 0.556

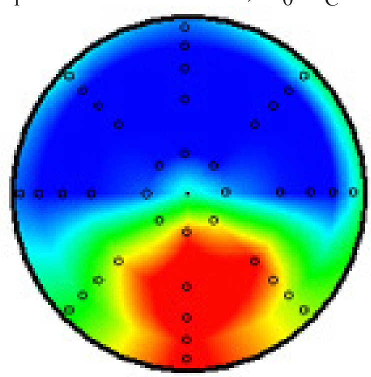

Ring	Intensity	Extent	DPRP
1(Hub)	0.041	147.8	-0.003
2	0.062	140.9	0.005
3	0.055	137.7	-0.001
4	0.046	135.4	-0.008
5(Tip)	0.038	131.1	0.006

$DPCP_{avg}$ = 0.048 $p_{t,2}/p_{t,\infty}$ = 0.963

(e) M = 0.832, Re/FT = 66.92 x 10^6.

Figure 19. - Continued.

Re/FT = 25.03 x 10^6, $T_{t,\infty}$ = 259.8 °R

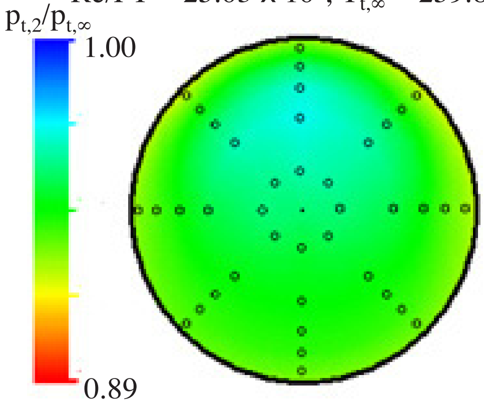

Ring	Intensity	Extent	DPRP
1(Hub)	0.004	168.8	-0.011
2	0.007	202.7	-0.008
3	0.007	218.4	-0.003
4	0.003	253.9	0.006
5(Tip)	0.003	94.5	0.016

$DPCP_{avg}$ = 0.005 $p_{t,2}/p_{t,\infty}$ = 0.947

Re/FT = 42.06 x 10^6, $T_{t,\infty}$ = 260.7 °R

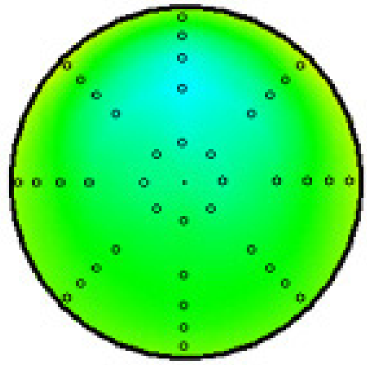

Ring	Intensity	Extent	DPRP
1(Hub)	0.004	170.2	-0.011
2	0.007	207.2	-0.009
3	0.006	222.4	-0.003
4	0.003	260.1	0.006
5(Tip)	0.003	85.5	0.017

$DPCP_{avg}$ = 0.005 $p_{t,2}/p_{t,\infty}$ = 0.949

Re/FT = 43.00 x 10^6, $T_{t,\infty}$ = 180.6 °R

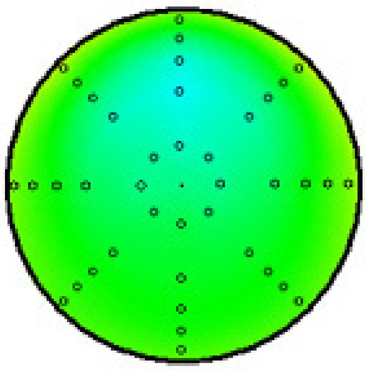

Ring	Intensity	Extent	DPRP
1(Hub)	0.004	167.3	-0.011
2	0.006	206.6	-0.008
3	0.006	223.0	-0.002
4	0.003	259.7	0.006
5(Tip)	0.003	90.0	0.015

$DPCP_{avg}$ = 0.004 $p_{t,2}/p_{t,\infty}$ = 0.949

Re/FT = 69.54 x 10^6, $T_{t,\infty}$ = 180.7 °R

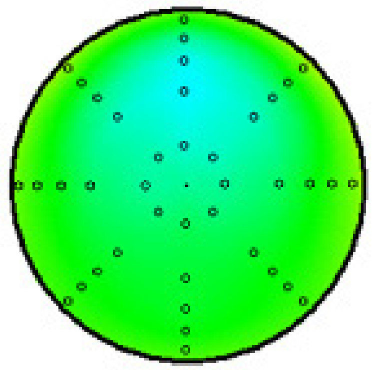

Ring	Intensity	Extent	DPRP
1(Hub)	0.004	176.3	-0.011
2	0.007	204.5	-0.008
3	0.006	224.8	-0.002
4	0.003	259.3	0.005
5(Tip)	0.004	92.3	0.015

$DPCP_{avg}$ = 0.005 $p_{t,2}/p_{t,\infty}$ = 0.951

(f) M = 0.830, W_{2C}/A_i = 20.42 lbm/sec-ft^2 (A_0/A_C = 0.308).

Figure 19. - Continued.

Re/FT = 24.82 x 10^6, $T_{t,\infty}$ = 259.6 °R

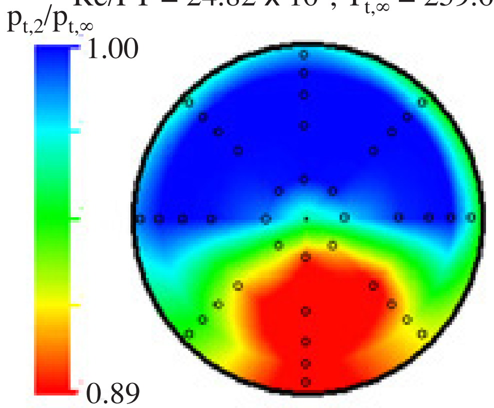

Ring	Intensity	Extent	DPRP
1(Hub)	0.042	151.1	-0.003
2	0.065	141.2	0.004
3	0.059	138.7	-0.002
4	0.050	136.2	-0.009
5(Tip)	0.039	131.9	0.009

$DPCP_{avg}$ = 0.051 $p_{t,2}/p_{t,\infty}$ = 0.959

Re/FT = 41.15 x 10^6, $T_{t,\infty}$ = 260.5 °R

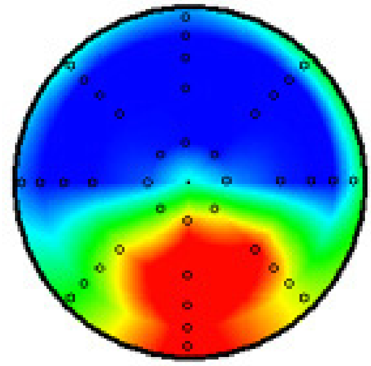

Ring	Intensity	Extent	DPRP
1(Hub)	0.038	147.5	-0.006
2	0.064	140.4	0.005
3	0.058	138.0	0.000
4	0.048	135.7	-0.007
5(Tip)	0.039	131.0	0.008

$DPCP_{avg}$ = 0.049 $p_{t,2}/p_{t,\infty}$ = 0.962

Re/FT = 41.56 x 10^6, $T_{t,\infty}$ = 179.7 °R

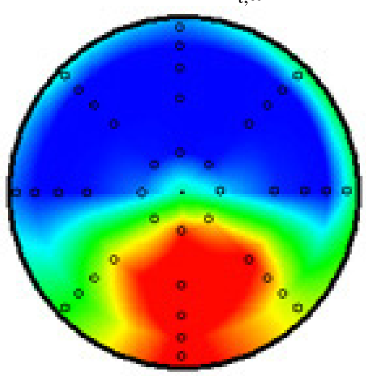

Ring	Intensity	Extent	DPRP
1(Hub)	0.042	150.6	-0.001
2	0.063	141.8	0.005
3	0.056	138.5	-0.002
4	0.047	135.9	-0.009
5(Tip)	0.038	131.3	0.007

$DPCP_{avg}$ = 0.049 $p_{t,2}/p_{t,\infty}$ = 0.961

Re/FT = 67.65 x 10^6, $T_{t,\infty}$ = 180.1 °R

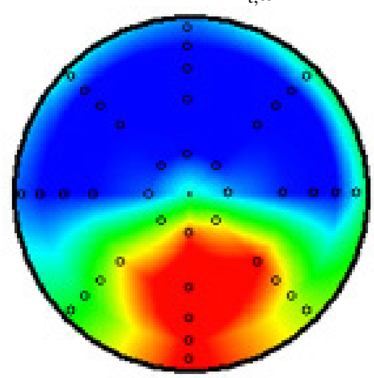

Ring	Intensity	Extent	DPRP
1(Hub)	0.041	147.8	-0.003
2	0.062	140.9	0.005
3	0.055	137.7	-0.001
4	0.046	135.4	-0.008
5(Tip)	0.038	131.1	0.006

$DPCP_{avg}$ = 0.048 $p_{t,2}/p_{t,\infty}$ = 0.963

(g) M = 0.832, W_{2C}/A_i = 36.73 lbm/sec-ft^2 (A_0/A_C = 0.560).

Figure 19. - Concluded.

$W_{2C}/A_i = 29.55$ lb/sec-ft^2, $A_0/A_C = 1.086$

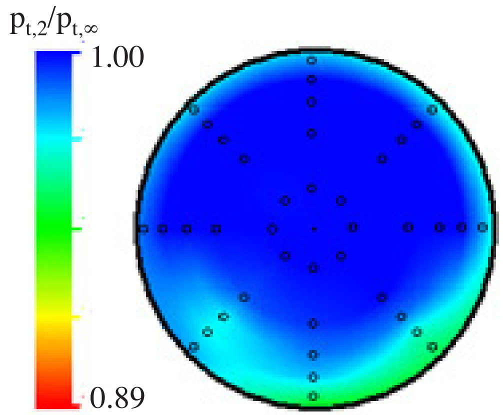

Ring	Intensity	Extent	DPRP
1(Hub)	0.00	78.8	-0.009
2	0.004	110.5	-0.007
3	0.009	146.0	-0.002
4	0.014	149.6	0.002
5(Tip)	0.013	118.9	0.016

$DPCP_{avg} = 0.008$ $p_{t,2}/p_{t,\infty} = 0.992$

$W_{2C}/A_i = 31.56$ lb/sec-ft^2, $A_0/A_C = 1.156$

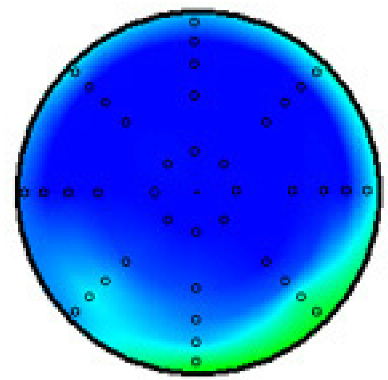

Ring	Intensity	Extent	DPRP
1(Hub)	0.00	78.8	-0.009
2	0.004	112.4	-0.007
3	0.008	142.5	-0.003
4	0.014	149.7	0.002
5(Tip)	0.016	117.8	0.017

$DPCP_{avg} = 0.008$ $p_{t,2}/p_{t,\infty} = 0.991$

(a) $M = 0.248$, $Re/FT = 33.47 \times 10^6$.

Figure 20. - Pressure recovery and distortion results for inlet A, fence on.

$W_{2C}/A_i = 29.53$ lb/sec-ft^2, $A_0/A_C = 0.716$

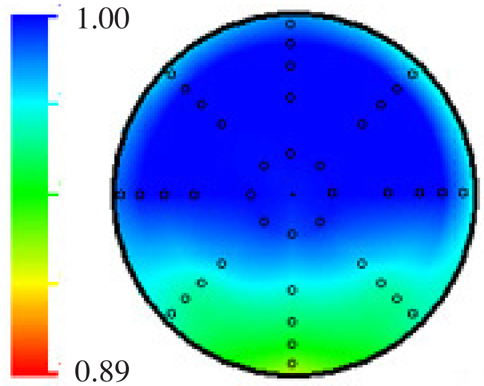

Ring	Intensity	Extent	DPRP
1(Hub)	0.003	123.8	-0.012
2	0.014	141.3	-0.004
3	0.020	143.5	0.000
4	0.024	141.9	0.003
5(Tip)	0.019	127.4	0.014

$DPCP_{avg} = 0.016$ $p_{t,2}/p_{t,\infty} = 0.986$

$W_{2C}/A_i = 33.53$ lb/sec-ft^2, $A_0/A_C = 0.812$

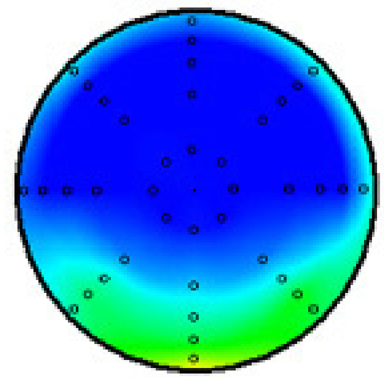

Ring	Intensity	Extent	DPRP
1(Hub)	0.001	73.1	-0.013
2	0.009	140.4	-0.007
3	0.018	145.3	-0.001
4	0.025	146.1	0.004
5(Tip)	0.021	131.6	0.017

$DPCP_{avg} = 0.015$ $p_{t,2}/p_{t,\infty} = 0.987$

(b) $M = 0.400$, $Re/FT = 50.78 \times 10^6$.

Figure 20. - Continued.

$W_{2C}/A_i = 29.62$ lb/sec-ft^2, $A_0/A_C = 0.527$

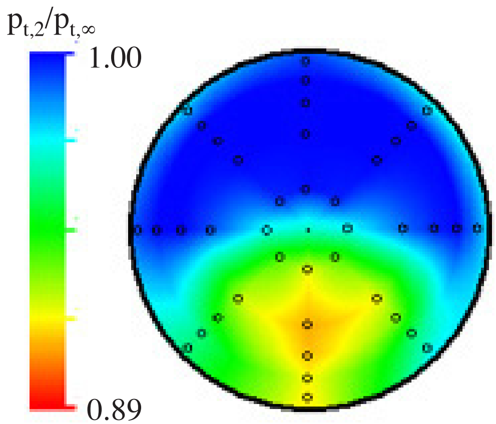

Ring	Intensity	Extent	DPRP
1(Hub)	0.028	167.9	0.006
2	0.042	148.8	0.005
3	0.039	142.0	-0.002
4	0.032	135.5	-0.008
5(Tip)	0.027	116.5	-0.001

$DPCP_{avg} = 0.034$ $p_{t,2}/p_{t,\infty} = 0.971$

$W_{2C}/A_i = 35.08$ lb/sec-ft^2, $A_0/A_C = 0.626$

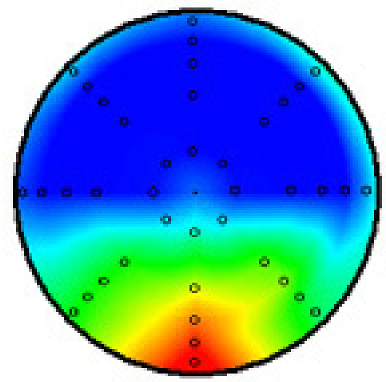

Ring	Intensity	Extent	DPRP
1(Hub)	0.014	140.7	-0.015
2	0.036	142.3	0.000
3	0.041	139.8	0.003
4	0.042	134.4	0.001
5(Tip)	0.038	120.1	0.012

$DPCP_{avg} = 0.034$ $p_{t,2}/p_{t,\infty} = 0.975$

(c) $M = 0.602$, $Re/FT = 68.53 \times 10^6$.

Figure 20. - Continued.

$W_{2C}/A_i = 29.74$ lb/sec-ft^2, $A_0/A_C = 0.454$

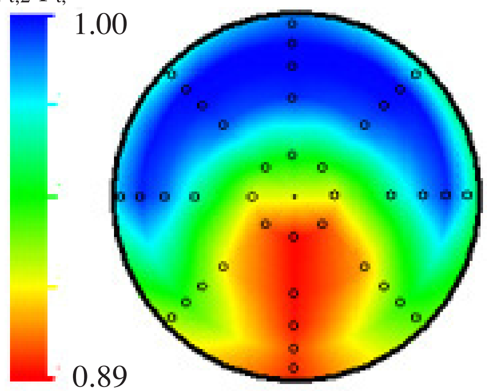

Ring	Intensity	Extent	DPRP
1(Hub)	0.020	181.0	0.035
2	0.039	162.1	0.001
3	0.042	147.1	-0.013
4	0.041	139.4	-0.019
5(Tip)	0.033	141.0	-0.003

$DPCP_{avg} = 0.035$ $p_{t,2}/p_{t,\infty} = 0.953$

$W_{2C}/A_i = 35.60$ lb/sec-ft^2, $A_0/A_C = 0.544$

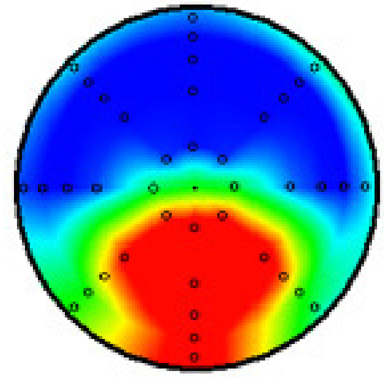

Ring	Intensity	Extent	DPRP
1(Hub)	0.048	167.9	0.035
2	0.066	147.6	0.001
3	0.059	141.1	-0.013
4	0.048	133.1	-0.019
5(Tip)	0.043	112.4	-0.003

$DPCP_{avg} = 0.053$ $p_{t,2}/p_{t,\infty} = 0.957$

(d) $M = 0.807$, $Re/FT = 68.29 \times 10^6$.

Figure 20. - Continued.

$W_{2C}/A_i = 29.69$ lb/sec-ft^2, $A_0/A_C = 0.447$

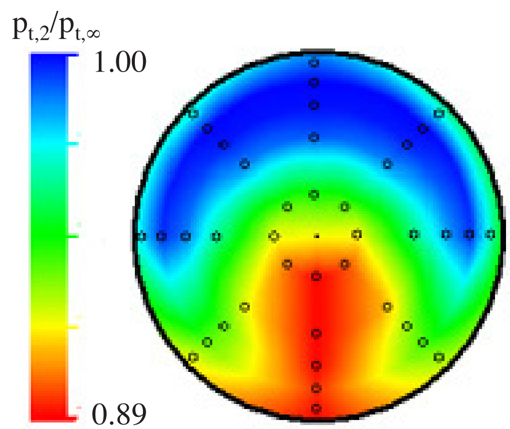

Ring	Intensity	Extent	DPRP
1(Hub)	0.018	176.2	0.035
2	0.037	159.6	0.001
3	0.041	145.7	-0.015
4	0.043	140.8	-0.020
5(Tip)	0.034	145.9	-0.001

$DPCP_{avg} = 0.034$ $p_{t,2}/p_{t,\infty} = 0.951$

$W_{2C}/A_i = 36.28$ lb/sec-ft^2, $A_0/A_C = 0.550$

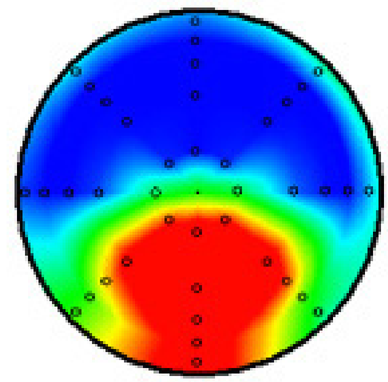

Ring	Intensity	Extent	DPRP
1(Hub)	0.050	166.7	0.013
2	0.069	147.1	0.007
3	0.061	141.0	-0.003
4	0.050	133.3	-0.014
5(Tip)	0.044	114.2	-0.004

$DPCP_{avg} = 0.055$ $p_{t,2}/p_{t,\infty} = 0.955$

(e) $M = 0.833$, $Re/FT = 68.56 \times 10^6$.

Figure 20. - Continued.

Re/FT = 24.98 x 10^6, $T_{t,\infty}$ = 260.8 °R

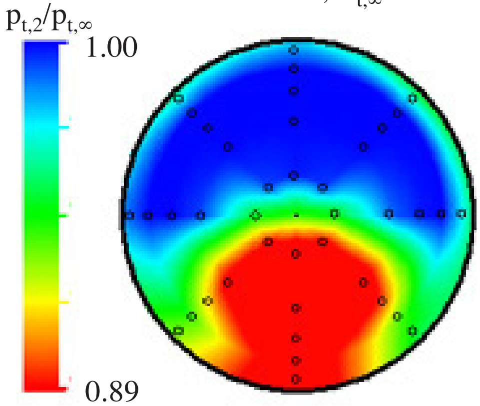

Ring	Intensity	Extent	DPRP
1(Hub)	0.051	167.9	0.015
2	0.070	146.7	0.005
3	0.062	140.3	-0.005
4	0.051	133.4	-0.015
5(Tip)	0.045	113.8	0.000

$DPCP_{avg}$ = 0.056 $p_{t,2}/p_{t,\infty}$ = 0.953

Re/FT = 41.05 x 10^6, $T_{t,\infty}$ = 261.4 °R

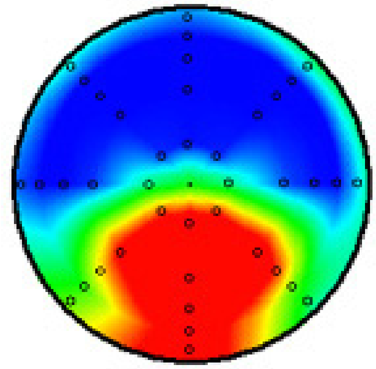

Ring	Intensity	Extent	DPRP
1(Hub)	0.051	162.1	0.011
2	0.070	145.9	0.007
3	0.062	140.3	-0.003
4	0.051	133.1	-0.013
5(Tip)	0.046	109.4	-0.001

$DPCP_{avg}$ = 0.056 $p_{t,2}/p_{t,\infty}$ = 0.955

Re/FT = 41.64 x 10^6, $T_{t,\infty}$ = 180.4 °R

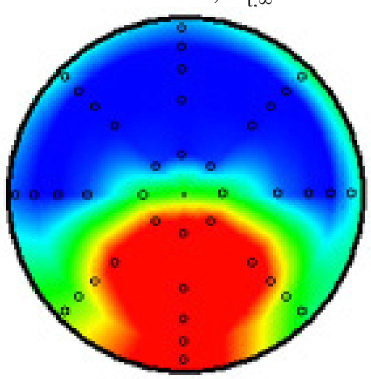

Ring	Intensity	Extent	DPRP
1(Hub)	0.052	169.3	0.016
2	0.070	147.3	0.006
3	0.062	141.0	-0.005
4	0.051	133.9	-0.015
5(Tip)	0.046	113.7	-0.002

$DPCP_{avg}$ = 0.056 $p_{t,2}/p_{t,\infty}$ = 0.953

Re/FT = 68.02 x 10^6, $T_{t,\infty}$ = 181.1 °R

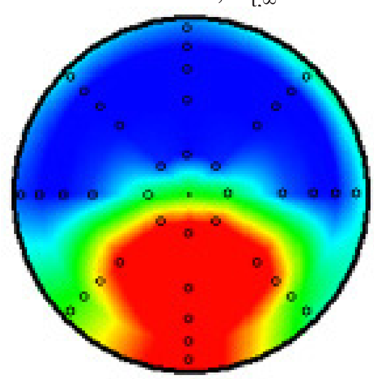

Ring	Intensity	Extent	DPRP
1(Hub)	0.050	166.7	0.013
2	0.069	147.1	0.007
3	0.061	141.0	-0.003
4	0.050	133.3	-0.014
5(Tip)	0.044	114.2	-0.004

$DPCP_{avg}$ = 0.055 $p_{t,2}/p_{t,\infty}$ = 0.955

(f) M = 0.831, W_{2C}/A_i = 36.63 lbm/sec-ft^2 (A_0/A_C = 0.555).

Figure 20. - Concluded.

$W_{2C}/A_i = 20.24$ lb/sec-ft^2, $A_0/A_C = 0.770$

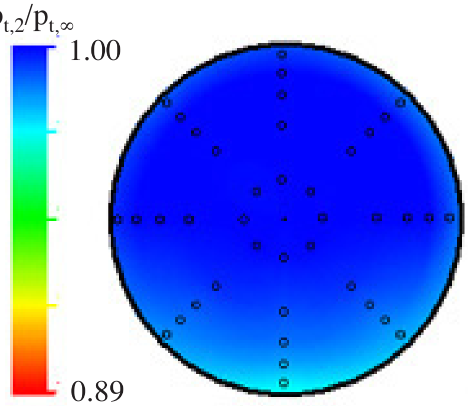

Ring	Intensity	Extent	DPRP
1(Hub)	0.000	67.5	-0.004
2	0.003	137.0	-0.003
3	0.005	143.2	-0.001
4	0.008	141.7	0.001
5(Tip)	0.008	133.4	0.007

$DPCP_{avg} = 0.005$ $p_{t,2}/p_{t,\infty} = 0.995$

$W_{2C}/A_i = 29.23$ lb/sec-ft^2, $A_0/A_C = 1.099$

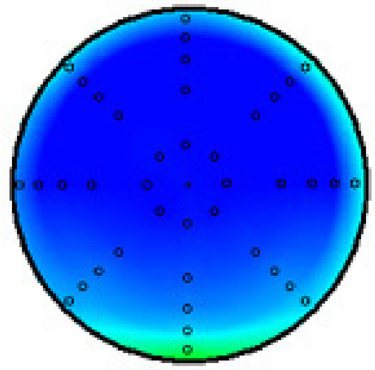

Ring	Intensity	Extent	DPRP
1(Hub)	0.001	101.3	-0.007
2	0.004	141.7	-0.005
3	0.007	144.8	-0.002
4	0.010	140.8	-0.001
5(Tip)	0.011	88.9	0.015

$DPCP_{avg} = 0.006$ $p_{t,2}/p_{t,\infty} = 0.993$

$W_{2C}/A_i = 33.08$ lb/sec-ft^2, $A_0/A_C = 1.258$

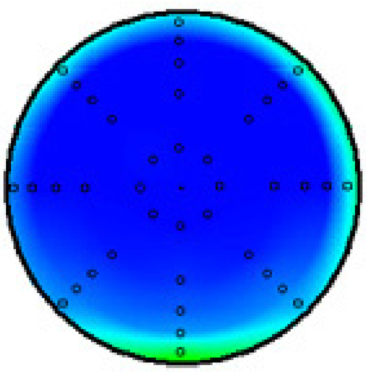

Ring	Intensity	Extent	DPRP
1(Hub)	0.000	78.8	-0.007
2	0.002	129.4	-0.006
3	0.005	142.9	-0.004
4	0.007	141.3	-0.002
5(Tip)	0.012	69.6	0.017

$DPCP_{avg} = 0.005$ $p_{t,2}/p_{t,\infty} = 0.993$

$W_{2C}/A_i = 33.92$ lb/sec-ft^2, $A_0/A_C = 1.262$

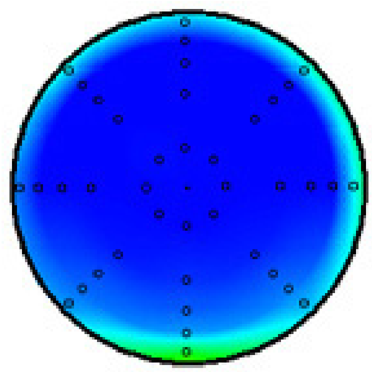

Ring	Intensity	Extent	DPRP
1(Hub)	0.000	78.8	-0.007
2	0.002	133.1	-0.006
3	0.005	144.1	-0.003
4	0.007	141.3	-0.002
5(Tip)	0.013	71.5	0.017

$DPCP_{avg} = 0.006$ $p_{t,2}/p_{t,\infty} = 0.993$

(a) M = 0.250, Re/FT = 33.27×10^6.

Figure 21. - Pressure recovery and distortion results for inlet B.

W_{2C}/A_i = 20.36 lb/sec-ft^2, A_0/A_C = 0.506

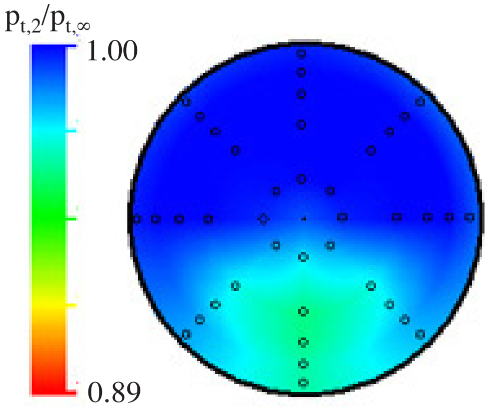

Ring	Intensity	Extent	DPRP
1(Hub)	0.009	147.6	-0.002
2	0.018	141.9	0.002
3	0.016	139.5	0.001
4	0.014	135.0	-0.001
5(Tip)	0.012	133.0	0.002

$DPCP_{avg}$ = 0.014 $p_{t,2}/p_{t,\infty}$ = 0.989

W_{2C}/A_i = 29.26 lb/sec-ft^2, A_0/A_C = 0.724

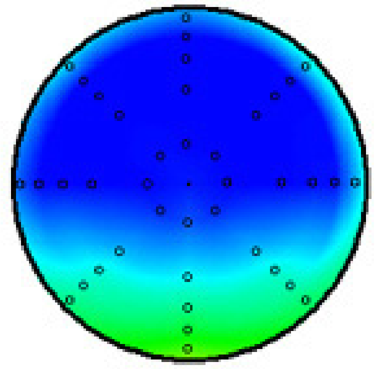

Ring	Intensity	Extent	DPRP
1(Hub)	0.003	129.4	-0.011
2	0.012	142.1	-0.005
3	0.018	143.7	-0.001
4	0.021	142.1	0.002
5(Tip)	0.019	134.1	0.015

$DPCP_{avg}$ = 0.015 $p_{t,2}/p_{t,\infty}$ = 0.986

W_{2C}/A_i = 33.27 lb/sec-ft^2, A_0/A_C = 0.815

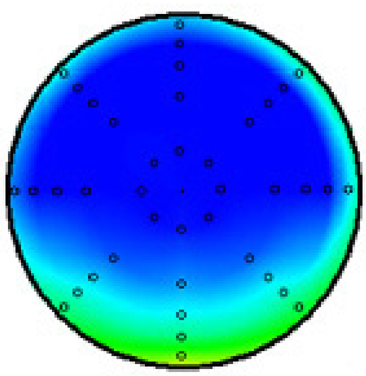

Ring	Intensity	Extent	DPRP
1(Hub)	0.001	73.1	-0.012
2	0.007	137.3	-0.008
3	0.013	143.2	-0.003
4	0.019	143.1	0.001
5(Tip)	0.018	133.9	0.021

$DPCP_{avg}$ = 0.012 $p_{t,2}/p_{t,\infty}$ = 0.988

W_{2C}/A_i = 35.27 lb/sec-ft^2, A_0/A_C = 0.875

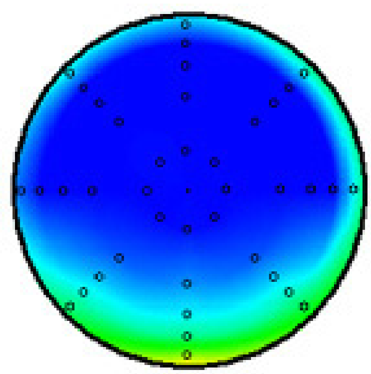

Ring	Intensity	Extent	DPRP
1(Hub)	0.000	67.5	-0.012
2	0.006	137.5	-0.008
3	0.012	143.0	-0.003
4	0.018	143.6	0.001
5(Tip)	0.019	135.6	0.022

$DPCP_{avg}$ = 0.011 $p_{t,2}/p_{t,\infty}$ = 0.988

(b) M = 0.402, Re/FT = 51.09 x 10^6.

Figure 21. - Continued.

$W_{2C}/A_i = 20.28$ lb/sec-ft^2, $A_0/A_C = 0.370$

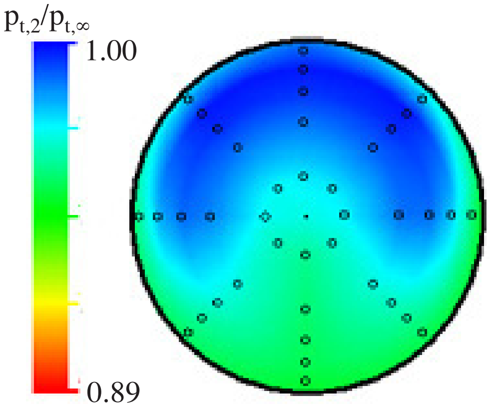

Ring	Intensity	Extent	DPRP
1(Hub)	0.005	148.1	0.005
2	0.013	142.0	-0.004
3	0.016	151.2	-0.007
4	0.015	177.9	-0.003
5(Tip)	0.010	209.7	0.009

$DPCP_{avg} = 0.012$ $p_{t,2}/p_{t,\infty} = 0.975$

$W_{2C}/A_i = 29.35$ lb/sec-ft^2, $A_0/A_C = 0.534$

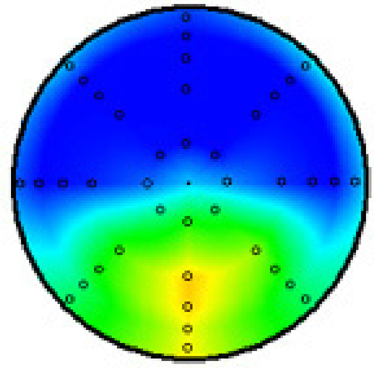

Ring	Intensity	Extent	DPRP
1(Hub)	0.021	155.4	-0.004
2	0.039	144.2	0.004
3	0.037	140.6	0.000
4	0.032	136.8	-0.004
5(Tip)	0.027	131.5	0.004

$DPCP_{avg} = 0.031$ $p_{t,2}/p_{t,\infty} = 0.975$

$W_{2C}/A_i = 33.41$ lb/sec-ft^2, $A_0/A_C = 0.609$

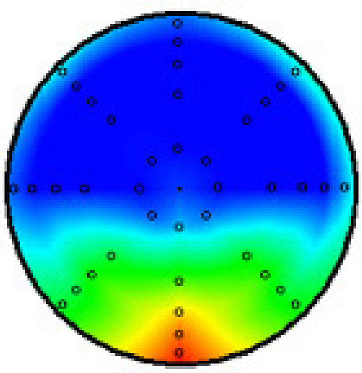

Ring	Intensity	Extent	DPRP
1(Hub)	0.008	133.0	-0.018
2	0.029	143.0	-0.002
3	0.037	140.4	0.003
4	0.038	134.8	0.002
5(Tip)	0.033	126.9	0.014

$DPCP_{avg} = 0.029$ $p_{t,2}/p_{t,\infty} = 0.978$

$W_{2C}/A_i = 35.92$ lb/sec-ft^2, $A_0/A_C = 0.658$

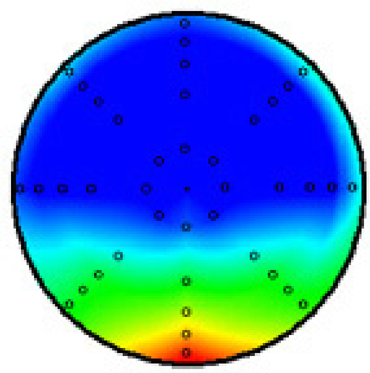

Ring	Intensity	Extent	DPRP
1(Hub)	0.005	125.4	-0.019
2	0.024	139.9	-0.006
3	0.034	141.2	0.002
4	0.038	139.0	0.004
5(Tip)	0.036	130.9	0.019

$DPCP_{avg} = 0.027$ $p_{t,2}/p_{t,\infty} = 0.982$

(c) M = 0.606, Re/FT = 67.67 x 10^6.

Figure 21. - Continued.

$W_{2C}/A_i = 20.25$ lb/sec-ft^2, $A_0/A_C = 0.317$

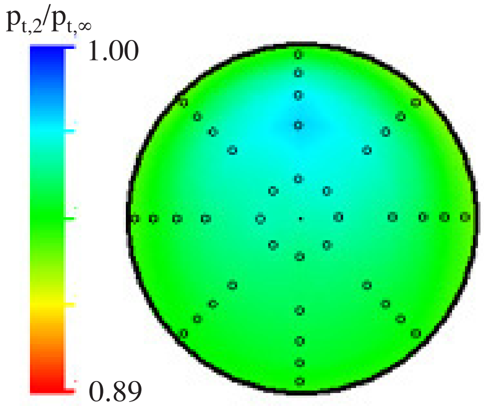

Ring	Intensity	Extent	DPRP
1(Hub)	0.004	165.9	-0.010
2	0.006	207.0	-0.007
3	0.006	218.9	-0.002
4	0.003	253.1	0.005
5(Tip)	0.004	97.1	0.015

$DPCP_{avg} = 0.005$ $p_{t,2}/p_{t,\infty} = 0.955$

$W_{2C}/A_i = 29.43$ lb/sec-ft^2, $A_0/A_C = 0.463$

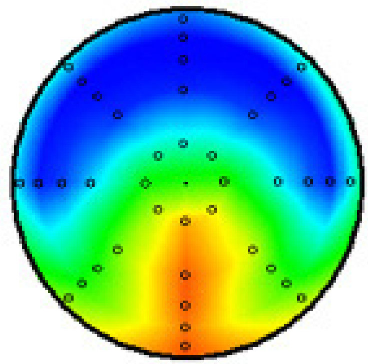

Ring	Intensity	Extent	DPRP
1(Hub)	0.019	174.1	0.021
2	0.037	153.9	-0.001
3	0.039	142.7	-0.010
4	0.040	140.1	-0.013
5(Tip)	0.033	143.6	0.003

$DPCP_{avg} = 0.034$ $p_{t,2}/p_{t,\infty} = 0.960$

$W_{2C}/A_i = 33.46$ lb/sec-ft^2, $A_0/A_C = 0.526$

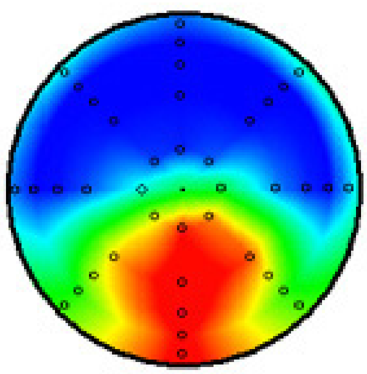

Ring	Intensity	Extent	DPRP
1(Hub)	0.038	167.3	0.009
2	0.054	146.9	0.003
3	0.051	140.6	-0.004
4	0.045	135.6	-0.011
5(Tip)	0.038	131.1	0.002

$DPCP_{avg} = 0.045$ $p_{t,2}/p_{t,\infty} = 0.961$

$W_{2C}/A_i = 36.23$ lb/sec-ft^2, $A_0/A_C = 0.571$

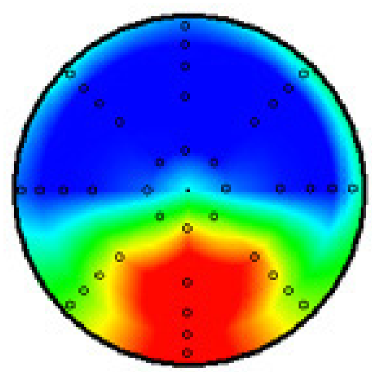

Ring	Intensity	Extent	DPRP
1(Hub)	0.035	147.7	-0.008
2	0.061	141.0	0.004
3	0.057	138.4	0.001
4	0.050	136.0	-0.005
5(Tip)	0.041	131.6	0.008

$DPCP_{avg} = 0.049$ $p_{t,2}/p_{t,\infty} = 0.963$

(d) $M = 0.804$, $Re/FT = 68.20 \times 10^6$.

Figure 21. - Continued.

W_{2C}/A_i = 20.29 lb/sec-ft^2, A_0/A_C = 0.313

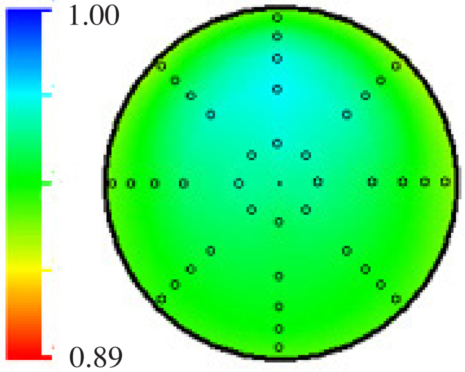

Ring	Intensity	Extent	DPRP
1(Hub)	0.004	174.4	-0.011
2	0.006	206.3	-0.008
3	0.006	222.6	-0.002
4	0.003	255.4	0.006
5(Tip)	0.004	96.9	0.015

$DPCP_{avg}$ = 0.004 $p_{t,2}/p_{t,\infty}$ = 0.951

W_{2C}/A_i = 29.43 lb/sec-ft^2, A_0/A_C = 0.457

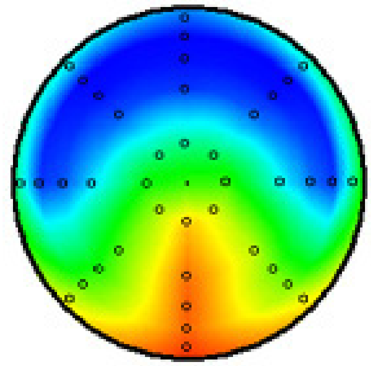

Ring	Intensity	Extent	DPRP
1(Hub)	0.017	169.5	0.019
2	0.034	152.5	-0.003
3	0.039	144.0	-0.011
4	0.041	142.9	-0.012
5(Tip)	0.033	153.0	0.008

$DPCP_{avg}$ = 0.033 $p_{t,2}/p_{t,\infty}$ = 0.958

W_{2C}/A_i = 33.47 lb/sec-ft^2, A_0/A_C = 0.521

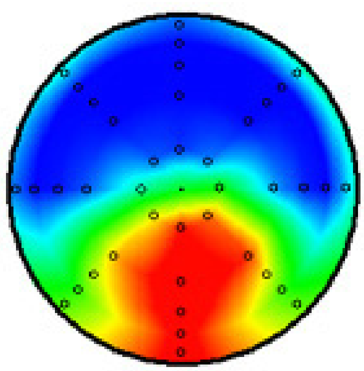

Ring	Intensity	Extent	DPRP
1(Hub)	0.037	171.7	0.012
2	0.055	147.6	0.003
3	0.051	140.5	-0.005
4	0.046	135.8	-0.012
5(Tip)	0.038	132.0	0.002

$DPCP_{avg}$ = 0.045 $p_{t,2}/p_{t,\infty}$ = 0.960

W_{2C}/A_i = 36.63 lb/sec-ft^2, A_0/A_C = 0.570

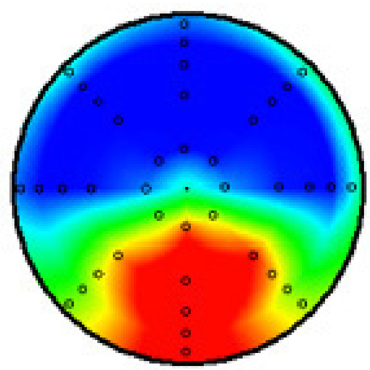

Ring	Intensity	Extent	DPRP
1(Hub)	0.039	149.1	-0.006
2	0.064	141.3	0.004
3	0.059	138.8	0.000
4	0.052	135.8	-0.006
5(Tip)	0.043	132.1	0.008

$DPCP_{avg}$ = 0.051 $p_{t,2}/p_{t,\infty}$ = 0.960

(e) M = 0.831, Re/FT = 68.05 x 10^6.

Figure 21. - Continued.

Re/FT = 24.97 x 10^6, $T_{t,\infty}$ = 260.9 °R

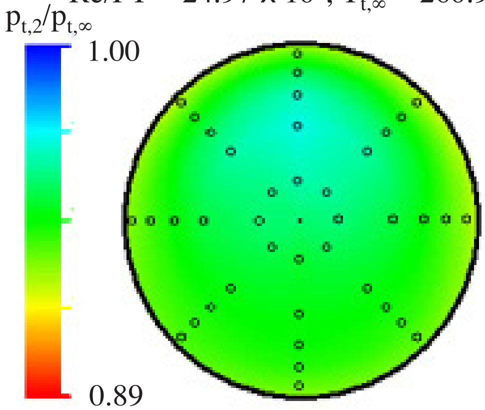

Ring	Intensity	Extent	DPRP
1(Hub)	0.004	177.2	-0.011
2	0.006	206.6	-0.008
3	0.005	222.1	-0.002
4	0.003	255.0	0.005
5(Tip)	0.003	97.7	0.016

$DPCP_{avg}$ = 0.004 $p_{t,2}/p_{t,\infty}$ = 0.947

Re/FT = 41.87 x 10^6, $T_{t,\infty}$ = 261.3 °R

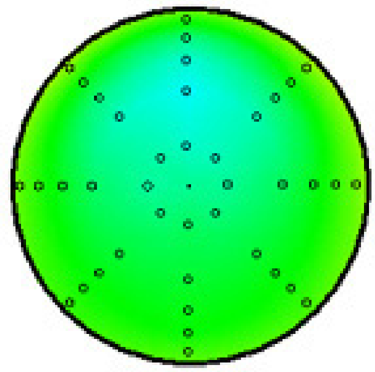

Ring	Intensity	Extent	DPRP
1(Hub)	0.003	171.6	-0.011
2	0.006	205.9	-0.008
3	0.005	222.1	-0.002
4	0.003	256.7	0.006
5(Tip)	0.003	95.0	0.015

$DPCP_{avg}$ = 0.004 $p_{t,2}/p_{t,\infty}$ = 0.950

Re/FT = 41.29 x 10^6, $T_{t,\infty}$ = 180.9 °R

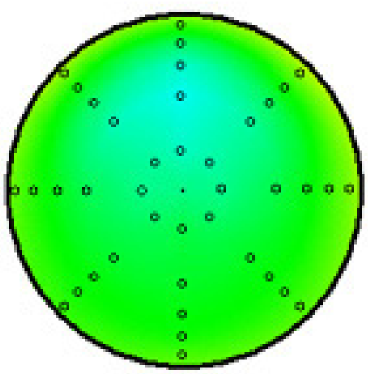

Ring	Intensity	Extent	DPRP
1(Hub)	0.004	165.9	-0.011
2	0.006	209.4	-0.008
3	0.005	224.5	-0.002
4	0.002	255.4	0.006
5(Tip)	0.004	101.9	0.015

$DPCP_{avg}$ = 0.004 $p_{t,2}/p_{t,\infty}$ = 0.949

Re/FT = 68.17 x 10^6, $T_{t,\infty}$ = 179.9 °R

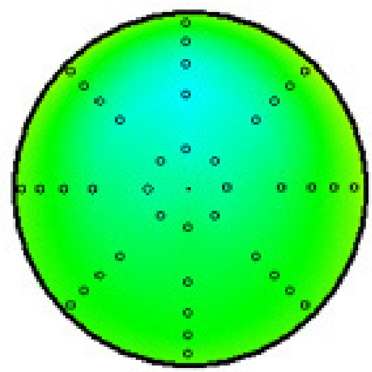

Ring	Intensity	Extent	DPRP
1(Hub)	0.004	174.4	-0.011
2	0.006	206.3	-0.008
3	0.006	222.6	-0.002
4	0.003	255.4	0.006
5(Tip)	0.004	96.9	0.015

$DPCP_{avg}$ = 0.004 $p_{t,2}/p_{t,\infty}$ = 0.951

(f) M = 0.830, W_{2C}/A_i = 20.37 lb/sec-ft^2 (A_0/A_C = 0.314).

Figure 21. - Continued.

Re/FT = 25.54 x 10^6, $T_{t,\infty}$ = 260.4 °R

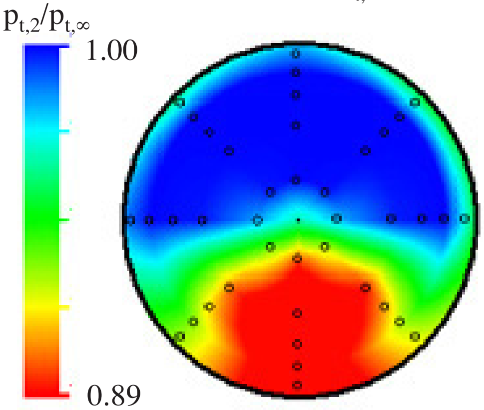

Ring	Intensity	Extent	DPRP
1(Hub)	0.039	150.9	-0.006
2	0.066	141.8	0.004
3	0.061	139.2	-0.001
4	0.054	135.9	-0.007
5(Tip)	0.044	131.1	0.010

$DPCP_{avg}$ = 0.053 $p_{t,2}/p_{t,\infty}$ = 0.958

Re/FT = 41.69 x 10^6, $T_{t,\infty}$ = 259.7 °R

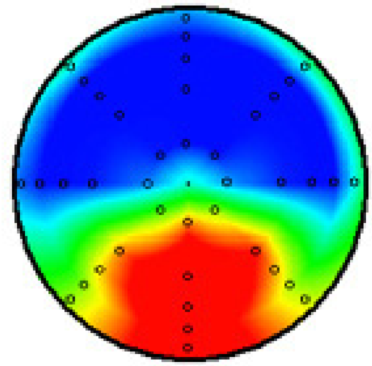

Ring	Intensity	Extent	DPRP
1(Hub)	0.038	148.8	-0.008
2	0.065	141.2	0.004
3	0.062	138.5	0.000
4	0.054	135.6	-0.006
5(Tip)	0.045	131.4	0.010

$DPCP_{avg}$ = 0.053 $p_{t,2}/p_{t,\infty}$ = 0.959

Re/FT = 42.39 x 10^6, $T_{t,\infty}$ = 180.1 °R

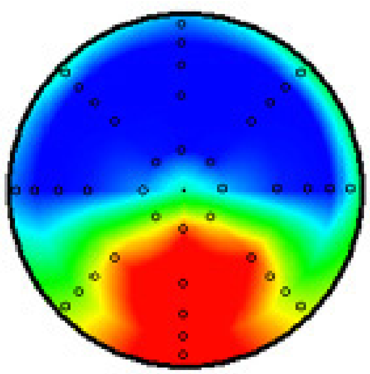

Ring	Intensity	Extent	DPRP
1(Hub)	0.040	151.0	-0.004
2	0.064	141.9	0.004
3	0.059	138.9	-0.001
4	0.052	135.9	-0.007
5(Tip)	0.043	132.1	0.009

$DPCP_{avg}$ = 0.052 $p_{t,2}/p_{t,\infty}$ = 0.959

Re/FT = 68.05 x 10^6, $T_{t,\infty}$ = 179.9 °R

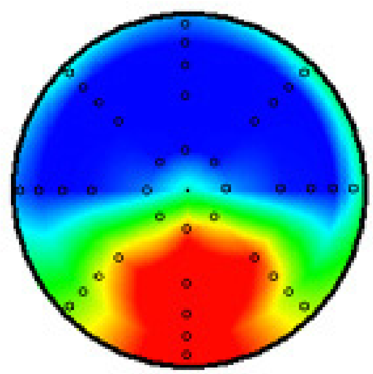

Ring	Intensity	Extent	DPRP
1(Hub)	0.039	149.1	-0.006
2	0.064	141.3	0.004
3	0.059	138.8	0.000
4	0.052	135.8	-0.006
5(Tip)	0.043	132.1	0.008

$DPCP_{avg}$ = 0.051 $p_{t,2}/p_{t,\infty}$ = 0.960

(g) M = 0.832, W_{2C}/A_i = 36.85 lb/sec-ft^2 (A_0/A_C = 0.573).

Figure 21. - Concluded.

W_{2C}/A_i = 19.82 lb/sec-ft^2, A_0/A_C = 0.734

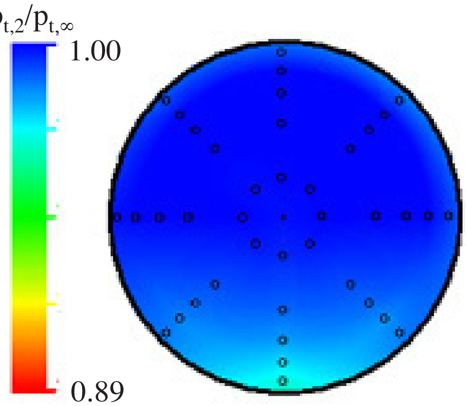

Ring	Intensity	Extent	DPRP
1(Hub)	0.001	129.4	-0.004
2	0.005	142.0	-0.002
3	0.007	140.1	-0.001
4	0.010	138.8	0.001
5(Tip)	0.009	109.1	0.006

$DPCP_{avg}$ = 0.006 $p_{t,2}/p_{t,\infty}$ = 0.995

W_{2C}/A_i = 28.81 lb/sec-ft^2, A_0/A_C = 1.059

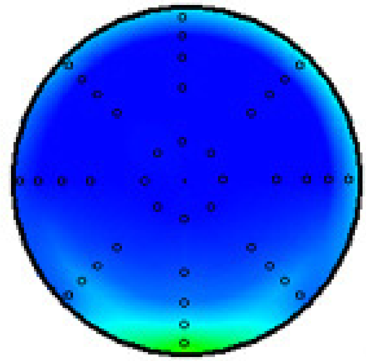

Ring	Intensity	Extent	DPRP
1(Hub)	0.000	67.5	-0.006
2	0.003	139.5	-0.004
3	0.006	142.9	-0.003
4	0.011	139.5	0.001
5(Tip)	0.017	75.2	0.012

$DPCP_{avg}$ = 0.008 $p_{t,2}/p_{t,\infty}$ = 0.993

W_{2C}/A_i = 32.36 lb/sec-ft^2, A_0/A_C = 1.195

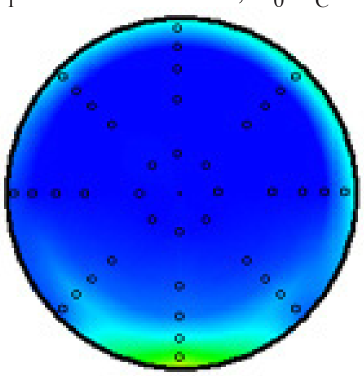

Ring	Intensity	Extent	DPRP
1(Hub)	0.000	67.5	-0.007
2	0.003	137.0	-0.005
3	0.006	142.0	-0.004
4	0.012	139.6	0.001
5(Tip)	0.021	70.5	0.015

$DPCP_{avg}$ = 0.009 $p_{t,2}/p_{t,\infty}$ = 0.992

W_{2C}/A_i = 33.49 lb/sec-ft^2, A_0/A_C = 1.217

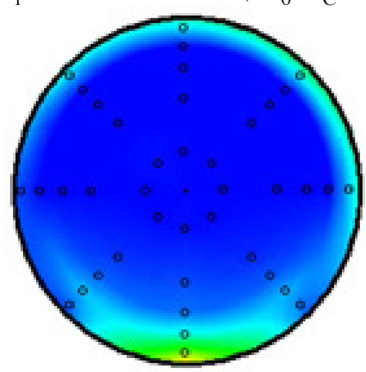

Ring	Intensity	Extent	DPRP
1(Hub)	0.000	67.5	-0.007
2	0.003	137.0	-0.005
3	0.005	143.2	-0.004
4	0.013	140.0	0.001
5(Tip)	0.022	68.7	0.015

$DPCP_{avg}$ = 0.009 $p_{t,2}/p_{t,\infty}$ = 0.992

(a) M = 0.252, Re/FT = 33.33 x 10^6.

Figure 22. - Pressure recovery and distortion results for inlet C.

$W_{2C}/A_i = 19.91$ lb/sec-ft^2, $A_0/A_C = 0.479$

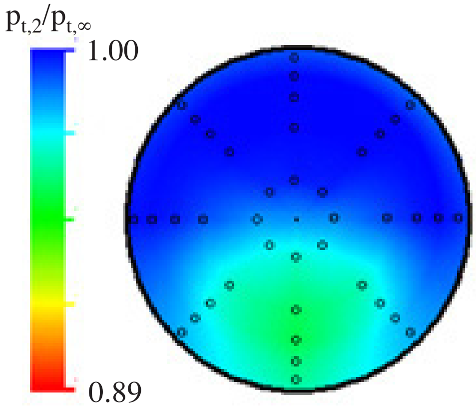

Ring	Intensity	Extent	DPRP
1(Hub)	0.010	176.9	0.002
2	0.018	151.3	0.002
3	0.018	141.7	0.000
4	0.016	136.5	-0.003
5(Tip)	0.013	125.9	-0.001

$DPCP_{avg} = 0.015$ $p_{t,2}/p_{t,\infty} = 0.986$

$W_{2C}/A_i = 28.83$ lb/sec-ft^2, $A_0/A_C = 0.694$

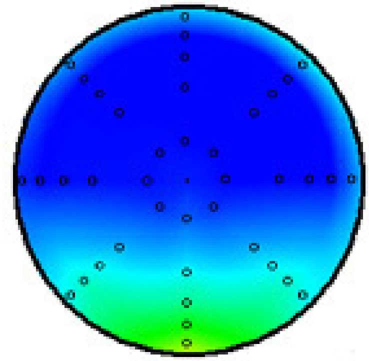

Ring	Intensity	Extent	DPRP
1(Hub)	0.004	135.6	-0.010
2	0.012	141.7	-0.004
3	0.017	141.4	-0.001
4	0.022	138.8	0.003
5(Tip)	0.021	113.5	0.012

$DPCP_{avg} = 0.015$ $p_{t,2}/p_{t,\infty} = 0.988$

$W_{2C}/A_i = 32.76$ lb/sec-ft^2, $A_0/A_C = 0.795$

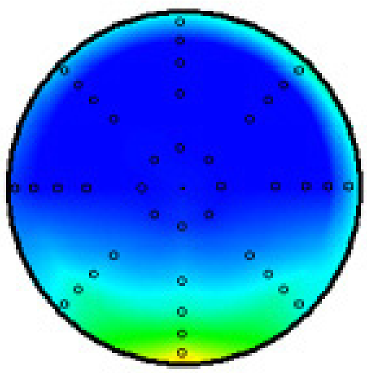

Ring	Intensity	Extent	DPRP
1(Hub)	0.002	123.8	-0.011
2	0.010	140.0	-0.006
3	0.015	141.3	-0.002
4	0.023	139.2	0.003
5(Tip)	0.025	100.8	0.016

$DPCP_{avg} = 0.015$ $p_{t,2}/p_{t,\infty} = 0.987$

$W_{2C}/A_i = 33.90$ lb/sec-ft^2, $A_0/A_C = 0.811$

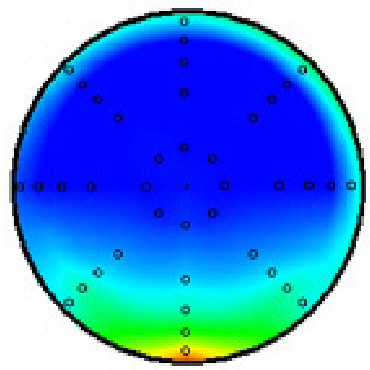

Ring	Intensity	Extent	DPRP
1(Hub)	0.002	118.1	-0.012
2	0.010	140.8	-0.007
3	0.015	141.3	-0.003
4	0.024	139.6	0.003
5(Tip)	0.029	89.2	0.019

$DPCP_{avg} = 0.016$ $p_{t,2}/p_{t,\infty} = 0.986$

(b) M = 0.400, Re/FT = 50.50 x 10^6.

Figure 22. - Continued.

W_{2C}/A_i = 19.87 lb/sec-ft^2, A_0/A_C = 0.351

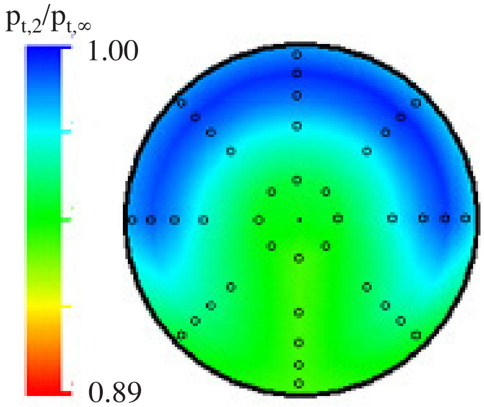

Ring	Intensity	Extent	DPRP
1(Hub)	0.005	155.6	0.021
2	0.013	141.2	0.003
3	0.019	141.1	-0.008
4	0.023	143.4	-0.012
5(Tip)	0.021	144.9	-0.004

$DPCP_{avg}$ = 0.016 $p_{t,2}/p_{t,\infty}$ = 0.966

W_{2C}/A_i = 28.99 lb/sec-ft^2, A_0/A_C = 0.514

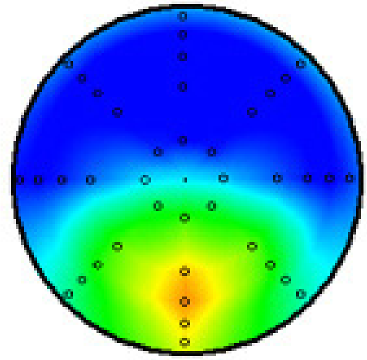

Ring	Intensity	Extent	DPRP
1(Hub)	0.021	170.0	0.001
2	0.038	149.4	0.004
3	0.039	141.6	0.001
4	0.035	136.1	-0.005
5(Tip)	0.028	124.0	-0.001

$DPCP_{avg}$ = 0.032 $p_{t,2}/p_{t,\infty}$ = 0.975

W_{2C}/A_i = 32.87 lb/sec-ft^2, A_0/A_C = 0.583

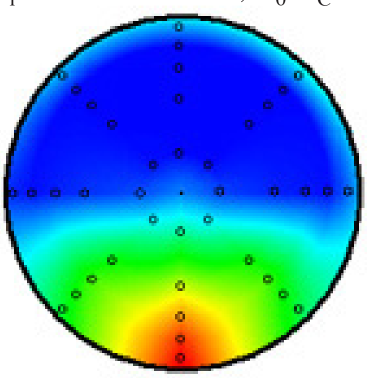

Ring	Intensity	Extent	DPRP
1(Hub)	0.015	151.9	-0.012
2	0.033	144.0	-0.001
3	0.039	141.6	0.002
4	0.041	136.6	0.002
5(Tip)	0.037	120.4	0.009

$DPCP_{avg}$ = 0.033 $p_{t,2}/p_{t,\infty}$ = 0.974

W_{2C}/A_i = 34.62 lb/sec-ft^2, A_0/A_C = 0.613

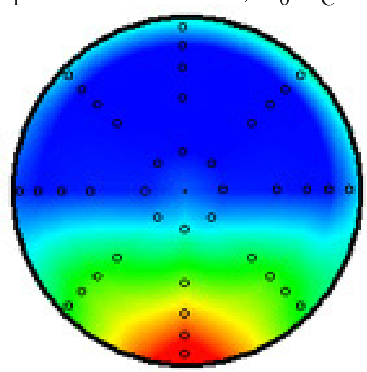

Ring	Intensity	Extent	DPRP
1(Hub)	0.012	144.5	-0.016
2	0.030	143.0	-0.004
3	0.039	141.2	0.002
4	0.043	138.1	0.004
5(Tip)	0.040	117.6	0.015

$DPCP_{avg}$ = 0.032 $p_{t,2}/p_{t,\infty}$ = 0.975

(c) M = 0.601, Re/FT = 67.90 x 10^6.

Figure 22. - Continued.

W_{2C}/A_i = 19.89 lb/sec-ft^2, A_0/A_C = 0.297

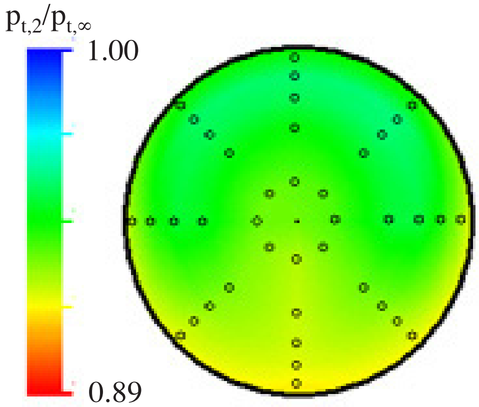

Ring	Intensity	Extent	DPRP
1(Hub)	0.004	133.9	0.006
2	0.011	136.5	-0.004
3	0.014	149.5	-0.006
4	0.014	176.5	-0.003
5(Tip)	0.010	198.8	0.007

$DPCP_{avg}$ = 0.011 $p_{t,2}/p_{t,\infty}$ = 0.938

W_{2C}/A_i = 29.00 lb/sec-ft^2, A_0/A_C = 0.438

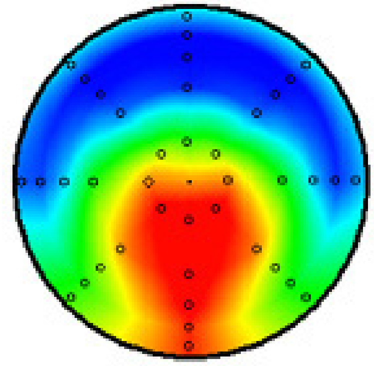

Ring	Intensity	Extent	DPRP
1(Hub)	0.020	189.2	0.046
2	0.037	180.3	0.005
3	0.041	151.1	-0.014
4	0.040	138.7	-0.023
5(Tip)	0.035	130.0	-0.013

$DPCP_{avg}$ = 0.035 $p_{t,2}/p_{t,\infty}$ = 0.949

W_{2C}/A_i = 33.01 lb/sec-ft^2, A_0/A_C = 0.500

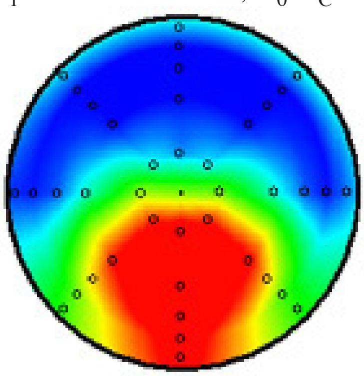

Ring	Intensity	Extent	DPRP
1(Hub)	0.036	181.5	0.023
2	0.058	156.2	0.007
3	0.055	143.1	-0.006
4	0.048	136.3	-0.016
5(Tip)	0.040	124.6	-0.008

$DPCP_{avg}$ = 0.048 $p_{t,2}/p_{t,\infty}$ = 0.953

W_{2C}/A_i = 35.13 lb/sec-ft^2, A_0/A_C = 0.534

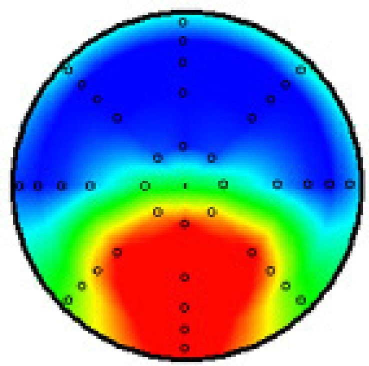

Ring	Intensity	Extent	DPRP
1(Hub)	0.038	171.9	0.006
2	0.064	148.6	0.007
3	0.063	140.4	-0.001
4	0.054	134.9	-0.010
5(Tip)	0.044	122.7	-0.002

$DPCP_{avg}$ = 0.053 $p_{t,2}/p_{t,\infty}$ = 0.955

(d) M = 0.802, Re/FT = 68.15 x 10^6.

Figure 22. - Continued.

W_{2C}/A_i = 19.87 lb/sec-ft^2, A_0/A_C = 0.292

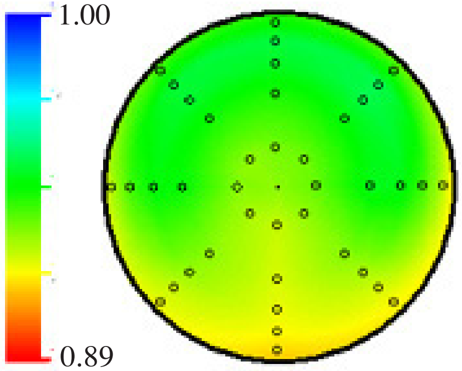

Ring	Intensity	Extent	DPRP
1(Hub)	0.004	133.9	0.005
2	0.010	136.3	-0.004
3	0.013	148.8	-0.006
4	0.013	174.1	-0.002
5(Tip)	0.009	200.1	0.007

$DPCP_{avg}$ = 0.010 $p_{t,2}/p_{t,\infty}$ = 0.934

W_{2C}/A_i = 28.95 lb/sec-ft^2, A_0/A_C = 0.431

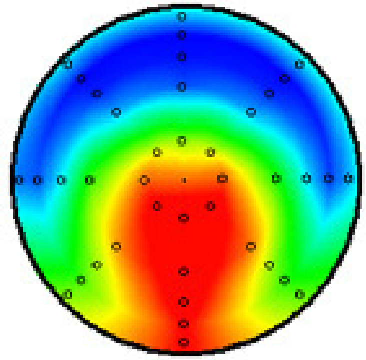

Ring	Intensity	Extent	DPRP
1(Hub)	0.018	187.2	0.047
2	0.036	177.8	0.005
3	0.041	152.2	-0.015
4	0.042	140.2	-0.025
5(Tip)	0.037	133.4	-0.013

$DPCP_{avg}$ = 0.035 $p_{t,2}/p_{t,\infty}$ = 0.945

W_{2C}/A_i = 33.40 lb/sec-ft^2, A_0/A_C = 0.499

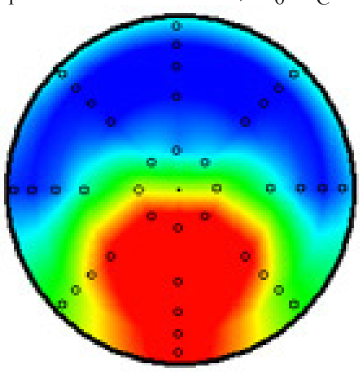

Ring	Intensity	Extent	DPRP
1(Hub)	0.038	183.2	0.027
2	0.060	157.5	0.008
3	0.058	143.2	-0.007
4	0.051	136.2	-0.018
5(Tip)	0.042	123.9	-0.009

$DPCP_{avg}$ = 0.050 $p_{t,2}/p_{t,\infty}$ = 0.950

W_{2C}/A_i = 35.55 lb/sec-ft^2, A_0/A_C = 0.533

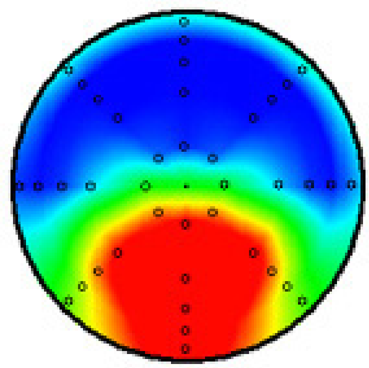

Ring	Intensity	Extent	DPRP
1(Hub)	0.040	174.7	0.010
2	0.067	149.4	0.008
3	0.066	140.8	-0.002
4	0.056	135.5	-0.012
5(Tip)	0.045	122.8	-0.003

$DPCP_{avg}$ = 0.055 $p_{t,2}/p_{t,\infty}$ = 0.952

(e) M = 0.832, Re/FT = 68.22 x 10^6.

Figure 22. - Continued.

Re/FT = 25.07 x 10^6, $T_{t,\infty}$ = 260.4 °R

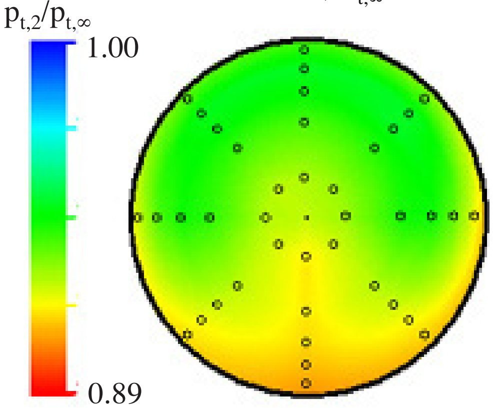

Ring	Intensity	Extent	DPRP
1(Hub)	0.004	131.7	0.006
2	0.011	134.6	-0.004
3	0.014	147.3	-0.006
4	0.014	169.8	-0.003
5(Tip)	0.010	196.4	0.007

$DPCP_{avg}$ = 0.011 $p_{t,2}/p_{t,\infty}$ = 0.930

Re/FT = 42.06 x 10^6, $T_{t,\infty}$ = 260.5 °R

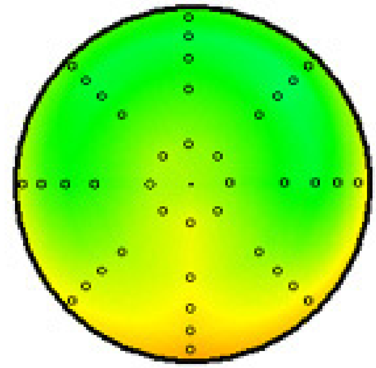

Ring	Intensity	Extent	DPRP
1(Hub)	0.003	173.0	0.006
2	0.011	135.4	-0.003
3	0.015	146.9	-0.006
4	0.015	168.8	-0.003
5(Tip)	0.010	194.6	0.007

$DPCP_{avg}$ = 0.011 $p_{t,2}/p_{t,\infty}$ = 0.933

Re/FT = 42.06 x 10^6, $T_{t,\infty}$ = 180.5 °R

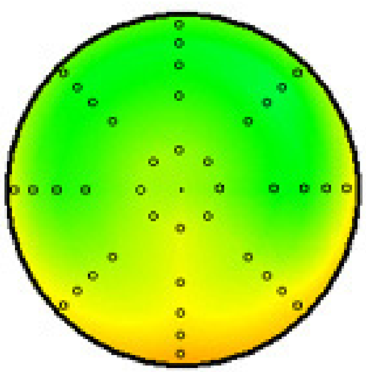

Ring	Intensity	Extent	DPRP
1(Hub)	0.003	187.5	0.004
2	0.010	140.0	-0.004
3	0.014	150.9	-0.006
4	0.013	174.1	-0.002
5(Tip)	0.010	196.7	0.007

$DPCP_{avg}$ = 0.010 $p_{t,2}/p_{t,\infty}$ = 0.931

Re/FT = 68.50 x 10^6, $T_{t,\infty}$ = 181.0 °R

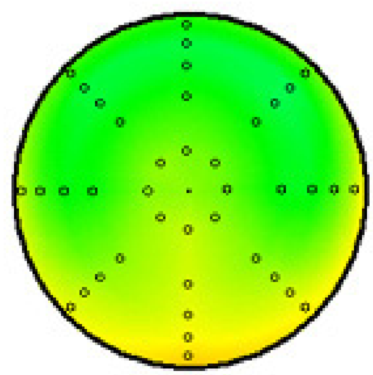

Ring	Intensity	Extent	DPRP
1(Hub)	0.004	133.9	0.005
2	0.010	136.3	-0.004
3	0.013	148.8	-0.006
4	0.013	174.1	-0.002
5(Tip)	0.009	200.1	0.007

$DPCP_{avg}$ = 0.010 $p_{t,2}/p_{t,\infty}$ = 0.934

(f) M = 0.832, W_{2C}/A_i = 19.96 lbm/sec-ft^2 (A_0/A_C = 0.293).

Figure 22. - Continued.

Re/FT = 25.10 x 10^6, $T_{t,\infty}$ = 259.7 °R

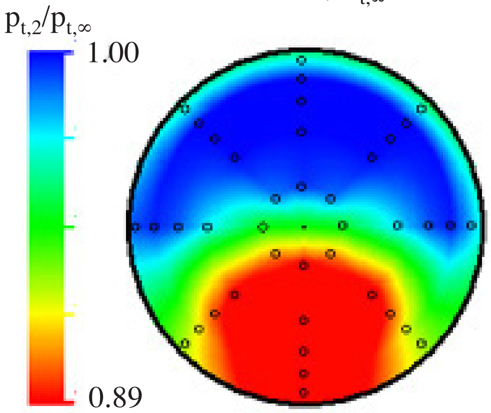

Ring	Intensity	Extent	DPRP
1(Hub)	0.039	174.2	0.006
2	0.066	150.5	0.006
3	0.069	141.4	-0.002
4	0.062	135.9	-0.011
5(Tip)	0.048	122.9	0.001

$DPCP_{avg}$ = 0.057 $p_{t,2}/p_{t,\infty}$ = 0.949

Re/FT = 41.76 x 10^6, $T_{t,\infty}$ = 260.1 °R

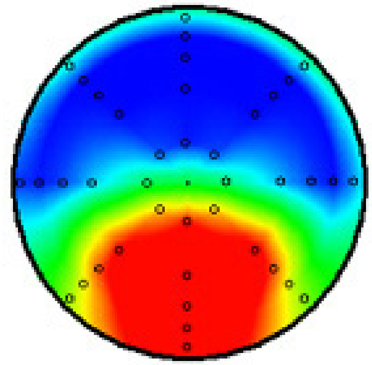

Ring	Intensity	Extent	DPRP
1(Hub)	0.037	170.6	0.002
2	0.066	148.8	0.006
3	0.068	140.9	0.000
4	0.062	135.2	-0.009
5(Tip)	0.049	122.4	0.001

$DPCP_{avg}$ = 0.056 $p_{t,2}/p_{t,\infty}$ = 0.952

Re/FT = 42.22 x 10^6, $T_{t,\infty}$ = 180.4 °R

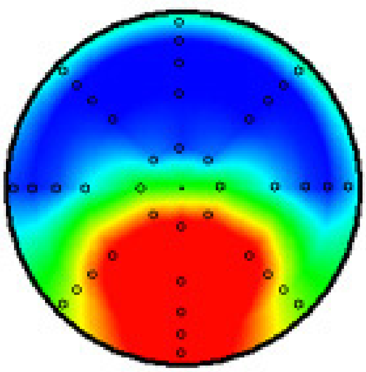

Ring	Intensity	Extent	DPRP
1(Hub)	0.040	176.0	0.011
2	0.067	150.6	0.007
3	0.067	141.0	-0.003
4	0.058	135.8	-0.013
5(Tip)	0.047	122.8	-0.002

$DPCP_{avg}$ = 0.056 $p_{t,2}/p_{t,\infty}$ = 0.950

Re/FT = 67.99 x 10^6, $T_{t,\infty}$ = 180.6 °R

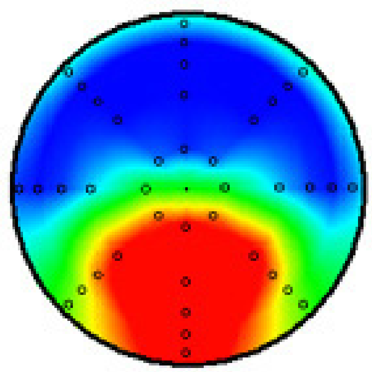

Ring	Intensity	Extent	DPRP
1(Hub)	0.040	174.7	0.010
2	0.067	149.4	0.008
3	0.066	140.8	-0.002
4	0.056	135.5	-0.012
5(Tip)	0.045	122.8	-0.003

$DPCP_{avg}$ = 0.055 $p_{t,2}/p_{t,\infty}$ = 0.952

(g) M = 0.829, W_{2C}/A_i = 36.20 lbm/sec-ft^2 (A_0/A_C = 0.543).

Figure 22. - Concluded.

W_{2C}/A_i = 19.79 lb/sec-ft^2, A_0/A_C = 0.770

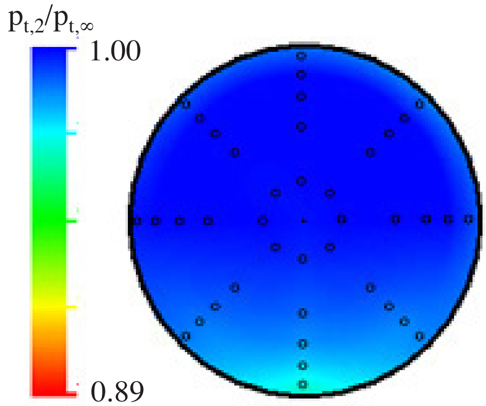

Ring	Intensity	Extent	DPRP
1(Hub)	0.001	129.4	-0.004
2	0.005	139.8	-0.002
3	0.007	140.3	-0.001
4	0.009	138.3	0.001
5(Tip)	0.009	112.0	0.006

$DPCP_{avg}$ = 0.006 $p_{t,2}/p_{t,\infty}$ = 0.995

W_{2C}/A_i = 28.90 lb/sec-ft^2, A_0/A_C = 1.107

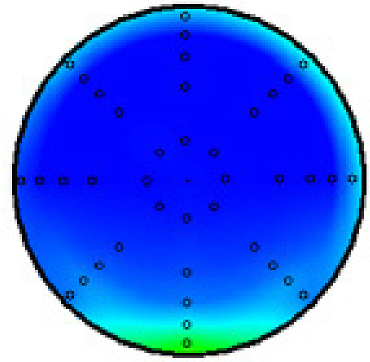

Ring	Intensity	Extent	DPRP
1(Hub)	0.001	123.8	-0.006
2	0.003	139.5	-0.005
3	0.006	142.0	-0.003
4	0.011	137.1	0.001
5(Tip)	0.017	75.5	0.013

$DPCP_{avg}$ = 0.007 $p_{t,2}/p_{t,\infty}$ = 0.993

W_{2C}/A_i = 32.28 lb/sec-ft^2, A_0/A_C = 1.245

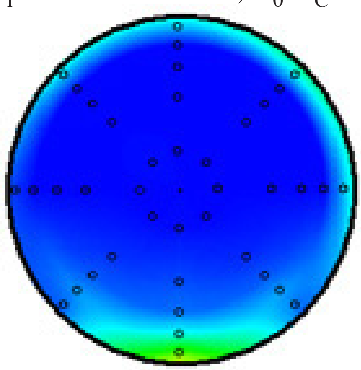

Ring	Intensity	Extent	DPRP
1(Hub)	0.000	67.5	-0.007
2	0.003	137.0	-0.005
3	0.005	142.5	-0.004
4	0.012	137.0	0.000
5(Tip)	0.021	69.6	0.016

$DPCP_{avg}$ = 0.008 $p_{t,2}/p_{t,\infty}$ = 0.993

W_{2C}/A_i = 32.89 lb/sec-ft^2, A_0/A_C = 1.254

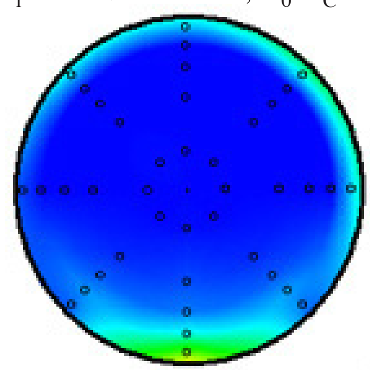

Ring	Intensity	Extent	DPRP
1(Hub)	0.000	67.5	-0.008
2	0.003	135.0	-0.006
3	0.006	141.2	-0.004
4	0.012	137.0	0.000
5(Tip)	0.021	68.5	0.017

$DPCP_{avg}$ = 0.008 $p_{t,2}/p_{t,\infty}$ = 0.992

(a) M = 0.248, Re/FT = 33.47 x 10^6.

Figure 23. - Pressure recovery and distortion results for inlet D.

W_{2C}/A_i = 19.79 lb/sec-ft^2, A_0/A_C = 0.498

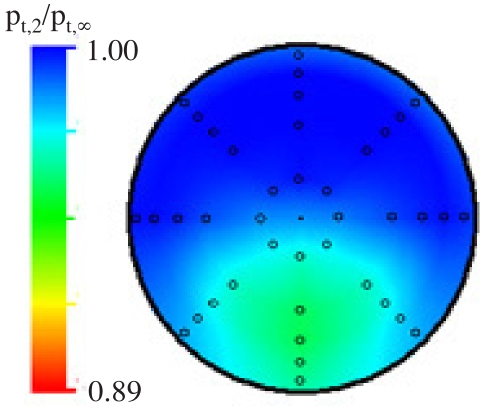

Ring	Intensity	Extent	DPRP
1(Hub)	0.010	172.3	0.002
2	0.018	150.9	0.002
3	0.018	142.8	0.000
4	0.016	137.1	-0.003
5(Tip)	0.013	124.4	-0.001

$DPCP_{avg}$ = 0.015 $p_{t,2}/p_{t,\infty}$ = 0.986

W_{2C}/A_i = 28.94 lb/sec-ft^2, A_0/A_C = 0.726

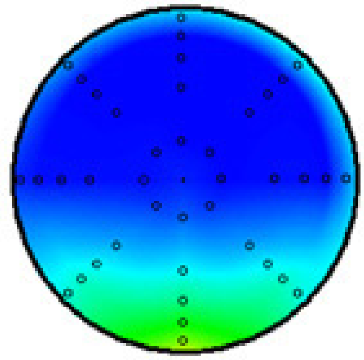

Ring	Intensity	Extent	DPRP
1(Hub)	0.004	137.2	-0.010
2	0.011	142.0	-0.004
3	0.017	141.5	-0.001
4	0.022	139.5	0.002
5(Tip)	0.021	117.2	0.013

$DPCP_{avg}$ = 0.015 $p_{t,2}/p_{t,\infty}$ = 0.987

W_{2C}/A_i = 32.78 lb/sec-ft^2, A_0/A_C = 0.823

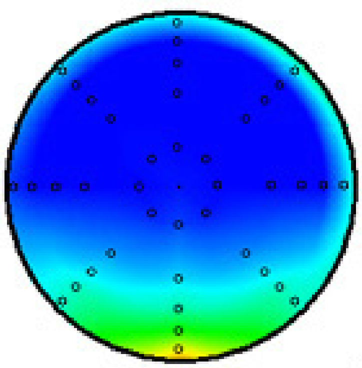

Ring	Intensity	Extent	DPRP
1(Hub)	0.003	119.1	-0.012
2	0.010	140.0	-0.006
3	0.016	140.8	-0.002
4	0.023	138.6	0.003
5(Tip)	0.024	107.4	0.018

$DPCP_{avg}$ = 0.015 $p_{t,2}/p_{t,\infty}$ = 0.987

W_{2C}/A_i = 34.05 lb/sec-ft^2, A_0/A_C = 0.851

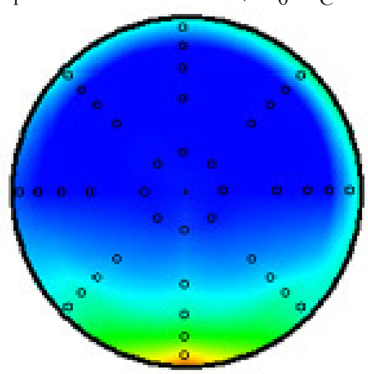

Ring	Intensity	Extent	DPRP
1(Hub)	0.003	119.1	-0.012
2	0.010	139.5	-0.007
3	0.015	140.2	-0.003
4	0.023	138.6	0.002
5(Tip)	0.026	99.1	0.019

$DPCP_{avg}$ = 0.015 $p_{t,2}/p_{t,\infty}$ = 0.987

(b) M = 0.401, Re/FT = 51.20 x 10^6.

Figure 23. - Continued.

$W_{2C}/A_i = 19.82$ lb/sec-ft^2, $A_0/A_C = 0.365$

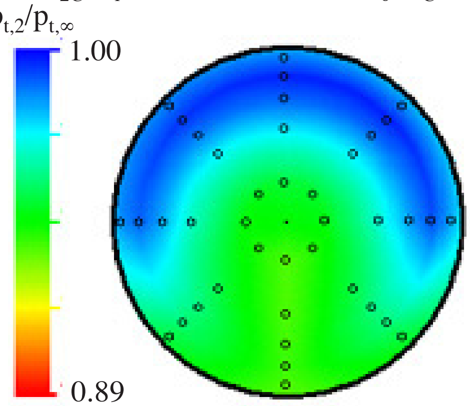

Ring	Intensity	Extent	DPRP
1(Hub)	0.005	162.7	0.022
2	0.013	149.0	0.004
3	0.019	145.6	-0.008
4	0.023	145.1	-0.013
5(Tip)	0.021	144.8	-0.005

$DPCP_{avg} = 0.016$ $p_{t,2}/p_{t,\infty} = 0.966$

$W_{2C}/A_i = 29.05$ lb/sec-ft^2, $A_0/A_C = 0.531$

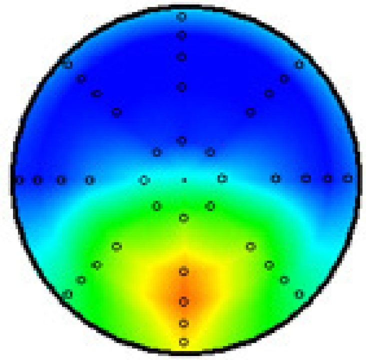

Ring	Intensity	Extent	DPRP
1(Hub)	0.022	172.1	0.003
2	0.039	150.6	0.004
3	0.040	141.8	0.000
4	0.035	136.2	-0.006
5(Tip)	0.029	125.2	-0.001

$DPCP_{avg} = 0.033$ $p_{t,2}/p_{t,\infty} = 0.971$

$W_{2C}/A_i = 32.95$ lb/sec-ft^2, $A_0/A_C = 0.610$

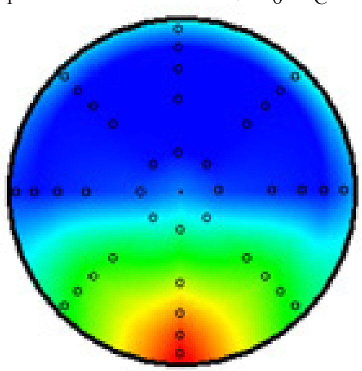

Ring	Intensity	Extent	DPRP
1(Hub)	0.014	152.3	-0.013
2	0.032	144.4	-0.001
3	0.039	141.6	0.002
4	0.041	137.2	0.002
5(Tip)	0.037	120.7	0.010

$DPCP_{avg} = 0.033$ $p_{t,2}/p_{t,\infty} = 0.974$

$W_{2C}/A_i = 35.22$ lb/sec-ft^2, $A_0/A_C = 0.644$

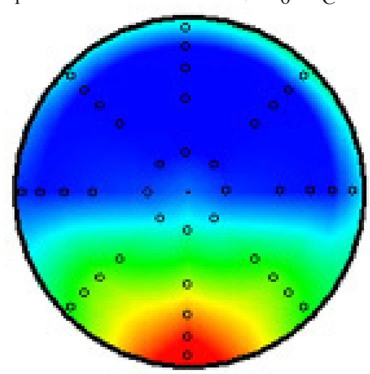

Ring	Intensity	Extent	DPRP
1(Hub)	0.013	150.2	-0.015
2	0.032	143.3	-0.004
3	0.041	141.8	0.002
4	0.044	138.6	0.003
5(Tip)	0.040	119.3	0.014

$DPCP_{avg} = 0.034$ $p_{t,2}/p_{t,\infty} = 0.973$

(c) M = 0.604, Re/FT = 67.80 x 10^6.

Figure 23. - Continued.

W_{2C}/A_i = 19.81 lb/sec-ft^2, A_0/A_C = 0.309

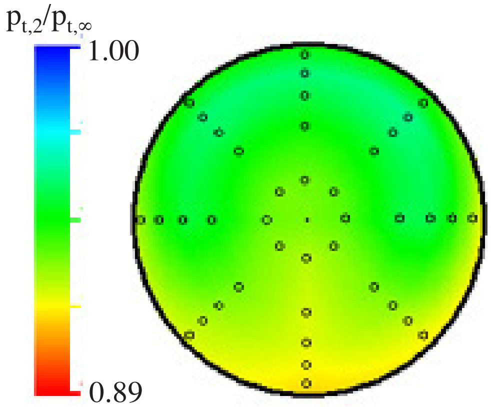

Ring	Intensity	Extent	DPRP
1(Hub)	0.004	131.7	0.006
2	0.012	132.7	-0.003
3	0.015	145.9	-0.006
4	0.015	172.5	-0.003
5(Tip)	0.011	197.3	0.007

$DPCP_{avg}$ = 0.011 $p_{t,2}/p_{t,\infty}$ = 0.938

W_{2C}/A_i = 29.11 lb/sec-ft^2, A_0/A_C = 0.457

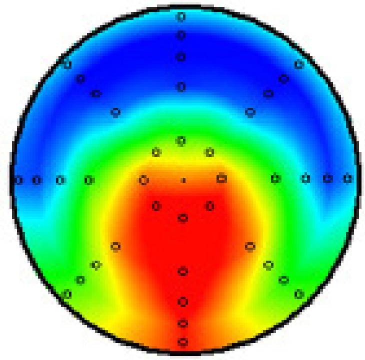

Ring	Intensity	Extent	DPRP
1(Hub)	0.019	190.8	0.047
2	0.038	180.1	0.005
3	0.041	152.1	-0.015
4	0.041	139.5	-0.024
5(Tip)	0.037	132.8	-0.013

$DPCP_{avg}$ = 0.035 $p_{t,2}/p_{t,\infty}$ = 0.947

W_{2C}/A_i = 33.06 lb/sec-ft^2, A_0/A_C = 0.520

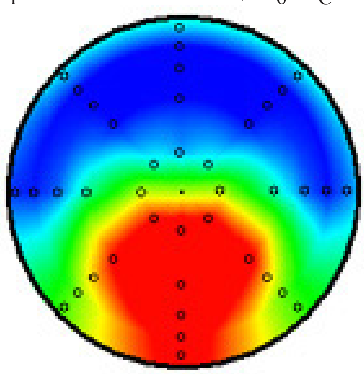

Ring	Intensity	Extent	DPRP
1(Hub)	0.037	183.6	0.026
2	0.058	158.1	0.007
3	0.056	143.4	-0.007
4	0.049	136.7	-0.017
5(Tip)	0.042	125.8	-0.009

$DPCP_{avg}$ = 0.048 $p_{t,2}/p_{t,\infty}$ = 0.951

W_{2C}/A_i = 35.79 lb/sec-ft^2, A_0/A_C = 0.567

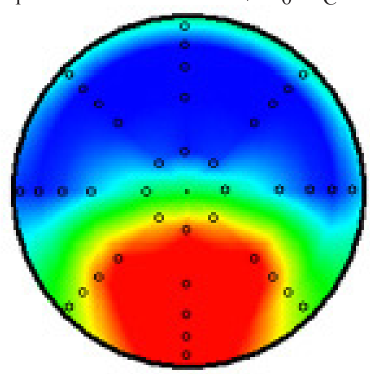

Ring	Intensity	Extent	DPRP
1(Hub)	0.035	171.1	0.002
2	0.063	149.2	0.006
3	0.066	141.3	0.000
4	0.058	136.3	-0.008
5(Tip)	0.046	122.5	0.000

$DPCP_{avg}$ = 0.054 $p_{t,2}/p_{t,\infty}$ = 0.954

(d) M = 0.802, Re/FT = 68.21 x 10^6.

Figure 23. - Continued.

W_{2C}/A_i = 19.83 lb/sec-ft^2, A_0/A_C = 0.303

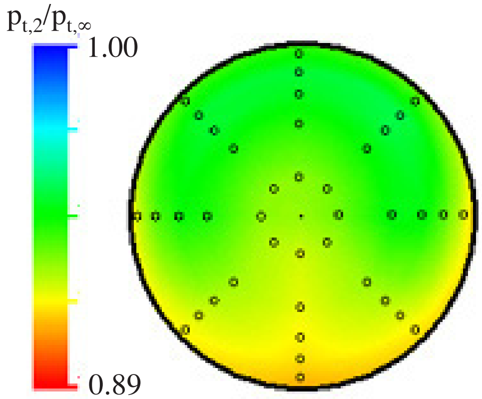

Ring	Intensity	Extent	DPRP
1(Hub)	0.004	138.3	0.005
2	0.011	138.0	-0.004
3	0.014	149.8	-0.006
4	0.014	177.0	-0.002
5(Tip)	0.010	202.5	0.008

$DPCP_{avg}$ = 0.010 $p_{t,2}/p_{t,\infty}$ = 0.933

W_{2C}/A_i = 29.11 lb/sec-ft^2, A_0/A_C = 0.452

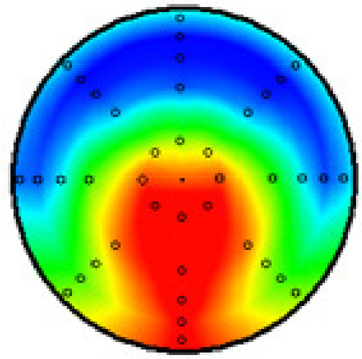

Ring	Intensity	Extent	DPRP
1(Hub)	0.018	189.7	0.048
2	0.036	180.1	0.005
3	0.041	152.6	-0.016
4	0.043	140.8	-0.025
5(Tip)	0.039	134.2	-0.013

$DPCP_{avg}$ = 0.035 $p_{t,2}/p_{t,\infty}$ = 0.945

W_{2C}/A_i = 33.10 lb/sec-ft^2, A_0/A_C = 0.516

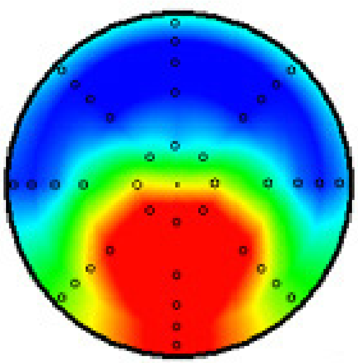

Ring	Intensity	Extent	DPRP
1(Hub)	0.037	184.8	0.031
2	0.057	161.2	0.007
3	0.056	144.4	-0.009
4	0.050	137.0	-0.019
5(Tip)	0.043	126.2	-0.010

$DPCP_{avg}$ = 0.049 $p_{t,2}/p_{t,\infty}$ = 0.948

W_{2C}/A_i = 36.01 lb/sec-ft^2, A_0/A_C = 0.562

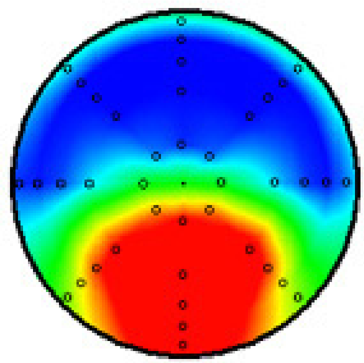

Ring	Intensity	Extent	DPRP
1(Hub)	0.039	173.5	0.007
2	0.066	150.3	0.007
3	0.068	141.6	-0.001
4	0.060	136.4	-0.010
5(Tip)	0.048	122.6	-0.002

$DPCP_{avg}$ = 0.056 $p_{t,2}/p_{t,\infty}$ = 0.951

(e) M = 0.829, Re/FT = 68.28 x 10^6.

Figure 23. - Continued.

Re/FT = 25.04 x 10^6, $T_{t,\infty}$ = 260.1 °R

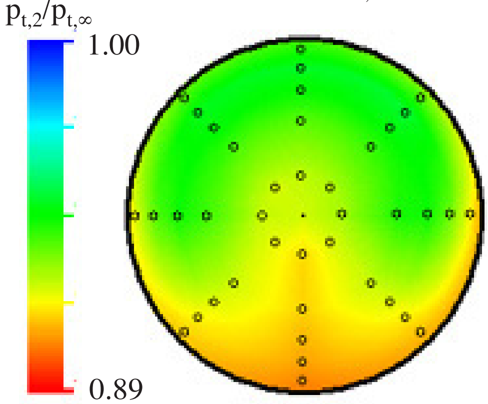

Ring	Intensity	Extent	DPRP
1(Hub)	0.004	128.9	0.007
2	0.011	134.3	-0.003
3	0.016	144.8	-0.006
4	0.016	170.4	-0.004
5(Tip)	0.011	197.9	0.007

$DPCP_{avg}$ = 0.012 $p_{t,2}/p_{t,\infty}$ = 0.928

Re/FT = 42.03 x 10^6, $T_{t,\infty}$ = 260.4 °R

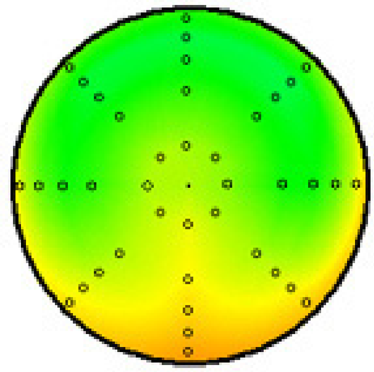

Ring	Intensity	Extent	DPRP
1(Hub)	0.003	169.2	0.006
2	0.011	138.4	-0.004
3	0.015	150.6	-0.006
4	0.015	177.2	-0.003
5(Tip)	0.011	200.4	0.007

$DPCP_{avg}$ = 0.011 $p_{t,2}/p_{t,\infty}$ = 0.931

Re/FT = 42.01 x 10^6, $T_{t,\infty}$ = 180.2 °R

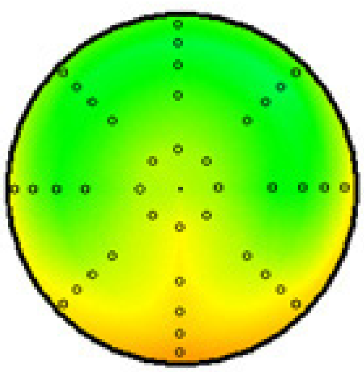

Ring	Intensity	Extent	DPRP
1(Hub)	0.004	131.6	0.006
2	0.011	137.0	-0.003
3	0.015	147.2	-0.006
4	0.015	174.2	-0.003
5(Tip)	0.010	199.2	0.006

$DPCP_{avg}$ = 0.011 $p_{t,2}/p_{t,\infty}$ = 0.930

Re/FT = 68.60 x 10^6, $T_{t,\infty}$ = 180.6 °R

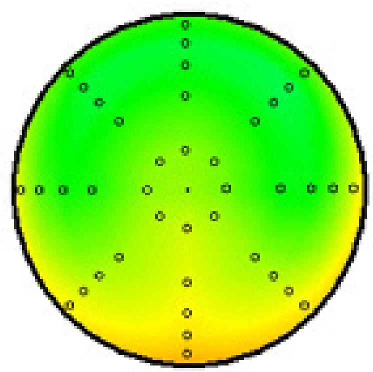

Ring	Intensity	Extent	DPRP
1(Hub)	0.004	138.3	0.005
2	0.011	138.0	-0.004
3	0.014	149.8	-0.006
4	0.014	177.0	-0.002
5(Tip)	0.010	202.5	0.008

$DPCP_{avg}$ = 0.010 $p_{t,2}/p_{t,\infty}$ = 0.933

(f) M = 0.829, W_{2C}/A_i = 19.91 lb/sec-ft^2 (A_0/A_C = 0.305).

Figure 23. - Continued.

Re/FT = 25.48 x 10^6, $T_{t,\infty}$ = 259.8 °R

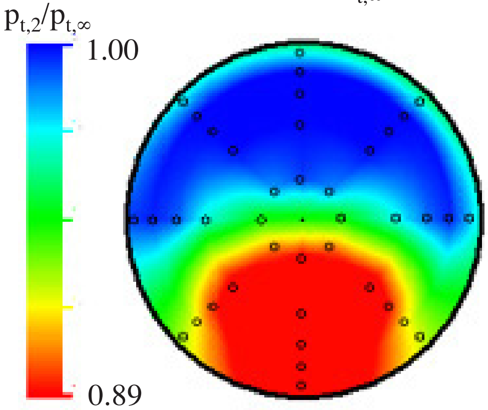

Ring	Intensity	Extent	DPRP
1(Hub)	0.038	176.0	0.007
2	0.067	152.8	0.007
3	0.069	142.6	-0.002
4	0.062	136.8	-0.011
5(Tip)	0.050	125.5	-0.001

$DPCP_{avg}$ = 0.057 $p_{t,2}/p_{t,\infty}$ = 0.948

Re/FT = 42.37 x 10^6, $T_{t,\infty}$ = 259.1 °R

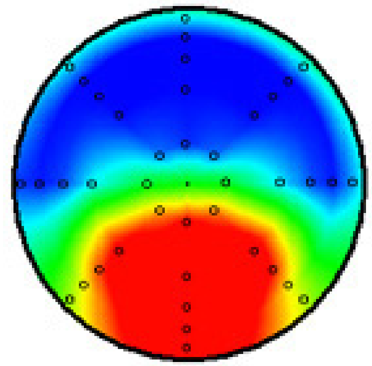

Ring	Intensity	Extent	DPRP
1(Hub)	0.038	174.7	0.005
2	0.067	151.2	0.007
3	0.070	141.6	-0.001
4	0.062	136.3	-0.010
5(Tip)	0.050	125.4	-0.001

$DPCP_{avg}$ = 0.058 $p_{t,2}/p_{t,\infty}$ = 0.950

Re/FT = 42.38 x 10^6, $T_{t,\infty}$ = 180.6 °R

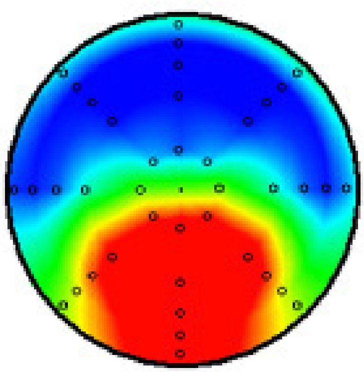

Ring	Intensity	Extent	DPRP
1(Hub)	0.039	180.0	0.015
2	0.067	154.3	0.008
3	0.067	142.7	-0.004
4	0.059	136.7	-0.015
5(Tip)	0.047	125.4	-0.005

$DPCP_{avg}$ = 0.056 $p_{t,2}/p_{t,\infty}$ = 0.947

Re/FT = 68.40 x 10^6, $T_{t,\infty}$ = 180.4 °R

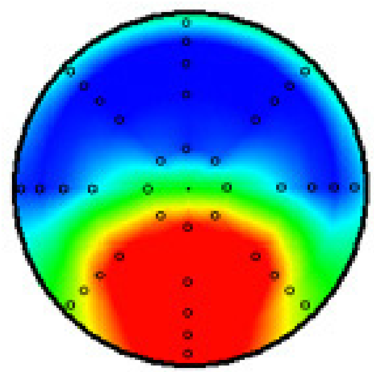

Ring	Intensity	Extent	DPRP
1(Hub)	0.039	173.5	0.007
2	0.066	150.3	0.007
3	0.068	141.6	-0.001
4	0.060	136.4	-0.010
5(Tip)	0.048	122.6	-0.002

$DPCP_{avg}$ = 0.056 $p_{t,2}/p_{t,\infty}$ = 0.951

(g) M = 0.833, W_{2C}/A_i = 36.03 lb/sec-ft^2 (A_0/A_C = 0.561).

Figure 23. - Concluded.

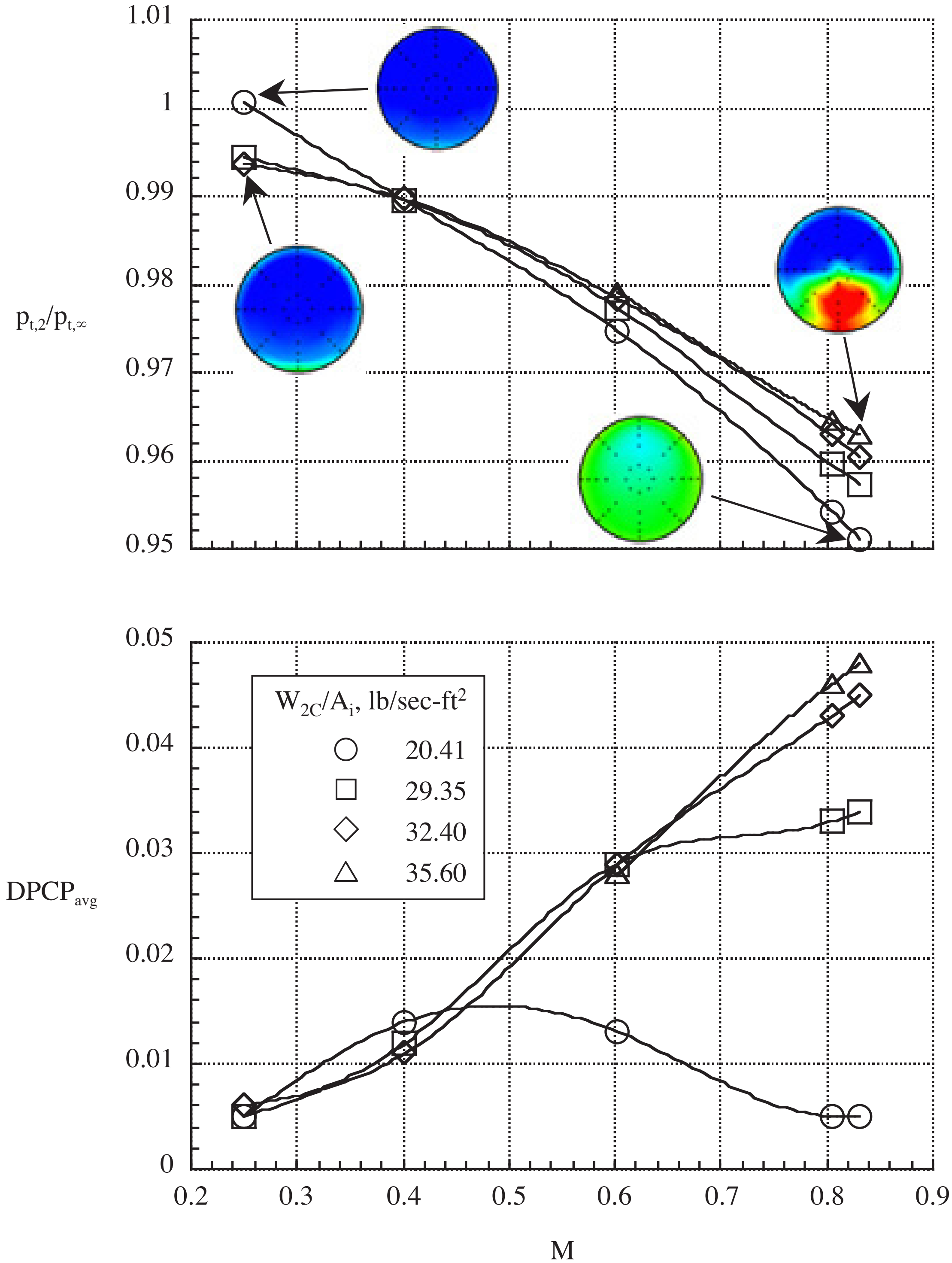

(a) Inlet A, fence off.

Figure 24. - Effect of Mach number and inlet mass-flow on pressure recovery and distortion.

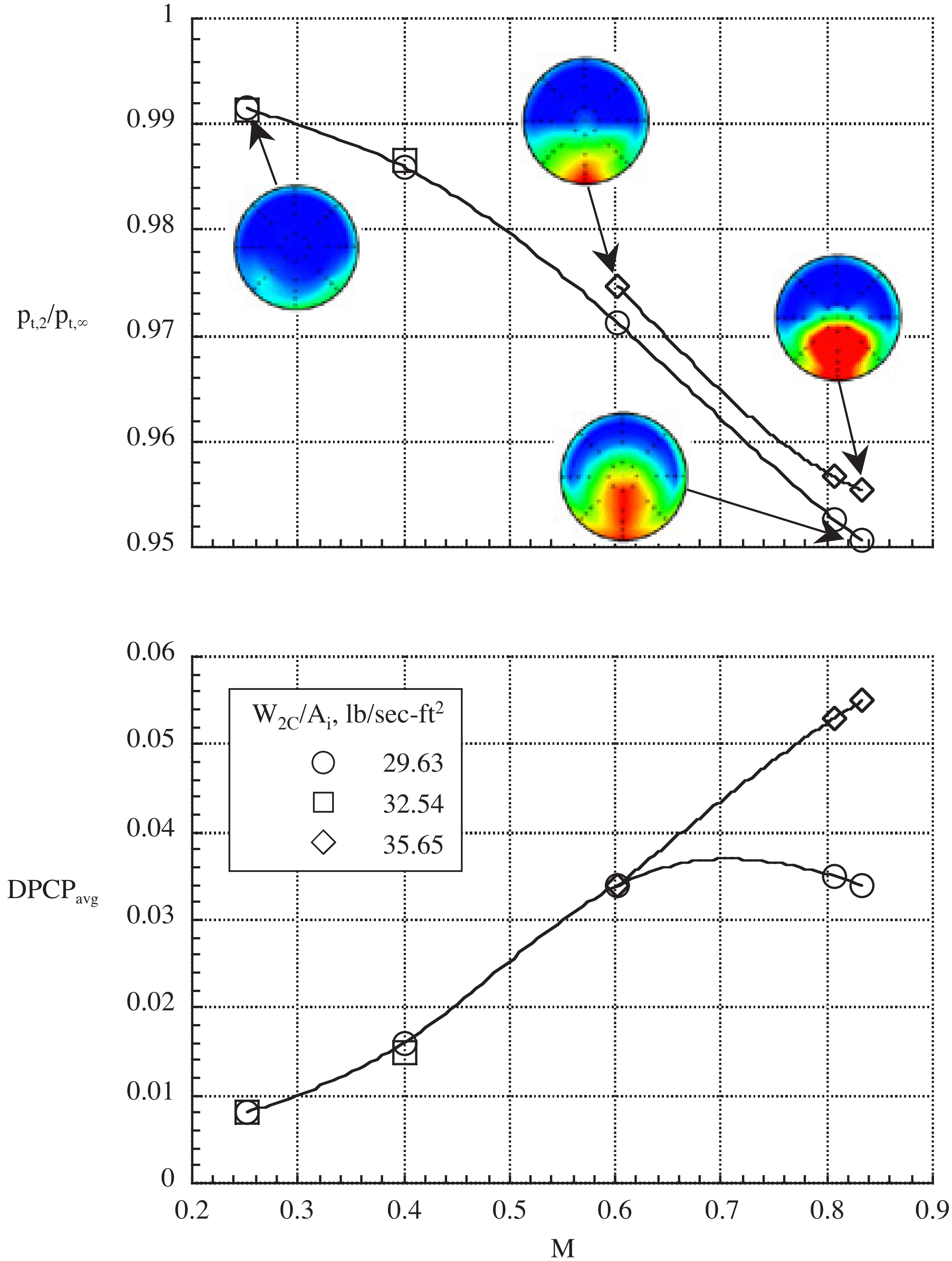

(b) Inlet A, fence on.

Figure 24. - Continued.

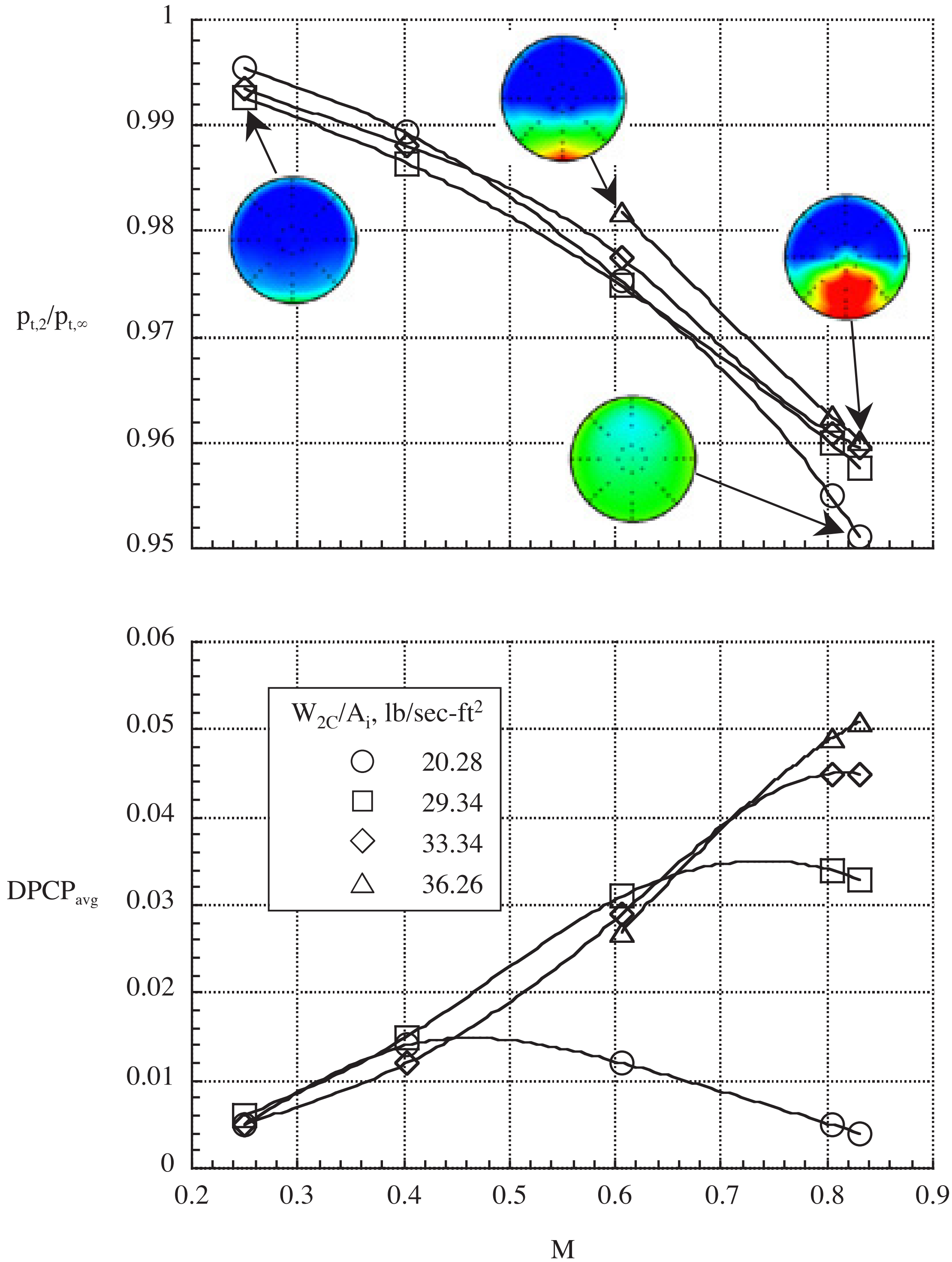

(c) Inlet B, fence off.

Figure 24. - Continued.

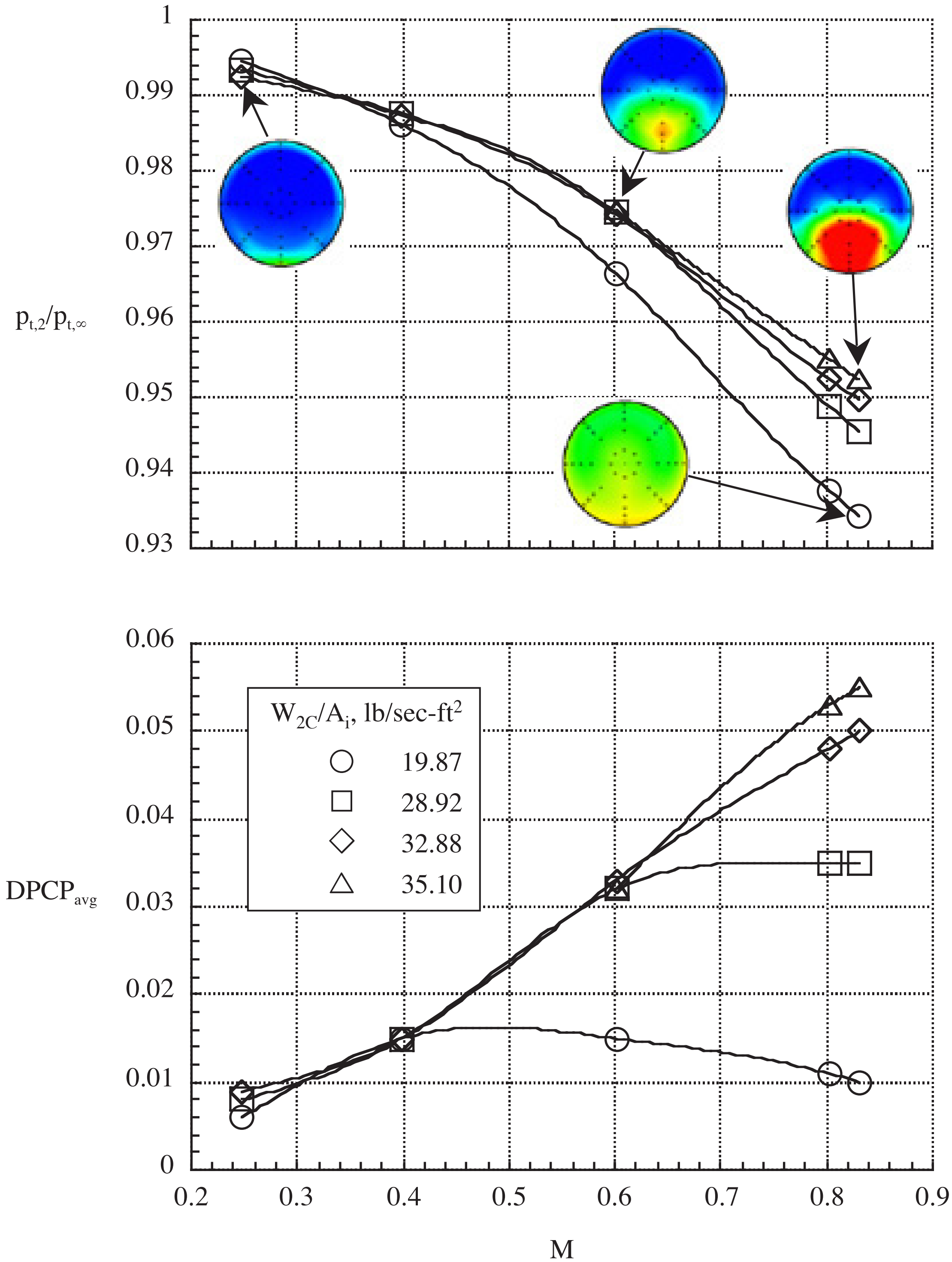

(d) Inlet C, fence off.

Figure 24. - Continued.

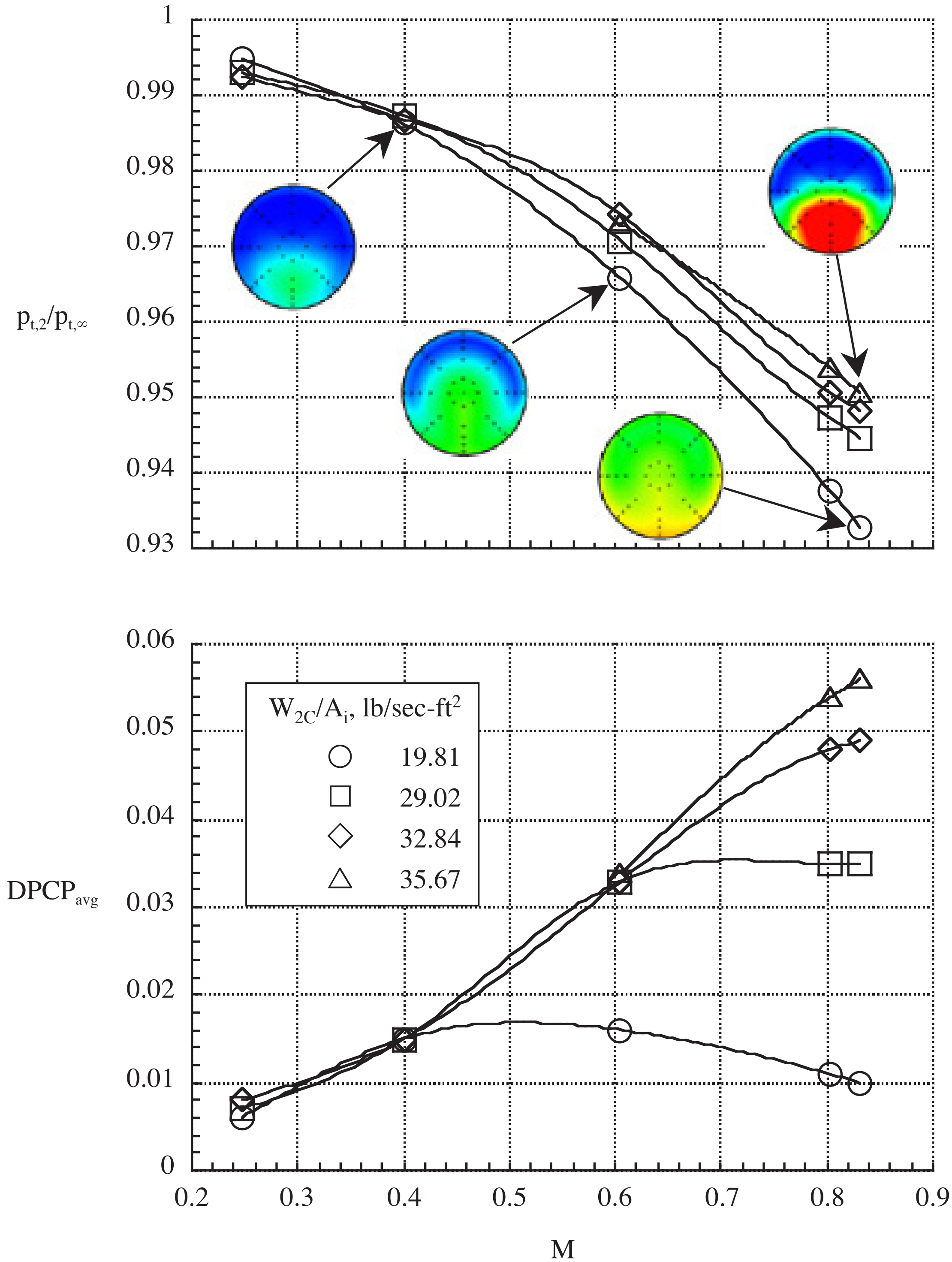

(e) Inlet D, fence off.

Figure 24. - Concluded.

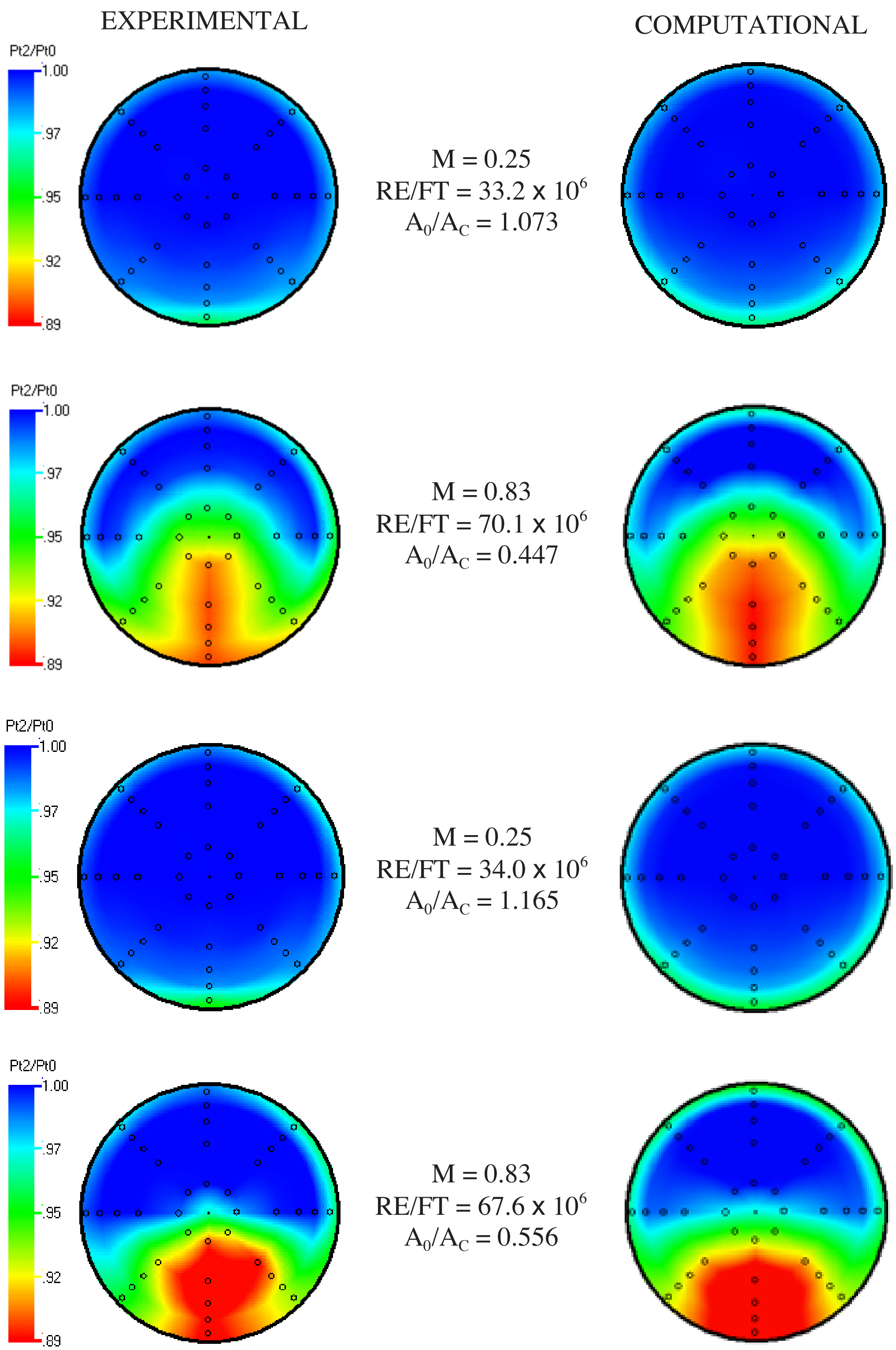

Figure 25. - Comparison of experimental and computational AIP total pressure contours for inlet A.

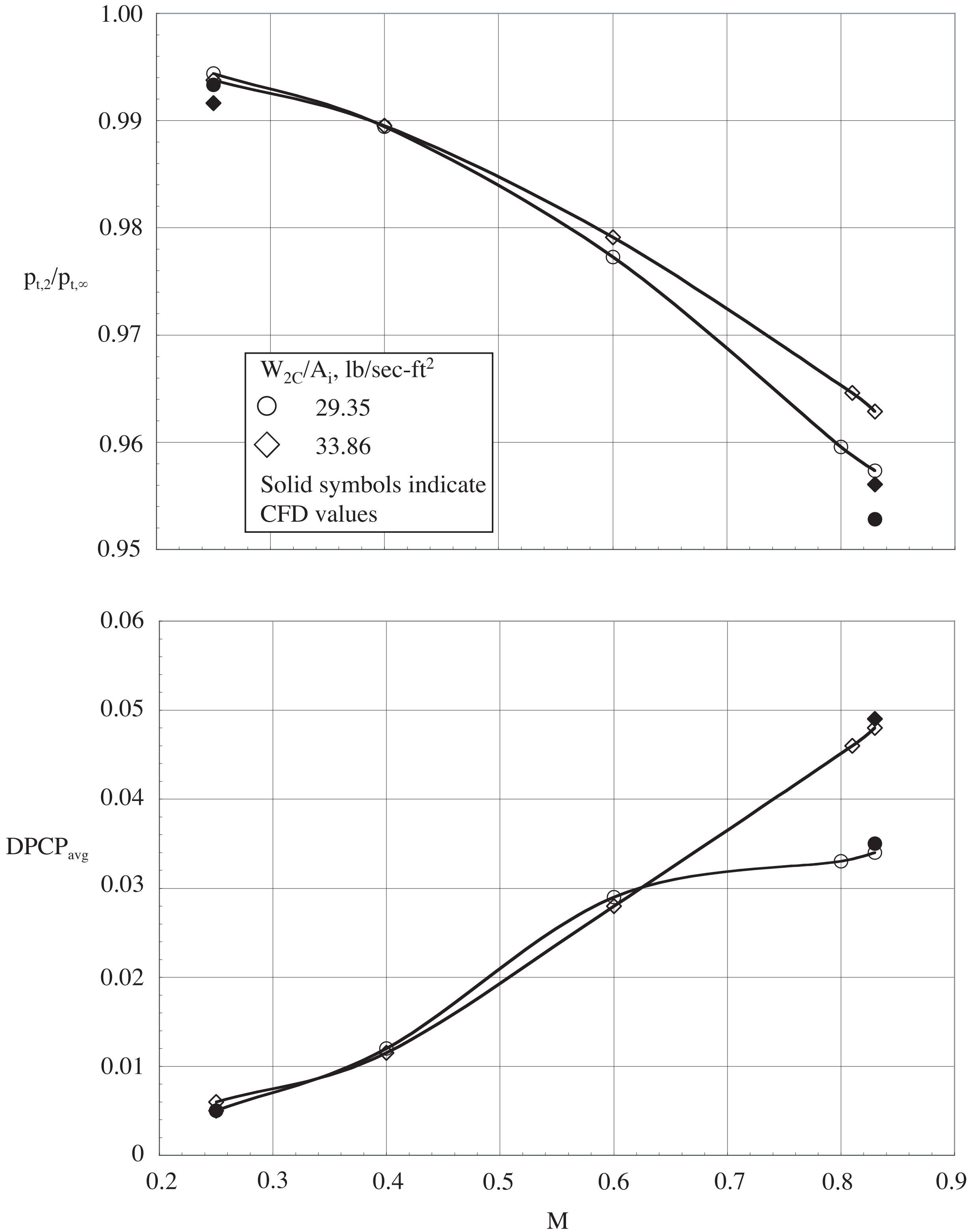

Figure 26. - Comparison of experimental and computational performance values for inlet A.

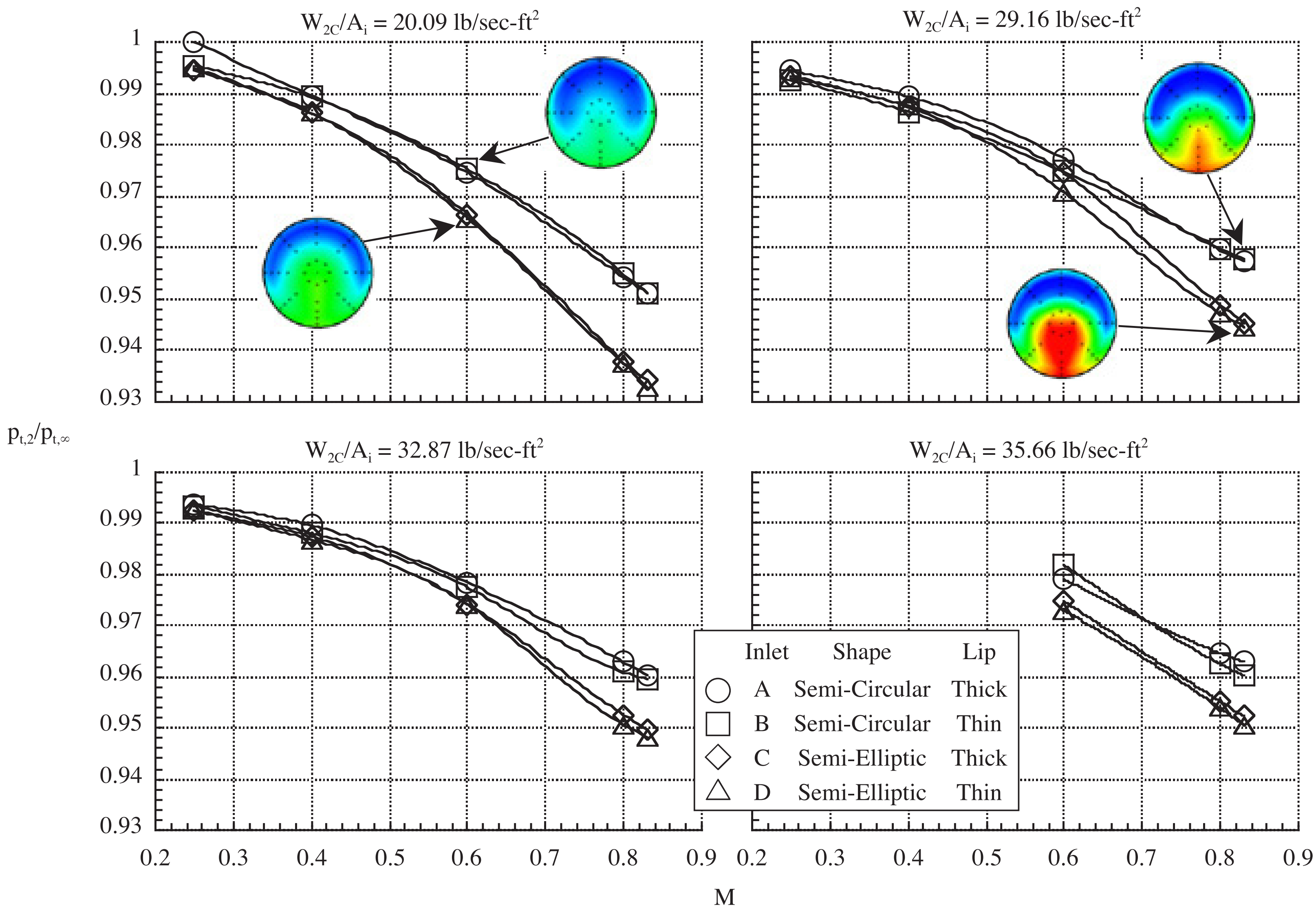

(a) Pressure Recovery.

Figure 27. - Effect of inlet geometry on inlet pressure recovery and distortion.

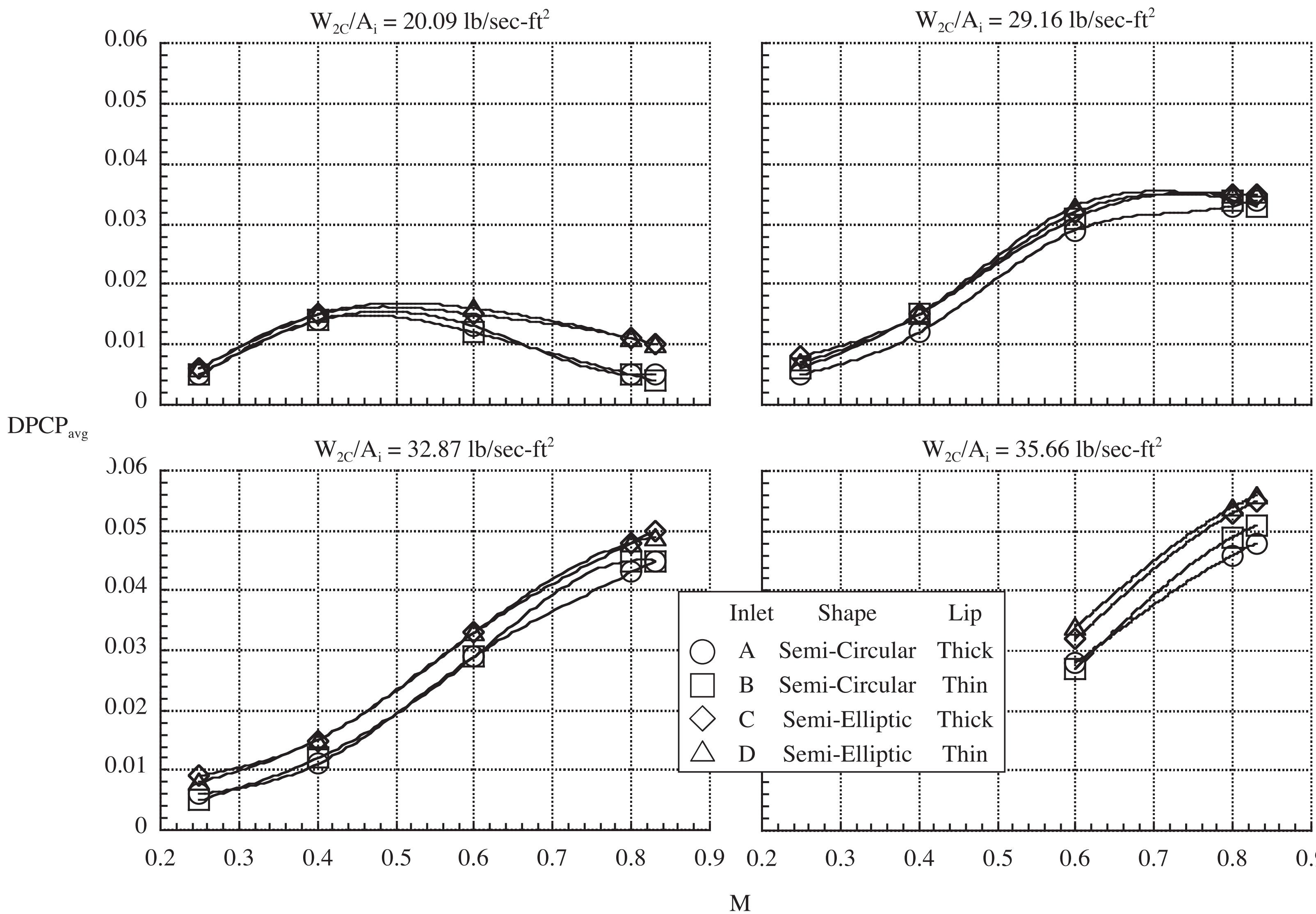

(b) Distortion.

Figure 27. - Concluded.

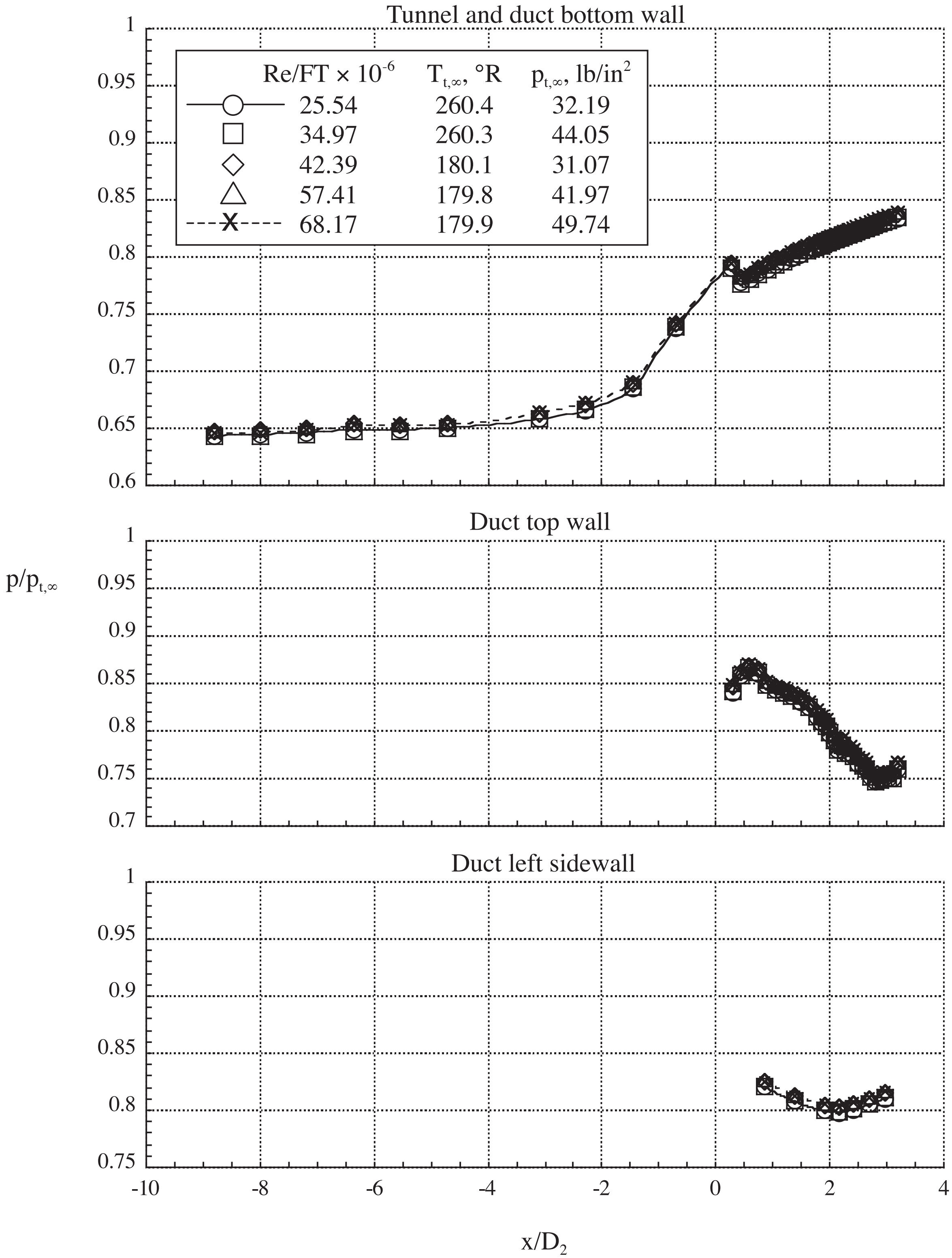

Figure 28. - Effect of Reynolds number on inlet B duct pressure distributions at $M = 0.832$ and $W_{2C}/A_i = 36.79$ lb/sec-ft^2 ($A_0/A_C = 0.573$).

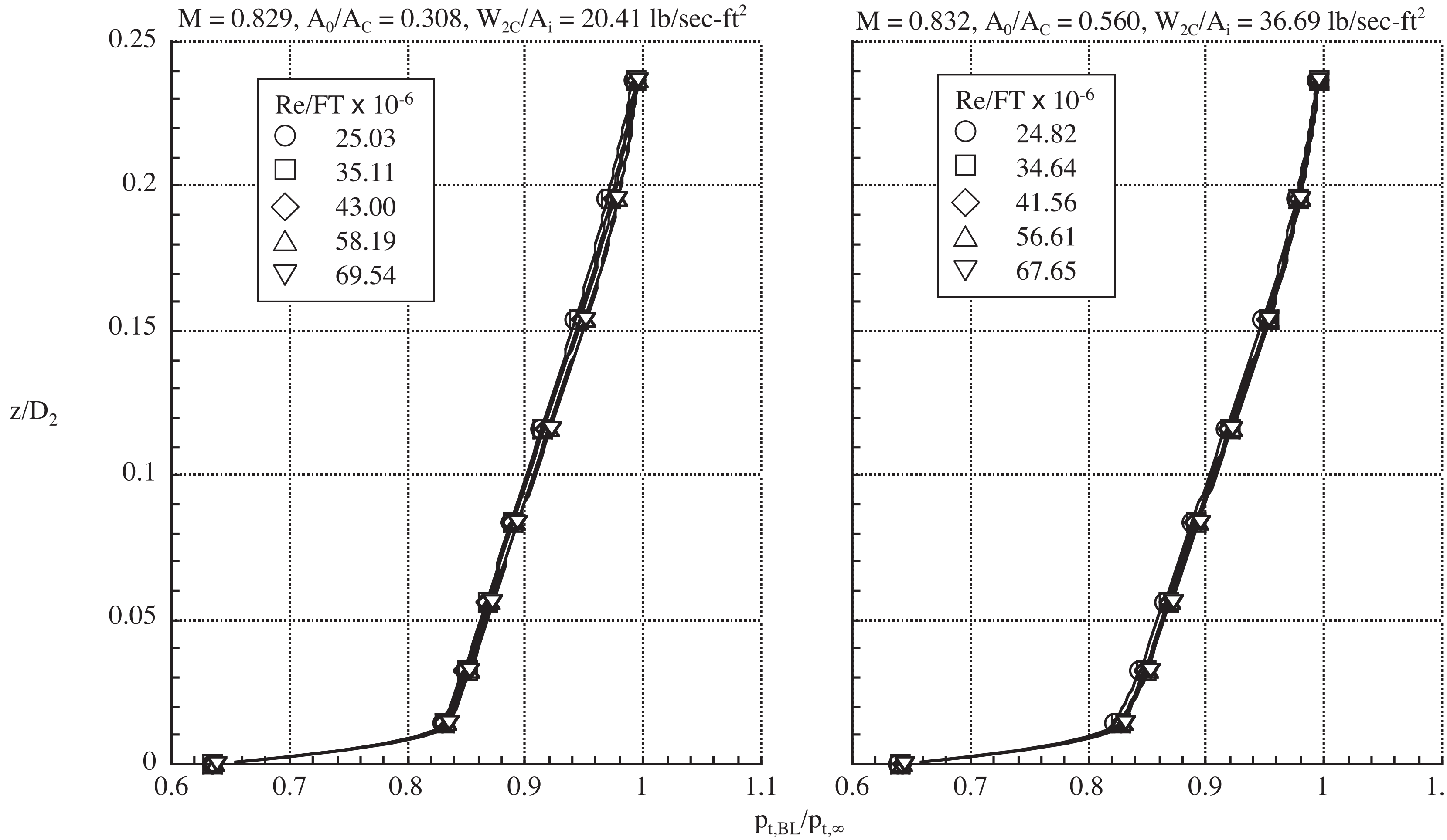

(a) Inlet A

Figure 29.- Effect of Reynolds number on tunnel wall boundary layer profiles.

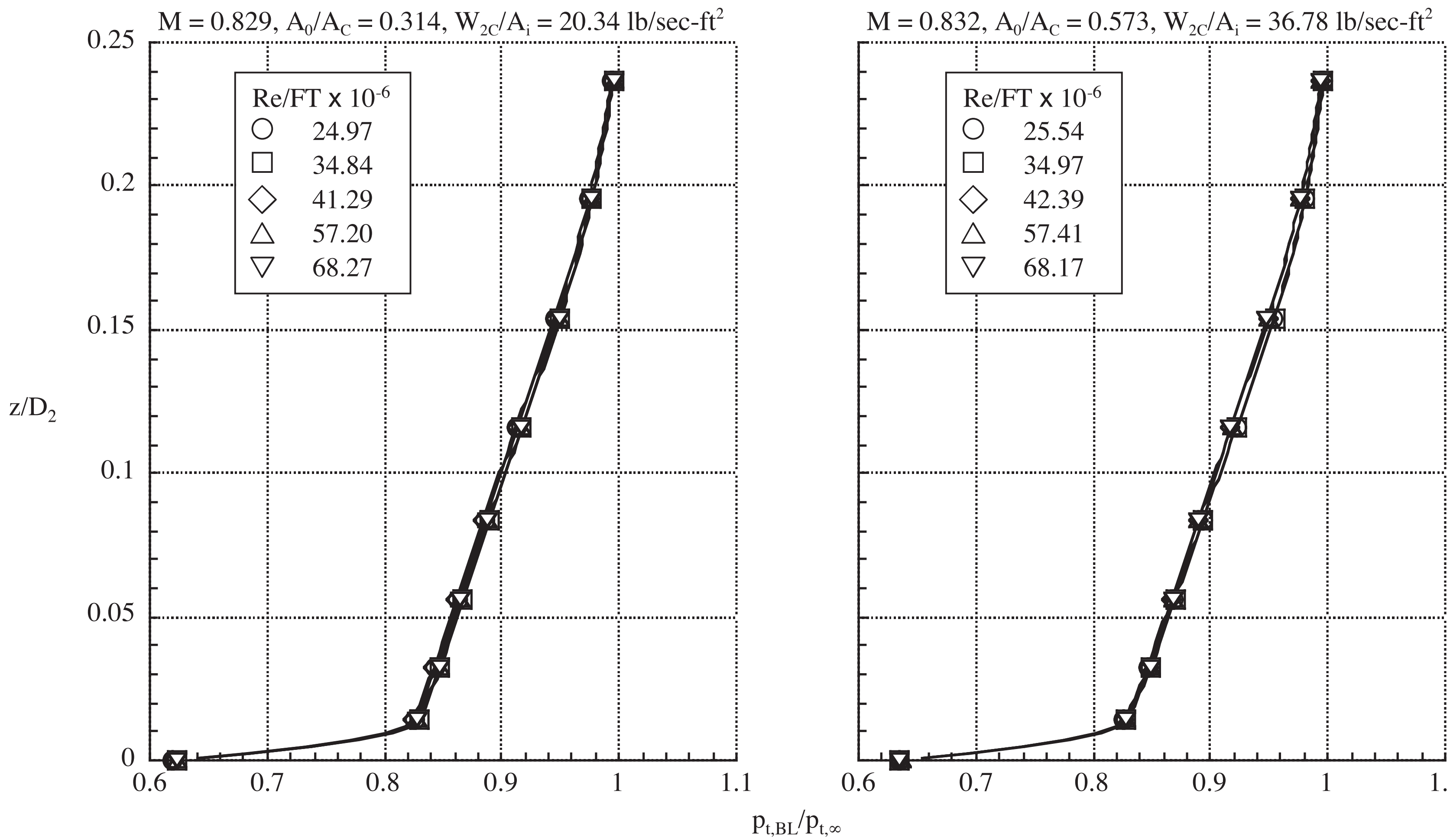

(b) Inlet B.

Figure 29.- Continued.

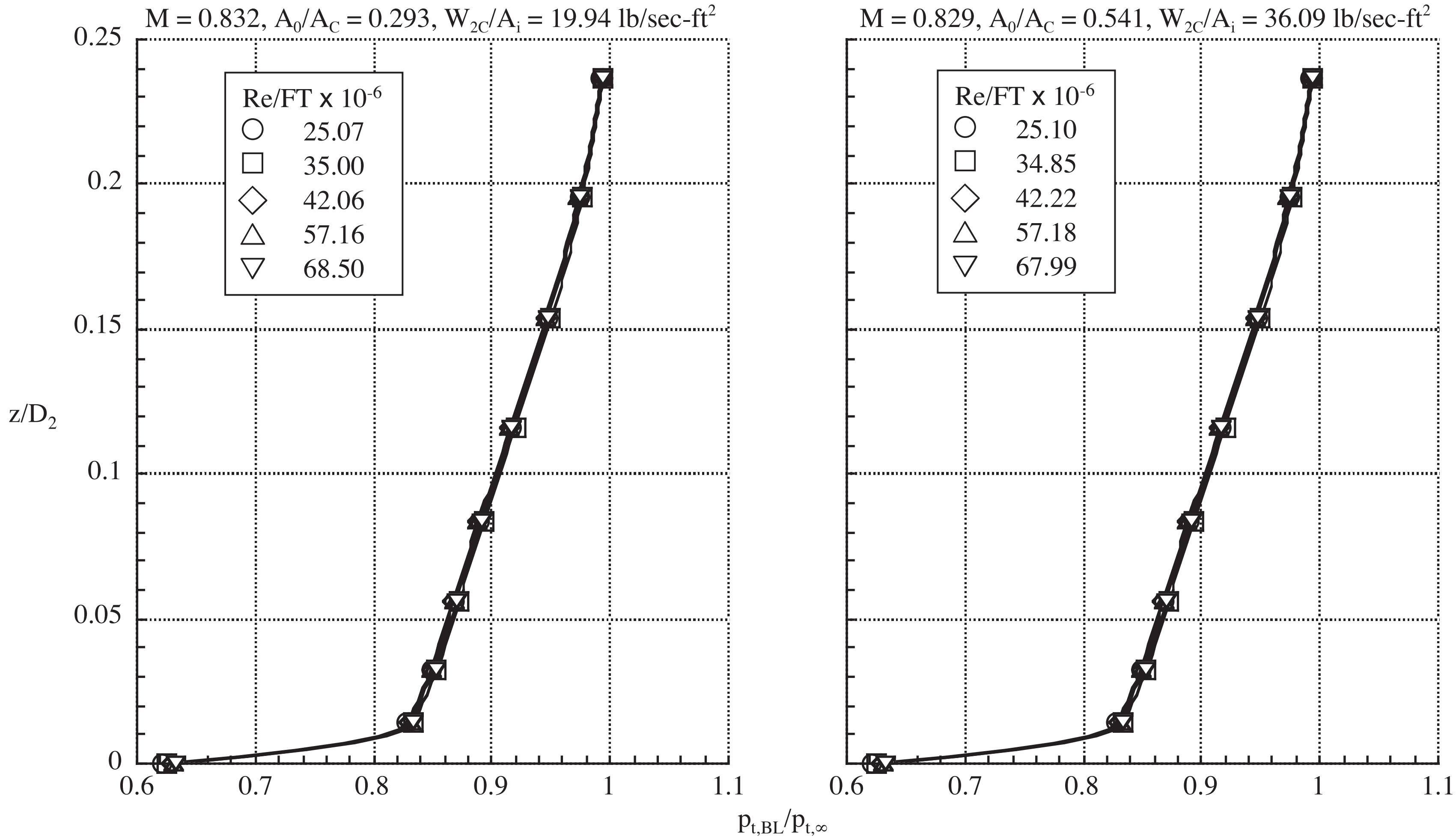

(c) Inlet C.

Figure 29.- Continued.

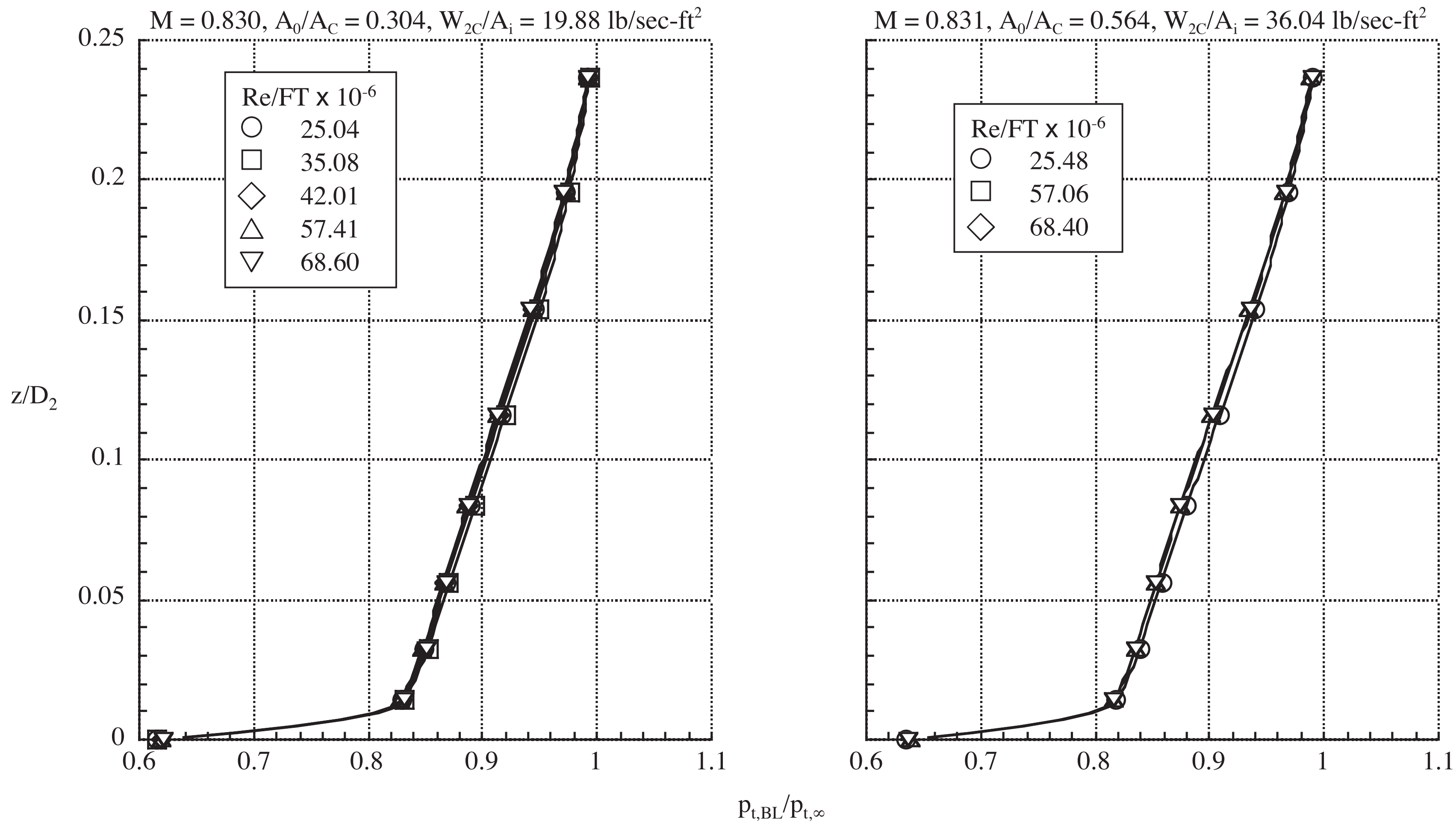

(d) Inlet D.

Figure 29.- Concluded.

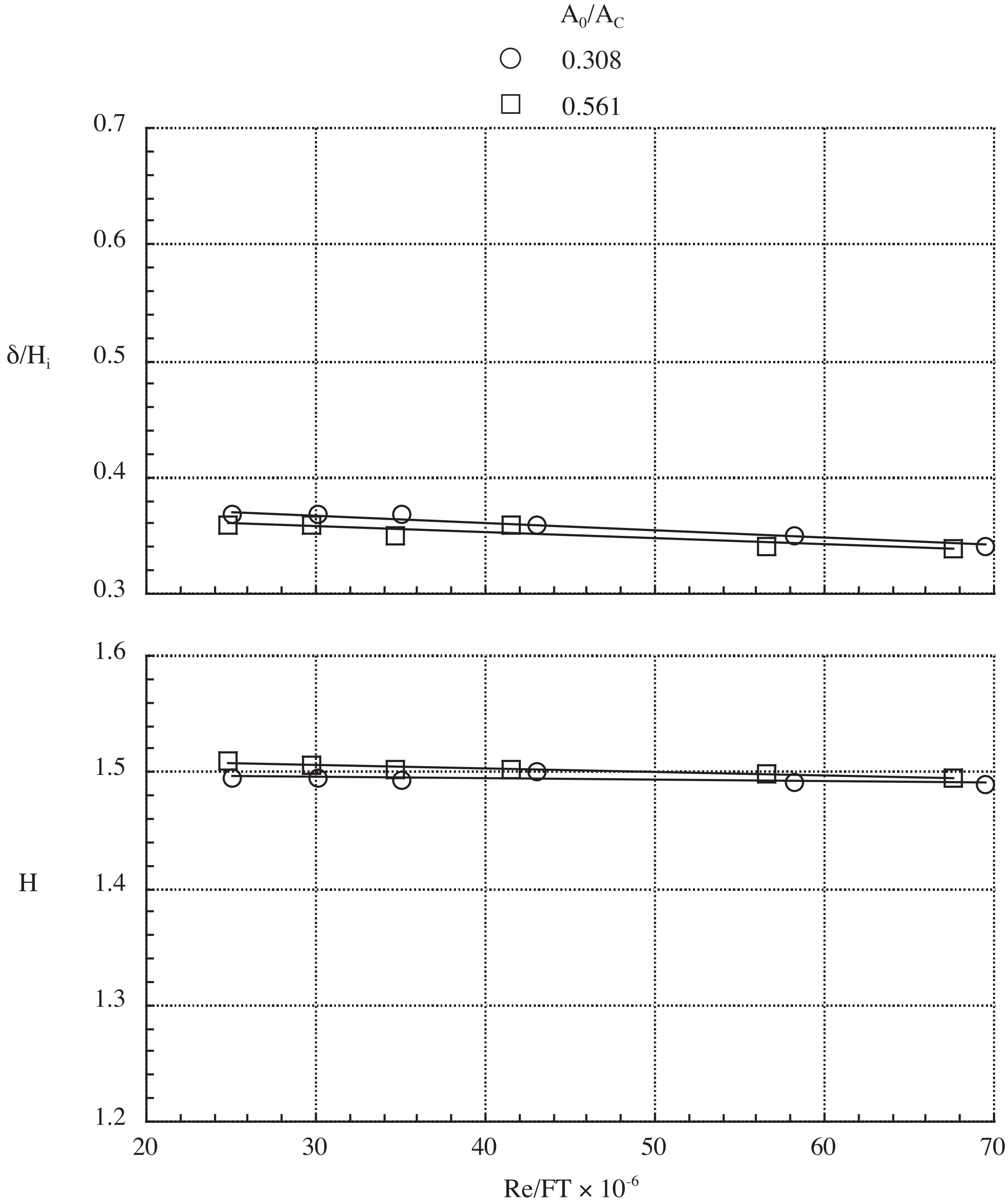

(a) Inlet A.

Figure 30. - Effect of Reynolds number on boundary layer thickness and shape factor. M = 0.83.

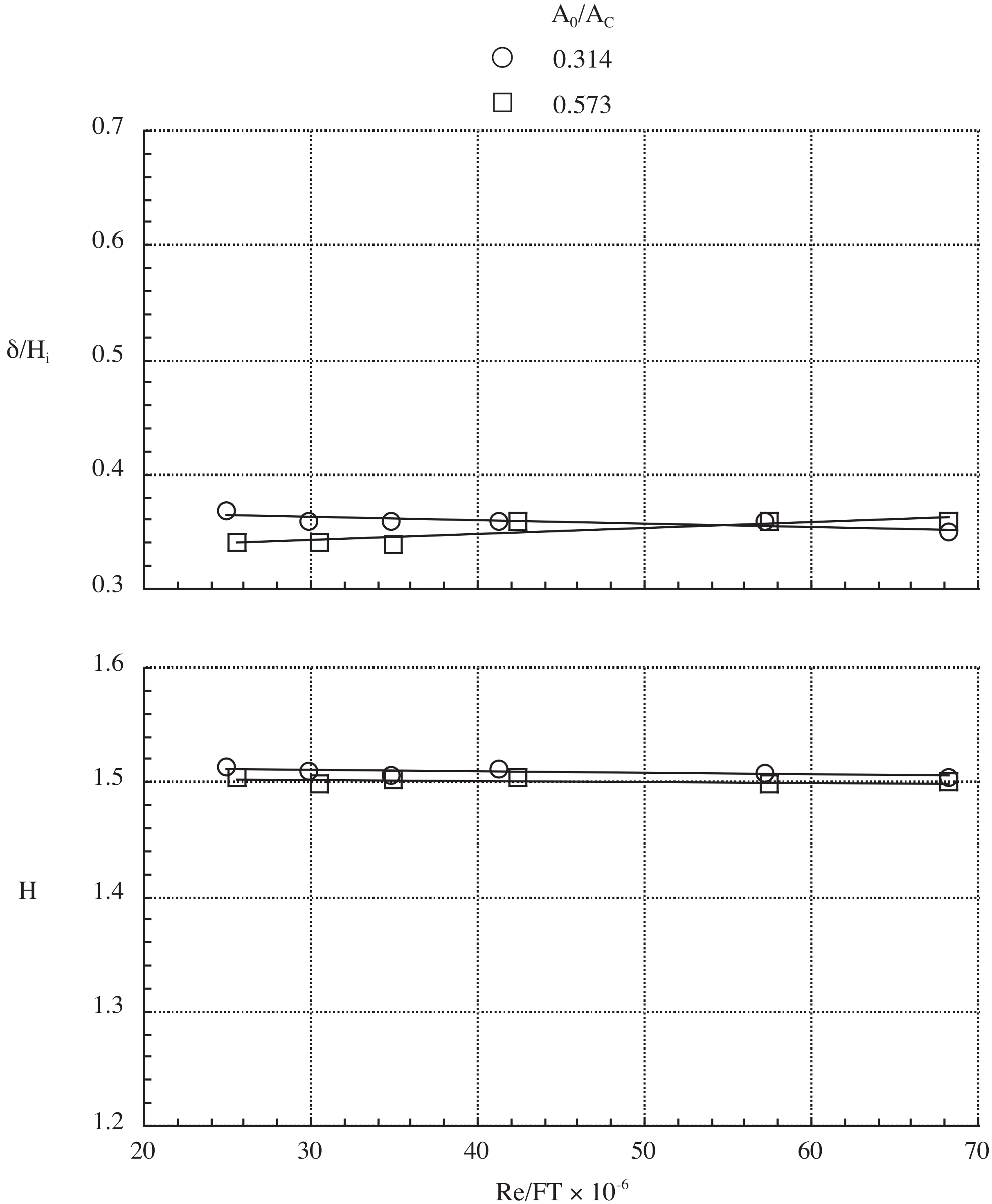

(b) Inlet B.

Figure 30. - Continued.

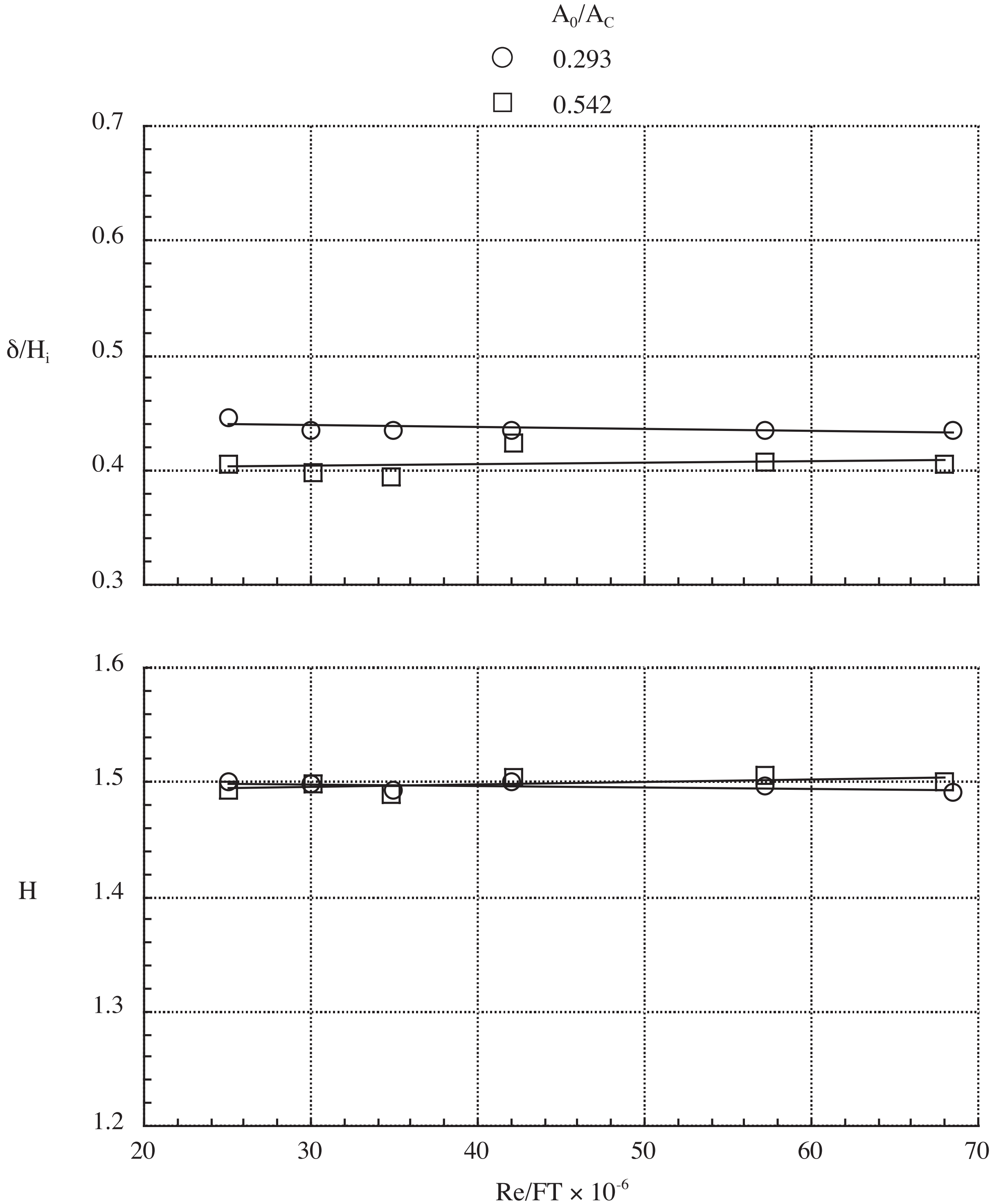

(c) Inlet C.

Figure 30. - Continued.

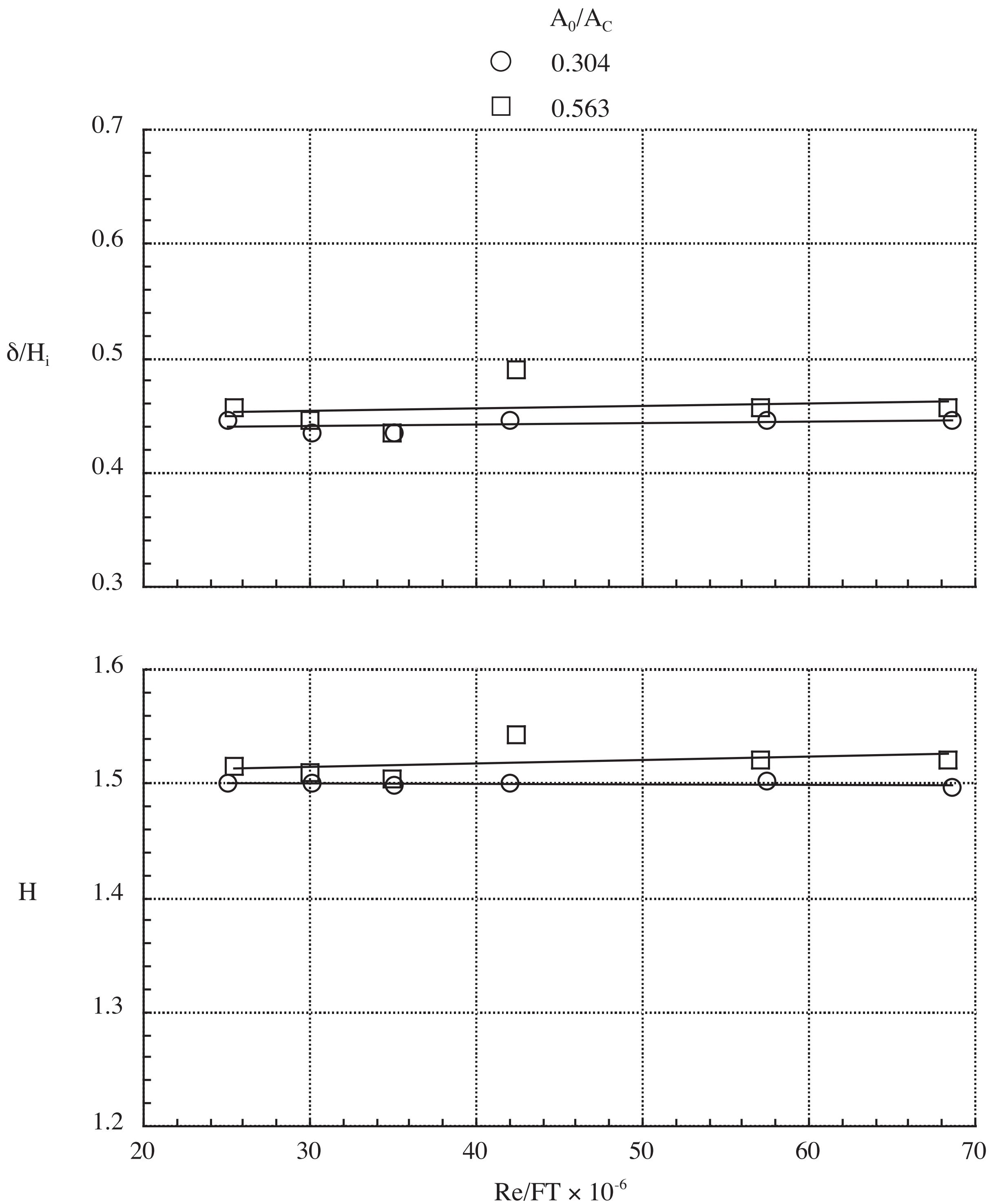

(d) Inlet D.

Figure 30. - Continued.

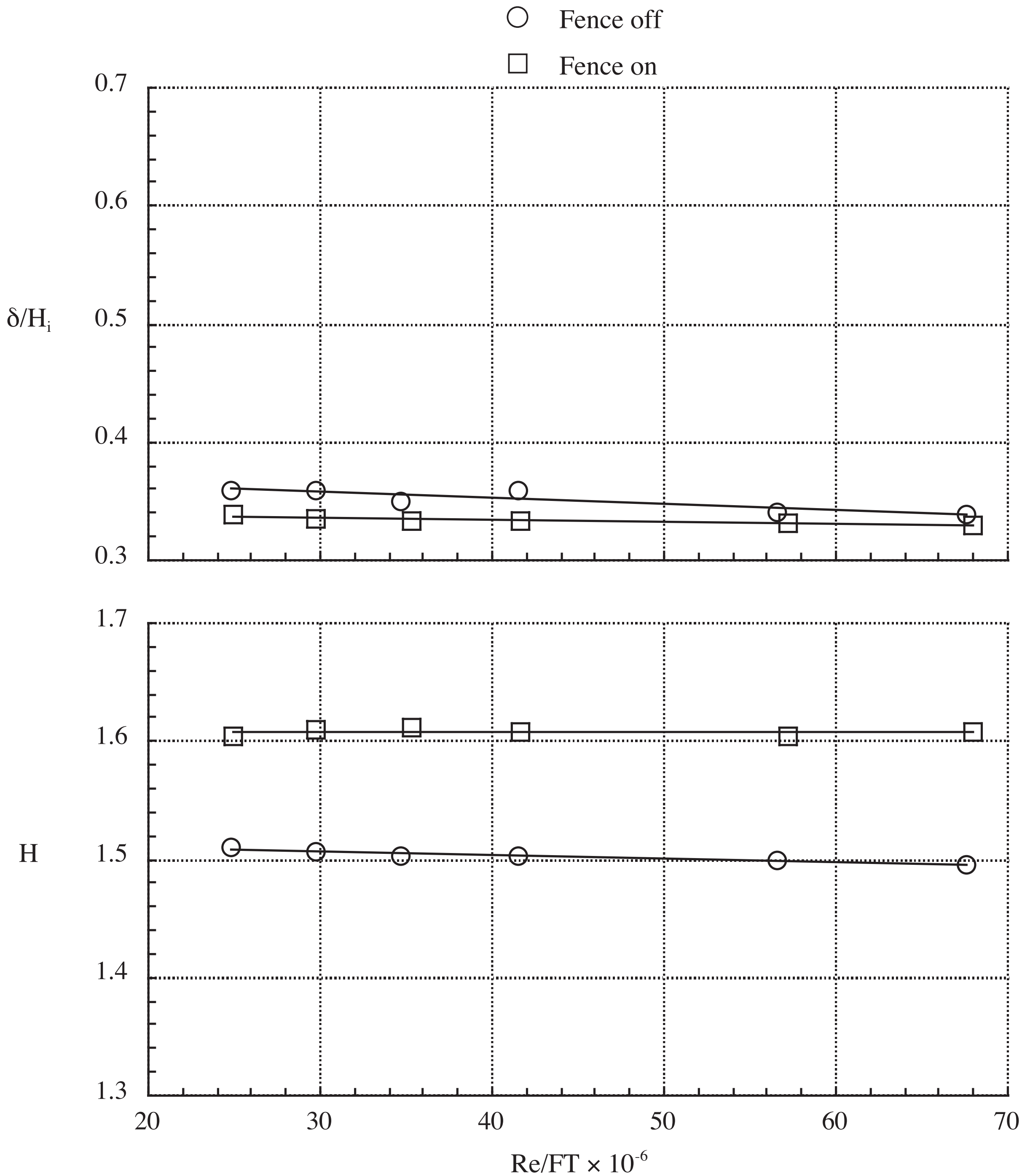

(e) Inlet A with and without boundary layer fence; $A_0/A_C = 0.558$.

Figure 30. - Concluded.

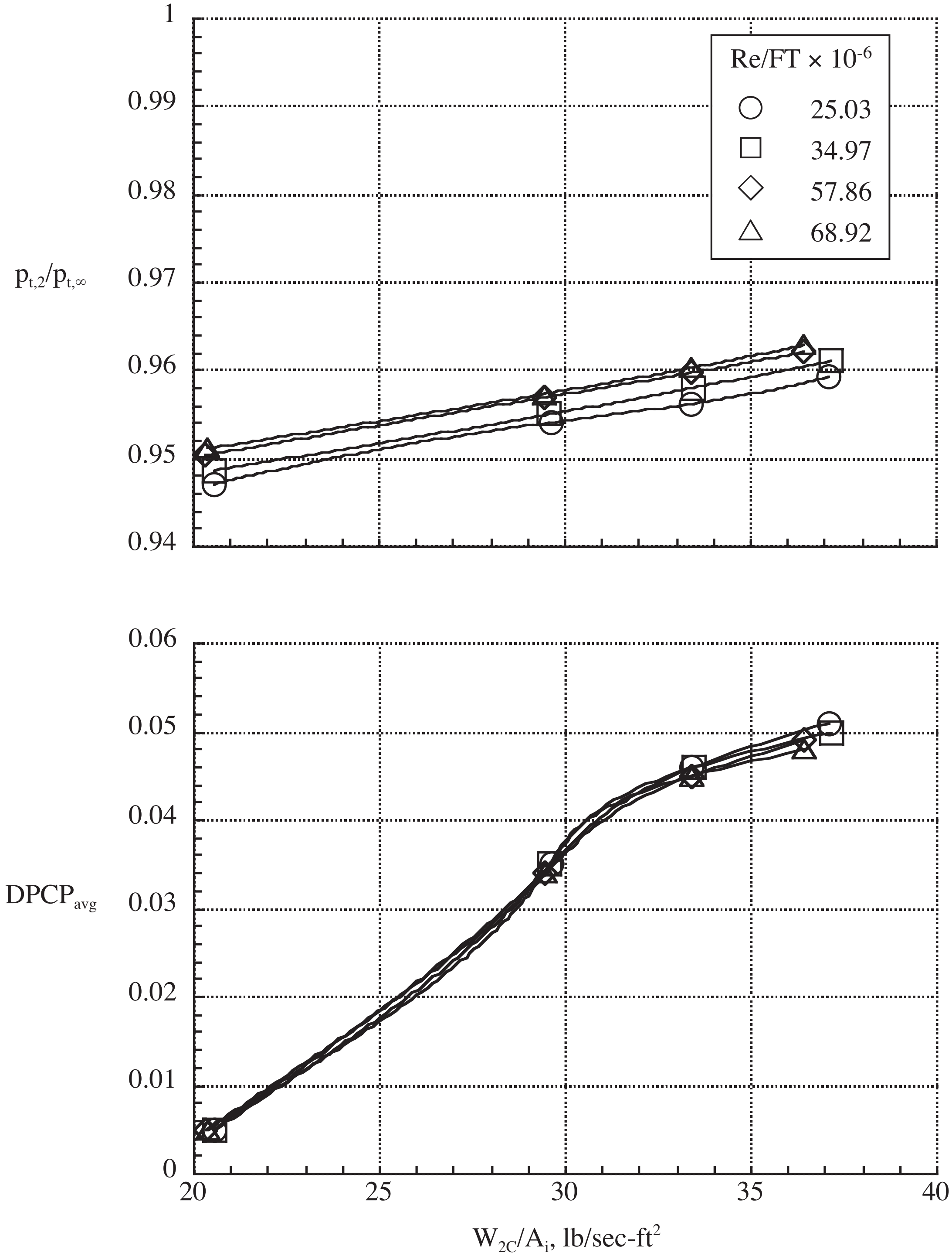

(a) Inlet A, fence off.

Figure 31. - Effect of Reynolds number on pressure recovery and distortion. M = 0.831.

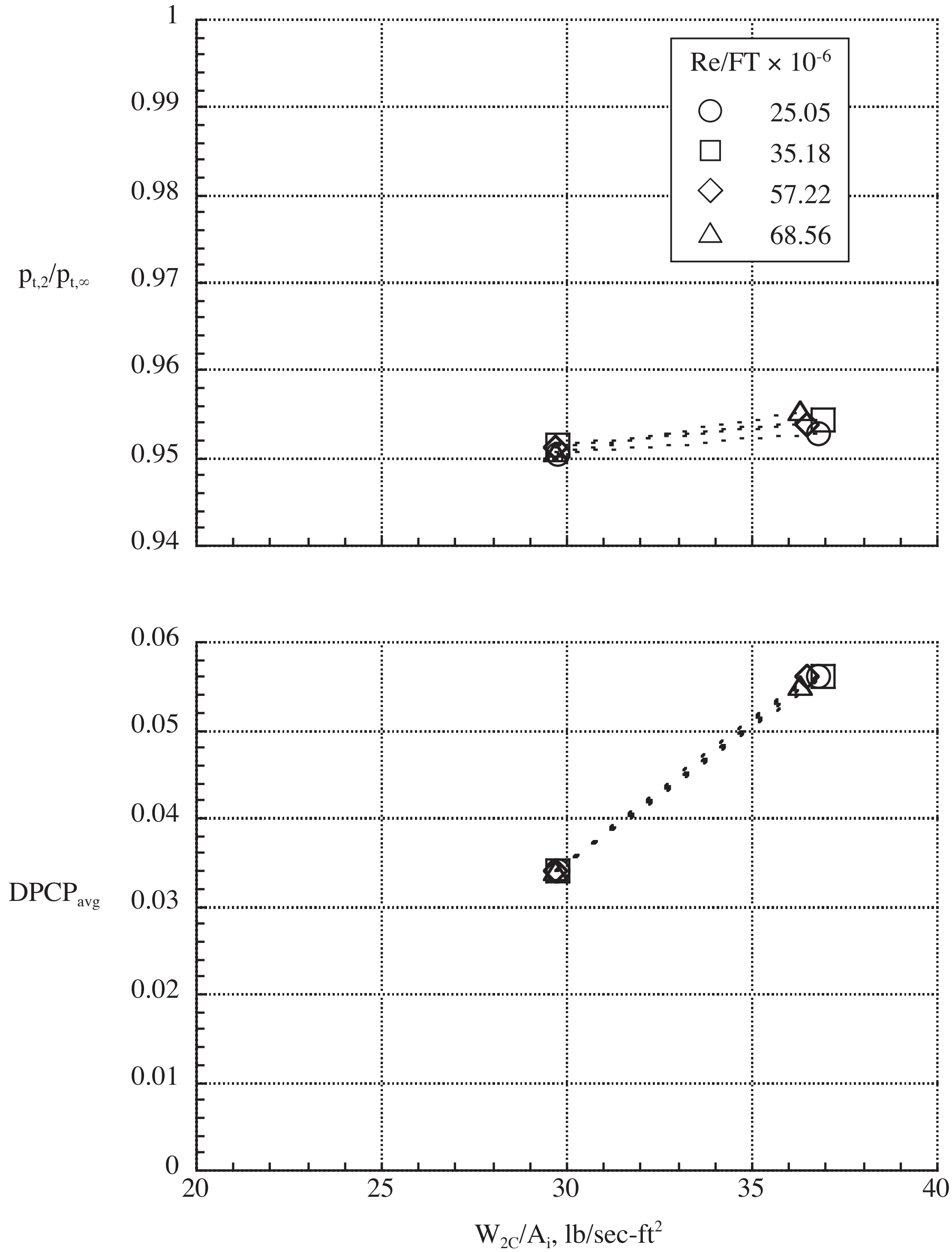

(b) Inlet A, fence on.

Figure 31. - Continued.

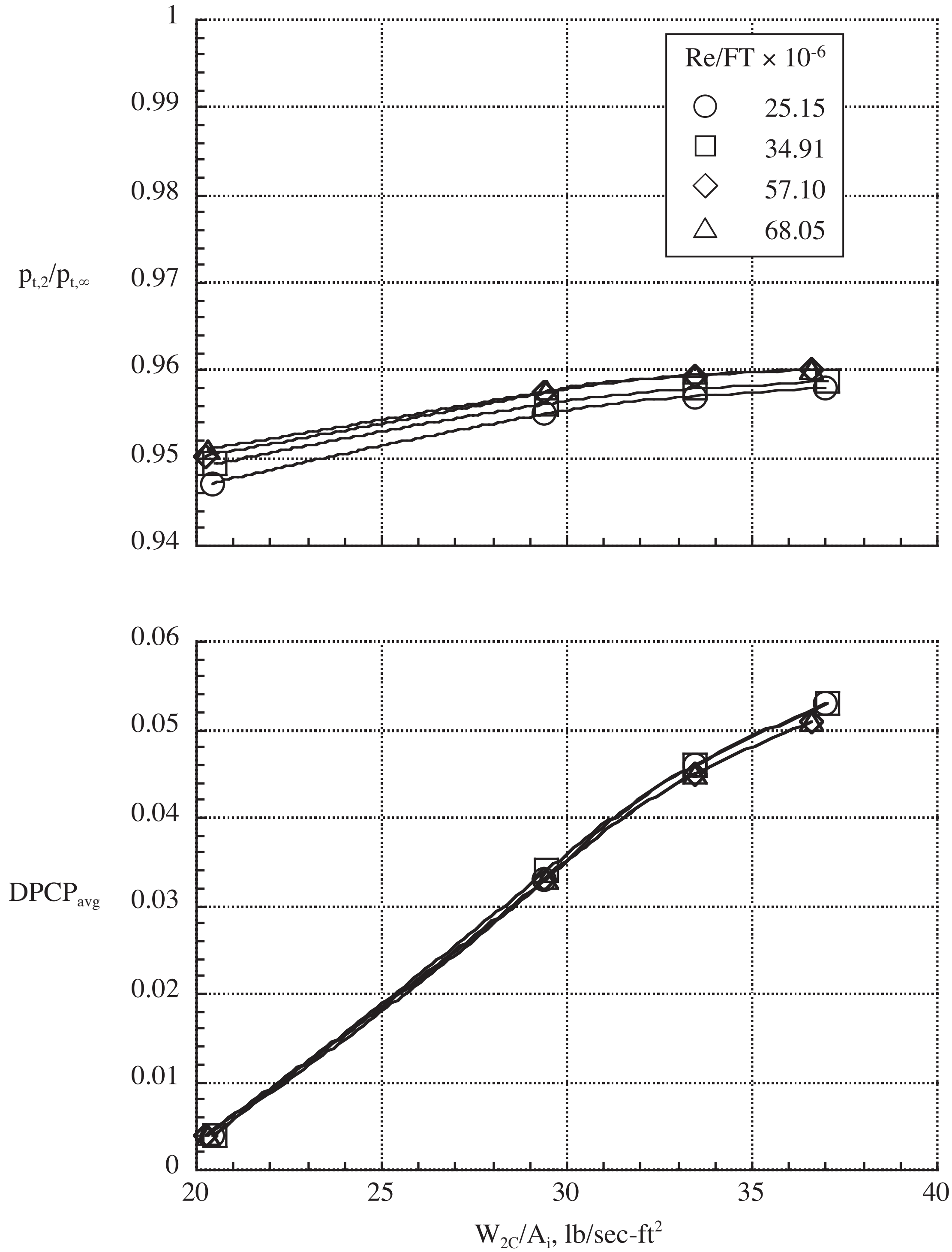

(c) Inlet B, fence off.

Figure 31. - Continued.

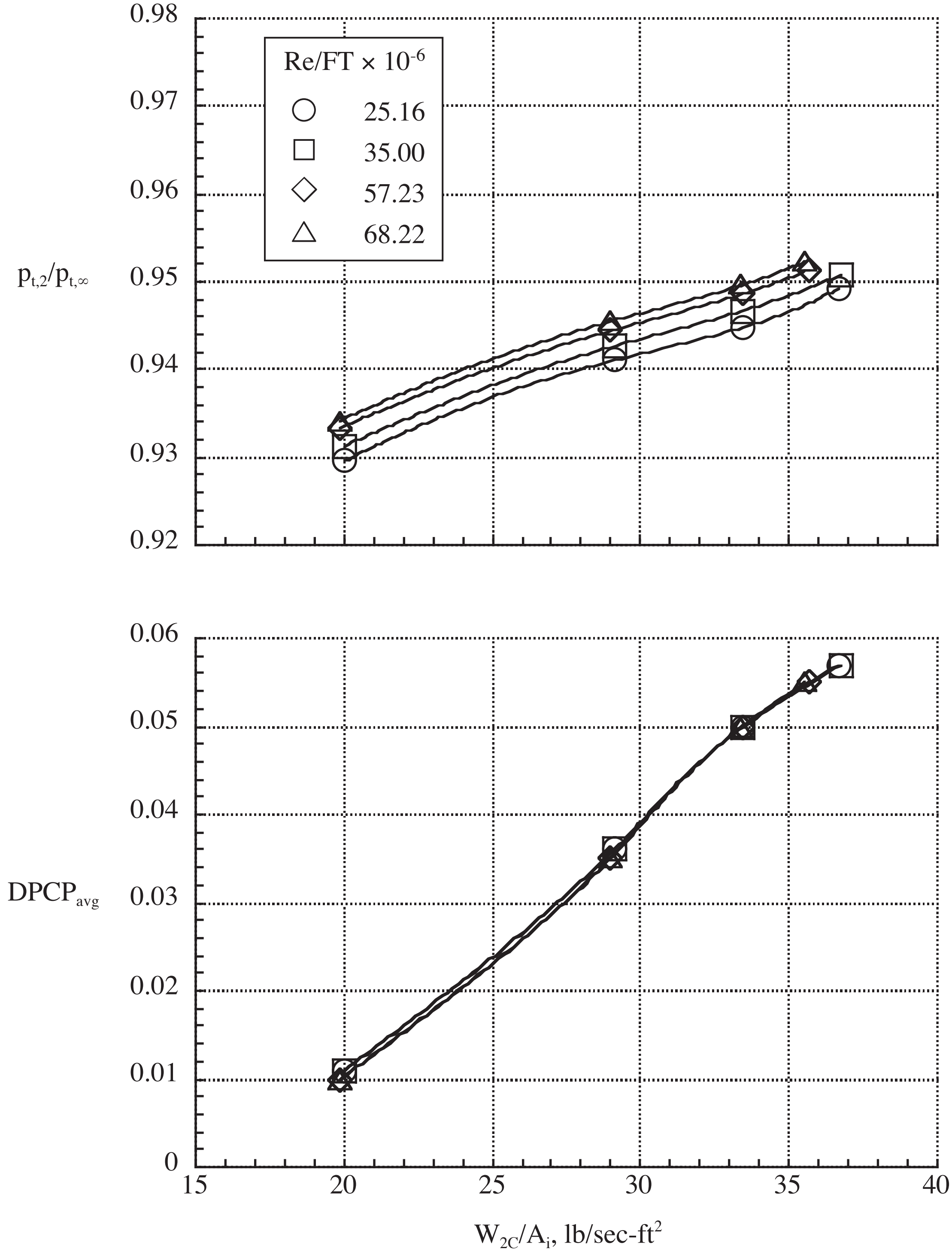

(d) Inlet C, fence off.

Figure 31. - Continued.

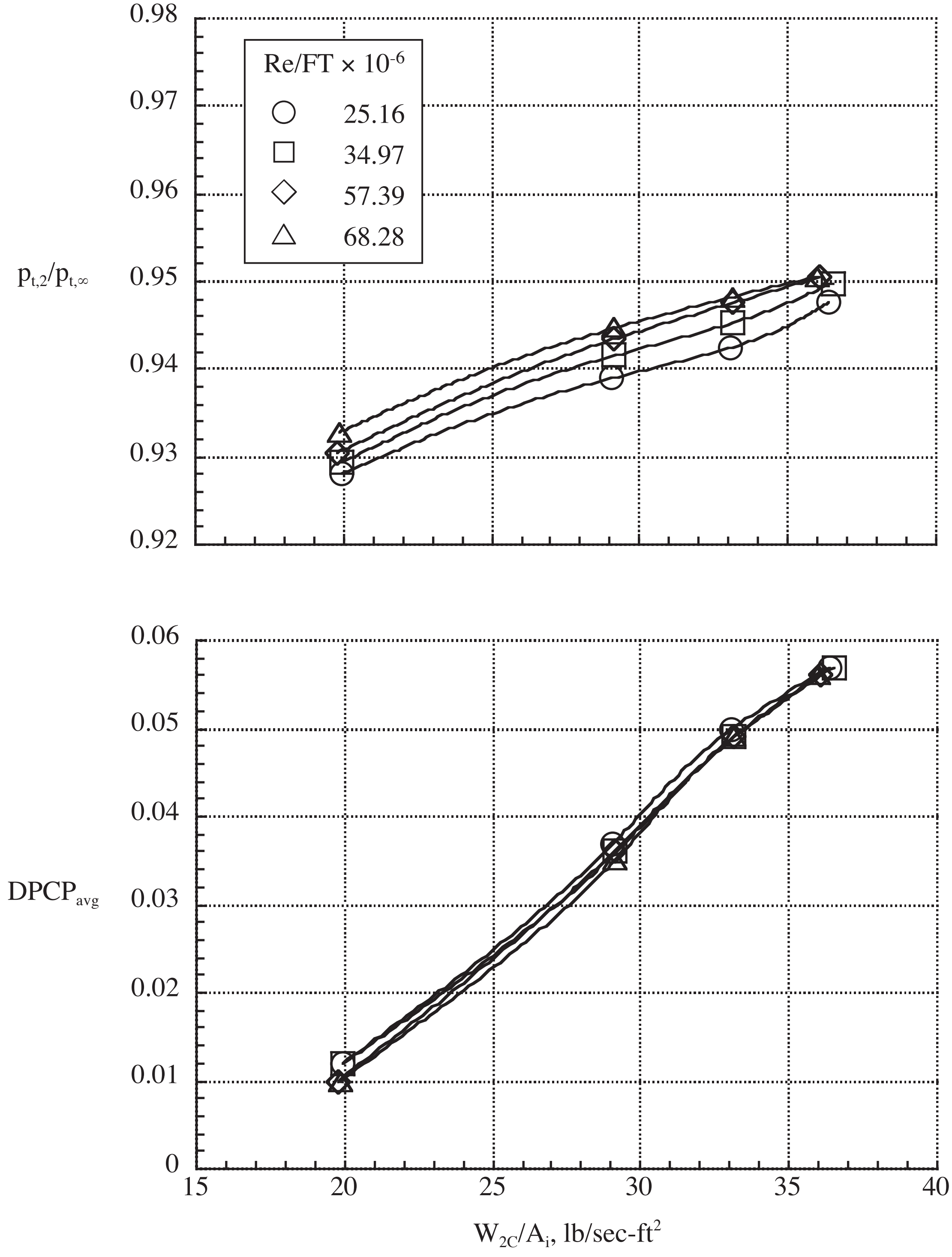

(e) Inlet D, fence off.

Figure 31. - Concluded.

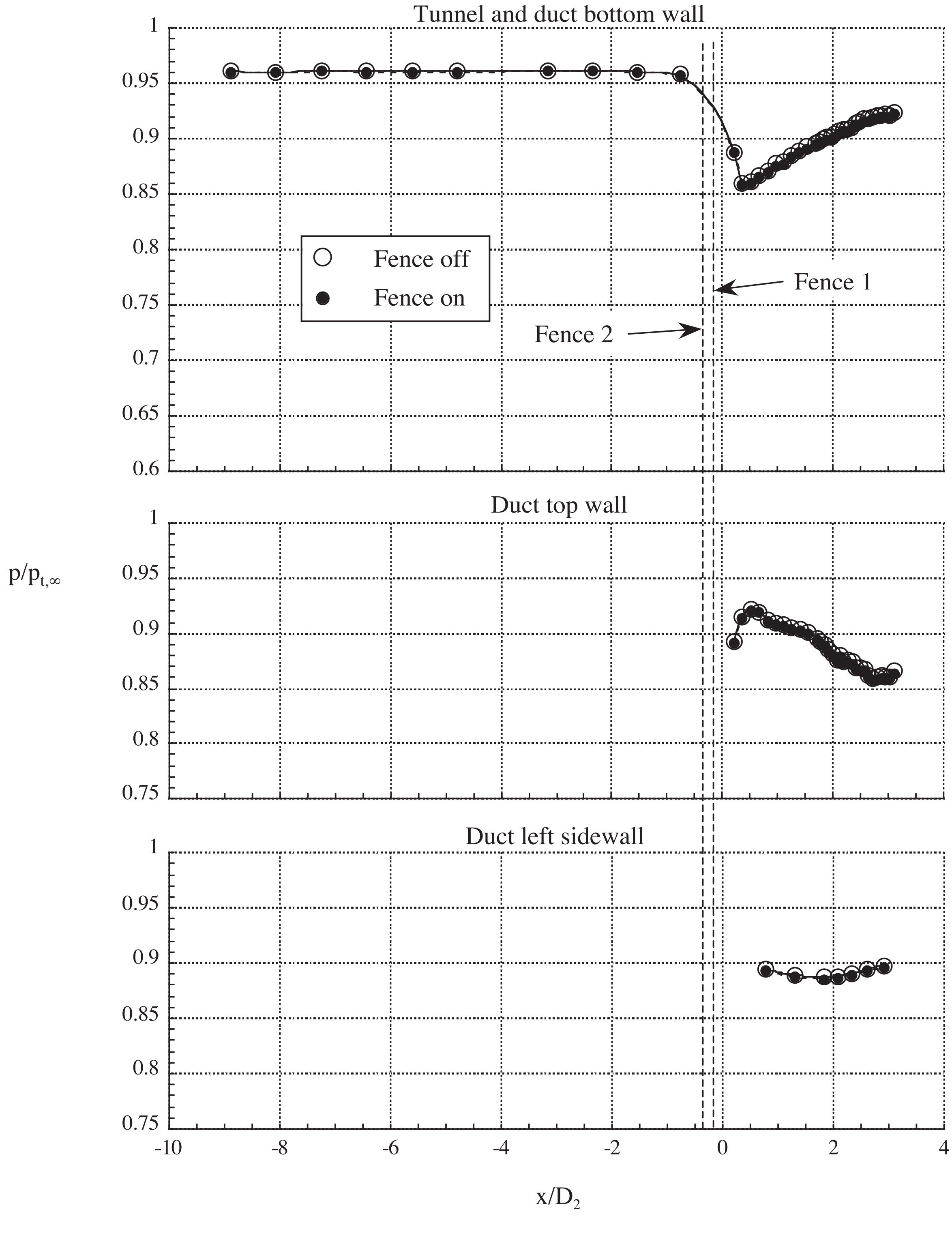

(a) M = 0.251, Re/FT = 33.94 x 10^6, A_0/A_C = 1.161, W_{2C}/A_i = 31.60 lb/sec-ft^2.

Figure 32.- Effect of boundary layer fence on Inlet A duct pressure distributions.

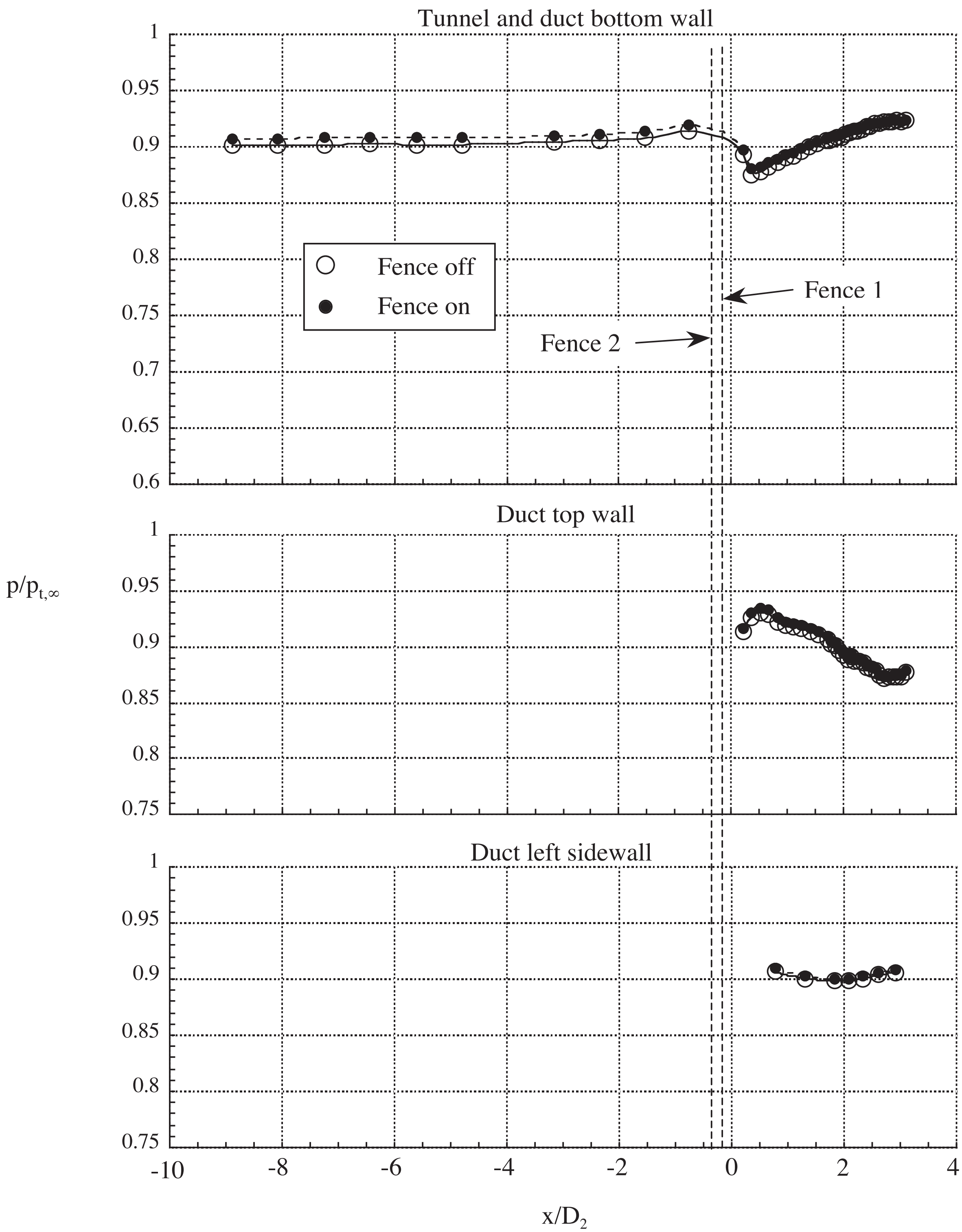

(b) $M = 0.401$, $Re/FT = 51.46 \times 10^6$, $A_0/A_C = 0.714$, $W_{2C}/A_i = 29.44$ lb/sec-ft^2.

Figure 32.- Continued.

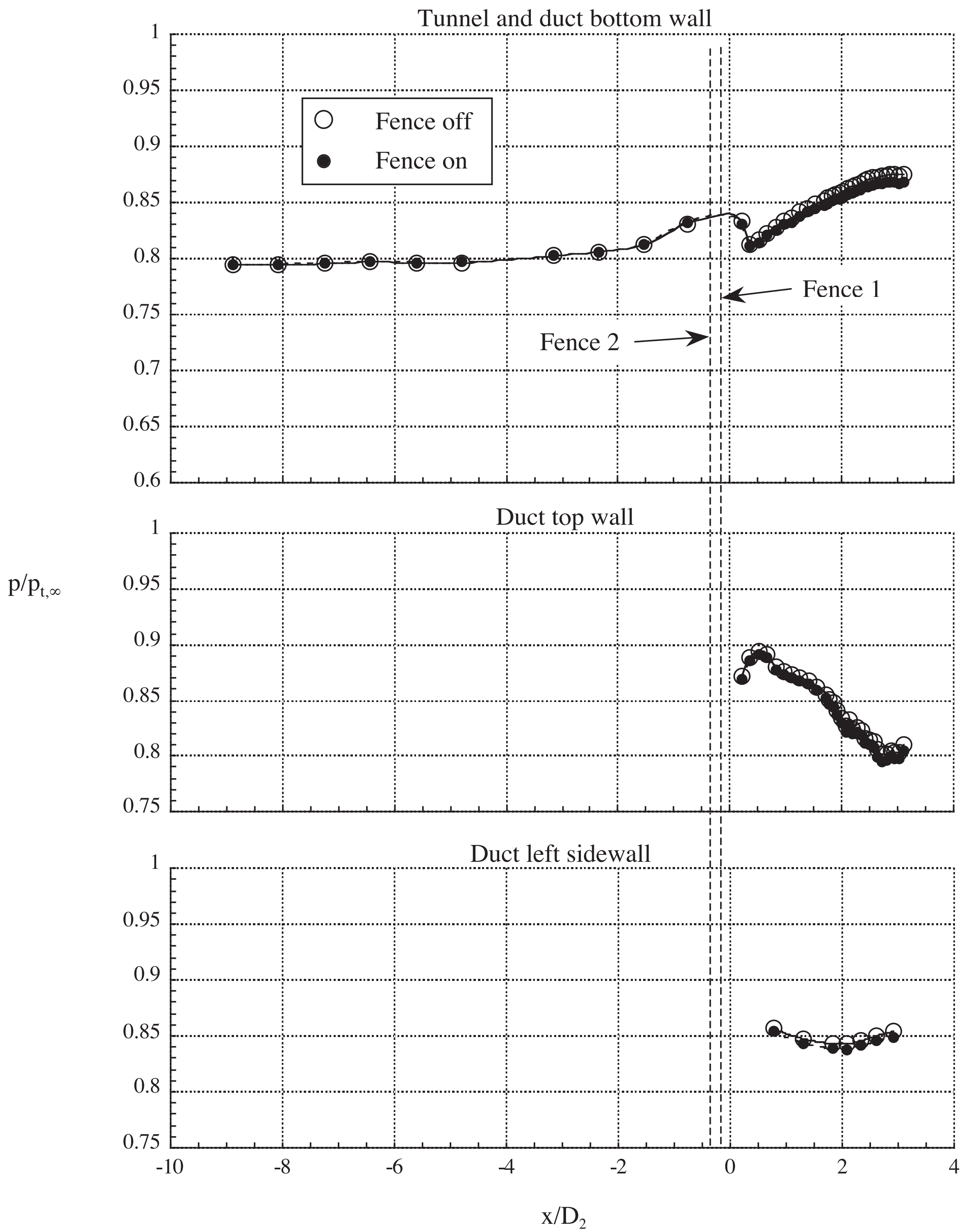

(c) M = 0.603, Re/FT = 68.69 x 10^6, A_0/A_C = 0.627, W_{2C}/A_i = 35.06 lb/sec-ft^2.

Figure 32.- Continued.

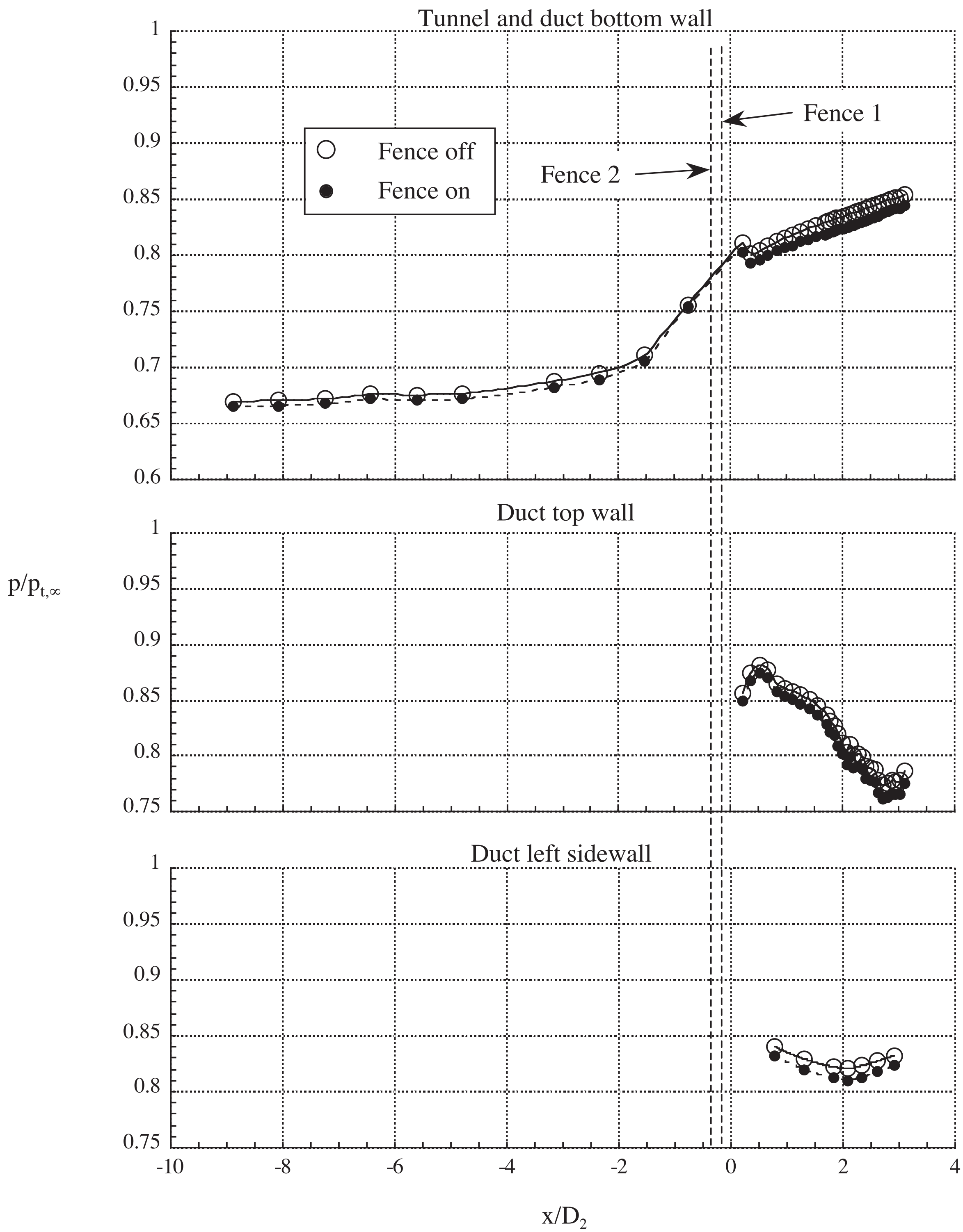

(d) M = 0.809, Re/FT = 68.58 x 10^6, A_0/A_C = 0.545, W_{2C}/A_i = 35.47 lb/sec-ft^2.

Figure 32.- Continued.

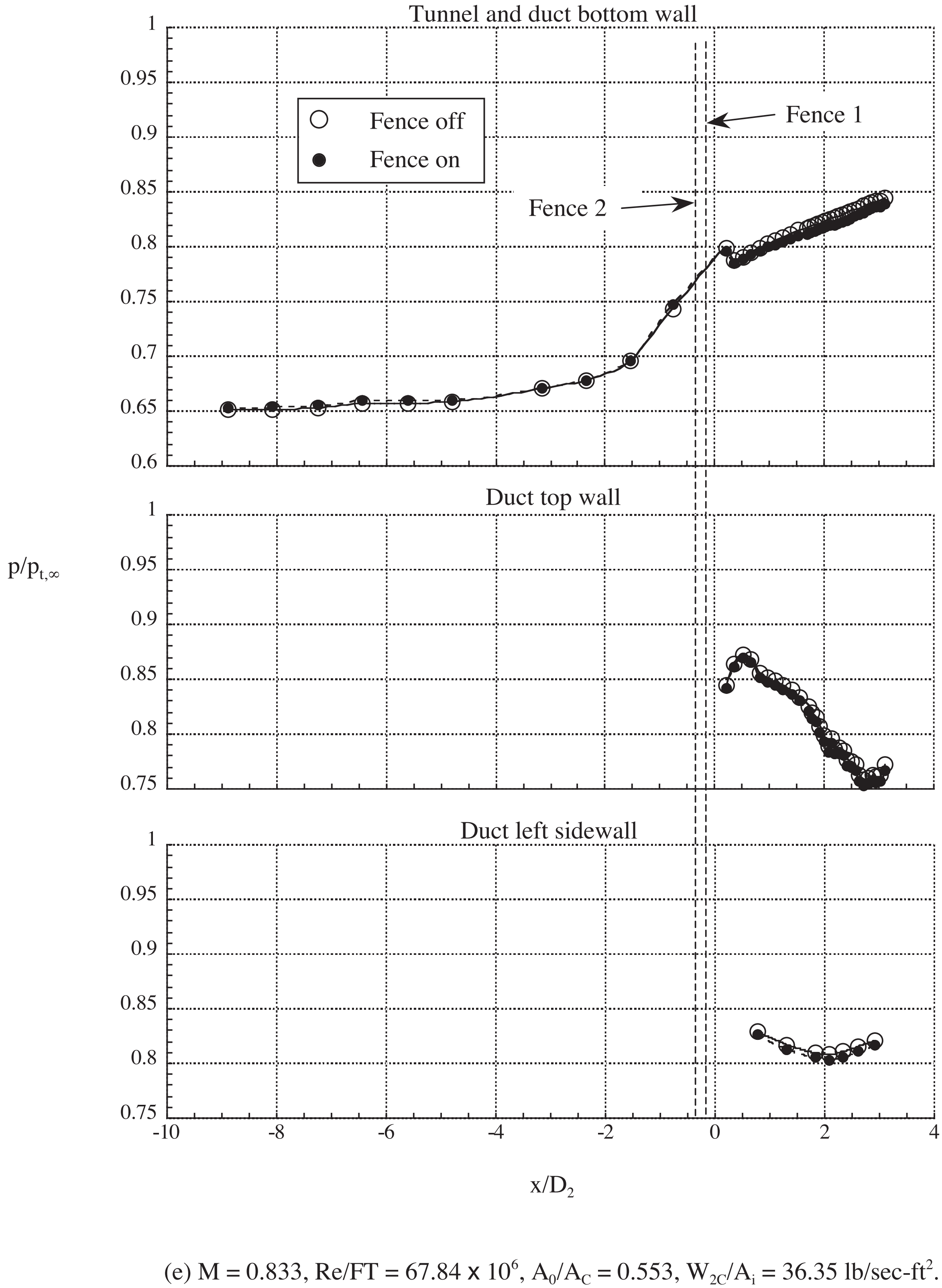

(e) M = 0.833, Re/FT = 67.84 x 10^6, A_0/A_C = 0.553, W_{2C}/A_i = 36.35 lb/sec-ft^2.

Figure 32.- Concluded.

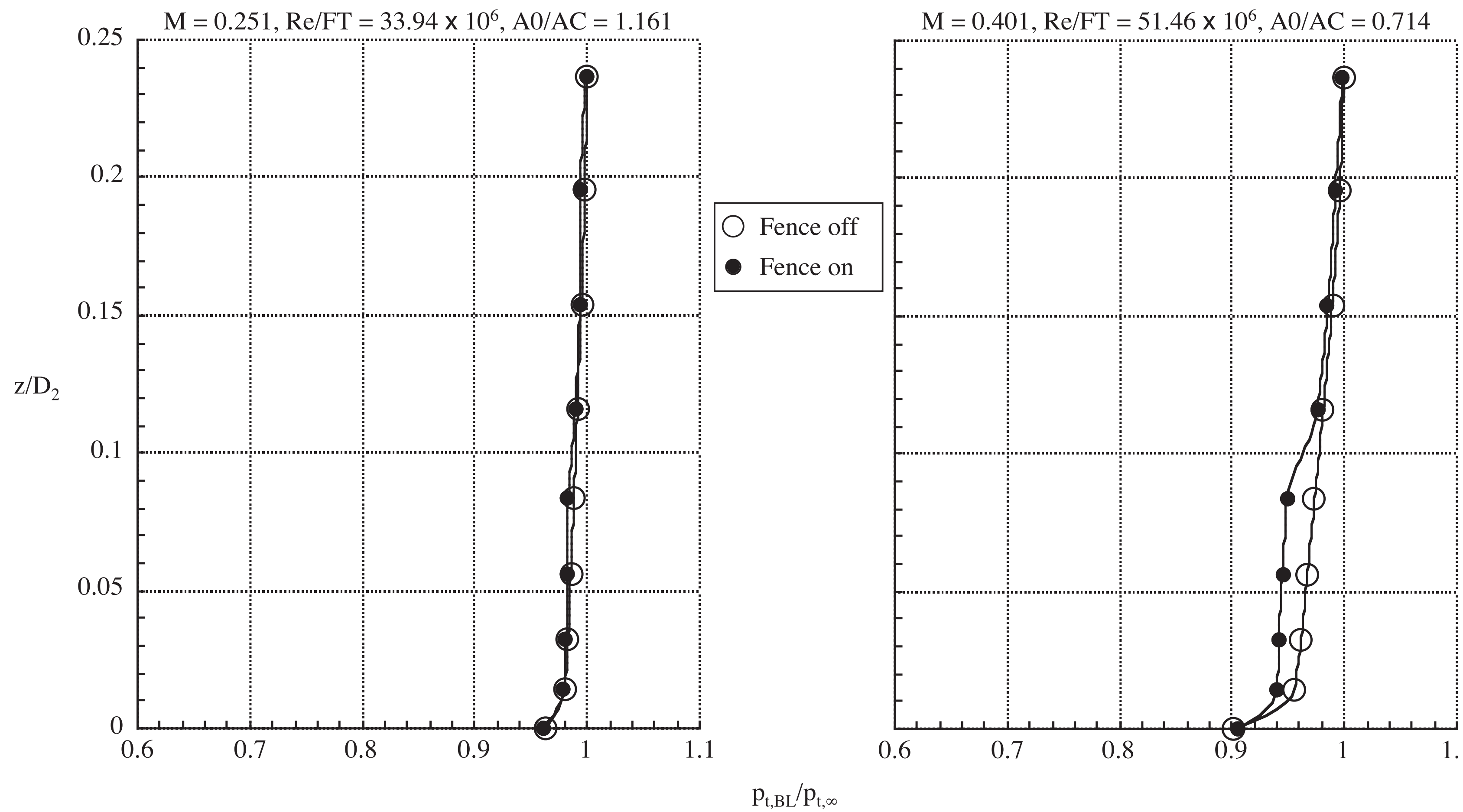

(a) M = 0.251 and M = 0.401.

Figure 33.- Effect of fence on tunnel wall boundary layer profiles. Inlet A.

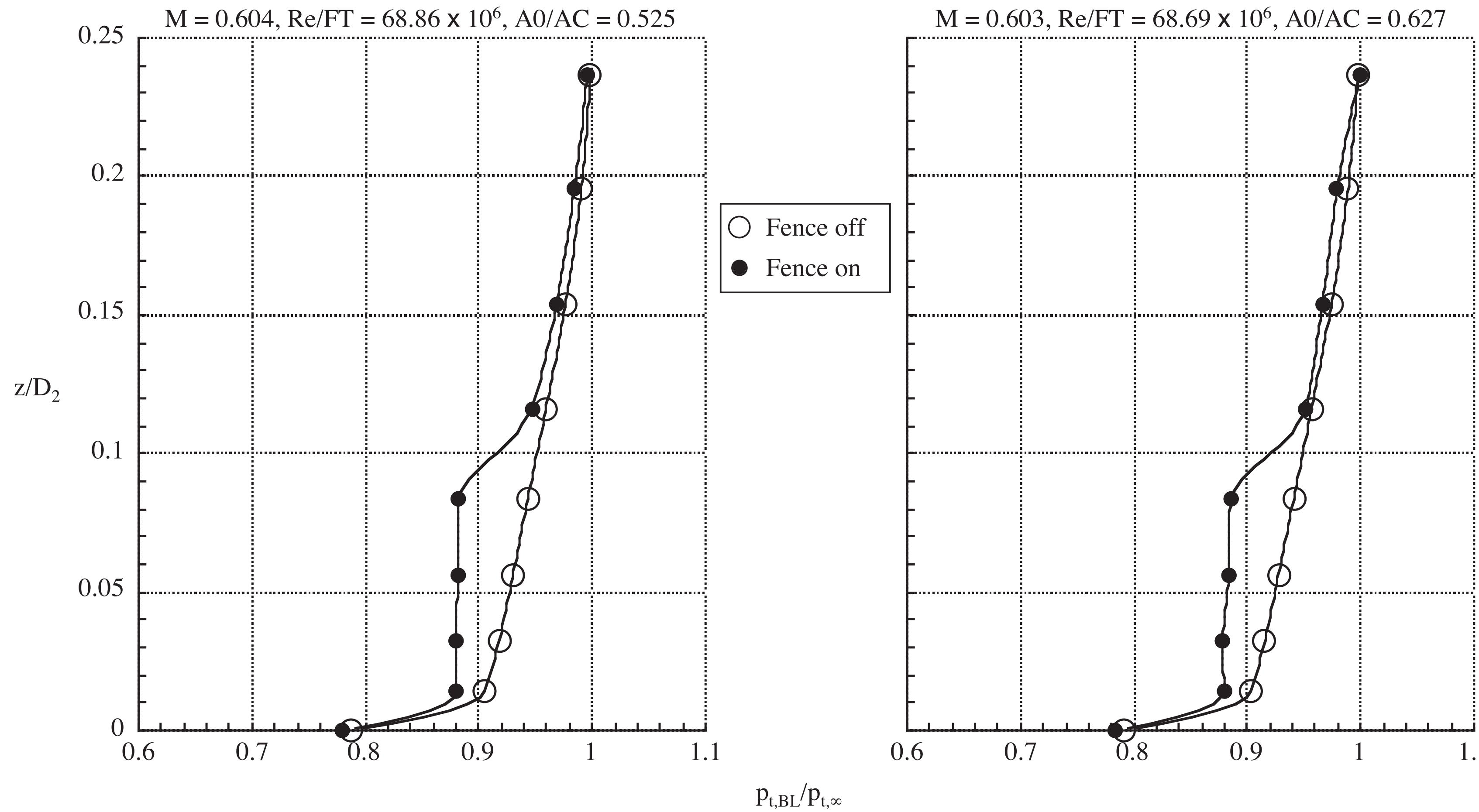

(b) M = 0.60.

Figure 33.- Continued.

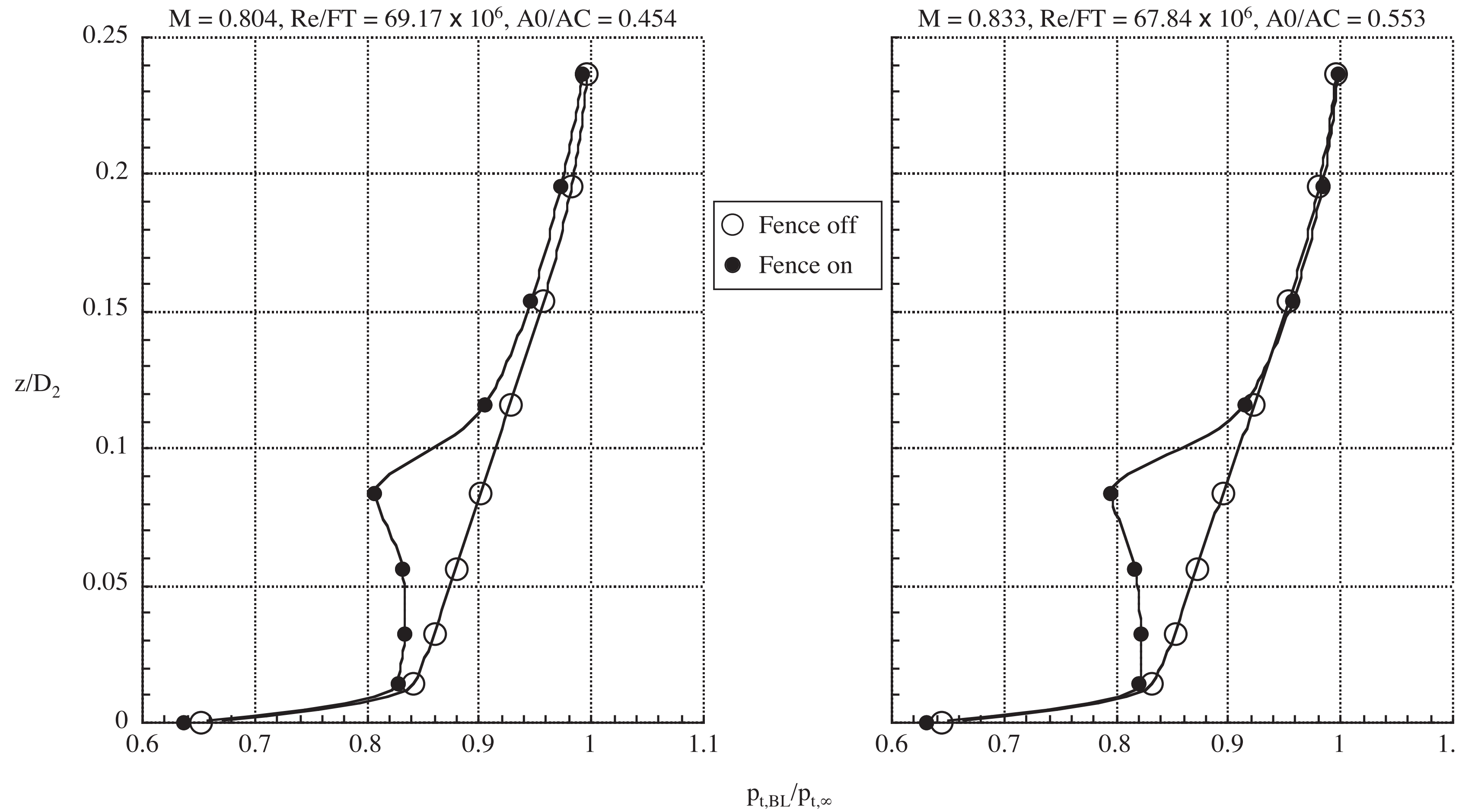

(c) M = 0.804 and M = 0.833.

Figure 33.- Concluded.

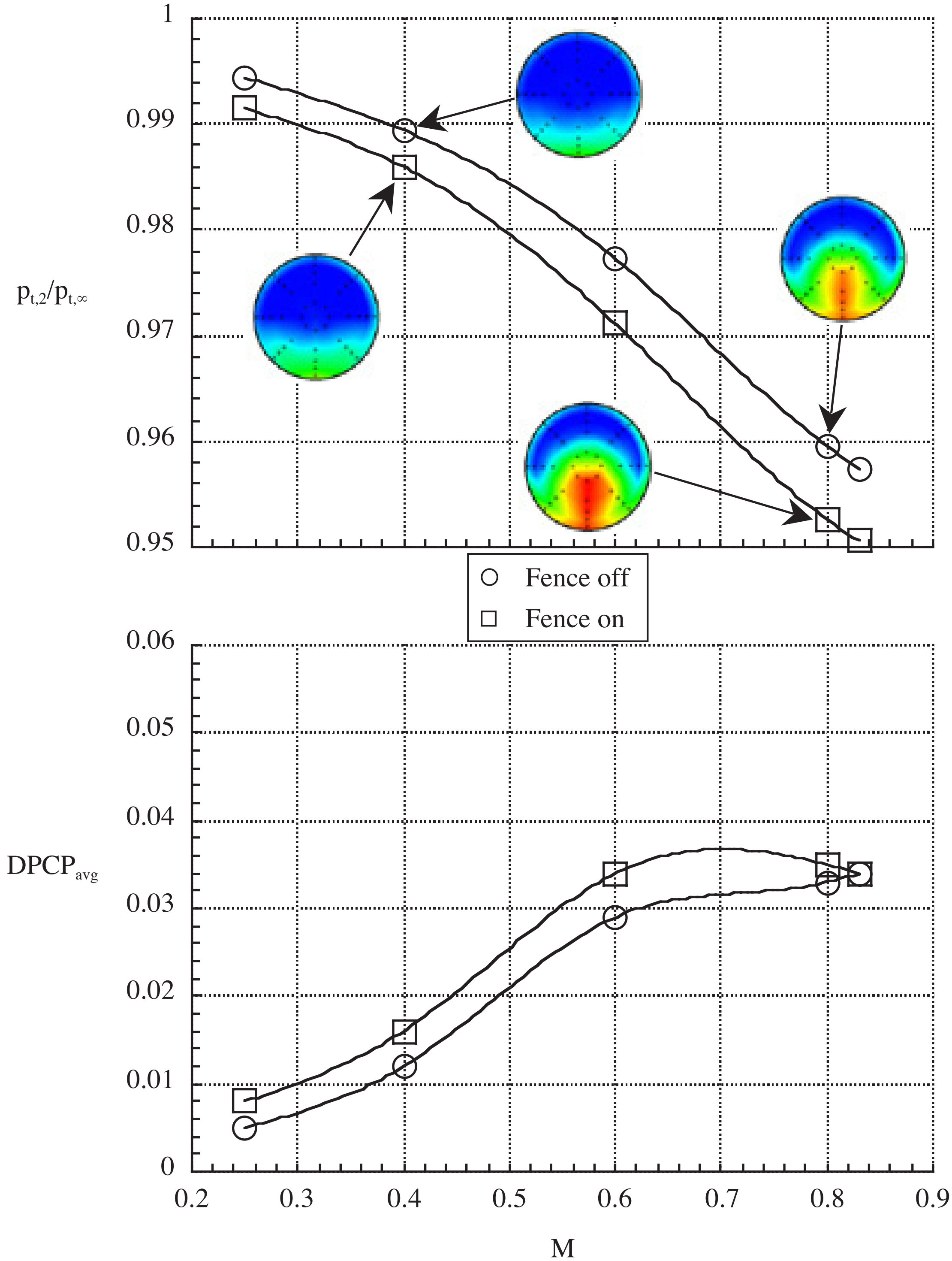

(a) $W_{2C}/A_i = 29.40$ lb/sec-ft^2.

Figure 34. - Effect of distorted entrance boundary layer profile on inlet performance.

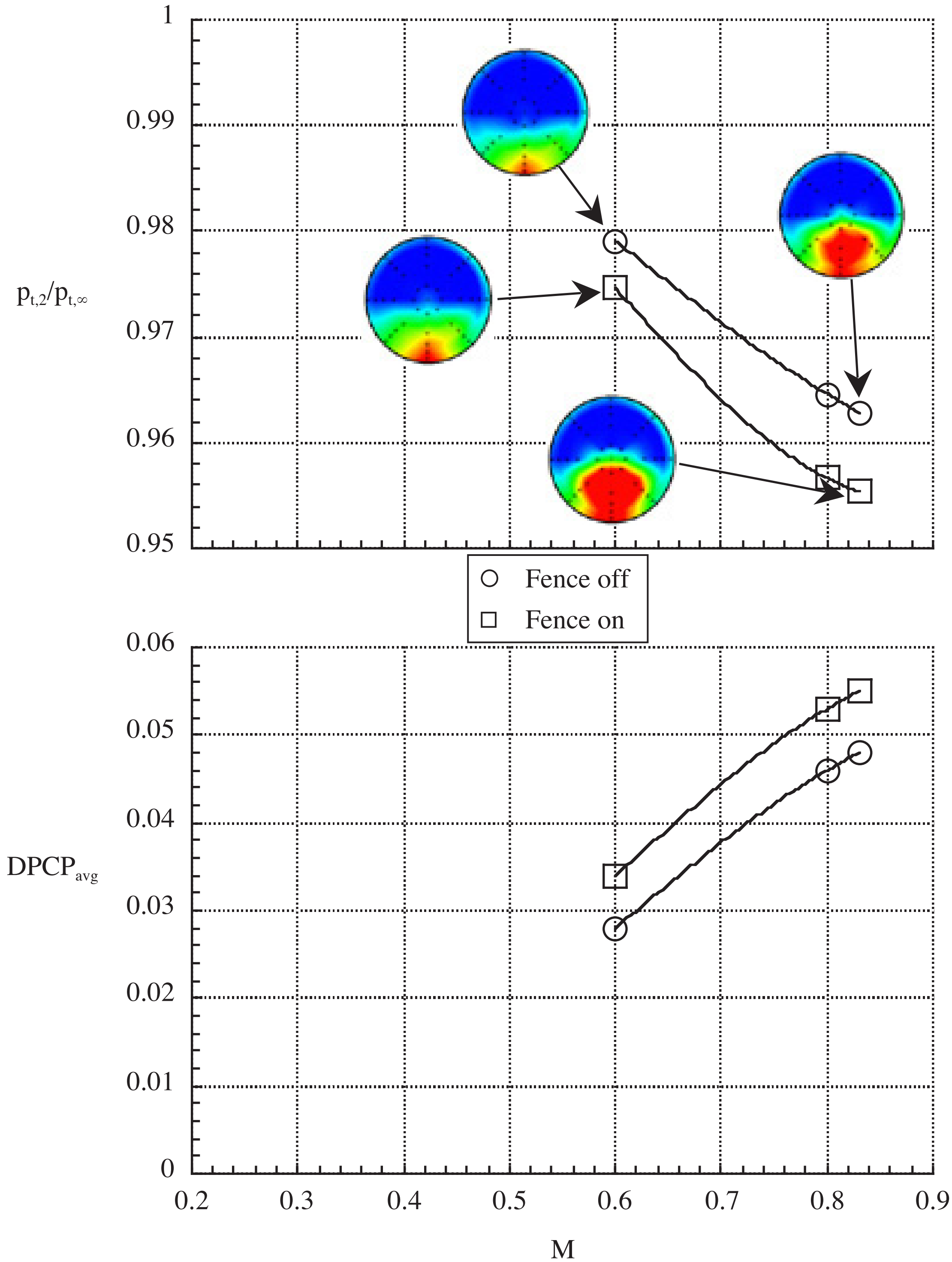

(b) W_{2C}/A_i = 35.66 lb/sec-ft^2.

Figure 34. - Concluded.

REPORT DOCUMENTATION PAGE

Form Approved
OMB No. 0704-0188

1. REPORT DATE *(DD-MM-YYYY)*	2. REPORT TYPE	3. DATES COVERED *(From - To)*
01- 09 - 2005	Technical Publication	

4. TITLE AND SUBTITLE
High Reynolds Number Investigation of a Flush-Mounted, S-Duct Inlet With Large Amounts of Boundary Layer Ingestion

5a. CONTRACT NUMBER

5b. GRANT NUMBER

5c. PROGRAM ELEMENT NUMBER

6. AUTHOR(S)
Berrier, Bobby L.; Carter, Melissa B.; and Allan, Brian G.

5d. PROJECT NUMBER

5e. TASK NUMBER

5f. WORK UNIT NUMBER
23-066-50-AE

7. PERFORMING ORGANIZATION NAME(S) AND ADDRESS(ES)
NASA Langley Research Center
Hampton, VA 23681-2199

8. PERFORMING ORGANIZATION REPORT NUMBER
L-19131

9. SPONSORING/MONITORING AGENCY NAME(S) AND ADDRESS(ES)
National Aeronautics and Space Administration
Washington, DC 20546-0001

10. SPONSOR/MONITOR'S ACRONYM(S)
NASA

11. SPONSOR/MONITOR'S REPORT NUMBER(S)
NASA/TP-2005-213766

12. DISTRIBUTION/AVAILABILITY STATEMENT
Unclassified - Unlimited
Subject Category 02
Availability: NASA CASI (301) 621-0390

13. SUPPLEMENTARY NOTES
Berrier, Carter, and Allan, Langley Research Center, Hampton, VA.
An electronic version can be found at http://ntrs.nasa.gov

14. ABSTRACT
An experimental investigation of a flush-mounted, S-duct inlet with large amounts of boundary layer ingestion has been conducted at Reynolds numbers up to full scale. The study was conducted in the NASA Langley Research Center 0.3-Meter Transonic Cryogenic Tunnel. In addition, a supplemental computational study on one of the inlet configurations was conducted using the Navier-Stokes flow solver, OVERFLOW. Tests were conducted at Mach numbers from 0.25 to 0.83, Reynolds numbers (based on aerodynamic interface plane diameter) from 5.1 million to 13.9 million (full-scale value), and inlet mass-flow ratios from 0.29 to 1.22, depending on Mach number. Results of the study indicated that increasing Mach number, increasing boundary layer thickness (relative to inlet height) or ingesting a boundary layer with a distorted profile decreased inlet performance. At Mach numbers above 0.4, increasing inlet airflow increased inlet pressure recovery but also increased distortion. Finally, inlet distortion was found to be relatively insensitive to Reynolds number, but pressure recovery increased slightly with increasing Reynolds number.

15. SUBJECT TERMS
Inlet; S-duct, Offset; Boundary layer ingestion; Distortion; Pressure recovery

16. SECURITY CLASSIFICATION OF:			17. LIMITATION OF ABSTRACT	18. NUMBER OF PAGES	19a. NAME OF RESPONSIBLE PERSON
a. REPORT	b. ABSTRACT	c. THIS PAGE			STI Help Desk (email: help@sti.nasa.gov)
					19b. TELEPHONE NUMBER *(Include area code)*
U	U	U	UU	170	(301) 621-0390

Standard Form 298 (Rev. 8-98)
Prescribed by ANSI Std. Z39.18